Holocene ice-ocean interactions in the Ross Sea and Adélie Land regions

Katelyn M Johnson

A thesis
submitted to the Victoria University of Wellington
in fulfillment of the requirements for the degree of
Doctor of Philosophy

Victoria University of Wellington
School of Geography, Environment and Earth Sciences
2020

ABSTRACT

Antarctica's coastal margins are areas of complex oceanographic, atmospheric, and biological interactions. Characterising interactions and change in these regions is important for several reasons. First, variations in sea-ice extent, primary productivity, ocean circulation, and bottom water formation are important components of global heat distribution, the carbon cycle, and climate system. Second, multi-decadal to sub-decadal climate oscillations are inferred to affect sea ice and primary productivity in these areas, yet these influences are hard to quantify due to spatially and temporally limited data sets. Lastly, ice sheet margins resting on continental shelves with retrograded slopes, such as in the Ross Sea and along the Wilkes-Adélie Land Margin, are highly sensitive to climate and oceanographic fluctuations and future warming. Wind-driven changes in ocean currents that transfer heat on to Antarctica's continental shelf, are inferred to be the primary driver of ice shelf thinning and grounding line retreat following the Last Glacial Maximum, and are also leading to freshening of surface waters along Antarctica's continental margins. As the Ross Sea and Wilkes-Adélie Land Margin are thought to produce up to 25% of modern Antarctic Bottom Water and are major carbon sinks, developing high resolution paleoclimate records in these areas critically supports future climate projections.

Two new high-resolution paleoclimate records allow for the reconstruction of ice-ocean-atmosphere interactions throughout the last ∼11,400 years in the Ross Sea and Adélie Land regions. The RICE ice core was drilled at Roosevelt Island at the northeastern edge of the Ross Ice Shelf. The high accumulation rate (∼20 cm water equivalent per year) at the site provides an annually resolved record of ice-ocean-atmosphere interactions in the Ross Sea. Downstream from, and thus influenced by the Ross Sea, lies the Adélie Basin where IODP sediment core U1357B was drilled. Sedimentation rates at this location are higher than any other published marine sediment record and average ∼2 cm/year throughout the Holocene. This creates a unique opportunity to develop a near-annually resolved record which captures biologically influenced sedimentation from one of Antarctic's largest coastal polynyas. The focus of this PhD is to first develop and interpret the IODP U1357B Holocene record. The second is to integrate this record with the RICE ice core in order to understand how each of these regions evolved during the Holocene, and to identify any interactions between these oceanographically linked sites.

Using X-ray Computed Tomography, and supported by X-ray fluorescence data, lipid biomarkers, and other physical properties, a record of near annual biogenic bloom events is developed and linked to changing environmental conditions throughout the Holocene. Baseline shifts in

laminae frequency correspond with changes in El Niño-Southern Oscillation (ENSO) frequency, as noted in other Holocene paleoclimate records. The precise assessment of this relationship is complicated by the fact that the Southern Annular Mode (SAM) and Indian Ocean Dipole (IOD), which moderate the impact of ENSO on Adélie Land, are not yet well defined in the paleoclimate record. In addition, the presence of coastal sea ice appears to play an important role in modulating the oceanographic and biological response to ENSO forcing. This suggests the sea ice state acts as a tipping point in the system to modulate low-to-high latitude teleconnections.

New analysis on previously measured grain size distributions of light and dark laminae, in conjunction with examination of sediment advection rates, and laminae thickness data indicate that these distributions provide a relative estimate of current speed throughout the Holocene. These data indicate wind-driven currents are a primary control on laminae deposition and help drive bloom events through upwelling of nutrients.

Measurement of major ions (Cl^-, NO_3^-, SO_4^{2-}, MSA^- , Na^+, K^+, Mg^{2+}, Ca^{2+}) in the RICE ice core from the Early Holocene (∼10.6 to 7.3 ka BP) are used to characterize aerosol delivery at the RICE site, and provide context for the interpretations of the continuous flow analysis Ca^{2+} record, which has been measured for the entire Holocene. The RICE continuous flow analysis Ca^{2+} and deuterium isotope record are then used in conjunction with data from the Taylor Dome ice core, Talos Dome ice core, and the Adélie Basin sediment core to track changes in atmospheric circulation and biological productivity as the Ross Ice Shelf retreated to its modern-day position.

Two significant events are recorded in all records at ∼8.9-8.5 ka BP and ∼5-4.5 ka BP, and are linked to the reorganization of atmospheric transport pathways and the presence of cooler and fresher surface waters due to the formation of the Ross Ice Shelf cavity. Modification of atmospheric and oceanic systems as the Ross Ice Shelf grounding line retreated increased the sensitivity of Adélie Land to changes in the Ross Sea.

Together, this thesis provides a new Holocene reconstruction of current speed and biological productivity in Adélie Land, East Antarctica. Comparison with the RICE ice core record and other Ross Sea records highlight the sensitivity of these regions to one another, and suggest future change in the Ross Sea will have large downstream impacts on primary productivity, Antarctic Bottom Water Formation, and the global carbon cycle.

Contents

List of Tables

List of Figures

ACKNOWLEDGEMNTS

First and foremost, I'd like to thank my supervisors, Rob McKay and Nancy Bertler, for your endless support over the last three years. I am especially grateful for your advice, patience, and open door policy which has made this PhD all the more enjoyable.

Next, the wonderful community within the Antarctic Research Centre. This centre is truly like a family and the support provided to the students is outstanding. Thank you all for making this such an enjoyable place to work the last three years. Special shout out to Michelle and Dao, we all know this place would not run without you. Thank you for going above and beyond to help keep our lives in order.

To Rebecca, Lukas and I could not have measured all those samples without you. Thank you for your guidance, support, and always lending an ear.

Lukas and Abhi, thank you for sharing many hours in the lab, freezer, and in front of Chromeleon together. You all were great fun to work with and made the tough days all the more easier.

This research has been supported by multiple funding sources: the Royal Society of New Zealand Marsden Grant; ARC Endowed Development Fund; VUW Faculty Strategic Research Grants; VUW Submission Scholarships; and the Irene Pestov Memorial Scholarship.

To all the friends who made Wellington a home, thank you for the countless meals, coffees, chats, and good times. I am all the more grateful for your support and selflessness during the last few months.

To my mom, thank you. You have always been my number one supporter and I would not be here without your constant encouragement, love, and strength.

To my siblings, it has been a wild few years for all of us. I am so thankful we have each other and a shared sense of humor.

And to Jamey, thanks for going on this adventure with me. It has been an eventful and awesome ten years – thanks for always reminding me how lucky we are.

DEDICATION

To the ones we lost along the way

Chapter 1

Introduction

1.1 Context and rationale

The marine based sectors of the Antarctic Ice Sheet (AIS) are cited as one of the largest uncertainties for future sea level rise projections as the climate warms, on account of a lack of understanding regarding ice sheet dynamics and ice sheet-ocean interactions (Masson-Delmotte et al., 2013). Marine-based ice sheets have numerous aspects that could make them vulnerable to future warming. Extensive portions of the West Antarctic Ice Sheet (WAIS) margin are characterised by large floating ice shelves which exert back-pressure onto the ice sheet and act as buttresses, preventing the ice sheet from flowing rapidly into the ocean. In addition, many regions of the AIS rest on reverse sloping continental shelves, including in West Antarctica and the Wilkes Land margin, and are susceptible to Marine Ice Sheet Instability (MISI), a runaway process of grounding line retreat (Weertman, 1974; Schoof, 2007). Models indicate that the loss of the Ross Ice Shelf, combined with the reverse slope bathymetry, would lead to runaway retreat of the WAIS and is largely the consequence of the Ross Ice Shelf's sensitivity to the ocean (Pollard and DeConto, 2009). Recent models also suggest that many of the EAIS marine-based sectors are also vulnerable to significant ice loss under moderate scenarios of future atmospheric and oceanic warming (Golledge et al., 2015; DeConto and Pollard, 2016; Rignot et al., 2019). Today, iceberg calving and ocean-forced melting of floating ice shelves are the primary ways the AIS loses mass (Jacobs et al., 1992, 1996; Depoorter et al., 2013; Rignot et al., 2014). Wind driven upwelling of Circumpolar Deep Water (CDW), and subsequent formation of modified Circumpolar Deep Water (mCDW) which circulates under ice shelves, is currently observed to be a leading cause of ice shelf thinning and ice sheet mass balance loss in the West Antarctic (Wåhlin et al., 2010; Pritchard et al., 2012; Favier et al., 2014; Ja-

cobs et al., 2011). While mCDW incursions are comparatively limited under the Ross Ice Shelf (RIS) today, wind driven incursions of CDW onto Antarctic continental shelves are increasing (Dinniman et al., 2012; Pritchard et al., 2012; Jacobs et al., 1992). Additionally, despite the absence of large ice shelves in East Antarctica, thinning of outlet glaciers due to these oceanic processes is also thought to be occurring along the Wilkes Land margin (Rignot et al., 2013; Miles et al., 2016; Rignot et al., 2019). Long considered stable, recent evidence suggest this part of East Antarctica is also susceptible to MISI due to the reverse bed slope of the Aurora and Wilkes Subglacial Basins (Cook et al., 2014; Young et al., 2011).

As water mass exchange and ocean circulation on the continental shelf play an important role in ice sheet mass balance, understanding the long term trends, as well as the drivers of variability of this exchange is important for future predictions. However, ocean circulation on Antarctica's continental shelves are highly dynamic, and a result of the interplay between complex atmospheric and oceanographic systems. These systems in turn have large implications for biological productivity which are a critical component to Earth's climate system via the carbon cycle. Strong katabatic winds flowing off the Antarctic continent drive sea ice away from the coast and form latent heat polynyas, areas within the sea ice zone which have little to no sea ice year-round (Smith et al., 1990; Barber and Massom, 2007). Due to the surface cooling of katabatic winds, polynyas are areas of active sea ice production, contributing up to 10% of the total sea ice produced in all of the Southern Ocean (Tamura et al., 2008, 2016). Brine rejection from these polynyas contributes to the formation of dense shelf waters and other precursor water masses to Antarctic Bottom Water (Cavalieri and Martin, 1985; Bindoff et al., 2000, 2001). Formation of these dense shelf waters on the reverse slope continental shelf results in density-driven transport of heat towards the grounding line, acting to melt the base of ice shelves (Jacobs et al., 1992; Jenkins, 1991). Polynyas and the marginal ice zone are also areas of high primary productivity (Smith and Nelson, 1986; Arrigo and van Dijken, 2003; Arrigo and Van Dijken, 2004), and as such are important part of Antarctic ecosystems and the Southern Ocean's ability to act as a CO_2 sink (Arrigo et al., 2008a).

The advection of sea ice and water masses from polynyas are also partially driven by katabatics, as these winds turn offshore and merge with the nearshore easterly winds (Parish and Bromwich, 1987). These winds help drive the Antarctic Coastal Current and Antarctic Slope Current, which are fundamental in regulating water mass exchange around the continental margin, and between the Antarctic Continental Shelf and Southern Ocean (Whitworth, 1988; Gill, 1973; Heywood et al., 1998; Thompson et al., 2018). Any changes in wind strength, and subsequent current strength affect the delivery of heat, salt, and nutrients to the margins of Antarctica's marine based ice sheets, hence these currents are a first order control on ice sheet

mass balance, bottom water formation, and primary productivity (Jacobs et al., 1992; Whitworth et al., 1998; Carter et al., 2008; Joughin and Alley, 2011; Moreau et al., 2019; Williams et al., 2016). Recent changes in surface water properties related to these wind-driven currents, including upwelling processes and advection of glacial and seasonal sea ice meltwater from the Amundsen and Ross Sea sectors, are already altering Antarctic Bottom Water formation processes in the Ross Sea and Adélie Land regions (Jacobs et al., 2002; Aoki et al., 2005; Rintoul, 2007; Spence et al., 2014; Haumann et al., 2014; Thompson et al., 2018). Primary productivity is also affected, as upwelling of mCDW and meltwater from sea ice and glaciers, modulate primary productivity by providing nutrients and affecting stratification, but the response is not the same in all regions (Moreau et al., 2019; Death et al., 2014; Gerringa et al., 2012; Arrigo et al., 2015). Modelling studies suggest a reduction in AABW formation due to increased meltwater will weaken global thermohaline circulation (Kusahara and Hasuma, 2013), but the impact of ice sheet change on primary production and Southern Ocean carbon uptake are unclear (Gruber et al., 2019).

Collapse of the West Antarctic Ice Sheet due to ice shelf thinning and MISI, the shutdown of Antarctic Bottom Water Formation, or alteration of the Southern Ocean's role as a global carbon sink are considered critical thresholds, or "Tipping Points" in the global climate system (Lenton et al., 2008; IPCC, 2019; Hoegh-Guldberg et al., 2018). "Tipping points" in this state refer to a critical threshold at which the response of a system changes abruptly to perturbations or forcings, even if the changes precipitating the threshold occurred gradually, and have the profound ability to completely alter the global climate system (Lenton et al., 2008; IPCC, 2019). As atmospheric and oceanic dynamics along Antarctica's coastal marine margins play a key role in these tipping points, high-resolution paleoclimate records along these margins are necessary to deconvolve natural variability from present change and to help identify what these tipping points may be. Holocene reconstructions are particularly useful, as the dynamic retreat of the Ross Ice Shelf during the Holocene may provide an analogue for recent and future change.

1.2 Research objectives

The focus of this thesis to develop two annually-resolved paleoclimate records in the Ross Sea and Adélie Land margin to identify the drivers of variability in atmospheric circulation, sea ice extent, primary productivity, and ocean circulation throughout the Holocene. The first record, and primary focus of this thesis is IODP sediment core U1357B, a continuously laminated Holocene record from Adélie Land, East Antarctica. The second record is from the Roosevelt Island Climate Evolution project (RICE) ice core, from the eastern Ross Sea, which lies oceano-

graphically upstream from Site U1357. Both of these records are influenced by large polynya systems and are major sites of Antarctica Bottom Water formation. As such, both records provide a plethora of information on how oceanographic and biological systems interact during times of deglaciation or change due to various climate modes of variability. Furthermore, these records provide the first opportunity to integrate a marine and ice core record at near comparable resolution and data precision. In this thesis, the following questions are addressed:

1. *What are the environmental controls on the depositional processes in Adélie Land?* Areas near polynyas have high biologically influenced particle flux to the sea floor (Dunbar et al., 1998; Cooper et al., 2002). Continuous light and dark laminations found in IODP sediment core U1357B suggest persistent, biologically influenced sediment advection in the Adélie Basin. However, to understand how biological activity has changed through time (objective #2), it is essential to first understand how sediment is advected to the site. In addition, understanding sediment advection can provide insights into the environmental drivers of laminae thickness and frequency.

2. *What are the drivers of biological productivity in Adélie Land and how has this changed through the Holocene?*

   Most modern day studies on Antarctic primary productivity are limited to satellite based or numerical model methods (e.g. Arrigo et al., 1997; Arrigo and van Dijken, 2003; Moore and Abbott, 2000) or are temporally limited (e.g. Moreau et al., 2019; Smith et al., 2000; Vaillancourt et al., 2003), and therefore provide incomplete records of Antarctic primary productivity (Arrigo et al., 2008b). Primary productivity on Antarctica's coastal margins is a dominant force in the Southern Ocean's role as a CO_2 sink, but predictions of how this will change due to future climate change is uncertain (Gruber et al., 2019). Paleoclimate reconstructions of bloom events can provide longer term records of how primary productivity responds to changing environmental conditions, and to long and short term climate oscillations. This information is critical to understanding the response of the carbon cycle to future climate change.

3. *How does the observed environmental change at Roosevelt Island and Adélie Land correspond to known Ross Ice Shelf grounding line dynamics?* The timing and pattern of the retreat of the Ross Ice Shelf (RIS) is a subject of much debate. Various suggestions have been put forth, but lack of age constraints on these models inhibit further determination. Given that IODP Site U1357 is oceanographically downstream from the Ross Sea, both records in this project are likely to be profoundly affected by changes in the Ross Ice Shelf

grounding line. Through comparison of the RICE, Taylor Dome, and TALDICE ice cores, and the Adélie Basin sediment core, regional change of sea ice extent, atmospheric circulation, and primary productivity are discussed in relation to Ross Ice Shelf grounding line retreat.

1.3 Thesis outline

The collection, processing, and data set development of the RICE ice core and IODP U1357B are the products of massive, international scientific collaboration, of which this thesis is a component. Members of both the RICE community and IODP Expedition 318 scientists (which collected U1357) have contributed datasets to this thesis which are essential to maximise the datasets I have obtained and enhance the interpretations in this thesis. Contributions of other authors are noted in the subsections below, but I have taken the lead in the integrated interpretation of all datasets presented here.

This thesis is divided into seven chapters. The following format is used to develop the Adélie sediment core and RICE ice core records, and address the objectives above.

1.3.1 Chapter 2

Chapter 2 provides a brief overview of the Holocene epoch (∼11.7 ka BP to present), before providing a more detailed review of Antarctica's evolving ice sheet as it retreated from its maximum extent during the Last Glacial Maximum (∼26 to 19 ka BP) towards its present-day configuration. A discussion of the main climatic and oceanic controls influencing Antarctica in the modern day is also provided, highlighting the role of the Antarctic Ice Sheet and Southern Ocean in the global climate system. Finally, the chapter concludes with site specific geologic, oceanic, and climatic information for both Adélie Land and the Ross Sea region to provide context for the paleoclimate records and interpretations discussed within this thesis.

1.3.2 Chapter 3

Chapter 3 outlines the methodology for analysing the U1357B and RICE ice core records.

The first section outlines the acquisition and processing of the X-ray Computed Tomography (CT) data to obtain a high resolution record of laminae deposition at IODP Site U1357. Integral to the interpretation of this dataset is the development of the age model which was

developed by Rob Dunbar (Stanford University, United States) and Rob McKay (Victoria University of Wellington, New Zealand), but is currently unpublished, and therefore, detail on the current state of this age model is provided here. However, this work on laminae frequency is a fundamental addition to the age model, as it provides independent assessment of shifts in sedimentation rates that helps to validate the age model by ^{14}C dating. Supporting unpublished datasets to characterise the geochemical nature of the laminae in the core are also discussed, but were analysed by other scientists working on IODP site U1357 in collaboration with this work. The continuous line scan X-ray fluorescence (XRF) dataset provided by Francis J. Jiménez-Espejo (University of Granada, Spain), allows for the assessment of the biogenic versus terrigenous content changes between light and dark laminae, while lower resolution lipid biomarker (Highly Branched Isoprenoids) datasets, were provided by Johan Etourneau (University of Bordeaux, France) and provide insights into background shifts in sea ice state that may influence laminae deposition.

The IODP methods provide key insights essential for all of the following chapters. Consequently, numerous components of this chapter, in conjunction with data from Chapter 4 were combined and submitted (mostly as supplementary material) for a short format manuscript (centered on the results in Chapter 5) entitled, "El Niño-Southern Oscillation Influences on East Antarctic Biological Productivity". In addition, aspects of this chapter will be incorporated into collaborative papers on the age model for the U1357 cores, and geochemical papers lead by the authors listed above.

The second section introduces the methodology used to measure major ions (MSA^-, SO_4^{2-}, Cl^-, NO_3^-, Na^+, Ca^{2+}, Mg^{2+}, K^+) in the RICE ice core using ion chromatography (ICS). Additional unpublished datasets measured using continuous flow analysis (CFA) data include deuterium isotopes (δD) and calcium (Ca^{2+}) and were provided by Nancy Bertler (Victoria University of Wellington, New Zealand) and Paul Vallelonga (University of Copenhagan, Denmark), respectively. All of these datasets were used to develop the interpretations of the calcium ion data which is used in Chapter 6.

The development of the RICE ice core record is a substantial collaborative effort involving scientists from nine countries. As such, data sets are developed with agreed protocols that govern the measurement and processing of data to ensure consistency across different teams and laboratories. My contribution to this effort includes the laboratory work and associated data processing of the Early Holocene ICS data. The laboratory work for samples containing the Early Holocene was shared with fellow PhD student Lukas Eling. Processing of the data was performed jointly and any issues arising from the processing was discussed with the ice core team (Nancy Bertler, Rebecca Pyne, Lukas Eling, and Abhijith Ulayottil Venugopal). I

performed the statistical analysis on the data and led the interpretations presented in Chapters 3.

The RICE data contributes to Chapter 6 which integrates the RICE ice core and IODP U1357B records. While the Early Holocene data will be incorporated into several standalone publications led by myself and Lukas Eling, the complete integration of the RICE and IODP U1357B record is a focus over the next several years.

1.3.3 Chapter 4

Chapter 4 establishes the depositional environment relating to dark and light laminae occurrence in core U1357B. Analyses of mass accumulation rates (MARs) and grain size distributions have previously been performed as part of Albot (2017). In that prior work, there was an attempt to link sedimentological data to laminae frequency derived from core linescan photographs. However, these core photograph data were unreliable due to differential oxidation of the core face after core splitting, resulting in obscuration of subtle laminae features. Consequently, Albot (2017) recommended CT-scanning of the cores to better characterise the laminae in the context of her grain size results. In line with this recommendation, the new CT-scan data derived in this work (Chapter 3) are used to examine how changes in physical sedimentology and laminae thickness differ for light and dark laminae downcore. The XRF-data, and physical core properties, help ground the CT-scan greyscale curve and laminae events as a proxy for high productivity bloom events through the Holocene. New analysis on the grain size data is also presented, including assessment of the sortable silt parameter which was not conducted by Albot (2017). As primary productivity in many parts of the Antarctica's coastal regions is strongly linked to wind-driven upwelling processes, this chapter evaluates how changes in grain size can be used to investigate changes in wind-driven currents, which may influence dark and light laminae characteristics through the Holocene. Further, this investigation aims to provide an understanding of seasonal differences in laminae deposition, as well as centennial to multi-millennial changes in current strength through the Holocene. For this chapter, I performed the analyses and interpretation of the CT-scan data, the evaluation of the sortable silt parameter, and lead the synthesis of all datasets.

1.3.4 Chapter 5

Chapter 5 focuses on sub-decadal drivers of laminae frequency and synthesising all available paleoenvironmental datasets for U1357B into a global context of low-to-high latitude telecon-

nections of Holocene climate.

Chapter 5 has been prepared as a manuscript and is in review as:

Katelyn M. Johnson, Robert M. McKay, Nancy A.N. Bertler, Johan Etourneau, Francis J. Jiménez-Espejo, Anya Albot, Christina R. Riesselman, Huw J. Horgan, Xavier Crosta, James Bendle, Carlota Escutia, Robert B. Dunbar. *El Niño-Southern Oscillation Influences on East Antarctic Biological Productivity*.

1.3.5 Chapter 6

Chapter 6 is the first attempt to correlate isotopic and ion data from the RICE, Taylor Dome, and Talos Dome (TALDICE) ice cores, with the Adélie Drift sediment core to create a Holocene reconstruction of the Adélie Land margin, and the eastern and western Ross Sea. In addition to the datasets developed above, and the published Taylor Dome data, unpublished major ion data from the TALDICE ice core were provided by Rita Traversi (University of Florence, Italy). Large scale shifts in climate are identified in all records and the relative timing of these shifts is compared. This integrated approach allows us to understand how winds, sea ice extent, and biological productivity varied throughout the Holocene and identifies potential linkages between these records as the Ross Ice Shelf retreated. For this chapter, I led the statistical analysis and interpretations of the data sets.

1.3.6 Chapter 7

Chapter 7 summarizes the key results and contributions of this thesis to the wider scientific community. Recommendations for future work are also provided.

Chapter 2

Background

2.1 Climate states of the Holocene Epoch

The current interglacial, the Holocene, began ∼11.7 ka BP (Rasmussen et al., 2006). Globally, the Holocene can generally be characterised into three periods including: a period of gradual warming in Early Holocene from ∼11.7-7 ka BP; a generally stable, but warm Hypsithermal (also referred to as 'Holocene Thermal Maximum', 'Altithermal', 'Holocene Climate Optimum') between ∼8-7 and ∼5-4 ka BP; the cooler neoglacial from ∼4-5 ka BP onward (Walker et al., 2012; Wanner et al., 2011). A further division could be described from AD 1860, to mark warming due the Industrial Era (Wanner et al., 2011; Ljungqvist, 2010). While these shifts represent a global average, there is high regional variability in the relative timing and strength of these trends (Marcott et al., 2013; Wanner et al., 2011)

Antarctic Holocene climate reconstruction derived largely from ice core records, indicate an Early Holocene climate optimum between 11.5 ka and 9.0 ka BP, followed by another warm optimum interval between 7-5 ka BP in the Ross Sea region (Masson et al., 2000). However, East Antarctic ice core records suggest a temperature minimum at 8 ka BP, with the second optimum not occurring until 6 to 3 ka BP. This was then followed by a decline in temperatures (Masson et al., 2000)

Superimposed on these temperature trends are centennial- to millennial-scale fluctuations, which are associated with atmospheric circulation changes leading to aridity changes in the tropics and temperature shifts at the poles (Mayewski et al., 2004). These fluctuations have been attributed to changes in Earth's orbital configuration and solar insolation (Mayewski et al., 2004; Wanner et al., 2015). Eight millennial scale warm events are also evident in the Antarctic ice core records, with an apparent ∼1,200 year periodicity. The climatic signature of these millennial-scale variations is strongest at coastal sites, suggesting a coupling to sea ice and/or

ice shelf processes (Masson et al., 2000).

2.2 Ice sheet retreat from the Last Glacial Maximum through the Holocene

A statistical analysis suggests the timing of Last Glacial Maximum (LGM) was largely synchronous between hemispheres, occurring at ∼22.1 ± 4.3 ka BP in the Northern Hemisphere and ∼22.3 ± 3.6 ka BP in the Southern Hemisphere, when global temperatures were likely ∼4.9°C cooler than during Hypsithermal (Shakun and Carlson, 2010). Peak interglacial conditions were reached during the Early Holocene, around ∼8.0 ± 3.2 ka BP in the Northern Hemisphere and ∼7.4 ± 3.7 ka BP in the Southern Hemisphere (Shakun and Carlson, 2010). However, despite this apparent synchronous behaviour between hemispheres, there was large global variability in the timing of the LGM and subsequent temperature and ice volume change (Clark et al.; Shakun and Carlson, 2010).

During the LGM, the Antarctic Ice Sheet expanded toward the continental shelf edge, but the timing of its maximum extent, as well as its retreat during the LGM to its present day positions is also thought to have varied geographically (Figure 2.1). However, in most regions, ice sheet grounding lines reached the inner shelf by 10 ka BP, with notable exception(s) of the Ross Sea, and possibly the Weddell Sea, embayments (The RAISED Consortium et al., 2014). In the following section, a review of the retreat history near Roosevelt Island and Adélie Land is provided.

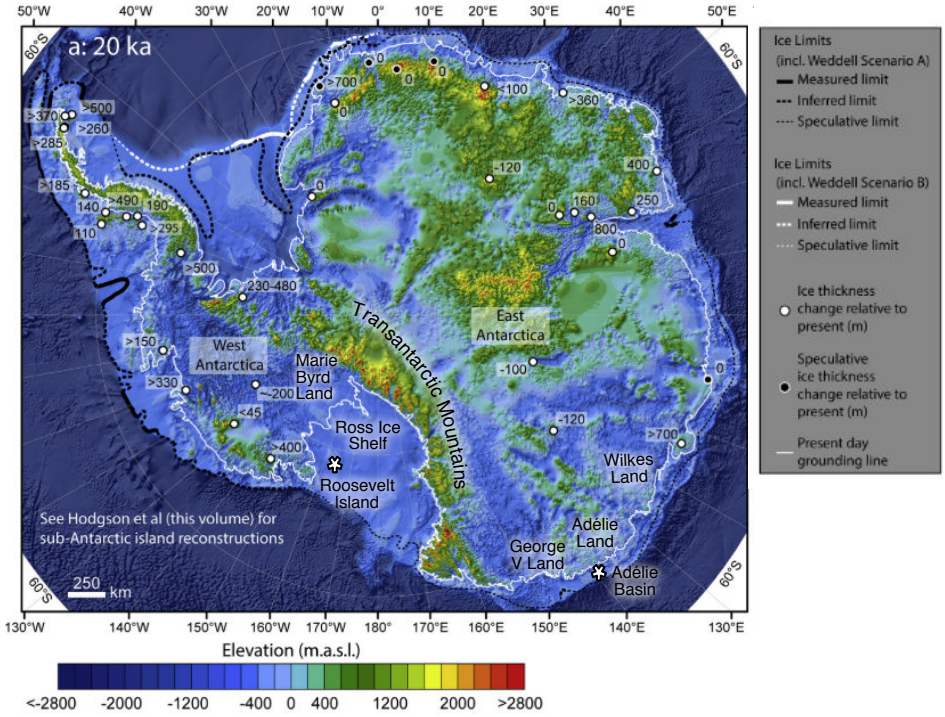

Figure 2.1: **Reconstruction of Antarctic ice extent at 20 ka BP.** Grounding line position at 20 ka and changes in ice sheet thickness relative to present elevation in meters (or reconstructed ice sheet elevation, Ross Sea) are plotted. Speculative grounding lines in East Antarctica and Ross Sea sectors are from (Livingstone et al., 2012), but full discussions of uncertainty can be found in Mackintosh et al. (2014) and Anderson et al. (2014). Weddell scenarios A and B refer to different grounding line positions at 20 ka, with a less extensive position in A. Roosevelt Island and the Adélie Basin are indicated by white stars. Modified from (The RAISED Consortium et al., 2014)

2.2.1 East Antarctica LGM-Holocene ice sheet retreat

The timing and retreat pattern on the East Antarctic Ice Sheet (EAIS) from the LGM into the Early Holocene is not well constrained due to sparse sampling of post-LGM records around the margin, and dating limitations in marine records due to a lack of carbonate material needed to obtain a reliable ^{14}C chronology of the retreat (Mix et al., 2001; Anderson et al., 2002; Mackintosh et al., 2014). Using a range of terrestrial and marine records, Mackintosh et al. (2014) suggested EAIS deglaciation was regionally asynchronous with ice sheet retreat occurring as early as 18 ka BP in the Lambert Glacier/Amery Ice Shelf system, followed by the majority of ice sheet retreat at ∼12 ka BP due to ocean warming (Mackintosh et al., 2011). The ma-

jority of the EAIS margin had reached its present day position by ∼6 ka BP (Goodwin, 1993; Mackintosh et al., 2007).

For the Adélie Land continental margin (136°E - 142°E), there are no onshore records providing geological constraints on the timing and retreat in this region (Mackintosh et al., 2014). Multiple bathymetric features (Section 2.5) along the coastline suggest that outlet glaciers extended to the shelf edge at the LGM, and that the Adélie Basin site (Figure 2.10) was primarily influenced by ice flow from the Zélée and Astrolabe Glaciers (Eittreim et al., 1995; Beaman and Harris, 2003; McMullen et al., 2006; Leventer et al., 2006; Beaman et al., 2011; Mackintosh et al., 2014). Offshore marine sediment records in the Mertz trough and George V Basin are often thin and contain significant amounts of reworked pre-LGM carbon that provide biased ages of the timing of sediment deposition using ^{14}C dating of bulk sediment. This reworking makes dating of retreat difficult in these locations. However, several cores in the Adélie Basin contain expanded sections of diatom ooze that are tens of metres thick and contain minimal input of reworked carbon, making them more reliable to date using ^{14}C dating of bulk sediment (Denis et al., 2009a; Crosta et al., 2007; Escutia et al., 2011; Mackintosh et al., 2014). Diatom oozes obtained from MD03-2601, a 40 m long piston core, are interpreted to reflect open water conditions after ice retreat sometime between ∼11.1 and 10.6 ka BP (Costa et al., 2007; Escutia et al., 2011). However, MD03-2601 did not sample glacial diamict at the base of the datiom ooze, unlike IODP site U1357. The development of the age model of the sediment older than 11,380 years in U1357B is ongoing, but ∼11.5 ka BP provides a likely minimum age estimate for the earliest retreat of grounded ice on the inner shelf to the Adélie Basin (Mackintosh et al., 2014).

In its current configuration, the modern EAIS contains $\sim 21.8 \times 10^6$ km^3 of ice including grounded ice sheets and fringing ice shelves and glacier tongues. It contains approximately 19.2 m of sea level equivalent of ice that is grounded below sea level (Lythe and Vaughan, 2001; Fretwell et al., 2013). While much of the EAIS is generally considered stable due to most of its ice being grounded above sea level (Lythe and Vaughan, 2001; Fretwell et al., 2013), recent research suggest the Wilkes Land Region is undergoing accelerated ice loss, and may become further unstable in the future due to declines in sea ice concentration, and its reverse bed slope (Mengel and Levermann, 2014; Miles et al., 2016; Shen et al., 2018; Rignot et al., 2019).

2.2.2 Ross Sea LGM-Holocene ice sheet retreat

Attempts to reconstruct the Ross Ice Shelf (RIS) grounding line retreat during the Holocene are also ambiguous due to lack of reliable age constraints. The majority of age constraints in the Ross Sea region are based on ^{14}C radiocarbon dates from marine sediments, which, as mentioned previously, can render compromised ages due to reworking of the sediments incorporating younger and/or older carbon into the sample (Andrews et al., 1999; Anderson et al., 2014; McKay et al., 2016).

Conway et al. (1999) proposed the 'swinging gate' model of glacial retreat, whereby the RIS retreated at the end of the Last Glacial Maximum (LGM) southward along the western edge, while becoming pinned around Roosevelt Island on the eastern side (Figure 2.2a). However, recent age constraints from marine sediment cores, seafloor multibeam bathymetric data and model experiments indicate that the RIS retreat commenced from the center (Figure 2.2b), with ice margins along the coast lingering (McKay et al., 2016; Halberstadt et al., 2016; Lee et al., 2017; Lowry et al., 2019). It is theorized that this marine-based ice retreat was initiated by an increase in oceanic heat along the Pacific sector of the WAIS, and the delayed and asynchronous pattern of retreat is caused by the complex bathymetry of the Ross Sea (Golledge et al., 2014; McKay et al., 2016; Halberstadt et al., 2016). Consequently, retreat in this sector of Antarctica continued through the Holocene due to the effects of the reversed slope continental shelf and marine ice sheet instability (Thomas and Bentley, 1978; Schoof, 2007; McKay et al., 2016).

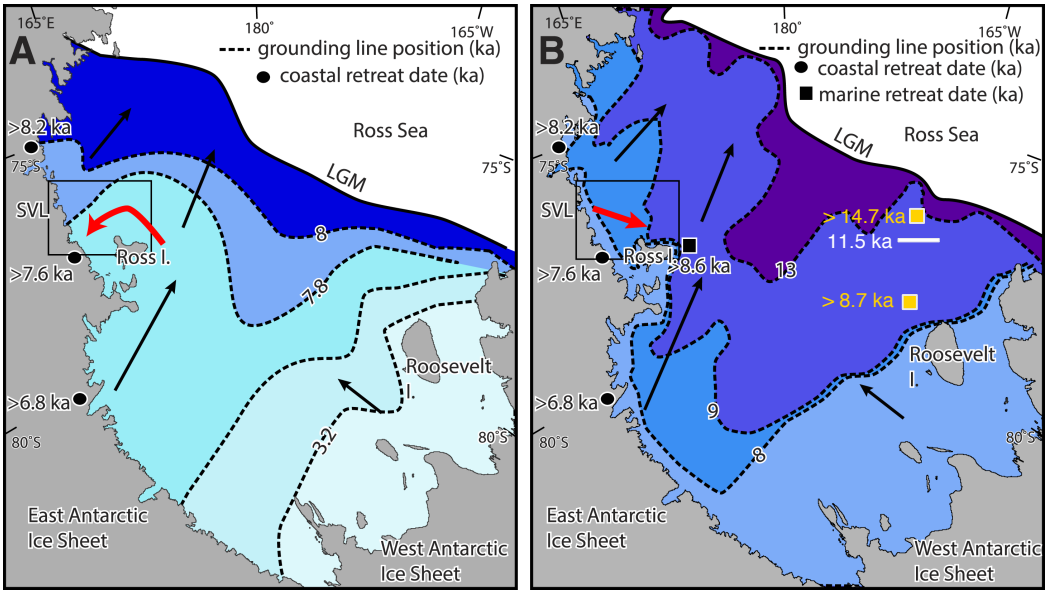

Figure 2.2: (A) Data based reconstruction from Conway et al. (1999) termed the 'Swinging gate', black circles indicate dates used to constrain retreat. Red arrows indicate direction of ice flow during retreat. (B) Data/model based reconstruction of RIS retreat from the center. Black dots and squares indicate dates used to constrain retreat (McKay et al., 2016). Orange squares indicate sub-ice shelf dates from (Bart et al., 2018). White line is estimated grounding line position at 11.5 ka, prior to rapid retreat towards Roosevelt Island (Bart et al., 2018). Red arrows indicate expansion of local outlet glaciers during retreat. Modified from Lee et al. (2017)

While Conway's model suggests retreat solely in the Holocene, McKay et al. (2016) used a numerical model and data-based comparison to propose earlier grounding line retreat in the central Ross Sea Embayment, which may have initiated prior to the Holocene. Building on this, Bart et al. (2018) obtained a series of carbonate derived ^{14}C dates in the eastern Ross Sea that imply a rapid retreat from the outer continental shelf towards Roosevelt Island after 11.5 ka BP (Figure 2.2b). These recent results remain consistent with the central Ross Sea Embayment model of McKay et al. (2016), but further age constraints from the central embayment are required to fully test these hypotheses. The mismatch between chronologies from coastal terrestrial samples and marine sediment cores lies in the fact that coastal ages may in fact represent the final local retreat of EAIS glaciers, rather than the broader embayment itself (Lee et al., 2017)(Figure 2.2).

2.3 The Southern Ocean

The Southern Ocean encompasses the entire Antarctic continent and is connected to all the major oceans through the Antarctic Circumpolar Current (ACC) and thus, influences global climate and ocean circulation (Carter et al., 2008; Rintoul, 2018). The Southern Ocean also plays an important role in the carbon cycle, and is responsible for the uptake of up to 40% of anthropogenic CO_2 (Devries, 2014) and 25% of all global CO_2 (Takahashi et al., 2002). It also influences global biogeochemical cycles by exerting control over nutrient transport to the lower latitudes through sea ice and current interactions (Moore et al., 2018).

2.3.1 Physical oceanography

The main feature of the Southern Ocean is the easterly flowing Antarctic Circumpolar Current (Figure 2.3), which is the world's largest ocean current and connects all the major oceans (Whitworth, 1988; Carter et al., 2008). The ACC's zonal flow inhibits geostrophic meridional flow, thereby isolating the Antarctic continent from the warmer waters to the north (Rintoul et al., 2001; Rintoul, 2018). Zonal surface flow of the ACC is mostly driven by westerly winds, and any meridional surface flow is due to Ekman transport, which drives surface waters primarily northwards (Ekman, 1905; Orsi et al., 1995; Carter et al., 2008; Rintoul et al., 2001; Rintoul, 2018). As surface waters move northwards, southward transport at depth ensues to maintain mass balance in the water column, leading to upwelling of Circumpolar Deep Water (CDW) along the continental slope (Wyrtki, 1961; Rintoul et al., 2001; Carter et al., 2008).

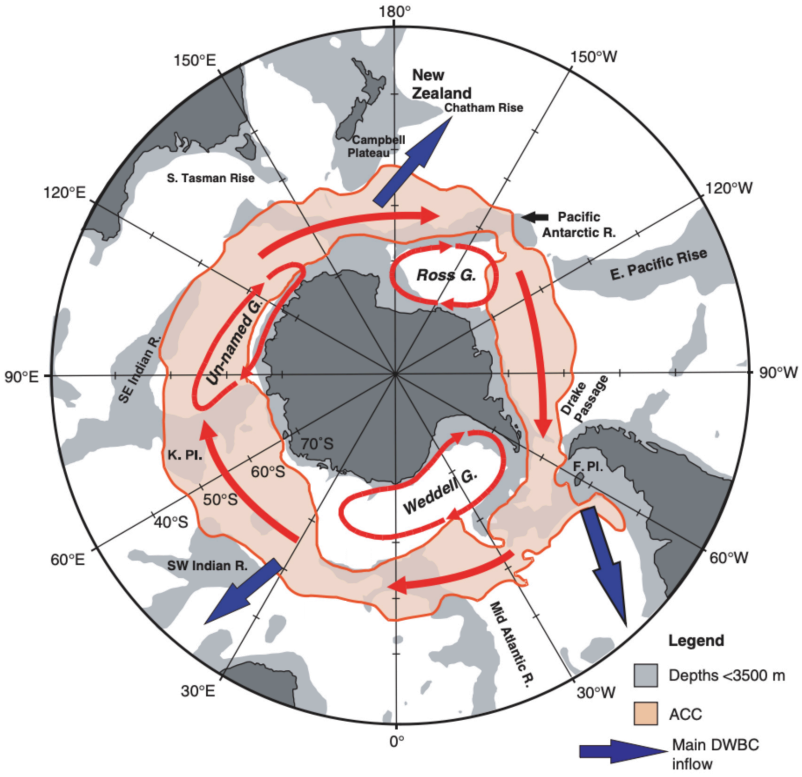

Figure 2.3: Major oceanographic features of the Southern Ocean. Bathymetric features are also noted. R. is an abbreviation for Ridge; K.Pl, Kerguelen Plateau; and F. Pl., Falkland Plateau. Modified From Carter et al. (2008), base image modified from (Orsi and Whitworth, 2005).

CDW is the largest water mass in the Southern Ocean, and is composed of Lower Circumpolar Deep Water (LCDW) and Upper Circumpolar Deep Water (UCDW). Together, LCDW and UCDW form two meridional cells driving the thermohaline overturning circulation in the Southern Ocean (Carter et al., 2008; Rintoul et al., 2001) (Figure 2.4). LCDW and UCDW are characterized through their oxygen, salinity, and nutrient contents, with LCDW being very saline and UCDW being oxygen depleted and high in nutrients (Gordon, 1975; Orsi et al., 1995).

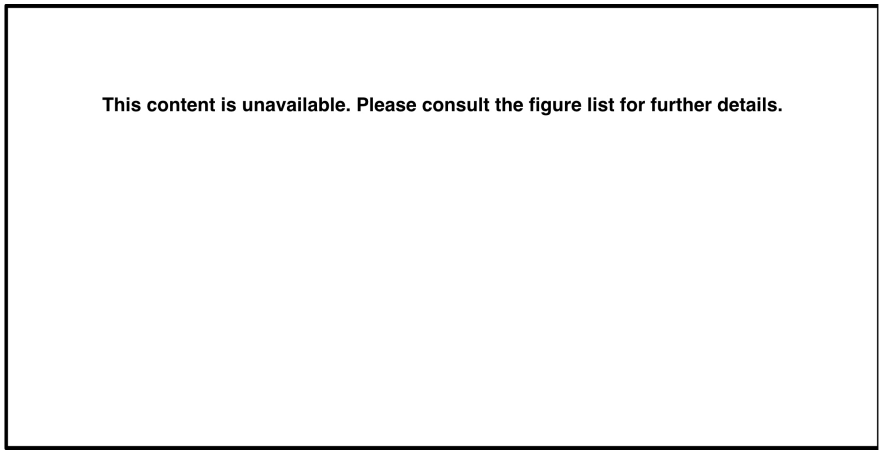

Figure 2.4: Schematic of the Southern Ocean overturning circulation, as well as the zonal flow. Modified from Olbers and Visbeck (2005) and (Speer et al., 2000)

Bathymetric constraints combined with density driven thermohaline circulation governs ACC pathways at depth (Figure 2.3). Cold, dense waters are produced along Antarctica's coastal margins due to brine rejection from sea ice formation and supercooling from interactions with floating ice shelves (Figure 2.4). LCDW upwells along the continental slope of Antarctica and mixes with cold, dense, shelf water, which enhances circulation of LCDW, and also contributes to Antarctic Bottom Water (AABW) production (Carter et al., 2008). Deep Western Boundary Currents (DWBC) branch off from the ACC at depth and carry these dense waters (AABW and LCDW) northwards into the abyssal basins of the Atlantic, Pacific, and Indian Oceans (see Figure 2.3) (Carter et al., 2008; Sloyan and Rintoul, 2001).

Remaining LCDW is transported northwards, and is subsequently depleted in oxygen due to biological activity (Rintoul et al., 2001). Further mixing with fresher waters leads to a less dense and lower oxygenated water mass that returns southward to make up UCDW (Rintoul et al., 2001). UCDW is then converted to Antarctic Intermediate water (AAIW), through air-sea buoyancy fluxes as it is upwelled along the ACC, and transported northwards as part of the Ekman layer (Rintoul et al., 2001; Speer et al., 2000).

Closer to the coast lies the easterly flowing Antarctic Slope Current (ASC), also known as the East Wind Drift (Deacon, 1937), and the Antarctic Coastal Current (ACoC) (Heywood et al., 2004; Carter et al., 2008). The ACoC is a narrow, and at times rapid, current that flows along

the coastal continental shelf and along ice shelves, where present (Jacobs, 1991; Carter et al., 2008). The ACoC is most prevalent in areas where the continental shelf is wide, as it can be difficult to differentiate the ACoC from the ASC in areas where the shelf is narrow (Heywood et al., 1998; Carter et al., 2008).

The ASC is thought to form due to the prevailing easterly winds along Antarctica's coast which lead to Ekman transport of surface waters towards the coast, creating a gradient in sea surface height and leading to a geostrophic westward flow at depth (Deacon, 1937; Whitworth et al., 1998; Heywood et al., 2004). The along-slope flow of ASC on the continental rise interacts with cold, dense water masses sinking downslope to the abyssal plain, and helps drive upwelling of warmer CDW onto the shelf (Gill, 1973; Ainley and Jacobs, 1981; Jacobs, 1991; Whitworth, 1988; Carter et al., 2008). Consequently, the oceanographic regime in this region is highly dynamic, driving exchanges of heat, salt, nutrients, and gases along this front, resulting in an area of high primary productivity (Jacobs, 1991).

The ASC is instrumental in regulating the vigorous mixing of upwelled CDW with other water masses on the continental shelf forming modified Circumpolar Deep Water (mCDW) (Jacobs et al., 1970; Whitworth et al., 1998; Jacobs and Giulivi, 1999; Gordon et al., 2000; Orsi and Wiederwohl, 2009; Dinniman et al., 2011). mCDW can supply heat to continental shelf (Jacobs, 1991; Rintoul, 1998; Jacobs et al., 2011) and has been linked to polynya dynamics (Jacobs and Comiso, 1989; Rintoul, 1998), and increases in primary productivity (Prezelin et al., 2000). mCDW is also an important precursor water for AABW formation, as these saline waters are modified by ice-ocean interactions on the continental shelf, through brine rejection during sea ice formation and supercooling by floating ice shelves (Jacobs et al., 1970; Orsi et al., 1995; Rintoul, 1998; Orsi et al., 2001; Orsi and Wiederwohl, 2009). This acts to create an extremely dense water that eventually recirculates off the continental shelf and sinks into the abyssal plain to form AABW.

Areas of high AABW formation occur in areas associated with increased brine rejection (Orsi et al., 1995), such as polynyas where sea ice production rates are high (Cavalieri and Martin, 1985; Zwally et al., 1985; Rintoul, 1998; Massom et al., 1998). The most significant regions of AABW formation around Antarctica include the Ross Sea (Jacobs et al., 1970; Jacobs, 2004),the Wilkes/Adélie Land land margin (Gordon and Tchernia, 1972; Rintoul, 1998; Orsi et al., 1999; Bindoff et al., 2000; Fukamachi et al., 2000; Rintoul, 2007; Williams et al., 2008), and the Weddell Sea (Foster and Carmack, 1976; Gordon et al., 1993). The northward flow of AABW represents the lower cell of the Atlantic Meridional Overturning Circulation, whose counterpart in the north sends North Atlantic Deep Water southward to complete the global thermohaline overturning circulation of the ocean (Buckley and Marshall, 2015).

2.3.2 Ice shelf-ocean interactions

Ice shelf-ocean interactions have an important effect on the mass balance of the Antarctic Ice Sheet. Recent modelling studies suggest that marine based ice sheets are vulnerable to catastrophic retreat when their margins are exposed to changes in oceanic heat flux, regardless of the presence of atmospheric warming (Bassis et al., 2017). Iceberg calving and ocean-forced melting of floating ice shelves are the primary ways the Western Antarctic Ice Sheet (WAIS) loses mass (Jacobs et al., 1992; Depoorter et al., 2013; Rignot et al., 2014).

Several mechanisms contribute to basal melting of ice shelves. Shallow water mixing due to tides and other shallow water processes can transport heat from near-surface waters beneath the ice shelf (Jacobs et al., 1992; Joughin and Alley, 2011), while intrusions of warm CDW under the ice shelf can cause accelerated melting (Jacobs et al., 1992; Joughin and Alley, 2011). On the Ross Sea continental shelf, CDW is vigorously mixed with surface waters creating fresher, less dense, mCDW (Jacobs and Giulivi, 1999). While circulation of mCDW under the RIS is relatively limited today, wind driven incursions of CDW and subsequent formation of mCDW on Antarctic continental shelves appears to be increasing in many regions (Pritchard et al., 2012; Jacobs et al., 1992). In most circumstances, the primary driver of basal melting is high-salinity shelf water (HSSW), produced through mixing of saline CDW and surface waters that have undergone brine rejection and cooling through sea ice formation (Joughin and Alley, 2011). As the southern Ross Sea is the largest producer and exporter of sea ice for the Pacific sector of the Southern Ocean, HSSW is present in abundance (Jacobs et al., 2002). HSSW is extremely dense, and therefore flows towards the grounding lines of the ice shelves, where it melts the ice as the freezing point decreases with depth, and subsequently mixes with meltwater from the base of the ice shelves to form Ice Shelf Water (Fujino et al., 1974; Jacobs et al., 1992).

Once a retreat is initiated, the WAIS is thought to be particularly susceptible to process known as Marine Ice Sheet Instability (MISI), as it rests on a bed sloping inland of its ice shelves (Weertman, 1974; Thomas and Bentley, 1978; Schoof, 2007). In such a setting, as warm waters (e.g. CDW, mCDW) penetrate onto the Antarctic continental shelf, they act to enhance basal melt of the ice shelves. This eventually leads to a flotation threshold being met, allowing warm water to further penetrate beneath the ice sheet. This leads to grounding line retreat and as this passes into a progressively deeper basin, an ever thicker mass of ice is exposed at the grounding line. Consequently, the flux of ice passing through this gate increases with thickness of the ice exposed at the grounding line, leading to ever accelerating and runaway grounding line retreat, even in the absence of sustained increases in heat forcing (Schoof, 2007).

2.3.3 Sea ice

Antarctic sea ice extent is unbounded by land mass to the north and nearly 15×10^6 km^2 of ice forms and melts each year in an annual seasonal cycle (Eayrs et al., 2019). Extent is primarily restricted by the Antarctic Circumpolar Current, which marks the boundary of the stable, cold water masses necessary for sea ice formation (Martinson, 2012). On average, sea ice extent reaches its maximum in September, and retreats to its minimum in February, with some coastal areas sustaining ice year round (Parkinson, 2014; Eayrs et al., 2019).

Sea ice extent in Antarctica has been increasing over the last three decades, but is only statistically significant (95%) Antarctic-wide in Autumn (Maksym, 2019). Outside of the autumn trend, increases in sea ice extent are only significant in the Ross Sea year round (Yuan et al., 2017). Satellite-based observations indicate that since 2014, decreases in annual sea ice extent have eliminated the increasing trend in only three years (Parkinson, 2019).

Winds directly influence sea ice variability in Antarctica, with offshore winds driving sea ice northward and cooling of the sea surface producing more ice (Kwok et al., 2016; Holland and Kwok, 2012; Maksym, 2019). Conversely, warmer onshore winds can act to compact sea ice nearshore and warm the surface inhibiting sea ice growth further offshore (Maksym, 2019). The sensitivity of sea ice to the direction and magnitude of winds, and air temperature in Antarctica also makes it responsive to major climate oscillations and circulation features. These are discussed in section 2.4.

Sea ice also plays a key biological and physical role in the Southern Ocean's carbon uptake. Biologically, it acts as substrate for algal biomass and also affects nutrient delivery, water stratification, and solar insolation which control mass phytoplankton bloom events that act as a strong carbon sink (Barber and Massom, 2007; Arrigo et al., 2008b; Smith and Comiso, 2008; Takahashi et al., 2009). In the wintertime, extensive sea ice cover physically prevents the outgassing of CO_2 from the ocean, thus increasing CO_2 concentrations under the ice as deep waters mix at the surface (Tréguer and Pondaven, 2002; Takahashi et al., 2009). However, these physical and biological sea ice processes, as well as the sinking and upwelling of various water masses, leads to a nearly zero net flux of CO_2 from the Southern Ocean to 35°S (Gruber et al., 2019; Takahashi et al., 2002).

Recently, it has been suggested that a reduction in sea ice will lead to a reduction in biological productivity, thereby reducing CO_2 uptake in the coastal southern ocean (Brown et al., 2019). Additionally, paleo-studies have suggested that enhanced westerly winds increase outgassing of CO_2 at the surface (Saunders et al., 2018). However, future projections of the Southern Ocean's behaviour as a carbon sink remains highly ambiguous, as exemplified by a

large range of model variability (Gruber et al., 2019).

2.3.4 Primary productivity in the Southern Ocean

Despite high levels of macronutrients (e.g. nitrate, phosphate, silicate), the Southern Ocean only has moderate rates of primary productivity (Arrigo et al., 1998; Smith and Gordon, 1997; Moore and Abbott, 2000). Low levels of micronutrients, such as iron, have been identified as the limiting factor controlling biological productivity (Takeda, 1998; Boyd, 2002). However, intense phytoplankton bloom events can occur around the Southern Ocean, leading to substantial temporal and spatial variations in Southern Ocean productivity (Arrigo et al., 2008b; Smith and Nelson, 1986). Areas of high productivity include the marginal ice zone (Smith and Nelson, 1986), the continental shelf (Smith and Gordon, 1997; Arrigo and Van Dijken, 2004), coastal polynyas (Arrigo and van Dijken, 2003; Arrigo and Van Dijken, 2004), as well as areas within oceanic frontal zones where nutrient rich waters are brought to the surface (Comiso et al., 1993; Moore and Abbott, 2000; Sokolov and Rintoul, 2007). The marginal ice zone is the transitional area between sea ice and open ocean. Mass phytoplankton bloom events at the marginal ice zone are suggested to be induced by a comparatively fresh surface layer from seasonal sea ice melt that stabilizes the water column, which allows sunlight to more easily illuminate this layer relative to water beneath sea ice, promoting bloom growth (Smith and Nelson, 1986).

Polynyas are regions of persistently anomalous open water and/or reduced sea ice conditions within the sea ice zone that vary in size from tens to tens of thousands of square kilometers (Barber and Massom, 2007). There are two types of polynyas, the *sensible heat polynya*, whereby upwelling of warmer waters prevents surface freezing, and the *latent heat polynya*, where katabatic winds continually drive ice away from a particular area, allowing it to remain open and ice free. Spring blooms in coastal polynyas are controlled by surface light conditions, mixing due to katabatic winds, stratification of the water column, and ice cover (Vaillancourt et al., 2003; Arrigo and van Dijken, 2003).

In the regions of interest studied in this thesis, three polynyas are relevant: the Mertz, Ross Sea, and Dumont d'Urville. Coastal polynyas, such as the Ross Sea and Mertz are generally driven by a combination of katabatic and synoptic scale winds, with only a marginal sensible heat component and are therefore considered latent heat polynyas (Zwally et al., 1985; Jacobs and Comiso, 1989; Bromwich et al., 1993; Jacobs and Giulivi, 1998; Massom et al., 2001; Williams and Bindoff, 2003; Marsland et al., 2004; Barber and Massom, 2007). The Dumont d'Urville polynya is primarily forced by strong katabatics winds off the coast (Adolphs and

Wendler, 1995).

The majority of high productivity events around Antarctica are limited to November-January, which corresponds to winter sea ice break up and retreat, and increased availability of light (Wefer et al. 1988; Abelmann and Gersonde 1991). However, green frazil ice associated with late summer algal blooms has recently been suggested as a major contributor to primary productivity in the Southern Ocean (DeJong et al., 2018). Phytoplankton bloom events are often exported to the sea floor, with measured data suggesting a two month lag between export and peak production (Rigual-Hernández et al., 2015). These bloom events are preserved in the Adélie Basin record (U1357B) and are discussed in detail in Chapters 3, 4, and 5.

2.4 Major climate modes, circulation features and impacts

This following subsections provide an overview of the major circulation features and climate modes affecting the Antarctic Region.

A defining feature of Antarctica is the strong, cold katabatic winds that drain from high elevations down to the coast. As these winds flow offshore, they turn and merge with nearshore easterly winds. A second prominent circulation feature is the Antarctic Circumpolar Trough (ACT), a zone of frequent low pressure systems between 50°S and 70 °S (King and Turner, 1997). The low pressure of the ACT relative to high pressures in lower latitudes drives the intense westerly winds encircling the continent.

2.4.1 Southern Annular Mode

The Southern Annular Mode (SAM), also referred to as the high-latitude mode and the Antarctic Oscillation, quantifies the differences in the zonal mean sea-level pressures of the Southern Hemisphere mid- and high-latitudes, which drives zonal wind strength (Gong and Wang, 1999; Limpasuvan and Hartmann, 1999; Rogers et al., 1982; Thompson and Wallace, 2000a). Multiple indices using various methods, data sets, and time periods are used to quantify SAM (Ho et al., 2012, & references therein). The most common methods of defining SAM are:

1. The first principal component (leading empirical orthogonal function) of sea level pressure and geopotential height variability from 20°N to the pole in the Southern Hemisphere (Thompson and Wallace, 2000b).

2. The differences in the normalized zonal mean pressure from 65°S to 40°S (Gong and Wang, 1999)

SAM is in its positive phase when pressures in the mid-latitudes are higher than those over Antarctica, thereby strengthening the circumpolar vortex and associated westerlies around Antarctica (Marshall, 2003). Furthermore, poleward heat flux is reduced, the Antarctic Circumpolar Current is strengthened, and sea ice is advected away from the continent leading to more sea ice coverage (Hall and Visbeck, 2002; Holland et al., 2017; Turner et al., 2017b). During negative SAM, the opposite occurs, where poleward heat flux increases, the Antarctic Circumpolar Current weakens and sea ice coverage is reduced. Impacts of SAM on Antarctic surface air temperatures do not differ greatly among seasons, with positive SAM leading to cooler temperatures across most of the Antarctic continent, and warm temperature anomalies in the Antarctic Peninsula region (Kwok and Comiso, 2002b; Marshall and Thompson, 2016). The spatial pattern of the SAM and the associated changes during the positive phase of the SAM are shown in figure 2.5.

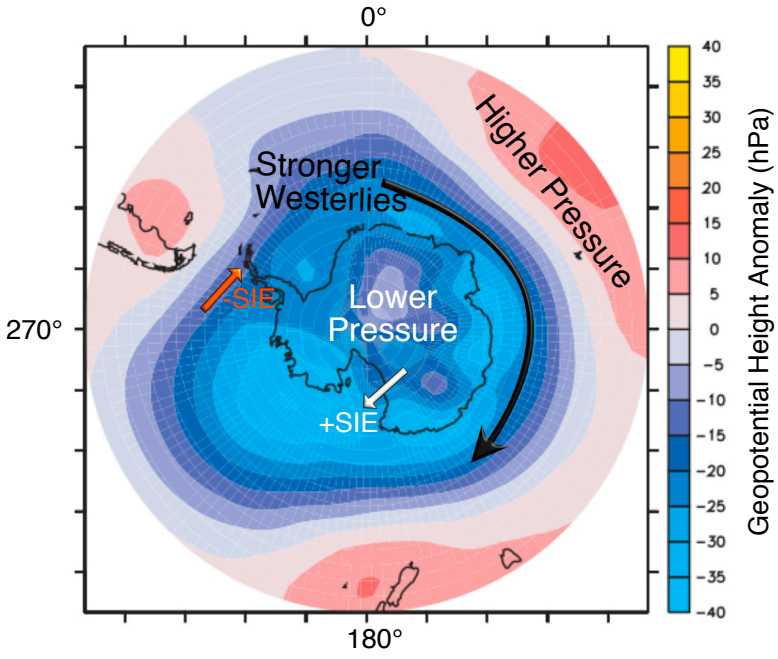

Figure 2.5: **Southern Annular Mode.** Positive phase of the Southern Annular Mode. Higher pressures in mid-latitudes strengthen the westerlies (black arrow), and lead to cold offshore flows (white arrow) and increase in sea ice extent (SIE) . The peninsula experiences warm onshore flows (orange arrow) and reduced SIE. Base map shows the spatial SAM pattern derived from the NCEP-R1 850 hPa anomaly (Lenton and Matear, 2007)

SAM variability and subsequent fluctuations in surface pressures can shift on both short

(Baldwin, 2001) and long-term timescales (Kidson, 1999; Marshall, 2003). Variability is difficult to predict, but paleoclimate reconstructions show that SAM has been increasingly positive since 1400 AD and is at its most positive phase in the last 1000 years (Abram et al., 2013). The positive phasing in more recent decades has been attributed to depletion in the ozone hole and increasing greenhouse gas emissions, however, as the ozone hole is recovering, the phasing of the SAM in future decades is uncertain (Thompson et al., 2011).

The SAM can act to influence the El Niño-Southern Oscillation (ENSO) and make the teleconnections to the poles stronger or weaker, with positive phases of SAM reinforcing La Niña (and therefore positive SOI) conditions and negative SAM reinforcing El Niño (negative SOI) conditions (Fogt and Bromwich 2006; Fogt, Bromwich, and Hines 2011; L'Heureux et al. 2006; Stammerjohn et al. 2008).

2.4.2 El Niño-Southern Oscillation

The El Niño-Southern Oscillation describes a see-saw pattern in temperature and pressure anomalies across the tropical Pacific, whereby the zonal Walker Circulation strength and location is altered (Bjerknes, 1969; Walker, 1923, 1924). The Walker Circulation describes an airflow model where dry air sinks over the cold waters off South America, and high pressure at the surface drives air west towards low surface pressure in the Indo-Pacific region, creating the Trade Winds. As the air moves over progressively warmer waters, it too warms, and leads to convection in the Indo-Pacific region. ENSO events are monitored using the Southern Oscillation Index (SOI), which calculates the pressure anomalies over the western Pacific, and the Niño sea surface temperature indices which calculate sea surface temperature anomalies in the eastern Pacific. During an El Niño event, the Walker Circulation is weakened, as warmer sea surface temperatures off the coast of Peru weaken sea surface temperature and pressure gradients across the Pacific. El Niño typically reaches peak intensity during the Southern Hemisphere summer in December-January-February (DJF) and lasts for 18-24 months (Rasmusson and Carpenter, 1982; Trenberth et al., 1998).

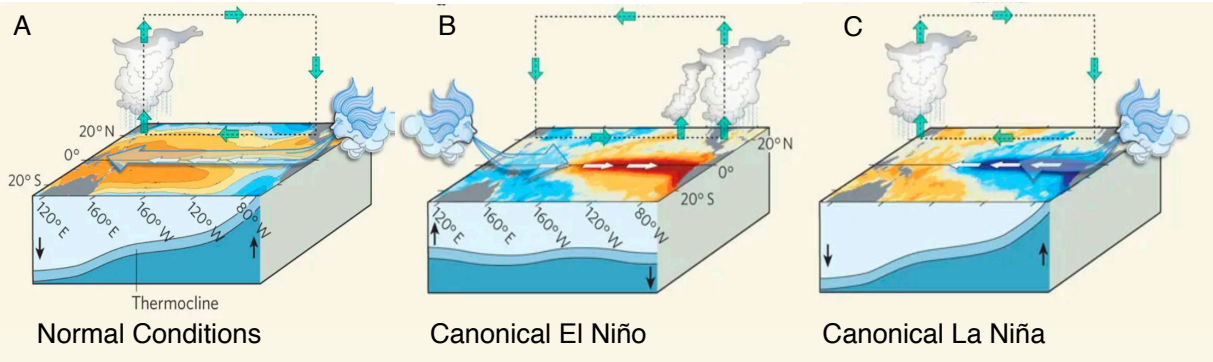

Figure 2.6: Schematic of normal conditions in the Pacific (A), followed by conditions present during a canonical El Niño (B) and La Niña (C). The Walker circulation is indicated by the green arrows, with surface wind directions indicated by the light blue arrow. Shaded contours in the ocean indicate sea surface temperature anomalies. Also present is the change in thermocline position, which demonstrates reduced upwelling along the eastern Pacific during El Niño conditions, and enhanced upwelling during La Niña conditions. Modified from Ashok and Yamagata (2009)

In recent decades, ENSO has been categorized into two different types. The first is the canonical El Niño and La Niña event described above, where sea surface temperature anomalies develop in the eastern Pacific along the Peruvian coast. The other type is called the El Niño Modoki (Ashok et al., 2007), which has also been variably referred to as the Trans-Niño (Trenberth and Stepaniak, 2001), Warm Pool El Niño (Kug et al., 2009), and the Central Pacific El Niño (Kao and Yu, 2009; Yeh et al., 2009). El Niño Modoki events are characterized by warm sea surface temperature anomalies in the central Pacific, with cooler sea surface temperature existing in the western and eastern Pacific, resulting in two different Walker cells and spurring teleconnections from both cells (Ashok et al., 2007; Kug et al., 2009). El Niño Modoki events are predicted to increase in frequency due to future climate change (Yeh et al., 2009).

El Niño reaches its peak in December-January-February (DJF), but tropical forcing of southern high latitude teleconnections is typically strongest during the spring (September-October-November; SON), with ENSO events triggering the Pacific South American patterns (PSA), a series of alternating pressure/height anomalies, that work to influence Antarctica (Karoly, 1989; Mo and Paegle, 2001; Trenberth et al., 1998; Turner, 2004; Yuan, 2004; Jin and Kirtman, 2009). PSA 1 is typically associated with canonical ENSO (positive PSA1, El Niño; negative PSA1, La Niña) (Mo and Paegle, 2001; Schneider et al., 2012), whereas PSA2 is linked to ENSO Modoki events (Rodrigues et al., 2015). Understanding ENSO's role in affecting Antarctica and vice versa is difficult because triggers of ENSO events are not well understood. Moreover, as ENSO events vary widely in development and location, so do the teleconnections (Ciasto et al.,

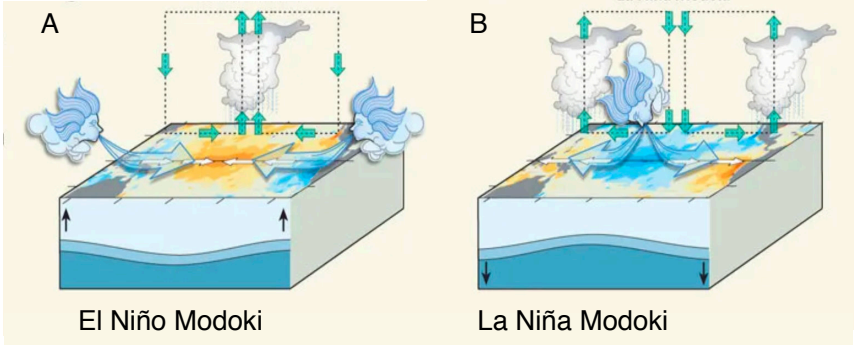

Figure 2.7: Same as 2.6, but showing conditions during El Niño Modoki (A) and La Niña Modoki (B). Modified from Ashok and Yamagata (2009)

2015; Gergis et al., 2006; Kug et al., 2009; Ashok et al., 2007). The majority of Antarctic ENSO studies have focused on the Antarctic Peninsula, Amundsen Sea, and Ross Sea regions where teleconnections are strongest (e.g Bertler et al., 2004; Kwok and Comiso, 2002a; Turner, 2004; Yuan, 2004; Yuan and Li, 2008).

Numerous studies indicate a link between canonical ENSO and Antarctic sea ice variability (Chiu, 1983; White and Peterson, 1996; Yuan and Martinson, 2000; Kwok and Comiso, 2002a; Yuan, 2004; Stammerjohn et al., 2008; Raphael and Hobbs, 2014). During an El Niño event, warm temperature anomalies in the eastern Ross sea lead to reduced sea ice, whereas cold temperature anomalies in the Bellingshausen and Weddell sea sector lead to more sea ice, as shown in Figure 2.8 (Yuan, 2004). The opposite is true during a La Niña event. Regional sea ice changes during ENSO events are largely driven by wind changes resulting from pressure anomalies, but these pressure anomalies also occur during changes in the Southern Annular Mode (SAM) (Stammerjohn et al., 2008).

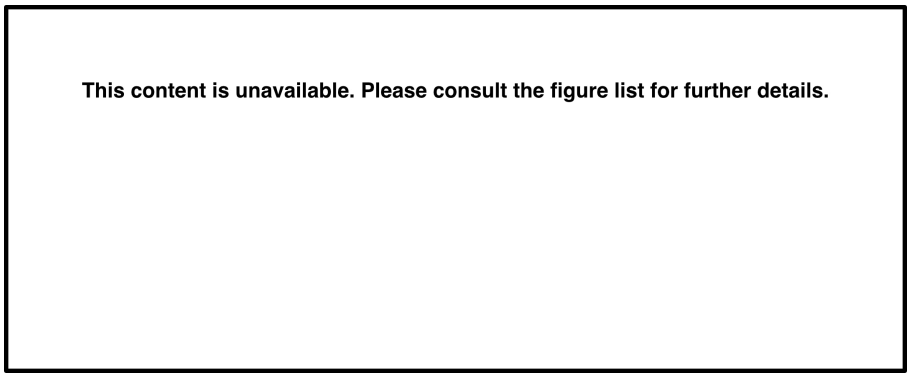

Figure 2.8: Schematic depicting El Niño (a) and La Niña (b) on zonal circulation and meridional heat flux, and associated impact on sea ice. Shaded contours indicate sea surface temperature anomaly composites during these events. From Yuan (2004).

El Niño Modoki impacts on Antarctica are increasingly being studied. Ding et al. (2011) found that winter warming in the Antarctic Peninsula is linked to anomalous sea surface temperature warming in the central Pacific. El Niño Modoki events are also associated with a weakening of the polar jet and stratospheric warming during austral summer (Hurwitz et al., 2011).

In the modern day, ENSO events occur at 2-7 year frequencies. However, the frequency of ENSO likely changed throughout the Holocene (Rodbell et al., 1999; Koutavas et al., 2002; Donders et al., 2005, 2008; Moy et al., 2002; McGlone et al., 1993; Pausata et al., 2017; Sandweiss et al., 1996). Several records suggest that the onset of the modern day frequency occurred around ∼4.5 ka BP (Sandweiss et al., 1996; Donders et al., 2008; Carré et al., 2014).

2.4.3 Interdecadal Pacific Oscillation

The Interdecadal Pacific Oscillation (IPO) is the second empirical orthogonal function of low frequency global sea surface temperature anomalies (Power et al., 1999), but has recently been quantified by a tripole index of decadal sea surface temperature variability across the Pacific (Henley et al., 2015). The IPO is closely related to the Pacific Decadal Oscillation (Mantua et al., 1997) and oscillates on ∼15-35 year time frame (Magee et al., 2017). The positive phase of the IPO is marked by warm sea surface temperature anomalies in the tropical Pacific, with cold sea surface temperature anomalies flanking either side at higher latitudes (Power et al., 1999). The IPO modulates ENSO's regional influence on the Southern Hemisphere (Power et al., 1999; Salinger et al., 2001; Henley et al., 2015). When IPO and ENSO occur in phase together (positive IPO/El Niño and negative IPO/La Niña), typical ENSO teleconnections are

amplified (Magee et al., 2017).

IPO causes negative sea surface temperature anomalies around Antarctica in its negative phase, as well as leading to surface pressure and wind changes that lead to increased sea ice extent (Meehl et al., 2016) (Section 2.6.3). Reanalysis data suggest the IPO has a profound influence in the Antarctic Indian Ocean sector as well (Vance et al., 2016).

2.4.4 Amundsen Sea Low

The Amundsen Sea Low (ASL), (Baines and Fraedrich, 1989; Kreutz et al., 2000; Bertler et al., 2004; Raphael et al., 2016; Turner et al., 2013) is a climatological center of low pressure that greatly affects the atmospheric conditions around West Antarctica. The ASL's center migrates seasonally, existing at its most southerly position near the Ross Sea in winter, then moving northward towards the Bellingshausen Sea during the austral summer (Schneider et al., 2012; Bromwich and Wang, 2008; Turner et al., 2013). The clockwise motion of the ASL affects meridional flow, surface air temperature, and sea ice. Along the eastern side of the low, anomalous northerly flow raises surface air temperatures and compacts sea ice along the coast, thereby reducing sea ice extent (Hosking et al., 2013; Massom et al., 2008). Along the western edge, flow is offshore, thereby increasing sea ice extent and creating negative temperature anomalies (Hosking et al., 2013; Massom et al., 2008).

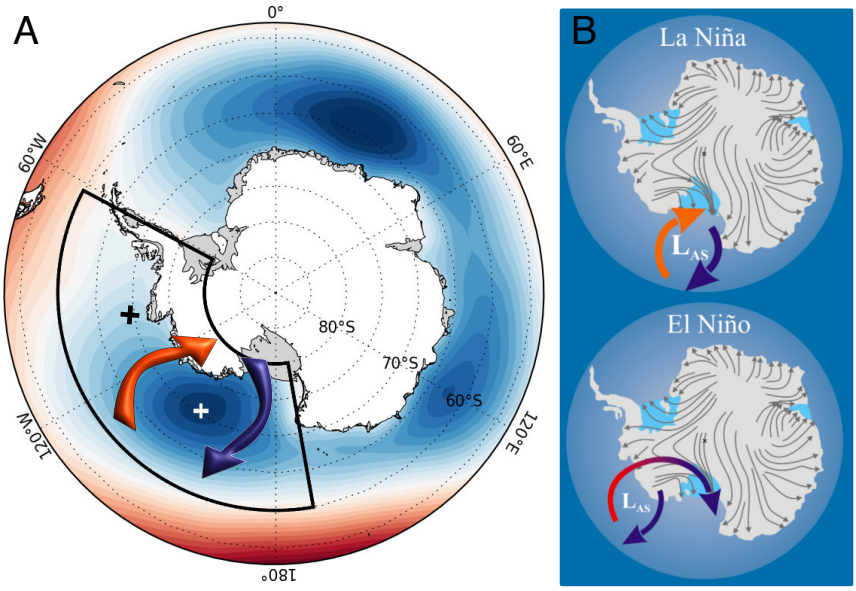

Figure 2.9: **Amundsen Sea Low.** (A) A schematic of seasonal mean sea level pressure (SLP) around Antarctica. ASL position is marked in by white '+'. ASL indices are derived from SLP anomalies within the black outline. ASL migrates towards the black '+' in the austral summer (DJF). Red arrows indicate warm onshore flow, while blue arrow indicates cold offshore flow. Modified from Hosking and National Center for Atmospheric Research Staff (2019). (B) Schematic showing spatial changes of ASL during ENSO events. During a La Nina, the ASL deepens (indicated by size of L_as), and the warm onshore air masses (red arrows) are not as warm as those during an El Niño. Cold air masses are represented by blue arrows. From Bertler et al. (2004)

The ASL is affected by other tropical modes of climate variability such as the ENSO and SAM (Raphael et al., 2016; Turner et al., 2013). ENSO affects the depth of the ASL, with a deepening occurring during La Niña and a weakening occurring during El Niño (Bertler et al., 2004; Raphael et al., 2016; Turner et al., 2013). This relationship is strongest during the spring (Raphael et al., 2016). Additionally, the SAM affects the meridional position of the ASL with the low positioned further northward during positive SAM conditions (Turner et al., 2013).

2.4.5 Indian Ocean Dipole

The Indian Ocean Dipole (IOD) is a coupled ocean-atmosphere phenomenon similar to ENSO that exists in the Indian Ocean (Saji et al., 1999; Webster et al., 1999; Ashok et al., 2003; Wang et al., 2016). During a negative IOD, sea surface temperatures are cooler than average and conditions are dryer in the western Indian Ocean, with warmer than average sea surface temperatures and increased rainfall occurring closer to Indonesia (Saji et al., 1999). In its

positive phase, warm temperature and positive rainfall anomalies occur in the western Indian Ocean, with cold temperature and negative rainfall anomalies existing in the eastern Indian Ocean.

The complex relationship between the IOD and ENSO is an area of active research. IOD events can exist independently of ENSO events (Saji et al., 1999; Ashok et al., 2003; Wang et al., 2016), but ENSO events can influence the IOD and vice versa (Saji et al., 1999; Webster et al., 1999; Lee Drbohlav et al., 2007; Stuecker et al., 2017; Wang et al., 2019; Izumo et al., 2010; Jourdain et al., 2017). ENSO interactions with IOD events differ based on type of El Niño occurring (Capotondi et al., 2015; Wieners et al., 2017). Additionally, analysis of sea surface temperature anomalies during various IOD events have suggested the existence of an IOD Modoki state, characteristic of the ENSO Modoki, with different teleconnection patterns (Endo and Tozuka, 2016).

When IOD does interact with canonical ENSO events, positive IOD events are typically associated with El Niño events, whereas negative IOD events are associated with La Niña events (Stuecker et al., 2017). These interactions lead to a Rossby wave train that then affects the high southern latitudes and the area around the Wilkes Land Margin (Section 2.5.3) (Saji and Yamagata, 2003; Cai et al., 2011; Saji et al., 2005; Nuncio and Yuan, 2015).

2.5 IODP U1357B

This section gives an overview of the geologic, oceanographic, and climatic controls at Site U1357 (66.4133°S, 140.42617 °E) (Figure 2.10). Site U1357 was drilled at a water depth of ∼1017 m on the Antarctic continental shelf, in the Adélie Basin, offshore East Antarctica (Escutia et al., 2011). Three separate holes were cored (U1357A, U1357B, U1357C), but a spliced composite core has not been developed due to low signal to noise ratio in the physical properties logs, resulting from the highly ephemeral nature of the organic-matter and water-rich diatom ooze recovered.

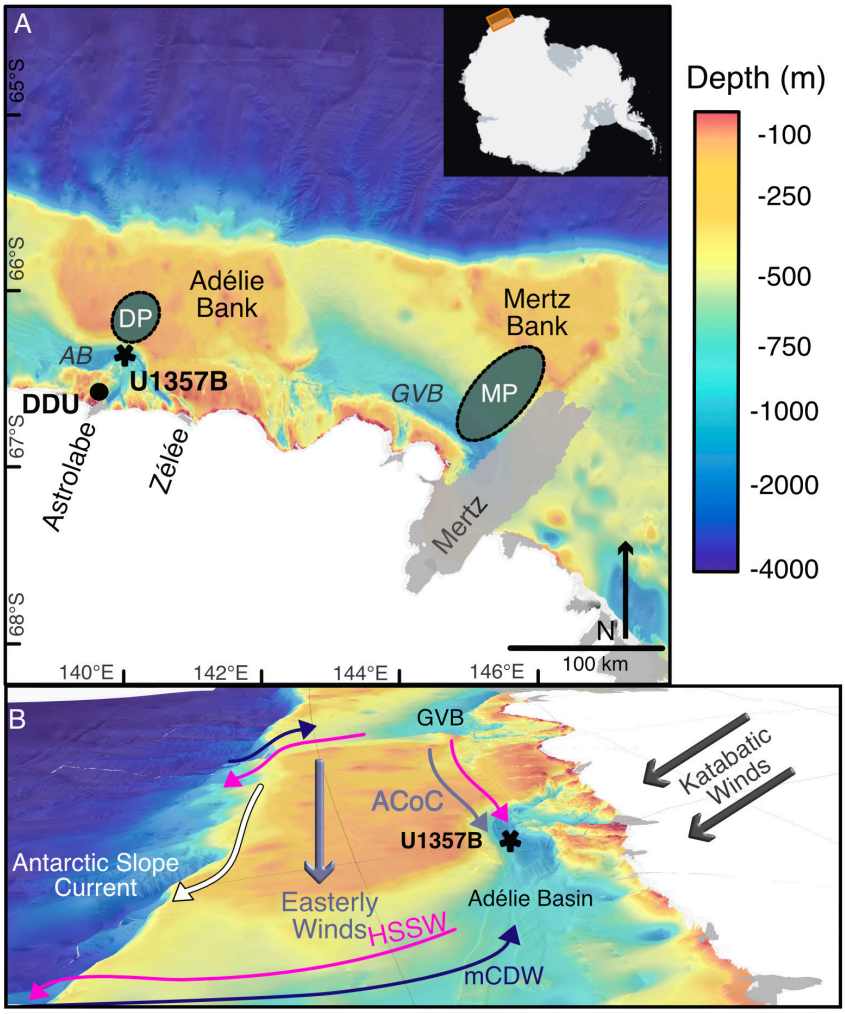

Figure 2.10: (A) Map of Adélie Land bathymetry. The Mertz, Astrolabe, and Zélee glaciers are labelled. Dumont d'Urville weather station is indicated by black dot. Black star indicates U1357B location. The Adélie Bank, Mertz Bank, Adélie Basin (AB), and George V Basin (GVB) are also highlighted. The approximate location of the Mertz Polyna (MP) and Dumont d'Urville polynya (DP) are indicated by green ellipses (Arrigo and van Dijken, 2003). (B) 3D oblique easterly view of the regional bathymetry. Direction and position of the ASC (white), Antarctic Coastal Current (ACoC, light grey) high salinity shelf water (HSSW; pink), and modified circumpolar deep water (mCDW, dark blue) indicated. Katabatic and easterly winds are indicated by straight dark grey and light grey arrows, respectively. Bathymetry data from Beaman et al. (2011).

2.5.1 Geological setting

The Adélie Basin lies offshore Adélie Land (136°E - 142°E), with the Wilkes Land Margin (100°E - 136°E) to the west and George V Land (142°E - 153°E) to the east. The overdeepened continental shelf is characteristic of isostatic adjustment and glacial scouring due to ice loading in previous glaciations (Anderson, 1991). Mega-scale glacial lineations and multiple grounding zone wedges indicate several glacial advances and retreats, with the seafloor sediments consisting mostly of diamicton, but overlain by drifts of diatomaceaous sediments in places (McMullen et al., 2006; Beaman and Harris, 2003). The continental shelf is marked by the large, shallow, and relatively flat Adélie and Mertz Banks (Beaman et al., 2011). These banks range in depth from ∼200-280 m and are incised by the deep (>1200m) George V Basin (also known as the Adélie depression or Mertz-Ninnis trough) and Adélie Basin (also known as the Dumont d'Urville Basin), which were formed by ice streams during the Last Glacial Maximum (Beaman et al., 2011; Eittreim et al., 1995). Closer to Site U1357 lies the Astrolabe and Zélée Glacier Tongues, which flow into smaller deeply-incised valleys along the inner-shelf (Beaman et al., 2011). Narrow canyons link the Adélie and George V Basins to these smaller valleys (Beaman et al., 2011) (Figure 2.10). Sediment is winnowed from the shallow banks to the east and deposited into concentrated sediment drifts in these troughs (Dunbar et al., 1985). The lack of large proglacial fan systems in local outlet glaciers feeding into the Adélie Basin indicates that sediment advection from the east forms the primary sediment supply to U1357B, rather than turbid meltwater discharge from local outlet glaciers (Dunbar et al., 1985).

2.5.2 Oceanographic setting

The physical characteristics of the coastal ocean of Adélie Land are highly variable due to the diverse bathymetry, extensive sea ice cover, and highly productive polynyas. These features lead to a complex interaction of water masses along the continental shelf, which bathe Site U1357. Site U1357 is positioned near the marginal ice zone, but also lies nears the ACoC and ASC (e.g. Massom et al., 2001; Snow et al., 2016). Modern-day sea ice is typically at its maximum in July and September and then gradually retreats through the spring and summer, reaching a minimum in February (Campagne et al., 2016).

Strong katabatic winds flowing off the coast of Adélie Land help form and exert control on the size of the Mertz and Dumont d'Urville Polynyas (Adolphs and Wendler, 1995; Wendler et al., 1997; Massom et al., 2001; Barber and Massom, 2007). These winds turn westward 20-30 km off the coast, yet the Mertz Polynya extends much further offshore than the katabatic

winds (Bindoff et al., 2000; Massom et al., 1998). The greater extent of the Mertz Polynya is attributed to the Mertz Glacier Tongue (MGT) and regional icescape (i.e. ice shelves, icebergs, sea ice) which can facilitate a build up of fast ice to the east and act as barrier, preventing ice from the east advecting into the polynya (Massom et al., 2001; Barber and Massom, 2007). Polynyas act as sea ice factories as the strong katabatic winds freeze the surface waters and then export the sea ice away from the coast. Sea ice production in the Mertz Polynya is also affected by regional fast ice distributions to the west, where fast ice buildup can inhibit the northwestward flow of sea ice away from the coast (Massom et al., 2001). This occasionally leads to 'backfilling' of the polynya, shrinking the open water area and preventing new sea ice formation (Massom et al., 2001).

Surface cooling, as well as brine rejection from sea ice formation, increases the density of the water column and forms High Salinity Shelf Water (HSSW) (Bindoff et al., 2000). HSSW exists across the Wilkes-Adélie Land margin with maximum salinities found in the George V Basin (Adélie depression) between 142.5°E and 145.5°E, near the Mertz Polynya (Rintoul, 1998). This area is also affected by intrusions of modified Circumpolar Deep Water (mCDW), which further increases salinities in the regional shelf waters (Rintoul, 1998). Once a critical density is reached, these salty plumes then flow down the continental slope into the abyss as Adélie Land Bottom Water (ALBW) and then merge with other water masses, such as Ross Sea Bottom Water (RSBW) to form AABW (Bindoff et al., 2000; Rintoul, 1998). Relative to other precursor AABW water masses, ALBW is colder, less saline, and more oxygenated in areas west of 143°E than it is on other areas of the continental shelf, which suggests a high volume of ALBW is formed here, either masking RSBW contributions, or the RSBW flows off the shelf prior to reaching this location (Rintoul, 1998). The combination of ALBW and RSBW is thought to produce 25% of all modern AABW (Gordon and Tchernia, 1972; Rintoul, 1998; Morales Maqueda et al., 2004; Williams et al., 2008; Yuan and Li, 2008)

Recently, the AABW in this region has been freshening and cooling. While cooling suggests greater amounts of ALBW in the mix, the mechanism for the freshening cannot be clearly defined as RSBW has also been freshening in recent years (Section 2.6.2) (Whitworth, 2002; Jacobs, 2004; Aoki et al., 2005; Williams et al., 2008).

In 2010, iceberg B9B collided with the MGT, causing it to calve, shortening the length of the tongue to half its original size (Young et al., 2010; Cougnon et al., 2017). This altered the regional icescape around the Mertz Polynya reducing the ability of the MGT from acting as a barrier to westward sea ice advection from the Antarctic Coastal Current (Tamura et al., 2012; Barber and Massom, 2007; Massom et al., 2001). Subsequent satellite-based studies showed the event reduced the size of the Mertz Polynya by ∼70% relative to the 2003-2009 mean

(Dragon et al., 2014) and reduced sea ice production by up to ∼20% relative to the 2000-2009 mean (Tamura et al., 2012) during the 2010-11 winter seasons. Observational studies indicated a significant freshening of the water column and a reduction in HSSW density in the two years following the event (Shadwick et al., 2013; Lacarra et al., 2014). Density of HSSW was reduced to such an extent it was near the limit necessary for AABW formation (Shadwick et al., 2013; Lacarra et al., 2014). Additionally, increased meltwater from the breakout of multi-year ice that was previously held back by the MGT lead to large phytoplankton bloom events greatly enhancing carbon uptake (Shadwick et al., 2013). Sediment core paleoclimate studies suggest ∼70 year periodicity to these large calving events over the previous 250 years, which may be related to ice tongue dynamics (Campagne et al., 2015). However, several other factors such as fast ice extent (Massom et al., 2010), ocean dynamics (Mayet et al., 2013), and random impacts of large icebergs exert control on the stability of the MGT (Massom et al., 2015) and these may also affect the periodicity of calving. Regardless of the MGT calving, this region experiences large year-to-year variability in sea ice production and dense water formation (Marsland et al., 2004; Kusahara et al., 2011).

Repeat hydrographic measurements before and after the MGT calving, coupled with an inverse box model suggest distinct seasonal variability in ocean circulation near the George V Basin along the Adélie Land continental shelf (Figure 2.10) (Snow et al., 2016). Summertime circulation is dominated by the geostrophic ACoC, which balances the pressure gradient created by coastward Ekman transport due to the katabatic winds in the region, and does not appear to be affected by the calving of the MGT (Parish and Bromwich, 1987, 1997; Turner, 2015; Snow et al., 2016). During the winter, surface cooling and brine rejection leads to surface buoyancy losses which drives Dense Shelf Water off the shelf, and facilitates the flow of mCDW onto the shelf (Snow et al., 2016). Snow et al. (2016) suggests the reduced polynya activity after the MGT calving (e.g. Tamura et al., 2012; Dragon et al., 2014) likely weakened this cross shelf exchange. In summary, summertime circulation is largely defined by the wind-driven ACoC, while winter circulation features a cross-shelf exchange driven by buoyancy fluxes.

2.5.3 Climate setting

The Adélie Land region is known for strong, persistent katabatic winds, that reach some of the highest sea level wind speeds on Earth, typically averaging 20 ms^{-1} (Ball, 1957; Parish and Wendler, 1991; Wendler et al., 1997). These winds form as cold, dense air masses converge in the interior of the continent and are funnelled down the continental slope towards the coast due to the negative buoyancy (Parish and Bromwich, 1987; Parish and Wendler, 1991; Parish

and Walker, 2006). Analyses of these winds from coastal weather stations show that these winds are unidirectional, and are negatively correlated with temperature and pressure (Parish and Walker, 2006; König-Langlo et al., 1998). The mean wind intensity is strongest during the austral winter (June-July-August), with the mean wind intensity becoming 60% weaker during the austral summer (December-January-February) (Parish and Walker, 2006). As these strong winds flow offshore, the Coriolis force diverts them westward where they merge with the nearshore easterlies (Parish and Bromwich, 1987, 1997; Turner, 2015) helping to propel the ACoC (Snow et al., 2016). The Dumont d'Urville (DDU) (66.6628°S, 140.0014°E) is the closest Automatic Weather Station (AWS) to Site U1357B (Grazioli et al., 2017). It is situated on an island ∼41 m.a.s.l, about 1 km from the coast, and measured winter temperatures rarely exceed -30°C and summertime maxima are rarely above 0°C (König-Langlo et al., 1998; Grazioli et al., 2017).

Interactions between the Adélie Land climate and the major modes of climate variability (Section 2.4) are not well understood. As mentioned previously, most modern day and paleoclimate studies focus on climate mode interactions with the Ross Sea and Antarctic Peninsula. However, tropical teleconnections in East Antarctica have been identified and are increasingly being studied (Clem et al., 2018; Deb et al., 2014; Smith and Stearns, 1993; Vance et al., 2013; Cai et al., 2011; Nuncio and Yuan, 2015).

An austral autumn study (March-April-May) using station and reanalysis data has suggested that surface air temperatures at Dumont d'Urville are strongly influenced by sea ice rather than wind in the fall season, and that sea ice is strongly influenced by SAM, with positive SAM being associated with positive sea ice anomalies (Clem et al., 2018). While this study found a significant correlation with La Niña events in the western East Antarctic during the autumn months, the correlation was less strong in eastern East Antarctica, near our region of interest (Clem et al., 2018). Schneider et al. (2012) found that during the austral summer, a strong positive correlation existed between positive temperature and rainfall anomalies in the eastern Pacific (typical of a canonical El Niño event) and positive surface air temperatures anomalies along coastal East Antarctic weather stations. This would suggest that austral summer temperatures in Adélie Land are warmer than average during an El Niño event. Furthermore, the positive PSA2 pattern associated with El Niño Modoki (Section 2.4.2), is robustly associated with unusually high onshore winds and poleward heat fluxes (Marshall and Thompson, 2016). Additionally, the composite difference (PSA2 positive - PSA2 negative) in SAT anomalies at Dumont d'Urville (DDU) is 3.5°C, suggesting a warming at DDU during the positive PSA2 pattern (Marshall and Thompson, 2016).

Reversed temperature and pressure anomalies in the Wilkes Land Region in the year before,

during and after an Southern Oscillation Index minima (an index used to monitor pressure anomalies associated with ENSO) suggest an Antarctic influence on ENSO may also exist (Smith and Stearns, 1993). Pressure patterns associated with such an event induce cold air outflows near Dumont d'Urville, and the Ross Ice Shelf, reinforcing blocking patterns near New Zealand that may further affect the Southern Oscillation (Mo et al., 1987; Parish and Bromwich, 1987; Trenberth, 1980). However, summer sea salts in the Law Dome ice core record suggests the SOI and sea surface temperature changes precede the broad scale weakening of zonal winds along East Antarctica by 1-3 months, suggesting that ENSO influences Wilkes Land, and not the other way around (Vance et al., 2013). Regardless, ENSO's impact on Adélie Land is modulated by the phase of SAM, with ENSO imprinting onto SAM when the oscillations are in phase with one another (i.e. Positive SAM, La Niña; Negative SAM, El Niño) (L'Heureux and Thompson, 2006; Fogt et al., 2011; Schneider et al., 2012). If these oscillations are out of phase with one another, the teleconnection to this area is weak to non-existent (Fogt et al., 2011).

Further obscuring the teleconnection impacts at Adélie Land is ENSO's relationship with the IOD. During a year with a positive IOD, a Rossby wave train is directed just east of Site U1357, inducing cooler meridional air flows and greater sea ice concentration (Nuncio and Yuan, 2015). However, when a positive IOD occurs during an El Niño year, this wave train moves westward, directly over Adélie Land (2.11).

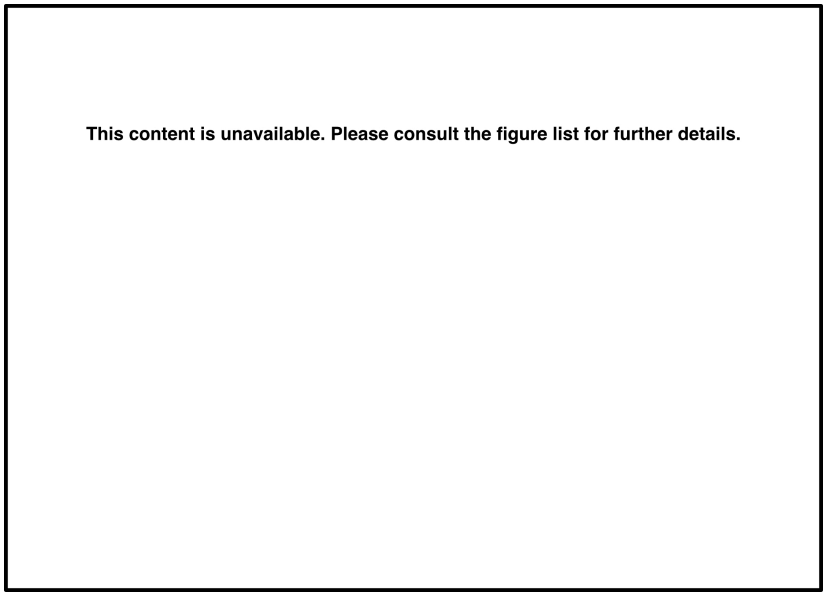

Figure 2.11: In-phase IOD-ENSO impact on Adélie Land. Blue area indicates increase in sea ice. Dashed arrows indicate cold meridional flows, while solid arrows indicate warm meridional flows. Orange star indicate approximate location of U1357B. Modified from Nuncio and Yuan (2015)

2.6 RICE

This section gives an overview of the geologic, oceanographic, and climatic controls at Roosevelt Island. The main features discussed in sections 2.6.1, 2.6.2, 2.6.3, are presented in Figure 2.12.

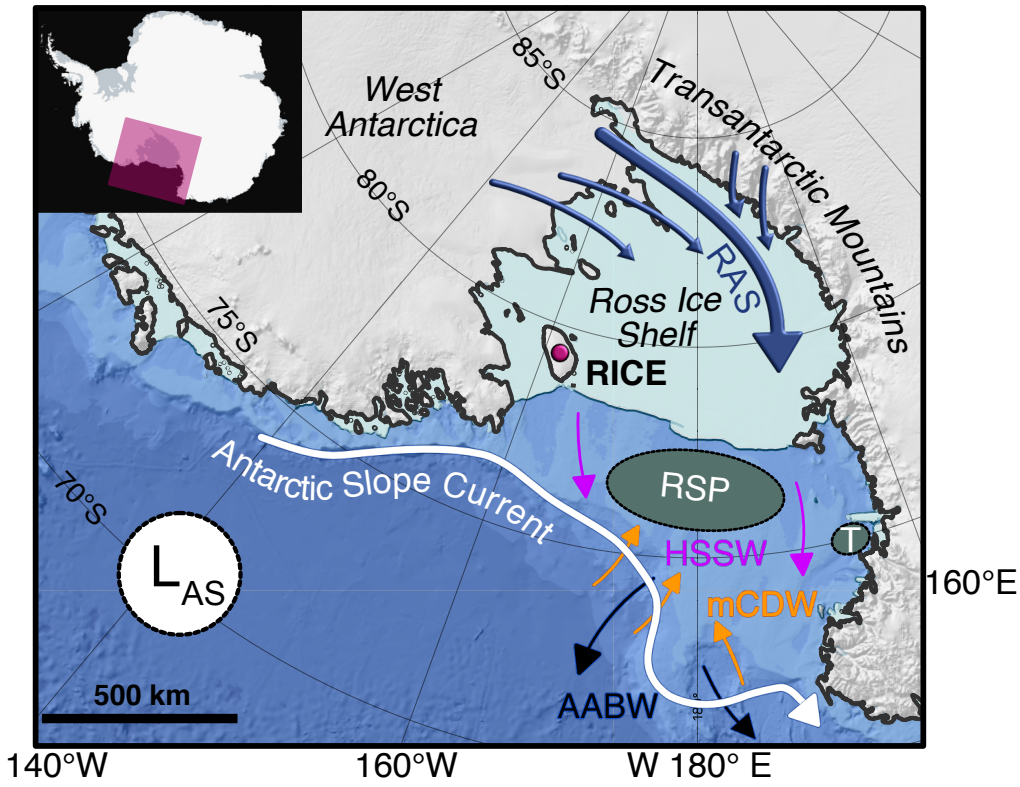

Figure 2.12: Map of Ross Sea region with RICE ice site location noted (magenta circle). The approximate location of the Ross Sea Polynya (RSP) and Terra Nova Bay Polynya (T) are indicated by green ellipses (Arrigo and van Dijken, 2003). Approximate direction and locations of the Antarctic Slope Current (white), High Salinity Shelf water (HSSW; pink), and modified Circumpolar Deep Water (mCDW, orange), and Antarctic Bottom Water (AABW; black) indicated (Smith Jr. et al., 2012). Ross Air Stream (RAS) indicated by blue arrows (Parish and Walker, 2006; Nigro and Cassano, 2014). Approximate location of Amundsen Sea Low (ASL; L_{as} in figure) (Hosking and National Center for Atmospheric Research Staff, 2019).

2.6.1 Glaciological setting

The 764 m RICE ice core (79.364°S, 161.706°W) was drilled near the summit of Roosevelt Island at an elevation of 550m above sea level (Bertler et al., 2018). Roosevelt Island is a grounded ice rise (214 mbsl) positioned in the northeastern edge of the floating Ross Ice Shelf (RIS) (Bertler et al., 2018). Ice accumulates locally at this site, with the Bindschadler, MacAyeal, and Echelmeyer ice streams flowing around the island as part of the RIS (Bertler et al., 2018). Distinct "Raymond Arches" (Raymond, 1983) present in ice penetrating radar surveys (Conway et al., 1999) indicate a stable ice divide for the past 3,000 years and perhaps longer. Within the last few centuries, the ice divide has migrated slightly, but the extent is too small to suggest a change in the accumulation gradient, buttressing pressure, or grounding line position (Bertler et al., 2018).

2.6.2 Oceanographic setting

Roosevelt Island lies at the southeastern margin of the Ross Sea Embayment, the largest producer and exporter of sea ice in the Pacific sector of the Southern Ocean (Jacobs et al., 2002). Much of the sea ice produced in the Ross Sea region is due to presence of the Ross Sea Polynya. While the greater Ross Sea region remains ice covered from March-November, areas directly along the RIS remain ice free due to strong katabatic winds pushing ice away from the RIS, helping the Ross Sea Polynya grow as large as 25,000 km^2 in the winter (Smith Jr. et al., 2012). The ACoC is also a critical influence as it brings fresher Antarctic Surface Water from the Amundsen Sea sector into the Ross Sea, encouraging development of sea ice (Smith Jr. et al., 2012; Jacobs et al., 2013). This in turn leads to the HSSW formation that sinks, intensifies and deepens density-driven stratification of water masses along the continental shelf, enabling the density driven inflow of CDW to the shelf (Ainley and Jacobs, 1981; Smith Jr. et al., 2012). The inflow of CDW and subsequent formation of mCDW has important implications for nutrient cycling, carbon cycling, and the freshening of other deep water masses which drive circulation (Killworth, 1983; Smith Jr. et al., 2012). The interaction of water masses within the Ross Sea lead to the area exporting as much as 30% of the total combined Shelf Water and Antarctic Surface Water to the deep ocean (Orsi et al., 2002). The Dense Shelf Waters eventually sink and form the precursor water mass, Ross Sea Bottom Water (RSBW), which is necessary for Antarctic Bottom Water (AABW) formation (Smith Jr. et al., 2012; Orsi et al., 2002). A diagram of these water masses is shown in figure 2.13.

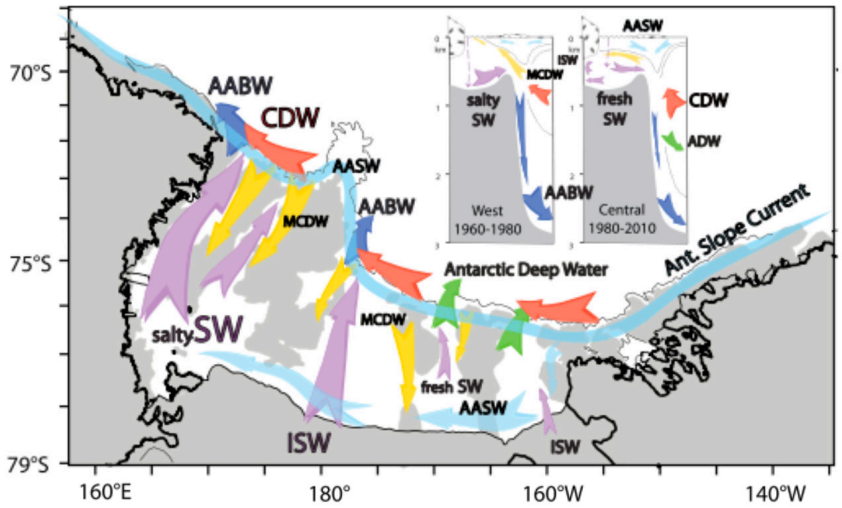

Figure 2.13: Observed ocean circulation over the last five decades. The relative strength of each flow is indicated by arrow width. Antarctic Surface Water (AASW) is shown in light blue, Shelf Water (SW) in purple, mCDW in orange, CDW in red, new Antarctic Deep Water (ADW) in green, New Antarctic Bottom Water (AABW) in dark blue. From Smith Jr. et al. (2012)

In recent decades, freshening of the shelf waters in the Ross Sea has been observed and is thought to be the result of increased glacial meltwater input transported via the ACoC from the Amundsen Sea sector (Jacobs and Giulivi, 1998; Jacobs et al., 2002; Jacobs and Giulivi, 2010; Budillon et al., 2011; Smith Jr. et al., 2012). Freshening of the RSBW has largely been attributed to freshening of Shelf Waters in the Ross Sea, as Ross Sea Shelf Waters make up over a third of RSBW (Jacobs et al., 1970; Orsi et al., 1999; Jacobs and Giulivi, 2010; Smith Jr. et al., 2012).

The Ross Sea region is one of the most biologically diverse waters in Antarctica (Smith Jr. et al., 2012). Phytoplankton vary seasonally, and sea ice dynamics are a governing factor of productivity (Tremblay and Smith, 2007; Smith Jr. et al., 2012). The Ross Sea Polynya has the highest annual rates of primary production in the Southern Ocean, and as such is an important carbon sink in the Southern Ocean (Arrigo et al., 2008b,a; Smith and Gordon, 1997).

2.6.3 Climate setting

Climate in the Ross Sea area is influenced primarily by the topography of the Transantarctic Mountains and East Antarctic Ice Sheet to the west, and active cyclogenesis in the Ross Sea (Parish et al., 2006; King and Turner, 1997). A primary climatological feature of the RIS is the Ross Air Stream, a persistent channelized flow of drainage winds from the ice sheets onto the western and central RIS (Parish and Walker, 2006; Nigro and Cassano, 2014). Onshore winds

on the RIS are warm and moist, while offshore winds (usually from WAIS) are cold and dry (Bertler et al., 2004, 2018).

An Automatic Weather Station (AWS) was deployed at the RICE drill site from November 2010 to November 2013. The Margaret AWS is the closest AWS to the RICE AWS, located 96 km to the southwest (80.0°S, 165.0°W) and 67 m.a.s.l (Bertler et al., 2018; Costanza et al., 2016). Measurements from these locations suggest Roosevelt Island experiences lower wind speeds compared to other areas on the Ross Ice Shelf as it lies outside the main Ross Air Stream channel flow (Costanza et al., 2016; Emanuelsson et al., 2018). Typically, winds come from the southeast, but can come from any direction (Costanza et al., 2016). Due to these circulation differences along the Eastern and Western RIS, climate at Roosevelt Island often differs from conditions in the Western Ross Sea (Bertler et al., 2018).

Estimates of the average annual temperature at the RICE drill site range from -26.6°C to -23.5°C (Bertler et al., 2018). From 2010-2013, the average annual snow accumulation at RICE was 22 ± 4 cm $w.e.yr^{-1}$ (water equivalent per year) (Bertler et al., 2018). High precipitation events at RICE can obscure smaller events in the ice core accumulation record (Emanuelsson, 2016). These large precipitation events at Roosevelt Island are driven by high pressure blocking events in the Amundsen Sea (Renwick, 2005) which reduce sea ice extent in the Eastern Ross Sea, and induce warm onshore flow due to anticyclonic rotation (Emanuelsson et al., 2018).

The Ross Sea region's sensitivity to SAM, ENSO, IPO, as well as the ASL (e.g Bertler et al., 2004; Kwok and Comiso, 2002a; Turner, 2004; Yuan, 2004; Yuan and Li, 2008; Stammerjohn et al., 2008; Raphael et al., 2019; Turner et al., 2017a) suggest that Roosevelt Island is sensitive to these climate modes. The associated impacts of these modes on the Ross Sea are discussed in the following paragraphs.

The phasing of the IPO affects the high pressure centers associated with the anomalously high rainfall events discussed above (Emanuelsson et al., 2018) moving them 20 degrees of latitude eastward to 100°W, affecting the location of onshore flow (Henley et al., 2015). The positive phase of the IPO leads to warm sea surface temperature anomalies in the Ross Sea, as well as the Amundsen and Bellingshausen Seas, with negative sea surface temperatures seen in all three locations during negative IPO (Henley et al., 2015).

During positive SAM, there is typically more sea ice and anomalous heat flux towards the tropics. However, Marshall and Thompson (2016) showed that the Western Ross Sea experiences poleward heat fluxes across the western RIS. However, this signal is not seen in surface air temperatures as cold temperature anomalies exist across the entire RIS during positive SAM (Marshall and Thompson, 2016). Near RICE, colder temperatures and increased sea ice extent are likely to exist during positive SAM.

The eastern Ross Sea experiences increased onshore airflow (Marshall and Thompson, 2016), warmer sea surface temperatures, warmer surface air temperatures and less sea ice during canonical El Niño events due to anomalous anticyclonic flow (Bertler et al., 2006; Yuan, 2004; Marshall and Thompson, 2016). However, the PSA2 pattern associated with El Niño Modoki patterns, shifts the center of this anticylonic flow westward, enhancing katabatics on the eastern RIS, and increasing onshore flow of marine air masses along the western RIS (Marshall and Thompson, 2016).

The breadth and position of the ASL (Section 2.4.4) determines the associated sea ice and temperature anomalies in the eastern Ross Sea (Raphael et al., 2016). Positive SAM and La Niña events intensify the ASL, which in turns enhances the associated anomalies (Fogt et al., 2011; Turner et al., 2013). Meehl et al. (2016) suggested the recent trend towards a negative IPO, which deepened the ASL, has led to the observed increase in sea ice extent in the Ross Sea across all seasons.

2.7 Connection between RICE and U1357

The RICE ice core lies upstream oceanographically from site U1357B in the Adélie Basin. As noted above, relatively warm and salty RSBW flows eastward by means of the ASC and then merges with the colder and fresher Adélie Land Bottom Water to form AABW for the entire Australian-Antarctic Basin (80°E-150°E) (Jacobs et al., 1970; Gordon and Tchernia, 1972; Ainley and Jacobs, 1981; Rintoul, 1998; Whitworth et al., 1998; Orsi et al., 1999; Fukamachi et al., 2000; Whitworth, 2002; Rintoul, 2007).

Preliminary modelling studies using a Lagrangian tracer model indicates a direct connection (<4 months) between Ross Sea surface waters and surface waters in the Adélie Land Region due to the strong along-coast flow, whereas deeper water masses take about three years to reach Adélie Land from the Ross Sea region (personal communication, Veronica Tamsitt and Matt England). The majority of deep water flowing towards Adélie Land does not flow directly over the drill site, instead hugging the continental shelf with the ASC, but surface waters in the Adélie Land are likely to be influenced by surface water changes in the Ross Sea.

Chapter 3

Developing the Adélie Basin sediment core and RICE Early Holocene major ion record

3.1 Foreword

The aim of this thesis is to develop the annually resolved IODP U1357B Adélie Basin sediment core record and the RICE ice core record, to create an integrated Holocene record that explores atmospheric circulation, sea ice extent, primary productivity, and ocean circulation throughout the Holocene. To achieve my aim, I analysed X-ray Computed Tomography (CT) scans of IODP U1357B and 3,160 ion chromatography samples from the RICE ice core. The underlying theories, methodologies, and additional datasets for the IODP U1357B record are presented first. Next, the same is presented for the RICE ice core, as well as outlining how the interpretation of the RICE continuous flow analysis calcium was made. Last, a brief section explaining the statistics used to identify abrupt change at RICE, Taylor Dome, TALDICE, and U1357B for Chapter 6 is provided.

3.2 IODP U1357B methods and data sets

3.2.1 Introduction

X-ray CT scans are increasingly being used as a non-destructive way to evaluate sediment cores for paleoclimate reconstructions. CT scans produce sub-millimetre resolved, 3-dimensional axial and coronal plane images that can be used to determine core density (Orsi et al., 1999), characterize stratigraphy (Boespflug et al., 1995), assess physical sediment properties (Orsi et al., 1994), and create high-resolution paleoclimate reconstructions (St-Onge and Long, 2009).

In this study, CT-scan images are used to quantify and characterise the continuously laminated diatom ooze in IODP core U1357B. This core has the highest resolution and is the longest Holocene marine core ever collected with sedimentation rates averaging ∼1.5-2 cm/yr. However, several aspects of the core have proven difficult to analyse. Firstly, the high amounts of organic matter resulted in rapid oxidation of the core surface which lead to highly ephemeral surface colour changes, making comparison of laminae using core photographs impossible (Albot, 2017). Secondly, laminae could not be characterised by physical property measurements due to the low signal to noise ratio in line-scan magnetic susceptibility, density, and natural gamma radiation (NGR) datasets, and this also made the development of a splice record difficult (see 3.2.2). Finally, high amounts of biogenic gas created large (several centimeters) to small (millimeter) scale gaps throughout the record that formed during the core recovery process and therefore resulted in expanded stratigraphy that has to be corrected for. While the larger gas expansion intervals can be manually corrected for, CT image processing can mask small-scale cracks, but more critically, can highlight more subtle laminae not visible on the line-scan photographs, with a higher signal-to-noise ratio and spatial resolution (sub-mm) than is possible with the other line-scan datasets (physical properties, XRF). As CT-scanning is measuring density, it is not affected by the differential oxidation issue that compromised the use of line-scan photographs to characterise the laminae (Albot, 2017).

A line profile taken from the long axis of the CT images can be converted to a greyscale curve that quantifies changing X-ray attenuation values over light and dark laminae. The greyscale curve is compared to the physical core properties and XRF data to verify that greyscale variance reliably captures changes in sedimentation and geochemical properties. In particular, XRF productivity proxies (Silica/Titanium and Barium/Titanium) ground the greyscale and laminae datasets as capturing changes in biosiliceous sediment associated with primary productivity. These quantitative datasets are complemented by manual identification of laminae (section 3.2.3.4) that allows for laminae thickness and frequency variations through time to be determined. Statistical time series analysis on the laminae datasets provide context for the age model and other paleoenvironmental proxies in the U1357B core.

3.2.2 Core acquisition and depth scale development

Three holes (U1357 A, B, and C) were drilled in the Adélie Basin as part of IODP Expedition 318 (Escutia et al., 2011). In the case of incomplete recovery, triple coring is a standard IODP procedure to allow for continuous stratigraphy to be recovered by splicing sections from individual holes to form a single stratigraphic section. This is usually achieved in IODP cores by

using physical core properties to guide the placement of the least disturbed, highest recovery intervals to be used in the spliced sections. However, cores from Site U1357 are problematic in this context as the extremely high biogenic and gaseous content precluded many physical property measurements, such as magnetic susceptibility and density, from being registered beyond typical noise levels. Further attempts to measure magnetic properties by U-channelling the sediment were also unsuccessful (Lisa Tauxe, personal communication). Due to the high biogenic content of these cores, the sediments rapidly degassed methane and hydrogen sulfide once brought to the surface. This caused several types of post-recovery disturbances, including mm- to cm-scale cracks, large gaps (up to 45 cm) in some core sections, and loss of sediment from the base of core runs. As this disturbance alters the true stratigraphic depth of the cores, it requires correction prior to any time series analysis.

Core recovery from each 9.5 m piston core run often exceeded 100% due to expansion as cores decompressed during recovery. In U1357B, recovery was 101%, whereas core A had 99% recovery and core C had 107% recovery. Data derived from these initial curated core lengths are termed the csf-a depth scale and are the depth scale for any physical property and shipboard based data. The CT image data are inherently on the csf-a scale.

The standard IODP procedure to correct for the expansion (and subsequent recovery exceeding 100%) is to apply a linear compression algorithm to scale recovery back to 100% and to create a new scale (csf-b), as it is assumed expansion is uniform in the core (similar to equation 3.2). However, at Site U1357, expansion due to biogenic gas was particularly high and resulted in discrete sections of core being pushed apart creating voids (greater than 1 cm) in the depth scale that did not represent real gaps in the stratigraphy. This meant the expansion was not linear and csf-b corrections were not fit for purpose. To account for this, the voids were mapped against the csf-a depth scale and subsequently numerically removed. The original csf-a depth scale was then adjusted to account for these voids, and if recovery still exceeded 100%, the standard IODP linear compression algorithm was applied. In this study, this is termed the csf-d scale, noting it is not an official IODP depth scale term.

To develop the csf-d scale, the csf-a scale was used for each core top and the new depths after void removal were scaled accordingly. This made the assumption that the majority of sediment was lost from the base of each core run during recovery, which is consistent with how sediment loss due to expansion occurs during the piston coring method. The recovery rate of U1357B was subsequently reduced to 90% after scaling to the csf-d depth scale.

This study primarily uses the csf-d scale when discussing the core. It should be noted that the csf-a depths from the CT data had to be compressed to a new csf-a depth due to minor core movement (max $\sim$2 cm) during storage (see Section 3.2.3.3). These depths and were then

linearly interpolated to the csf-d scale.

3.2.3 X-ray Computed Tomography

X-ray Computed Tomography (CT) scanners work by quantifying the amount of X-ray energy absorbed (attenuated) by a particular object and displaying the resulting attenuation coefficients in a greyscale image (St-Onge and Long, 2009). Pixel values within these images are expressed as relative greyscale values or Hounsfield units (HU) (also known as CT number) which are calculated by comparing the sample attenuation coefficient to that of water (Hounsfield, 1973; St-Onge and Long, 2009), as shown in the equation below.

$$HU = \frac{\mu_{sample} - \mu_{water}}{\mu_{water}} \times 1000 \tag{3.1}$$

X-ray attenuation, and therefore Hounsfield units are a function of density, porosity, chemical composition, and grain size of the sample (Boespflug et al., 1995). Brighter areas in the image represent higher attenuation, while darker areas represent lower attenuation. CT scans were completed on core U1357B using a Toshiba Aquilion TXL CT scanner at the Department of Petroleum Engineering at Texas A&M University in College Station, Texas. Axial scans were completed at 135 kVp and 200mA, and coronal slices were created in open-source HOROS software (HorosProject.org, 2017). The resolution averages 1.3 pixels per mm, and each core was exported as its own DICOM image stack which contained 512 images. The best image (e.g. accounting for cracks and other spaces in the core) from each stack was then selected and exported to another CT processing software, FIJI (Schindelin et al., 2012), for greyscale analysis and laminae counting.

3.2.3.1 Isolating cores and choosing DICOM slice

Due to time and computational constraints, most of the core sections were scanned in sets of twelve. All core sections from core number 18 and core number 19 were scanned singularly. Core sections 17H4, 17H5,17H6,17H7 were scanned in a set of four. For the sets of twelve, a coin was placed on the back, bottom right corner, of CT table to distinguish core orientation when looking at the DICOMs. Core placement when scanned in sets of multiples is shown in Figure 3.1.

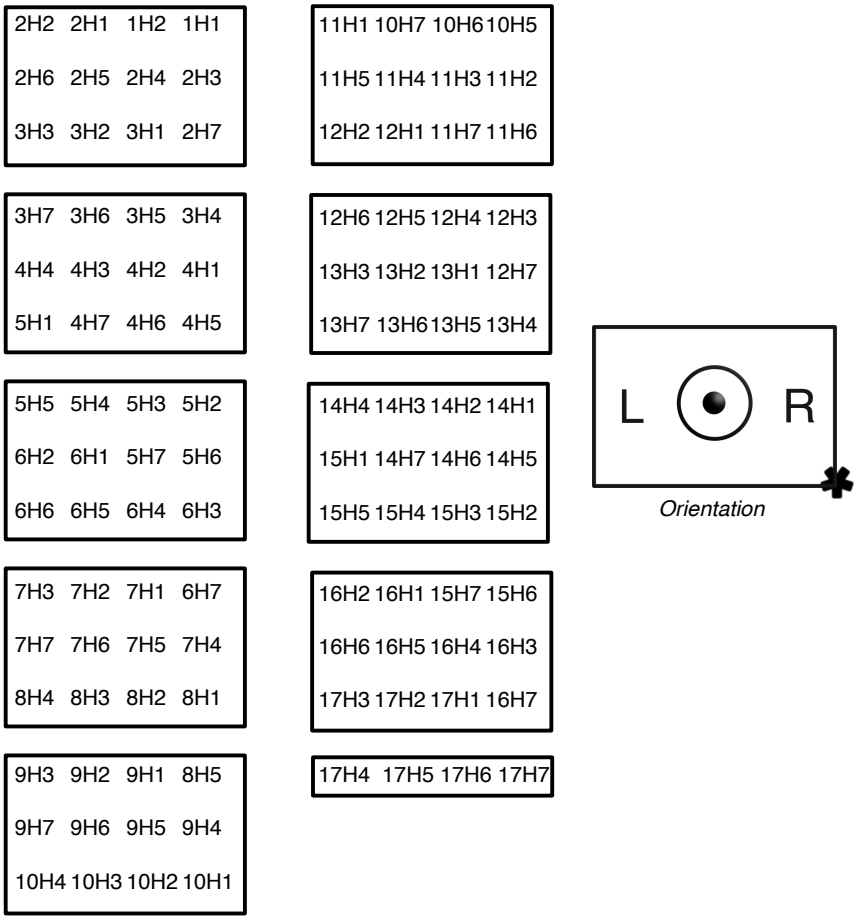

Figure 3.1: Core placement when scanned in X-Ray Computed Tomography Scanner. Each box represents one scan. Orientation is provided on the right. If the box represents the CT scanner, the orientation is out of the page towards the observer (as indicated by the circle with the dot in the center) and the top of each core section is closest to the reader. As the sections are scanned through the CT machine, the bottom of each core section comes out last, and is marked by a bright spot from the coin (black star in diagram) in the back, bottom right hand corner. *L* and *R* designate left and right, respectively.

All core catcher sections were also scanned. Core catchers were included in the same tube as core section 7 (2H7, 3H7, 4H7, etc.), except for core 8, which was included in core section 8H5 as core 8 only had five sections.

Core 9H6 was scanned singularly, and as a set of twelve to compare the resolution differences. The results on the greyscale curve are discussed in section 3.2.3.3.

To acquire the greyscale profile along the z-plane of the sediment core, core sections needed to be isolated from one another in the sets of twelve or four. The orientation of the core sections is flipped when viewing the DICOM images produced by the CT scanner on the computer, as

shown in Figure 3.2.

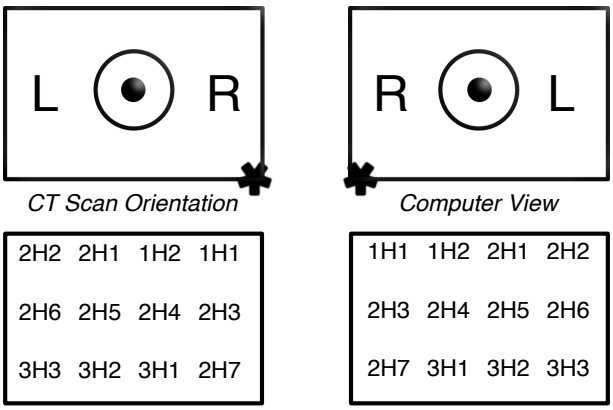

Figure 3.2: Core orientation in DICOM images when viewed on computer. Placement is flipped horizontally.

A closed polygon Region of Interest (ROI) was used to isolate a core section or layer of core sections (top, middle, or bottom rows shown in Figure 3.1) using Horos software (HorosProject.org, 2017). The ROI was propagated through the entire DICOM image sequence and all areas outside the selected ROI were deleted. This created a new image sequence solely containing the core section or sections of interest. From here, the image that provided the best view of each core section was chosen to create a greyscale profile and conduct laminae counting. As the core orientation was flipped, special care was taken to compare the final DICOM image to line scan photographs to ensure the core sections were labelled correctly during this process.

3.2.3.2 Image preparation

Several steps were taken to prepare single DICOM images for laminae counting and creating a greyscale profile. Single DICOM images were loaded into FIJI (Schindelin et al., 2012) software. DICOM images were cropped close to the core liners to remove the background color of the DICOM. The image type was then changed to a 32-bit image, as this allowed any greyscale value outside of a chosen 'threshold' greyscale range to be set to NaN. In this study, any greyscale value less than zero was converted to non-values (NaNs). Most CT studies on sediment cores where the CT scanner has been scaled to HU units use a lower threshold of 0, as a HU value of 0 is classified as water, and -1000 is classified as air (Hounsfield, 1973; Orsi et al., 1994; Reilly et al., 2017). The thresholded image preserved the relative greyscale values of the core, while eliminating noise from pervasive sub-mm to mm-scale cracks resulting from

expansion due the presence of biogenic gas in the cores (see figure 4.1).

After the image was thresholded, a new color table (mpl-viridis) was applied to visually enhance the light and dark laminae. The final image was saved as a TIFF and was used to produce the greyscale curve (section 3.2.3.3) and to manually count the light laminae in the core (section 3.2.3.4).

A few cores were scanned in two parts due to errors during the CT scanning. Cores scanned in two parts included 17H4, 17H5, 17H6, 18H2, and 19H4. Images for each section of the above cores were prepared using the methods described above.

3.2.3.3 Greyscale curve

A single greyscale curve was created for U1357B by taking a line profile of the greyscale image for each core using FIJI (Schindelin et al., 2012). The line profile was 4 pixels wide, with the value of each row being the average of these four pixels. The profile was chosen to minimize core disruptions. Many CT studies choose to average all rows along the whole width of the image, but this was not possible for this core due to the location of the U-Channel sample, and minor coring disturbance resulting in curved laminae along the core liner edge due to the piston coring methods (Escutia et al., 2011).

Additionally, several sections had missing intervals that were not CT-scanned. Whole round samples were collected during coring for optically stimulated luminescence (OSL) dating (cores 17H5 and 19H4, with ∼60 mm and ∼50 mm missing, respectively). For 3H3 and 18H2, this was a ∼40 mm and ∼80 mm void (respectively) at the bottom of the core that was not scanned in the CT image. All of these 'missing sections' still form part of the csf-d depth scale, and NaNs were put in to maintain the appropriate depth-pixel value relationship in the core.

Lastly, a curation error lead to the working half of section 19H1 being scanned instead of the archived half of 19H1. While this section was not U-channeled, it contained randomly distributed sampled locations across the core face which precluded a single line profile from being measured. Therefore, the entire core width (in this case, 300 pixels wide) was used to acquire the greyscale profile.

Some of the CT-scan profiles were longer or shorter than the curated length from the IODP repository. Slight changes in length were expected as the cores had been stored for several years and slight movements could have occurred in that period. A compression function was applied to scale the CT-scan measured depths to the curated lengths. The following equations were used:

$$Recovered\ Section = \frac{Measured\ CT\ Length}{Curated\ Section\ Length} \tag{3.2}$$

$$Core\ Compressed = TD_{section} + \frac{TD_{CTsample} - TD_{section}}{RecoveredSection} \tag{3.3}$$

where $TD_{section}$ is the **curated top depth** of a section and $TD_{CTsample}$ is the **measured CT top depth** of a section. The maximum difference between the measured CT length and curated length was ~22 mm, with the mean being ~6 mm.

The final compressed depths (equivalent to the original csf-a scale) were then interpolated to the csf-d scale, as well as to the age model to attain csf-d depths and ages of the greyscale curve and laminae derived from the CT-scan data.

To compare how scanning the cores in sets of twelve versus singularly affected the greyscale data, the profile from core section 9H6 which was scanned both as a set of twelve and singularly, was plotted and it demonstrated the same signal (Figure 3.3). The 9H6 profile from the core scanned singularly is of higher resolution at 0.212 mm spacing, and the profile from the set of 12 at 0.769 mm spacing.

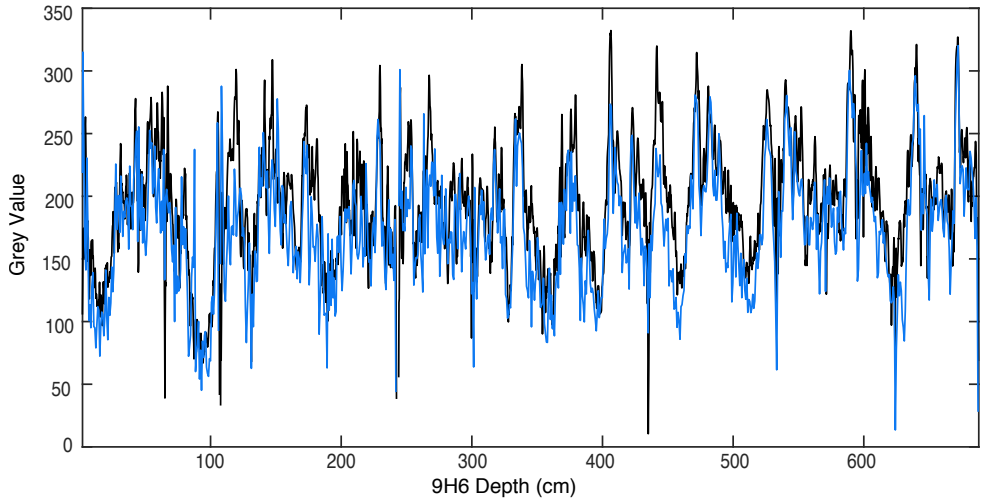

Figure 3.3: Comparison of greyscale profile from core 9H6 scanned singularly and as a set of 12. Black curve is the profile of the core scanned singularly. Blue curve is the profile of the core scanned as a set of 12. The entire right side (right of the U-Channel) of the core was used to create the plot profile in this example, as it was difficult to ensure perfect alignment of the ROI line profile from one image to another.

3.2.3.4 Manual identification of laminae

The top and bottom depths of bright laminae were identified manually throughout the entire core using the multi-point tool in FIJI (Schindelin et al., 2012). Hereafter, the manual identification and subsequent quantification of laminae are referred to as 'laminae counts', with light or dark preceding the term to reference the type of laminae being discussed. While manual identification has a subjective element to it, it is preferred over automated counting methods as some laminae had sharp divisions between bright and dark pixels, while others had a more gradual transition, and some boundaries were associated with expansion gaps in the core. In addition, some bright laminae were interspersed among a slightly lighter background, making it sometimes difficult to distinguish between multiple laminae and single events. Such intervals were counted as a single laminae, so as not to introduce extra laminae, but suggest these could represent seasons when there were multiple blooms or prolonged bloom events (Figure 3.4). Given the unique nature of this core and the issues noted above, as well as the variable gas expansion disturbance, automated methods would still require significant vetting of the dataset, and extensive algorithm training. To validate the manual identification method, an independent time series analysis is also conducted on the raw greyscale curve derived from the CT-scan data (Section 4.3.2).

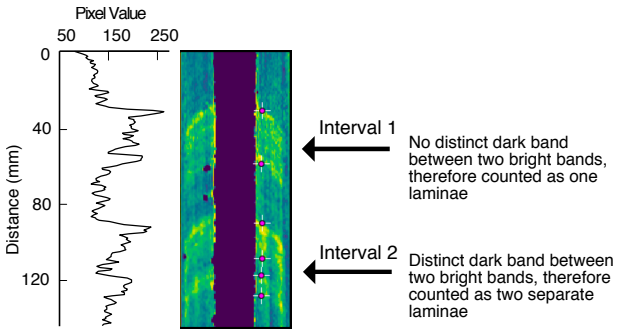

Figure 3.4: An example of laminae counts from 2H2 which shows the distinction between intervals considered one laminae event versus multiple. Note that two dots represent one laminae, as both the top and bottom of each laminae was marked in order to calculate laminae thickness. Interval 1 shows some brighter laminae interspersed between a slightly lighter background, with no distinct darker band, and is therefore counted as one laminae. Interval one could represent a season with multiple or prolonged blooms. Interval two shows two bright laminae, with a slightly lighter background and a distinct dark band between the laminae, and is therefore counted as two laminae. Greyscale profile shown on left.

3.2.4 Laminae thickness

Laminae thickness was calculated by measuring the distance between the top and bottom of single laminae (Figure 4.5).

3.2.5 Age model

The age model presented below for U1357B is preliminary and currently unpublished, and was developed from 87 ^{14}C dates from bulk organic carbon obtained by Rob Dunbar (Stanford University) to constrain the ages of the sediment between 11,400 cal. years BP and the modern day (Dunbar et al., *in prep*) (Figure 3.5). The laminae frequency dataset presented in this thesis is intended to help inform on the reliability of this age model.

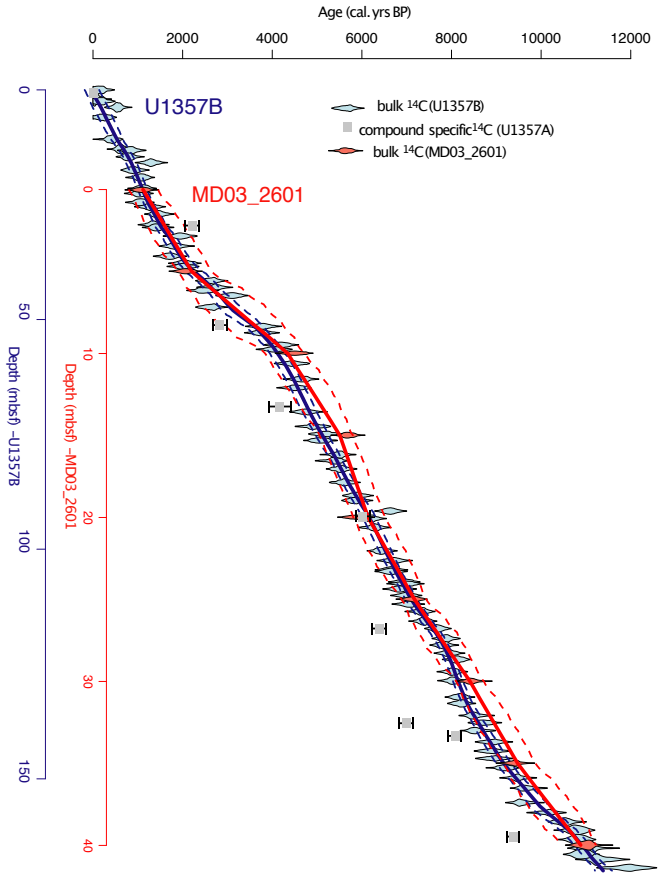

Figure 3.5: **Age model for U1357B and other nearby records.** Age model for U1357B (blue) and MD03-2601 (red) show that sediment advection is a regional signal as sedimentation rates covary. Compound specific ages from U1357A are shown in grey – see text for discussion. U1357B is a longer core with 87 ^{14}C dates, leading to a much higher resolution age model. U1357B also includes the last 1,000 years, which is lacking in MD03-2601. Note: MD03-2601 is discussed in more detail in Chapter 5

The age model in U1357B only resolves ages to 11.4 ka BP as ages older than this are anomalously old and assumed to be due to input of reworked carbon of pre-Last Glacial Maximum age. Ages younger than 11.4 ka BP are not likely to be affected by reworked carbon at the Adélie Drift site, as glacial influences were negligible, and the dominant carbon source is from local diatom bloom events. The consistent stratigraphic order of the radiocarbon ages and sedimentation rates through the Holocene support this interpretation. A reservoir correction age of 1,200±100 years (Gordon and Harkness, 1992; Berkman and Forman, 1996) was applied to the depth to age conversion calculated by BACON, which uses a Bayesian iteration scheme that invokes memory from dates above any given horizon and produces a weighted

mean and median age-depth curve (Blaauw and Christen, 2011). This correction is consistent with the uncalibrated age of the upper most sample of 1,310 years.

The age model is in good agreement with the majority of samples from a low resolution compound specific ^{14}C age model derived from C_{16} fatty acids from core U1357A. The exception to this is two compound specific ages at 117 and 138 mbsf that are much younger than the bulk ages (Yamane et al., 2014) (Figure 3.5, grey). These two outlier compound specific ages imply a rapid shift in sedimentation rate of up to 6.64 cm/yr between to 6,335 and 7,220 yrs BP, and then require a condensed section with sedimentation rates of 0.41 cm/yr to fit the deeper ages, that are similar to those from the bulk organic carbon age. As there is a consistent stratigraphic order to the bulk organic carbon ages which have a much higher sampling resolution, and these samples do not invoke anomalously large shifts in sedimentation rates, the preferred age model is that derived from the bulk organic carbon ages, and less weight is placed on these outlier compound specific ages. There are no major shifts in biological opal content (included in Mass Accumulation Rates, Si/Ti ratios, or grainsize (Chapter 4)) in this interval that imply a rapid shift in sediment advection rates or productivity increases at this time. Changes in laminae frequencies with depth (Figure 4.4) are used to assess the reliability of the bulk organic carbon age model, as are comparisons to age models from nearby core MD03-2601 (Figure 3.2.5). Regardless, the compound specific and bulk organic carbon age models are highly consistent for intervals younger ∼6,335 yrs BP.

The BACON methodology was also applied to the ^{14}C dates from MD03-2601(Crosta et al., 2007, 2008) to recalibrate the MD03-2601 age model. An earlier age model of this core (Crosta et al., 2007) used an inferred meteorite impact at ∼15 m to determine an age of 4 ka BP at that depth. The old age model also removed two ^{14}C dates at 4.4 and 5.6 ka BP due to the assumption that these ages were anomalously old relative to the meteorite impact. However, the meteorite age-depth correlation cannot provide absolute age control and the new age model presented here implies that the impact occurred around 5.4 ka BP. Comparison between the U1357B and new MD03-2601 age model show strong covariance in sedimentation rates and suggest sediment rates are influenced by regional processes (Figure 3.5).

3.2.6 X-ray fluorescence

X-ray Fluorescence data were measured using an AVAATECH XRF core scanner at the JRSO XRF facility, located at the Gulf Coast Repository at the Texas A&M University Research Park. Measurements were undertaken at a 0.5 cm resolution (where possible) with a 5mm slit size using generator settings of 10 kV and currents of 0.8 mA. The sampling time was set at 45

seconds and scanning took place directly at the split core surface of the archive half. The split core surface was covered with a 4-micron thin SPEXCerti Prep Ultralene1 foil to avoid contamination of the XRF measurement unit and desiccation of the sediment. All measurements were conducted by Francisco Jiménez-Espejo (University of Granada).

As light laminae are inferred to be caused by mass phytoplankton bloom events associated with sea ice melt (Denis et al., 2006; Maddison et al., 2012; Alley et al., 2018), XRF paleoproductivity ratios are of particular interest for this thesis. The mean estimate of diatom content from smear slides in U1357B is 91% (volume %)(Escutia et al., 2011). Biogenic silica (%BSi) content ranges from 30 to 63% (weight %), with an average of 48% (weight %) for the late Holocene. The difference between the volume % and weight % is attributed to the lower density of opal relative to terrigenous material. %BSi concentrations in high latitude marine sediments can be used to indicate diatom productivity (e.g Ragueneau et al., 2000; Iwasaki et al., 2014), and Silicon (Si) based ratios can be used to infer %BSi concentration in sediments (Brown, 2015). Often, the silicon is normalized to an inert, terrigenous element such as titanium (Ti) or aluminum (Al) to constrain contributions of biogenic silica, as silicon can come from both terrigenous and biogenic sources. The Si/Ti and Si/Al ratios provide relative records of silicious productivity (Agnihotri et al., 2008; Marsh et al., 2007; Rothwell and Croudace, 2015; Dickson et al., 2010). Barium (Ba) can also be indicative of productivity (Goldberg and G.O.S., 1958; Rothwell and Croudace, 2015) when normalized in similar ratios, such as Ba/Ti (Presti et al., 2011). While these ratios should be similar, a multiproxy approach to paleo-productivity studies is recommended (Rothwell and Croudace, 2015), and all three of these ratios are shown in future sections to add to the robustness of interpretations in Chapter 4.

3.2.7 Grain size analysis

Grain size analyses were conducted as part of the Albot (2017) thesis. A brief overview of the methods used are described below.

Grain size analysis was performed on 341 samples. Samples were treated twice with a 1M sodium hydroxide (NaOH) solution in an 80°C water bath for 24 hours to remove biogenic opal, and then treated with hydrogen peroxide (H_2O_2) to remove organic material. Smear slides of randomly chosen samples were inspected to ensure dissolution of the diatoms and organic material was complete. As terrigenous material formed a minor component of the bulk sediment, post treatment sample mass varied from ∼0.035-0.8 g. Samples were measured on a Beckman Coulter LS 13 320 Laser Diffraction Particle Size Analyser (LPSA). Eighty-four

sub-samples were taken after chemical treatment with NaOH and H_2O_2 to assess for reproducibility; while twelve samples were split in to two subsamples and chemical treatment was performed on each subsample to test for biases relating to subsampling and chemical dissolution. Correlations calculated using a least squares regression between the original and repeat measurements were r^2=0.74 for the post chemical treatment replicates and r^2=0.75 for the pre-chemical treatment replicates.

3.2.8 Mass accumulation rates

Mass accumulation rates (MARs) were also calculated as part of the Albot (2017) thesis, but derived from the unpublished age model presented in this chapter (section 3.2.5). A brief overview of the methods used are described below.

Terrigenous and Biogenic MARs were calculated using the following formula:

$$MAR = \%A \times (LSR \times BD) \tag{3.4}$$

where,

MAR = mass accumulation rate (g/cm^2/yr)
LSR = linear sedimentation rate (cm/yr)
A = the percent abundance of the component of interest (i.e. terrigenous or biogenic)
BD = bulk density (g/cm^3)

Bulk density measurements for U1357B do not exist. Moisture and density (MAD) bulk densities from core U1357A (taken at the same site location) are used instead, with a linear fit taken though these data to derive a downhole estimate of changing bulk density relating to potential changes in lithology and compaction (Escutia et al., 2011). The associated depths of these discrete samples were converted to age using the U1357A age-depth model. This model uses 36 bulk organic carbon dates and the same Bayesian approach used in the U1357B age model. A linear fit between the age and density measurements of U1357A was interpolated to the U1357B age scale to determine the downhole trend of dry bulk density for U1357B. Direct splits of the grain size samples (∼66 year resolution) were used to determine the biogenic silica and terrigenous percentage of light and dark laminae. The MARs were then calculated from these same couplets. Biogenic silica measurements (BSi%) were determined using alkaline extraction spectrophotometric methods, and were conducted by Christina Riesselman at University of Otago (Mortlock and Froelich, 1989).

3.2.9 Highly Branched Isoprenoid (HBI) lipid biomarkers

$IPSO_{25}$ (for Ice Proxy for the Southern Ocean with 25 carbon atoms) is another name for the Highly Branched Isoprenoid (HBI) lipid biomarker (diene II) and is a proxy for coastal fast-ice (Belt et al., 2007, 2016). The C25-highly branched isoprenoids (HBI) alkenes, in particular the di-unsaturated C25-HBI with a double bond, also referred to as diene II, were extracted at Laboratoire d'Océanographie et du Climat: Experimentations et Approches Numériques (LOCEAN) by Johan Etourneau.

Measurements for $IPSO_{25}$ are used in this thesis to infer coastal sea ice conditions in the Adélie Land Region, which are known to affect primary productivity.

3.2.10 Linear sedimentation rates

The linear sedimentation rates were calculated for every centimetre using the age-depth model in section 3.2.5. These rates were then averaged into 10 cm bins.

3.2.11 Statistical methods

3.2.11.1 Binning laminae and relationship to age model

Laminae events were binned by meter to assess frequency with depth and any age artefacts that may be introduced when trying to assess laminae frequency through time.

To understand laminae frequency through time, laminae were binned into 100-year intervals and 10-year intervals. For bins that contained missing years, i.e. the base of a 9.5 m core run where recovery was <100%, the binned laminae amounts were scaled to represent the actual number of years per bin. For the scaled 100-year bins, two data points were removed because the bins contained fewer than 20 years of data.

3.2.11.2 Evolutive harmonic analysis

Evolutive harmonic analysis (EHA) using the Thomson Multitaper method to determine the power spectra was performed in Astrochron (Meyers, 2014). The specific settings for each data set are described below, but resulting spectra was seen to be relatively insensitive to window width and step size. In all data sets analysed, power was normalized so that maximum power in each window is in unity.

3.2.11.2.1 Greyscale data

Prior to analysis, outliers were removed from the greyscale series using the 'Trim' function in Astrochron (Meyers, 2014). This function uses a boxplot algorithm with a coefficient of 1.5 to identify values greater than or less than 1.5 times the interquartile range from quartile 3 and quartile 1, respectively. After outlier removal, the data was interpolated to 0.1 year (from an average spacing of 0.041 year) using a piecewise linear interpolation. For the Evolutive Harmonic Analysis on the CT greyscale data, an MTM time-bandwidth product of 4, window width 100 years, and step size of 20 years was used.

3.2.11.2.2 XRF data

For the Si/Al, Si/Ti, and Ba/Ti ratios, outliers were removed using the same 'Trim' function described above. The XRF data were then interpolated to 0.4 years (from an average timestep of 0.44 years). Due to lower resolution XRF data, an MTM time-bandwidth product of 3, window width of 70 years, and step size of 10 years was used.

3.2.11.2.3 Laminae thickness

Laminae thickness data were linearly interpolated to a 2-year time step, approximating the average frequency of laminae occurrence (Chapter 4) and transformed to a log scale. A step size of 30 years, window width of 150 years and time-bandwith product of 3 was used for the laminae thickness data.

3.3 RICE ice core data and methods

3.3.1 Introduction

The chemical composition of ice cores provides a plethora of climatic information. Atmospheric concentrations of aerosols (i.e. organic compounds, salts, and particulates) precipitate either via dry deposition or through snow formation and are well preserved in the ice chemistry (Legrand and Mayewski, 1997). The chemical analysis of ice cores provides insight as to the source of these aerosols, the transport strength, the source strength, and mechanism by which contaminants were deposited (Legrand and Mayewski, 1997).

Here, I present the major ion record which includes high precision measurements of the cations sodium (Na^+), potassium (K^+), magnesium (Mg^{2+}), calcium (Ca^{2+}), and the anions

methanesulfonic acid (MSA^-), sulphate (SO_4^{2-}), nitrate (NO_3^-), and chloride (Cl^-).

Determining the sea-salt (ss) and non-sea-salt (nss or excess) aerosol components in ice core records is important for differentiating contributions of marine sea salt sources from terrigenous, biogenic, and anthropogenic contaminants in the ice core record. Calculating these components requires the assumption of a constant sea water composition (R_m or marine ratio) of the reference or conservative species (Keene et al., 1986). Usually, Na^+ or Cl^- are used as the conservative species (Legrand and Mayewski, 1997), which assumes that 100% of the species is derived from sea salt sources. At coastal sites, a high percentage of the aerosols are marine sourced. However, fractionation of the original marine ratio can occur over sea ice, during transport, or through post-depositional processes in the ice (Wolff et al., 2006; Rankin et al., 2000). The most prominent sea salt ratio is the Na^+/Cl^- ratio and either ion can be used to calculate sea salt/non-sea salt contributions in other ions (Legrand and Mayewski, 1997). While Cl^- can fractionate during transport or from postdepositional processes, Na^+ can be affected by frost flower formation on sea ice or local dust sources (Legrand and Mayewski, 1997). Through multiproxy analysis and a growing network of high resolution ice core records and atmospheric measurements, Antarctic ice core studies successfully use sea salt components as sea ice proxies (e.g. $ssNa^+$) and non-sea-salt components to infer dust concentrations which can be indicative of wind strength and direction (e.g. $nssCa^{2+}$, $nssMg^{2+}$) (e.g Mezgec et al., 2017; Pasteris et al., 2014; Wolff et al., 2006; Baggenstos et al., 2018; Schüpbach et al., 2013). As there are no proximal dust sources at Roosevelt Island, Na^+ is used as the conservative species to calculate the non-sea-salt and sea-salt components of the major ions in the RICE record and discuss the potential sensitivity of the record to sea ice variability.

A total of 3,160 samples were measured using ion chromatography (IC) from late 2016-2018, spanning the years ~7,285 to 10,625 cal yr BP (referenced as 'Early Holocene' in this chapter) to determine the concentrations of major ions in the RICE ice core. The non-sea-salt and sea-salt components are determined for SO_4^{2-}, Ca^{2+}, Mg^{2+}, to better understand the drivers of non-sea-salt and sea-salt variability at RICE.

In addition, continuous flow analysis (CFA) data of the water stable isotope deuterium (δD, Nancy Bertler, Victoria University of Wellington) and calcium (Ca^{2+}, Paul Vallelonga, University of Copenhagen) records for the Holocene are also presented. The interpretations of these data sets are brought into Chapter 6 to integrate the RICE record with the U1357B record and to compare with other Antarctic Holocene records.

3.3.2 RICE ice core

The RICE ice core was drilled over the 2011/12 and 2012/13 Antarctic field seasons as a part of a 9-nation collaborative project called the Roosevelt Island Climate Evolution Project (RICE). Roosevelt Island, an independent ice rise, is located on the north-eastern edge of the Ross Ice Shelf, with shelf ice flowing around the rise. The ice core was drilled to bedrock at 764m, some 250 m below sea level (Bertler et al., 2018). Core processing was conducted in 2013 and 2014 (Pyne et al., 2018). The average snow accumulation rate over the past 2,700 years is 25 cm water equivalent per year (Winstrup et al., 2019), providing a high resolution record. Annual layers of greater than 1 cm extend throughout the Holocene. For the past 2,700 years annual layer counts using geochemical data, black carbon, dust, 8 volcanic ash layers, and ice flow modelling supported a seasonally resolved record with exceptional age control (Winstrup et al., 2019). High resolution measurements of methane concentrations and tephra layers were matched to the well dated WAIS Divide (WAIS Divide Project Members) (Buizert et al., 2015; Sigl et al., 2016) and the NGRIP (NGRIP Community Members et al., 2004; Baumgartner et al., 2014) ice cores to develop the age model for the past 86,000 years (Lee et al., 2018).

3.3.3 Ice core processing

The RICE ice core was processed at the New Zealand Ice Core Research Facility at the National Isotope Centre of GNS Science in Lower Hutt, NZ. A schematic of the core cutting plan and national partners is shown in Figure 3.6. The inner section 'A' was transferred to the class 100 clean laboratory for continuous flow analysis (CFA).

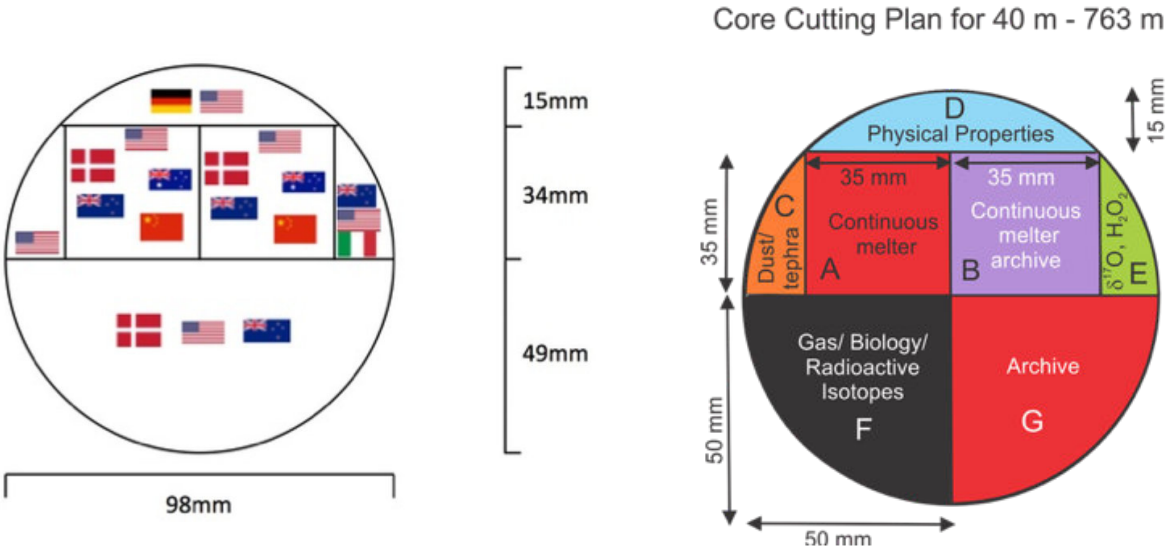

Figure 3.6: Core cutting plan.

Stable water isotopes (Emanuelsson et al., 2015), calcium (Kjær et al., 2016), black carbon, pH, conductivity, and atmospheric gases were measured using the continuous flow analysis system (Lee et al., in review). Over 20,000 samples of water for major ion analyses were collected and stored in the freezer at ∼35°C until samples could be analyzed.

3.3.4 Ion chromatography analysis

3.3.4.1 Machine set up

Major ion analyses were conducted on a Dionex Ion Chromatograph (ICS)-5000 Dual Pump using a dionex AS-HV auto-sampler. The cation side was configured with a Thermo Scientific Dionex IonPac™ CS12A 2*250 mm analytical column with a IonPac™ CG12A 2*50 mm guard column using 20 mM methanesulfonic acid (MSA^-) eluent. Cations measured were calcium (Ca^{2+}), sodium (Na^+), ammonium (NH_4^+), potassium (K^+), lithium (Li^+), and magnesium (Mg^{2+}). The anion side was configured with an IonPac™ AS18 2*250mm analytical column and an IonPac™ AG18 2*50 mm Guard column with a gradient elution of 20-40 mM of potassium Hydroxide (KOH). Anions measured were fluoride (F^-), methanesulfonic acid (MSA^-, $CH_3O_3S^-$), chloride (Cl^-), nitrite (NO_2^-), sulfate (SO_4^{2-}), nitrate(NO_3^-), bromide (Br^-), and phosphate (PO_4^{3-}). Instrument cleaning runs were conducted weekly. This involved running high eluent concentrations through the machine to clean off the columns and rinsing and refilling water reservoirs. Ultra-pure 18.2 MΩMilliQ water (henceforth referred to simply as 'MilliQ water') and blanks were then run through the system until background concentrations

returned to the machine baseline. Cleaning runs ensured that any accumulating drill fluid was removed from the columns before a new set of samples were run.

3.3.4.2 Calibration levels, quality controls, and standards preparations

Calibration levels, and cation and anion quality control (QC) samples were prepared through a series of dilutions using clean room practices. First, high concentration calibration levels referred to as "magnitude 1000" were created for anions and cations by pipetting a specific amount of purchased external single standard ion solutions into a single flask. The amount and concentration of each pipette is shown Table 3.1.

Cations			**Anions**		
	ppb	*microliter*		*ppb*	*microliter*
Lithium	100	12.5	Fluoride	100	12.5
Ammonium	100	12.5	Nitrite	100	12.5
Potassium	200	25	Bromide	100	12.5
Calcium	300	37.5	Phosphate	100	12.5
Magnesium	450	56.25	MSA	1000	62.5
Sodium	4000	500	Nitrate	600	75
			Sulphate	2500	312.5
			Chloride	6000	750

Table 3.1: Cation and anion concentrations and amounts in base calibration level.

The following steps were followed to make "magnitude 1000" (high concentration) solution for both cations and anions:

1. An acid cleaned 'rinse' container was rinsed three times with Milli-Q water, then filled with Milli-Q water.

2. A squeeze bottle with a needle point spray was rinsed three times with Milli-Q water, then filled with Milli-Q water.

3. New pipette tips were rinsed on the outside using the needle point spray bottle with Milli-Q water over a waste container to prevent backsplash from a sink.

4. Pipette tips were rinsed from inside using the Milli-Q water in the rinse container. The pipette was set to the uptake volume of the standard and rinsed five times from the inside with Milli-Q water. Care was taken to ensure that no water droplets remained inside the pipette tip.

5. An acid cleaned polypropylene flask was weighed five times.

6. The appropriate amount of single standard ion solution was then pipetted into the flask. Single standard ion solutions were added in order of ascending volume. A new pipette tip was used for each ion and rinsed in the same manner as described above.

7. The flask was weighed five times after each addition of an ion.

8. All weights were recorded into an excel spreadsheet which then calculated the concentrations of the final solution by average weight.

Calibration levels and QCs were created by diluting the above solutions with MilliQ water. The same clean room practices used above were used for the dilutions. Four calibration levels for both the anions and cations were selected to be used as QCs. These four levels covered the spread of concentrations seen in measurements. One anion and one cation QC were run every 10 samples, and then a full set of QCs (four anions and four cations) and unaltered certified international standards (e.g. AES) were run every 100 samples.

QCs were made in 40 mL batches and stored in a refrigerator. These would be used up in about 2.5 weeks, at which point they were remade. QCs with smaller concentrations (1-5 ppb range) degraded the fastest. These solutions were remade every 1.5 weeks or sooner if repeated measurements on the ICS showed degradation (measurements of increasingly smaller concentrations). Every version of QC was assigned a number, and made following the same protocol as above with all weights recorded. This provided a second a check to make sure the QC was not contaminated, and also allowed us to identify degradation in the QCs or a problem with the machine.

3.3.4.3 Machine calibration and regression settings

The ICS was calibrated prior to starting any new sample runs and after any machine shutdowns to ensure continued high data quality. Degradation of the machine columns and eluent, as well as changing flow speed can affect ion measurements in the ICS. Machine calibrations help prevent these issues from affecting measurements in samples, as well as helping to identify sample contamination.

Initially, a 34-point calibration was used for Early Holocene samples with 34 anion levels and 34 cation levels. This was adopted from Brightley (2017) where seasonally-resolved RICE data had large ranges of ionic concentrations (ppb to ppm) and required more calibration levels for accurate measurements.

Data from the ICS were processed using Chromeleon by ThermoFisher Scientific. When measuring calibration levels or samples, the ICS output is a chromatogram, a graph showing distinct peaks created by each ion concentration. To quantify chromatograph outputs, the area under the peak is calculated and transgressed into a concentration using samples (standards) of known concentration.

Typically, the ionic concentration and peak area have a linear relationship. However, this linearity breaks down at ultra low concentrations (Brinkmann et al., 2002). The linearity or non-linearity of these relationships are tested during the calibration when comparing the ICS measurements versus the weight-determined calibration levels. Peak integration methods and regression types for each ion were determined during the first 34-point calibration. Initially all ions are assumed to have a linear relationship with the peak area, but the polynomial degree is increased in a step-wise fashion until the R^2 between the peak area and expected concentration is greater than 0.999. Cubic regressions were chosen for K^+, Mg^{2+}, and Ca^{2+}. Quadratic linear regression settings were used for MSA^- and NO_3^-. Linear regression settings were used for ions with concentrations ranges greater than 50 ppb, such as Na^+, Cl^- and SO_4^{2-}.

After the first run of ∼1830 samples, the calibration was refined to eliminate calibration points that measured values outside of the data range of our annually resolved Early Holocene samples. This reduced the number of calibration levels to 20. The preparation of calibration levels, their measurement, and regression settings remained the same.

3.3.4.4 Analytical precision and uncertainty estimation

To estimate the analytical precision and uncertainty associated with each ion, the QC measurements are used. During the measurement campaign QC measurements were consistently monitored to ensure there were no issues with the machine.

Standard deviations and measurement uncertainty of the cations and anions in the QCs are low, suggesting precise measurements. A subset of QCs standard deviations and measurement uncertainties are provided as an example in Table 3.2. If measurement error is less than one ppb, but more than zero, the error is recorded as one ppb. Only ions that are interpreted in this thesis are presented.

Average measurement uncertainty is very small, on the order of 1-2 ppb. The largest error occurs for the M18 Na^+, but this is only a $\leq$1% error in measurement.

		Cations (ppb)			Anions (ppb)		
QC	*No. Meas.*	Na^+	Mg^{2+}	Ca^{2+}	Cl^-	SO_4^{2-}	MSA^-
M5	25	0.65(≤**1**)	0.26(≤**1**)	0.45(≤**1**)	0.54(≤**1**)	0.60(≤**1**)	0.19(≤**1**)
M9	24	1.1(≤**1**)	0.25(≤**1**)	0.38(≤**1**)	0.44(**2**)	0.67(**2**)	0.22(≤**1**)
M13	22	1.89(**2**)	0.59(≤**1**)	0.57(≤**1**)	0.56(**2**)	0.80(**2**)	0.29(≤**1**)
M18	21	4.21(**4**)	0.92(≤**1**)	0.82(**2**)	1.36(**2**)	1.23(**2**)	0.46(≤**1**)

Table 3.2: Standard deviation and measurement uncertainty of a subset of QCs. Standard deviation in plain font, while measurement uncertainty is in parentheses in **boldface**. These QCs were run while measuring samples 23350-22901. M5-M18 refer to the QC level with ion concentrations increasing from M5 to M18.

3.3.5 Data processing

3.3.5.1 Manual peak integration

Automatic processing parameters and peak detection settings in Chromeleon performs well at capturing and integrating ionic peaks to determine ionic concentration in samples. However, some ions such as MSA^-, Mg^{2+}, and Ca^{2+} are more difficult to detect with automatic detection settings. Ions such as SO_4^{2-} can be affected by drill fluid contamination. Therefore, after samples were run every ion peak in each chromatogram was manually checked to ensure that the peak area was integrated properly and the ionic concentration was calculated correctly.

For samples with poorly integrated peaks, a manual integration was applied whereby the peak detection settings were changed for that particular ion in order to capture the actual peak instead of any artifacts. Errors in SO_4^{2-} peak integration were primarily noticed in the older Holocene samples. Therefore, after the first 1800 samples were run, several tests were performed to determine the effects of drill fluid contamination on the peaks of the IC chromatograms. Drill fluid used during the RICE campaign consisted of a mixture of ESTISOL and COASOL (Bertler et al., 2018). Peaks associated with the drill fluid interfere with the peak integration of select ions, such as sulphate. Various microliter amounts of drill fluid were pipetted into six mL vials of Milli-Q water and QCs, and subsequently run on the ICS. Results showed that drill fluid produces a small peak just prior to the sulphate peak. The processing method was adjusted so that the drill fluid peak was not included in the sulphate peak integration going forward (Figure 3.7).

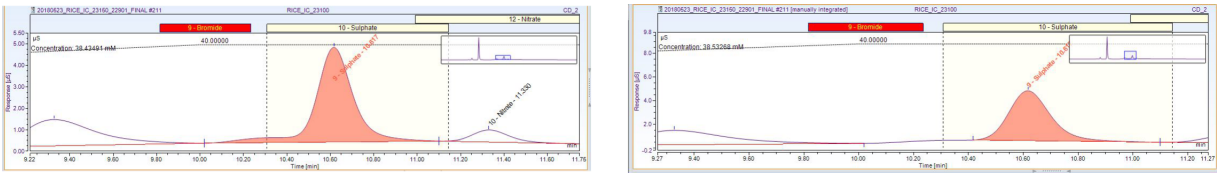

Figure 3.7: **Example of drill fluid contamination affecting SO_4^{2-} and subsequent manual peak integration**. (Left) before manual integration (Right) after manual integration. The small peak prior to the main sulphate peak is due to drill fluid contamination.

Overall, less than 3% samples had to be manually integrated, and have minimal impact on the overall results.

3.3.5.2 Outlier removal

Frequent quality control checks, a robust 20-point calibration and manual checks of every peak integration afford strong confidence in the data quality. Therefore, removal of outliers in the data set were fairly minimal and done manually, rather than using a blanket outlier removal algorithm.

For calcium, five measurements stood out as being erroneous, as the ppb measurements were above 300 ppb, nearly six times the next lowest maximum calcium value. These five measurements were removed and filled using a pchip interpolation.

3.3.6 Non-sea-salt versus sea-salt ion contributions

Several of the ions measured in this campaign can have both marine and terrestrial sources (Legrand and Mayewski, 1997). To quantify the marine and terrestrial contribution and correctly interpret ion data, it is necessary to separate these ions into non-sea-salt (nss) and sea-salt (ss) components. This is accomplished using a series of equations using a conservative ion (assumed to be of 100% sea salt origin) and the known marine and terrestrial aerosol ratios of an ion on interest to the conservative ion. Typically, sea-salt sodium ($ssNa^+$) is used as the conservative ion as it is a main component of the dominant sea salt (NaCl) aerosol in Antarctica. Chloride (Cl^-) is also used frequently but has been shown to be more volatile during air mass transport and affected by post-depositional processes (e.g Röthlisberger et al., 2002; Severi et al., 2017; Pasteris et al., 2014; Vega et al., 2018).

The following series of equations are used to calculate the nss and ss components of Na^+

and Ca^{2+}:

$$\begin{aligned} ssNa^{+} &= Na_{total} - \frac{nssCa^{2+}}{R_{terrestrial}} \\ nssCa^{2+} &= Ca^{2+} - R_{marine} \times ssNa^{+} \end{aligned} \tag{3.5}$$

where $R_{terrestrial}$ and R_{marine} are the mean mass ratios of Ca^{2+} to Na^{+} in the Earth's crust and bulk seawater, and equal to 1.78 and 0.038, respectively (Bowen, 1979).

Then the remaining equations can be applied to identify the non-sea-salt and sea-salt components of other ions.

$$\begin{aligned} nssX &= X_{total} - (R_{marine} \times ssNa^{+}) \\ ssX &= R_{marine} \times ssNa^{+} \end{aligned} \tag{3.6}$$

where,

$$R_{marine} = \frac{X_{marine}}{Na^{+}_{marine}}$$

which is the mean ratio of the ion X to Na^{+} in bulk sea water. In this thesis, we use the mean mass ratios as our ICS results are given in parts per billion (ppb).

As such, the following R_{marine} ratios shown in Table 3.3 are used.

	$\mathbf{R_{marine}}$ **to** $\mathbf{Na^{+}}$
$\mathbf{Mg^{2+}}$	0.12
$\mathbf{SO_4^{2-}}$	0.252
$\mathbf{Cl^{-}}$	1.79

Table 3.3: Bulk sea water ratios of various ions to Na^{+}

While several studies separate Na^{+} into non-sea-salt and sea-salt components (e.g Röthlisberger et al., 2002; Severi et al., 2017; Vega et al., 2018), dust leachable Na^{+} is extremely low in Antarctic coastal marine cores in the Holocene (Röthlisberger et al., 2002).

3.3.7 Other data sets

3.3.7.1 Continuous flow analysis calcium

In this thesis, calcium data are presented from CFA analysis provided by the University of Copenhagen (Paul Vallelonga, Helle Kjaer, and Mai Winstrup) and ICS analysis. The CFA cal-

cium data were measured in Wellington, New Zealand using a system modelled after the CFA system employed in Copenhagen (Kjær et al., 2016).

3.3.7.2 Deuterium

The deuterium (δD) data presented here are derived using a continuous-flow laser spectroscopy system with a Los Gatos off-axis integrated cavity output spectroscopy analyser (Emanuelsson et al., 2015) (Figure 3.8). The water samples were taken from the inner portion of the continuous flow analysis (CFA) melt head (Keller et al., 2018). Uncertainty of the δD data is $\pm 0.85‰$.

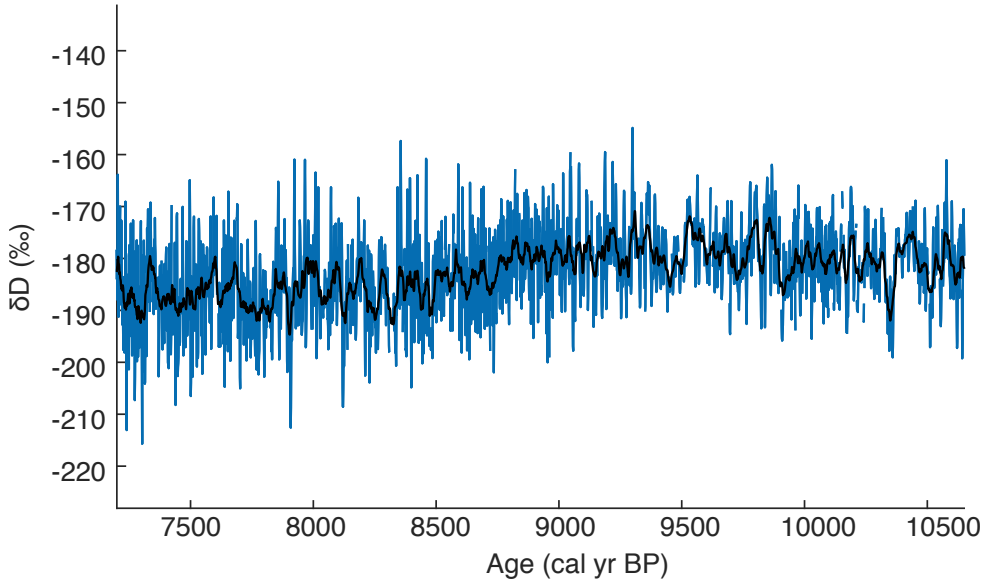

Figure 3.8: Early Holocene δD binned into 1-year intervals, with the mean of each bin plotted. Black line indicates a 25-point moving mean.

3.3.8 Age model

The RICE17 age model used in this thesis consists of two portions and is reported in calendar years before 1950 C.E. (yr BP). The last 2,649 yr BP (343.7 m depth) are determined using annual layer counts and are in good agreement with the WAIS Divide ice core (Winstrup et al., 2019).

The lower portion (ages older than 2,649 yr BP) was calculated using ice-age/gas-age modelling and gas synchronization with the WAIS Divide core (Lee et al., 2018). A firn densification

model was used to calculate the ice age-gas age offset which was then added to the gas age scale to determine the ice age (Lee et al., 2018). The lowest portion (746-752.95 m, 64.6-83 ka) contains ages older than those at WAIS Divide and was therefore visually compared to the NGRIP core (Lee et al., 2018).

For the last 12,000 years, the maximum ice age error was ∼183 years, the median was ∼81 years, the mean was ∼85 years, and the minimum was 50 years (Lee et al., 2018).

3.3.9 Determining the source of calcium variability in the Holocene

The continuous CFA calcium data provide an opportunity to interrogate the relationship between the RICE and IODP core to develop the Adélie Land-Ross Sea Holocene reconstruction in Chapter 6. To determine the source and drivers of calcium variability, whose interpretations are used in Chapter 6, the CFA calcium record was compared with the Early Holocene ICS data. The methodology for the calcium interpretation is presented here.

3.3.9.1 Major ions in the Early Holocene

Results of the Major anions (MSA^-, SO_4^{2-}, Cl^-) and cations (Na^+, Ca^{2+}, and Mg^{2+}) measured for the Early Holocene reveal that several ions follow similar trends (Figure 3.9).

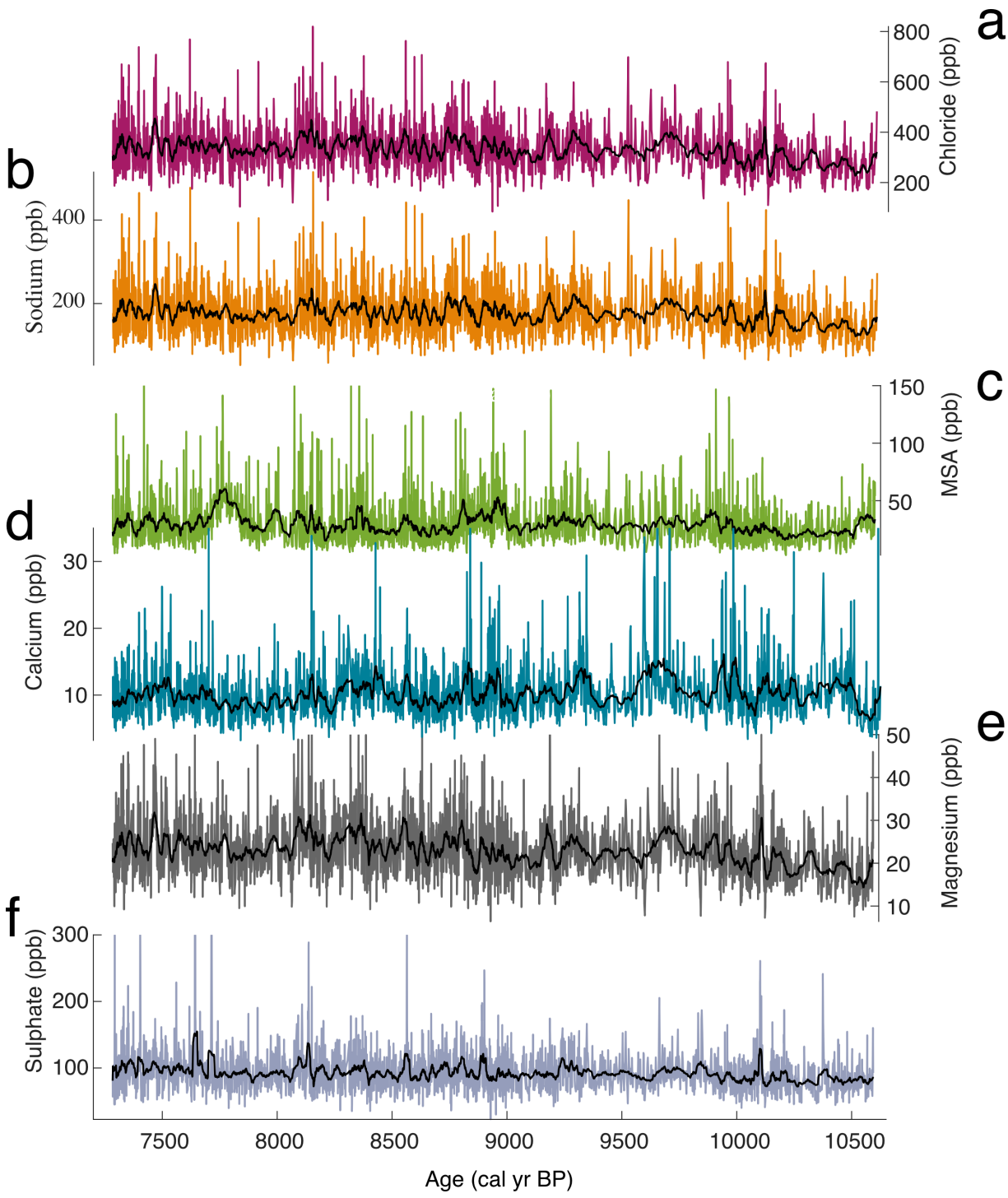

Figure 3.9: **Major Ions measured from ICS** (a) chloride , (b) sodium, (c) MSA, (d) calcium, (e) magnesium, (f) sulphate. Black lines are a 25-point moving mean of the data. All measurements are in ppb.

3.3.9.2 ICS calcium versus CFA calcium

The ICS data currently only exist for the Early Holocene (~7,285 to 10,625 cal yr BP). The CFA measurements extend through the Holocene, but have a few gaps in the data set. Over the period covered by the ICS data set, the largest break in the CFA data set is ~80 years. The mean resolution of the ICS data set during this period is 1.05 years, where as the CFA data is 0.8 years.

A comparison of the two records over a 200-year period interpolated to a common age scale (ICS age) is shown in figure 3.10

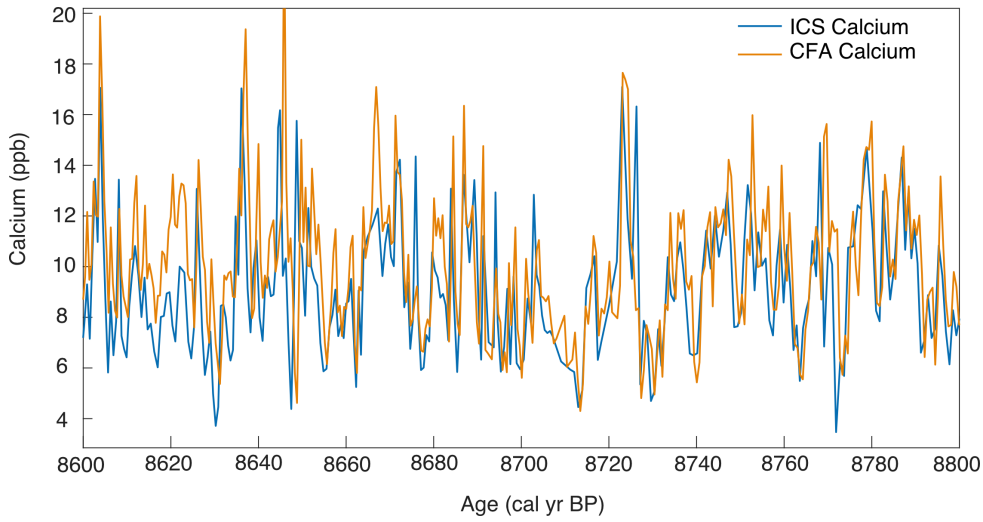

Figure 3.10: **CFA versus ICS Calcium data.** CFA calcium is shown in orange, while ICS calcium data is shown in blue.

CFA calcium data are closely correlated with the ICS measurements, with a Pearson correlation coefficient of 0.62. Gaps in the CFA data set and the differing resolution of the two data sets likely has some impact on the correlation coefficient.

3.3.9.3 Sea-salt versus non-sea-salt contributions of ions

The CFA calcium data do not have the equivalent sodium measurement needed for the nss/ss calculations. Given the high correlation between the ICS and CFA calcium, the ICS measurements are used to calculate the nss/ss calcium components in the Early Holocene (Figure 3.11). These findings are used to infer the relative nss/ss calcium components in the CFA data.

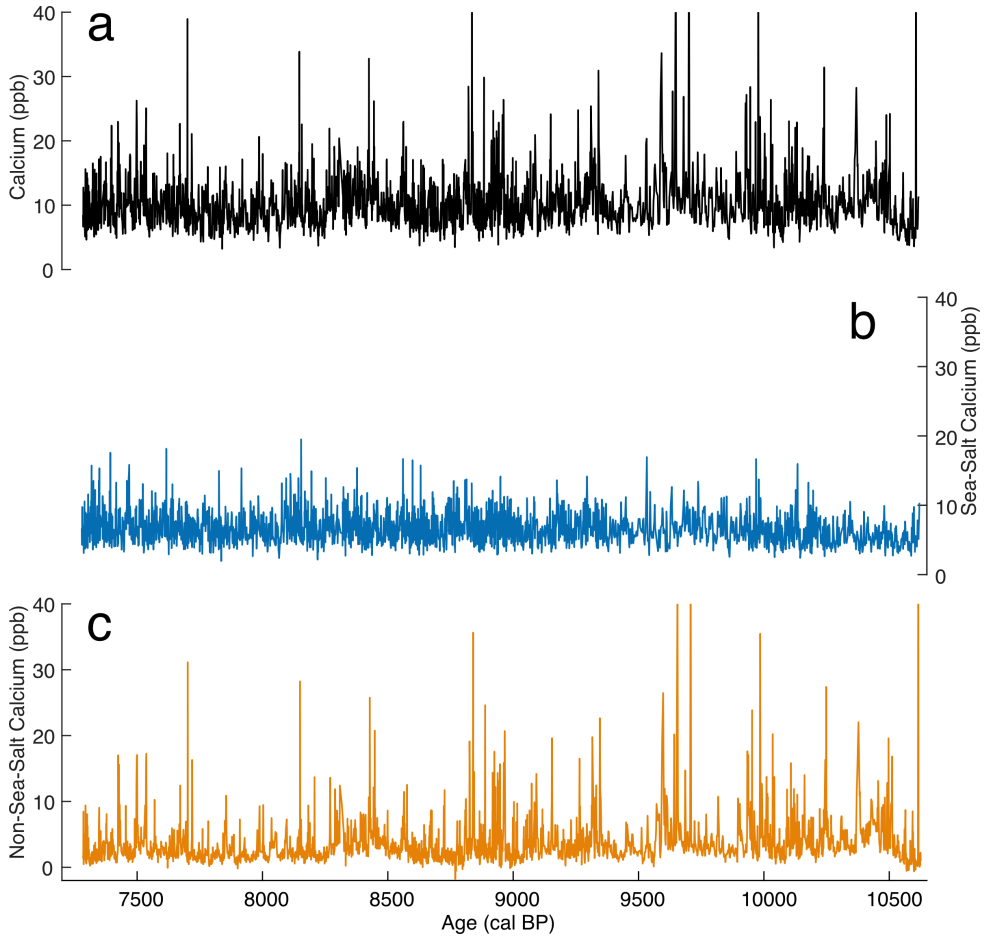

Figure 3.11: **RICE Early Holocene Calcium** (a) Total calcium (b) Sea-salt calcium (c) Non-sea-salt calcium for the RICE ICS Early Holocene record

Noticeable differences in the distribution of $nssCa^{2+}$ and $ssCa^{2+}$ concentrations exist (3.12). While there are some large spikes in $nssCa^{2+}$ content, the majority of $nssCa^{2+}$ is less than 4 pbb, with a mean value of 3.5 ppb. While some of these $nssCa^{2+}$ values are low and could be related to analytical uncertainty (see section 3.3.4.4), this does not explain some of the extremely high concentrations. Sea-salt calcium concentrations are consistently less than 10 ppb. The mean values for $ssCa^{2+}$ is 6.6 ppb. On average, $nssCa^{2+}$ accounts for ~30% of the Early Holocene RICE calcium record.

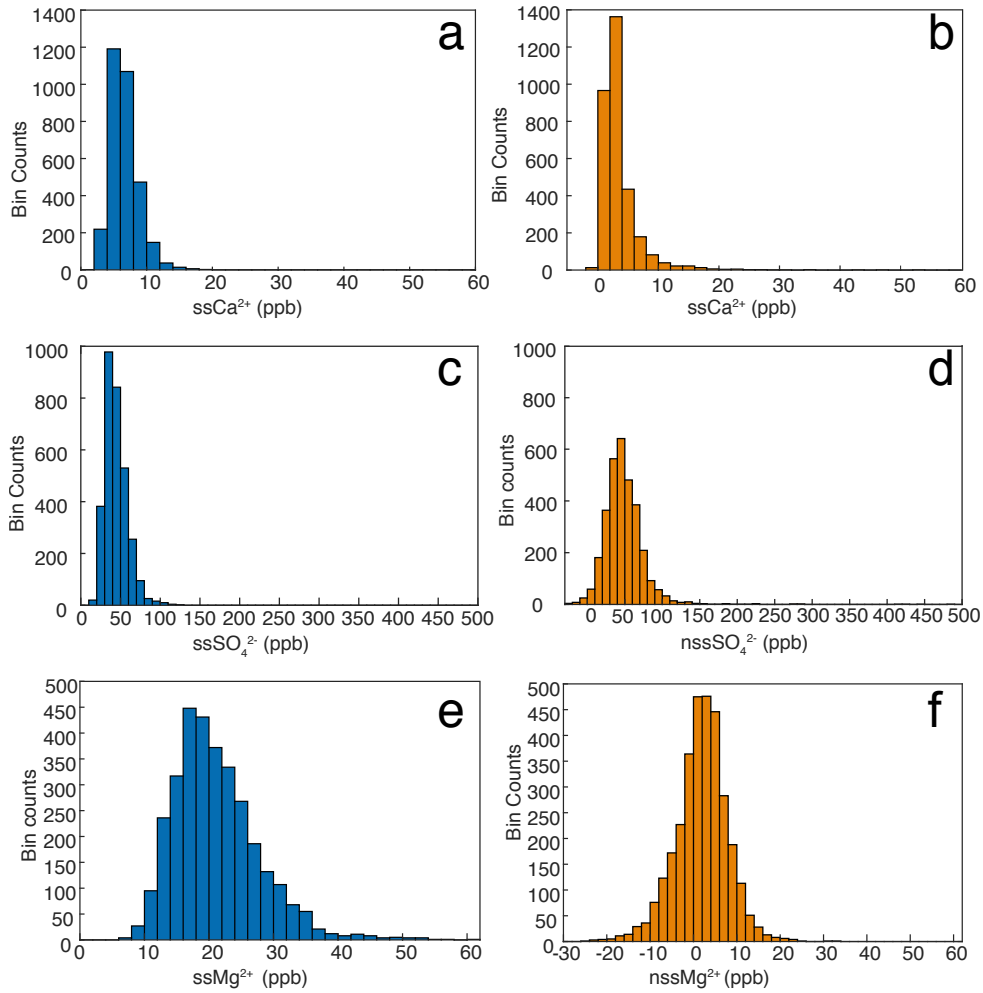

Figure 3.12: **Histogram for Non-sea-salt and sea-salt ions.** (a) Sea-salt Ca^{2+} (b) Non-sea-salt Ca^{2+}. Values are binned in steps of 2 for Ca^{2+} (c) Sea-salt SO_4^{2-} (d) Non-sea-salt SO_4^{2-}. Values are binned in steps of 10 for SO_4^{2-} . (e) Sea-salt Mg^{2+} (f) Non-sea-salt Mg^{2+}. Values are binned in steps of 2 for Mg^{2+}.

The non-sea-salt and sea salt contributions are also calculated for Mg^{2+} and SO_4^{2-} to compare with the calcium record (Figure 3.12 c-f). Around 50% of SO_4^{2-} comes from sea-salt contributions, and the non-sea-salt component remains positive. The normal distribution of the $nssSO_4^{2-}$ appears similar to $nssMg^{2+}$, but the $nssMg^{2+}$ has frequent negative contributions. If the non-sea-salt equation (section 3.3.6) is rearranged, we find that negative non-sea-salt contributions represent a depletion in Mg^{2+} to Na^{+} relative to the standard marine ratio (Table 3.3). To better illustrate the Mg^{2+} depletion, the Mg^{2+}/Na^{+} ratio is plotted against the marine ratio. Values below the marine ratio indicate aerosols depleted in Mg^{2+} and negative non-sea-salt contributions (Figure 3.13). Approximately one-third of samples are depleted in

Mg^{2+}.

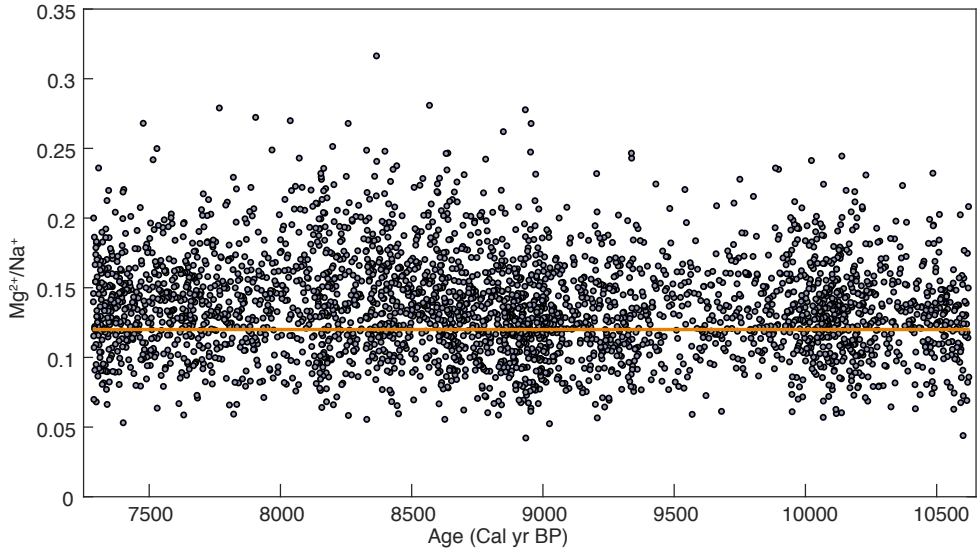

Figure 3.13: Mg^{2+}/Na^{+} ratio for the Early Holocene. All samples relative to the standard marine ratio of 0.12 (orange line). Samples below the orange line are depleted in Mg^{2+}

3.3.9.4 Evaluating sea-salt and non-sea-salt proxies in the RICE Early Holocene record

All of the major ions appear to follow similar trends in the Early Holocene (Figure 3.9), but likely have varying sea-salt and non-sea-salt components.

Sea salt aerosols are typically formed through bubble bursting and sea spray (de Leeuw et al., 2011) with deposition of these aerosols rapidly decreasing as an air mass moves inland (Guelle et al., 2001). Consequently, sea salt aerosols can be used to infer distance from open water (which increases with increased sea ice extent) and the transport strength over that distance (Abram et al., 2013). While bubble bursting and sea spray are major contributors to the sea salt concentrations, contributions from frost flowers on new ice (Rankin et al., 2000; Wolff et al., 2003) and blowing snow over sea ice (Yang et al., 2008; Levine et al., 2014) also exist. These sources are increasingly thought to be important drivers of sea-salt variability, as coastal locations around Antarctica show peaking sea-salt contributions during the winter (Wagenbach et al., 1998; Abram et al., 2013). Seasonal Na^{+} records at RICE also showed this pattern, with values peaking during winter (Eling, 2019).

Depleted values of SO_4^{2-} relative to Na^{+} (also seen as negative non-sea-salt concentrations) are typically indicative of frost flowers and blowing snow contributions over sea ice (Rankin et al., 2000; Levine et al., 2014). The $nssSO_4^{2-}$ record for the Early Holocene does not show these depleted values. However, Eling (2019) analysed seasonal records and found that sul-

phate depletion primarily occurred during austral winter and suggested that at least 30-40 % of the sea salt aerosols at RICE came from frost flowers or blowing snow on sea ice. The lack of sulphate depletion in the annually-resolved Early Holocene portion suggests open ocean contributions during the austral summer can overprint the winter sea ice signal on an annual basis (Eling, 2019). However, it is noted that at sites with high biogenic SO_4^{2-} contributions, as would be expected at RICE due to the proximity of the Ross Sea Polynya, the SO_4^{2-} to Na^+ ratio is difficult to interpret (Hara et al., 2012).

The non-sea-salt and sea-salt contributions of magnesium are curious given their frequent negative non-sea-salt values. Typically, non-sea-salt components are attributed to terrestrial sources, but negative values can indicate other processes are involved. As stated above, negative values of $nssSO_4^{2-}$ have been attributed to precipitation of sea salts and formation of frost flowers over sea ice surfaces (Rankin et al., 2000; Wagenbach et al., 1998; Levine et al., 2014). Magnesium based salts have also been observed in frost flowers, but do not precipitate onto the ice surface until temperatures are much colder at -34°C (Rankin et al., 2000; Hara et al., 2017). While the average annual temperature near RICE (section 2.6.3) does not reach this temperature, the nearby Margaret AWS has recorded temperatures far below -34°C in the winter (Bertler et al., 2018). However, measurements of frost flowers in Greenland showed Mg^{2+} enrichment relative to Na^+, but there was significant magnesium depletion in older snow on sea ice (Hara et al., 2017). The presence of these samples depleted in magnesium may indicate a blowing snow source for these ions rather than frost flowers, but do not explain why the sulphate signal is overprinted by summer precipitation and magnesium is not. Furthermore, these complexities prohibit the usage $nssMg^{2+}$ as a dust proxy. Future work is needed to explain the frequent depletion of magnesium in the ion record.

The CFA calcium data has been interpreted to largely reflect marine sourced calcium, as it is closely correlated with conductivity measurements indicating the calcium is from soluble sea salts (Kjær et al., 2016). However, the non-sea-salt/sea-salt ion contribution calculation on the ICS data where sodium data is available suggests ∼30% of calcium is non-sea-salt sourced. This percentage holds true for samples measured in the last 2000 years, indicating that the ∼30% nss percentage is perhaps consistent throughout the entire Holocene and may not be a reflection of deglacial environment of the Early Holocene.

The non-sea-salt component appears to have relatively low contributions on the background of periodic, low frequency peaks. Even if some of those large peaks are eliminated as outliers, or the very low concentrations are assumed to be erroneous, the pattern and distribution of the $nssCa^{2+}$ peaks remains similar. The Evolutive Harmonic Analysis of the $nssCa^{2+}$, $ssCa^{2+}$, and Ca^{2+} indicate that the $ssCa^{2+}$ is more sensitive to sub-decadal drivers than the $nssCa^{2+}$

component (Figure 3.14). For the Evolutive Harmonic Analysis on the IC calcium data, the data was interpolated to 1 year, then, an MTM time-bandwidth product of 2, window width 100 years, and step size of 10 years was used (Meyers, 2014).

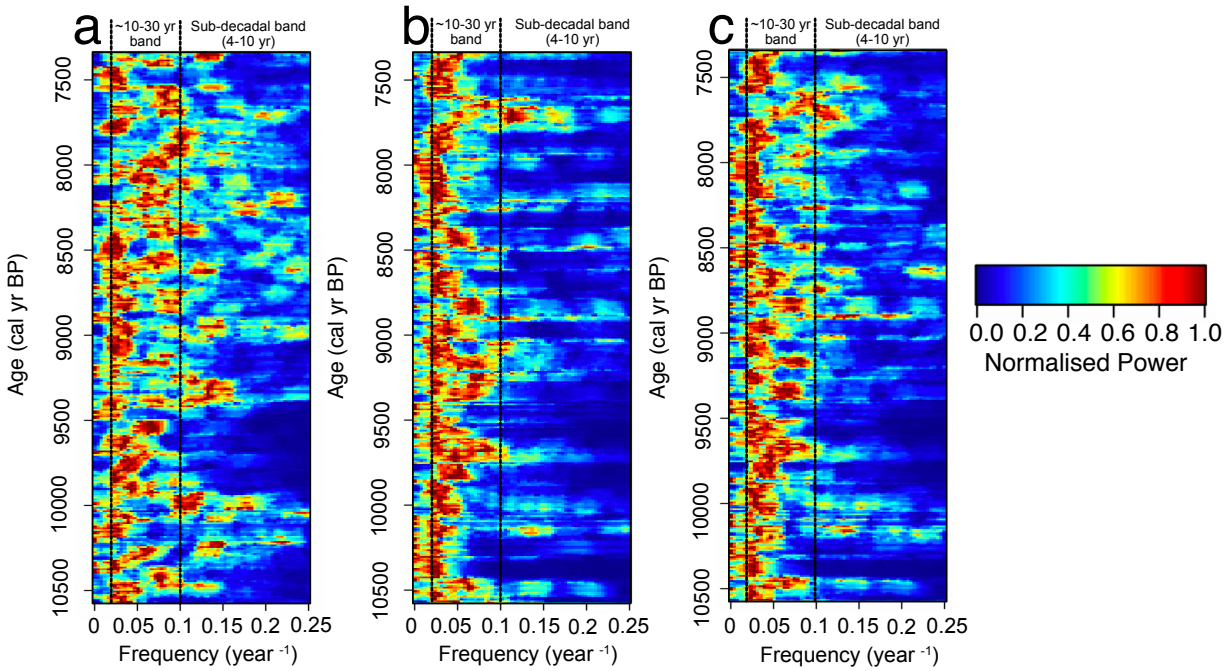

Figure 3.14: **Evolutive harmonic analysis RICE Early Holocene Ca^{2+}**. (a) $ssCa^{2+}$ (b) $nssCa^{2+}$ (c) Ca^{2+}. Power is normalized so that maximum power in each window (100 years) is in unity.

The $nssCa^{2+}$ record has a strong frequency band ∼30 years, with occasional increases towards 10 years. Dust contributions at RICE are likely sourced from New Zealand and Australia, and delivered via onshore flow at the site (Neff, 2014). Thus, the multidecadal frequency could be related to the IPO, which affects the strength of the ASL (Meehl et al., 2016) and position of high precipitation events affecting RICE (Emanuelsson et al., 2015). Shallow ice core studies in west central Antarctica have linked increased $nssCa^{2+}$ to the deepening of the ASL (Dixon et al., 2012). Dixon et al. (2012) also suggested that $nssCa^{2+}$ is primarily delivered to this area via storms with concentrations reflecting the strength of atmospheric circulation and not changing source emissions. Therefore, $nssCa^{2+}$ is interpreted to reflect changes in atmospheric circulation strength, with large excursions being related to IPO and ASL influences.

The $ssCa^{2+}$ is inherently highly correlated with the Na^{+} record. The Na^{+} record is difficult to interpret due to the seasonal signal indicating a sea ice source and the annual signal potentially reflecting an open ocean signal (Eling, 2019). Deposition at RICE is characterised by frequent, large austral winter precipitation events (Emanuelsson et al., 2015) when antarc-

tic sea ice extent is at its maximum. While this suggests that Na^+ and $ssCa^{2+}$ signal could be more sensitive to sea ice extent and winter precipitation, it may also reflect open ocean conditions (Eling, 2019). Regardless, Na^+ and $ssCa^{2+}$ reflect transport over the marine sector. The stronger decadal to sub-decal frequencies in $ssCa^{2+}$ at this time are a bit more difficult to interpret as changes in the Ross Ice Shelf likely overprinted any external influences on sea ice extent or open ocean conditions.

The combined Ca^{2+} EHA shows the distinct $nssCa^{2+}$ multidecadal band, but also shows dampened variability compared to the $ssCa^{2+}$. Given the lack of Na^+ data for the entire Holocene and the inability to discern sea-salt versus non-sea-salt contributions, the CFA Ca^{2+} must be interpreted as a combined signal. Other west Antarctic ice core records have used Na^+ to infer the atmospheric transport strength from marine sources as increased concentrations are associated with a deepening of the ASL (Kreutz et al., 2000; Raphael et al., 2016; Mayewski et al., 2017). Additionally, the $nssCa^{2+}$ signal is directly related to atmospheric transport. While the combined Ca^{2+} record is not a wholly marine signal, the CFA Ca^{2+} record is interpreted to represent transport strength to RICE rather than a distinct sea-ice signal.

3.4 Identifying synchronous and asynchronous change in the RICE and U1357B records

Tipping points in the climate system refer to periods of rapid change associated with a threshold being met after forcings (gradual or rapid) fundamentally change the system. These are increasingly being studied, particularly in the context of ice shelf retreat and ocean circulation changes (IPCC, 2019). In order to identify potential tipping points or periods of abrupt change in this thesis, changepoints are used. Changepoints identify the period at which there is an abrupt change in a statistical attribute in a signal or time series and are increasingly being used on climate data series (e.g. Trauth et al., 2009; Ruggieri et al., 2009; Yu and Ruggieri, 2019).

Here, changepoints are primarily identified by a shift in the mean value of the signal (e.g. isotopes, laminae counts, ions). The changepoint is identified by dividing the time series into sections, and calculating the mean and standard deviations of all points from that mean. The changepoint is identified when the total residual error on either side of the location reaches a minimum (Lavielle, 2005; Killick et al., 2012).

To identify phasing between records, linear changepoints (hereafter referred to as 'slope changepoints'), which identify shifts in the slope of the record are also considered, as changing

slopes are indicative of changing trends that lead to changes in the overall mean. As rates of change are different for each location, comparing the timing of slope changepoints versus mean changepoints can help infer the relative rate of change at each location.

Care must be taken when identifying changepoints as overestimating the number of changepoints in a series leads to over-fitting of the data. Identifying change points using mean shifts in series with long term trends can also introduce artificial changepoints (Gallagher et al., 2013). The maximum number of changepoints was initially varied for each series, and any changepoints identified were considered in conjunction with other proxy records to guide interpretations. Ultimately, a parameter of 2 maximum changepoints was considered most representative for identifying large regime shifts in the data. Changepoints were identified using both 100-year binned data and finer scale resampling (annual to decadal) to ensure changepoints identified were not due to interpolation.

While changepoint analysis provides distinct years for climatic shifts, one should be cautious in terms of interpreting the years as fixed (i.e. change happened exactly at that year) as these are reliant on the resolution of the data set and any age model errors. While changepoints are calculated using various resolutions, they are reported using the years provided by the 100-year binned analysis. This means years reported are to the nearest century relative to the changepoints identified in the more high resolution data sets.

3.5 Summary

This chapter presented the methodologies used to develop the U1357B sediment core record and RICE ice core record, as well as how asynchronous and synchronous change was identified between these records.

Through the use of X-ray Computed Tomography, a CT-scan greyscale profile and record of light laminae through manual selection was developed for U1357B. The age model, XRF, physical core properties, Highly Branched Isoprenoid (HBI) lipid biomarkers, linear sedimentation rates, mass accumulation rates, and grain size data were also introduced. Last, the statistical methods used on these datasets were also described.

For RICE, the major ion data from ~7,285 to 10,625 cal yr BP were measured using ion chromatography. The age model, deuterium data, and continuous flow analysis calcium data were also presented. Next the trends of all the ions and calculations of the non-sea-salt and sea-salt components of SO_4^{2-}, Ca^{2+}, and Mg^{2+} were used to identify the drivers behind ion variability. Particular focus was given to Ca^{2+}, which is inferred to represent transport strength

of marine air masses.

To compare these records in the Holocene, changepoint analysis provides a statistical measure of shifts in the mean or slope of the ice core and sediment core datasets.

Chapter 4

Environmental controls on laminae frequency and biological productivity in Adélie Land

4.1 Introduction

Laminated sediment cores are an important paleoclimate tool capable of capturing seasonal to inter-annual/decadal variability in marine and lacustrine sediments throughout the Holocene. Laminations are formed when chemical and biological variations alter sediment composition and there is a suitable environment for preservation, but determining the environmental drivers for laminae deposition can prove challenging (Kemp, 1996). Alternating light and dark laminations are often representative of biogenic and lithic sedimentation, respectively (Sancetta, 1996). Laminations in pelagic marine sediment can also provide a record of seasonal shifts in primary productivity in areas where wind stress enables coastal upwelling, creating large diatom mats that rapidly sink to the seafloor (Kemp, 1996; Sancetta, 1996). Around Antarctica's coastal margins, diatom analysis suggests light laminae are associated with these intense biogenic bloom events that rapidly sink and occur as sea-ice retreats in the spring, whereas dark laminae have increased terrigenous content and are associated with open water conditions when nutrient conditions are low (Leventer et al., 2002; Denis et al., 2006; Maddison et al., 2012). Since biological bloom events are usually associated with physical drivers, large scale climate oscillations have been shown to influence bloom events, and therefore are likely to influence laminae frequency in pelagic-dominated marine sediments (Bull and Kemp, 1996; Hagadorn, 1996). Consequently, analysing laminations in such sediments not only provides

a record of the biological productivity in a region, it can also be used to infer changes in the physical drivers and climate oscillations that influence bloom events.

Expanded sections of continuously laminated sediment records around Antarctica are rare, and only one other such published record on Antarctica's coastal margin has been published (core NBP0101 JPC41), but this record only extends back ∼2 ka BP (Alley et al., 2018). Uniquely, IODP site U1357 cored a continuously laminated record that extends almost through the entire Holocene (11.4-0 ka BP). Here, the results of X-ray Computed Tomography (CT), XRF data, grain size analysis, and physical properties are used to quantify the occurrence of these laminae and identify changes in sedimentary depositional processes throughout the Holocene. This site was cored in a drift deposit, that acts to focus locally-derived pelagic material and other suspended sediment advected by wind-driven currents towards the site from the east (Escutia et al., 2011).

Physical sedimentology of drift deposits can provide a powerful tool to assess relative changes in current strength through time. The application of the 'sortable silt' ($10-63\mu m$) measure, and similar variations in grain size, have long been used as a qualitative proxy for flow speed (e.g. Ledbetter, 1986a,b; McCave et al., 1995; McCave and Hall, 2006; Mao et al., 2018; Lamy et al., 2015). However, such proxies can be significantly influenced by changes in source of sediment supply through time, and should be interpreted in the context of the local sediment depositional setting. In glaciated regions, sediment supply could be influenced by the proximal position of glaciers, which in theory can lead to enhanced deposition of ice rafted debris and poorly sorted sediment from periodic discharge of meltwater plumes (McKay et al., 2009; Powell and Domack, 2002). This potentially makes assessing paleocurrent conditions problematic on Antarctica's continental shelf, as unsorted sorted glacial silt transported via ice rafting or meltwater plumes, and not by current, distorts the record (McCave and Andrews, 2019; Jonkers et al., 2015; Prins et al., 2002; McCave and Hall, 2006).

CT-scanning of the Adélie drift core reveals very little iceberg rafted debris (IRD) (Figure 4.10), with the only clear evidence of significant proximal glaciomarine input and IRD in the lowermost 0.7 m of the core, before rapidly transitioning to laminated sediment with minimal IRD (Figure 4.10). Grain size distributions along the adjacent bathymetric highs of the Mertz and Adélie banks (Figure 2.10) are poorly sorted diamicts consistent with subglacial or glaciomarine deposition, but are dominated by particles exceeding $>125\ \mu m$, and are indicative of partial winnowing of fine sands and mud (i.e. $<125\mu$m fraction) by bottom currents (Dunbar et al., 1985). In the bathymetric trough, several sediment drifts are present that act to capture and deposit this winnowed sediment from the banks. The morphology of one of these drifts in the Mertz Trough (the Mertz Drift), to the east of the U1357 site, can be assessed by

seismic profiles, and are indicative of a current controlled depositional process due to mounded and drape-and-fill architecture, alongside the notable absence of Holocene sediments on the Mertz Bank (Beaman and Harris, 2003; Harris and Beaman, 2003). The Adélie drift profile shows a similar structure, with an elongated east-west orientation on the northern flank of the Adélie Basin, thus suggesting U1357B deposition may be dominated by bottom currents focusing sediment into the basin (Escutia et al., 2011). Areas surrounding site U1357B also lack proglacial fan systems, providing further evidence that the majority of sediment is advected to the site comes from the east, rather than sourced from local glacial plumes (Dunbar et al., 1985).

Consequently, IODP Site U1357 is ideally suited to assess past shifts in Antarctic Coastal Current strength, while its variable sea ice conditions, and coastal polynya influences also allows for a range of proxies of past oceanographic and environmental conditions to be developed. Given the close proximity of U1357 to the Antarctic Slope Current and Antarctic Coastal Current, discerning the paleocurrent history may provide valuable insights into how changes in the current regime along the Wilkes Land Margin has influenced water mass variability and associated biological productivity in this globally important region of AABW formation (Chapter 2). The U1357 core provides a potential archive of sub-decadal variability of wind driven current variability over the Holocene, allowing for assessment of the natural baseline of variability in westward current strength at the margin of the largest marine-based glacial drainage basin of the East Antarctic Ice Sheet.

In this chapter, CT-scan imaging is used to characterise the biologically influenced laminae in U1357B. These results are then compared to physical core properties and XRF data to establish CT-greyscale variance as capturing changes in sedimentation. Changes in inferred XRF productivity proxies (Si/Ti and Ba/Ti) are examined to assess if the CT-scan derived laminae data sets accurately capture biosiliceous sediment related to primary productivity. These data sets are also used to independently assess the age model and sediment model at this location. Next, comparisons of grain size analysis, mass accumulation rates, and laminae thickness data derived from CT-scans are used to assess changes in the current flow velocity throughout the Holocene and assess how this may have influenced biological productivity related to the deposition of light and dark laminae. Finally, potential multi-decadal to centennial-scale drivers of bloom events and variation in laminae thickness are discussed. The methodology to obtain each dataset is discussed in Chapter 3.

4.2 Results

4.2.1 Manual laminae counts in comparison to CT-scan greyscale profile, linescan XRF, and physical properties data

Visual comparisons of line-scanned photographs of the split core face, CT images, a CT-scan greyscale curve, and the manual light laminae counts from the CT-scan were undertaken throughout the length of the core (e.g. Figure 4.1).

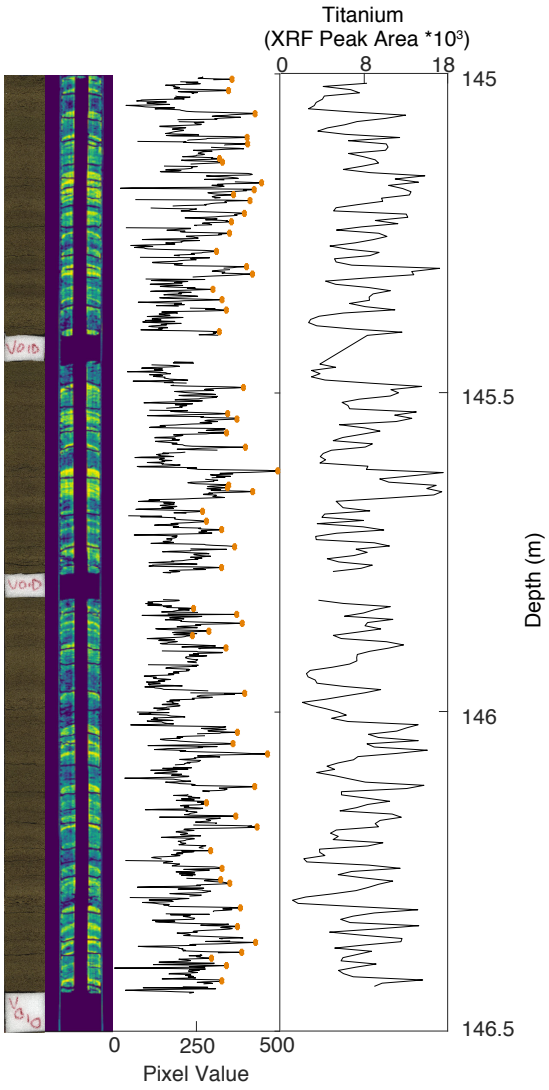

Figure 4.1: **Image Analysis Example.** From left to right: Line-scan core photo, CT image, raw CT-scan greyscale curve with light laminae counts in orange, and XRF titanium data. The CT image visually enhances the laminations, and provides a sub-mm resolved CT-scan greyscale curve that better captures the higher frequency shifts in sedimentation.

The CT-scan greyscale profile is used as a continuous dataset to quantify the rapid shifts in pixel values shown in the CT image. Manual counts of the light laminae occur at the appropriate peaks in the CT-scan greyscale curve. While the XRF titanium data also capture the general signal, the greyscale data is of much higher resolution and resolve rapid changes not seen in the XRF data (Figure 4.1). These relationships visually appear to be consistent through the entire length of the core.

To quantitatively assess how well the CT-scan greyscale profile reflected changes in sedimentation over the entire record, the CT-scan greyscale profile was also compared via regression analysis to the gamma-ray attenuation (GRA) bulk density profile, natural gamma radiation profile (NGR), and XRF silica (Si), titanium (Ti), and Si/Ti measurements (Figure 4.2).

The greyscale data have an average resolution of 0.7 mm. These data were smoothed using a 10-point moving mean and then linearly interpolated to the depth scales of the various proxies below. GRA bulk density measurements were measured at 2.5 cm intervals with a 10 second integration time using WRMSL (Escutia et al., 2011). These data are noisy due to the high gas content of the core and values less than 0.6 g/cm^3 were removed. Natural gamma radiation (NGR) measurements were undertaken at 10 cm intervals and are a more attenuated signal, and thus represent a very smoothed dataset that is unlikely to pick up cm-scale variations observed in the other datasets. Low levels of potassium, thorium, and uranium isotopes exist in this core because of the frequent, pure, diatom oozes which also result in a low signal-to-noise ratio (Escutia et al., 2011). To overcome this, a site specific background NGR measurement, as well as a long integration time of NGR measurements ensure lower error on these measurements, even though the measurements themselves remain low (Escutia et al., 2011).

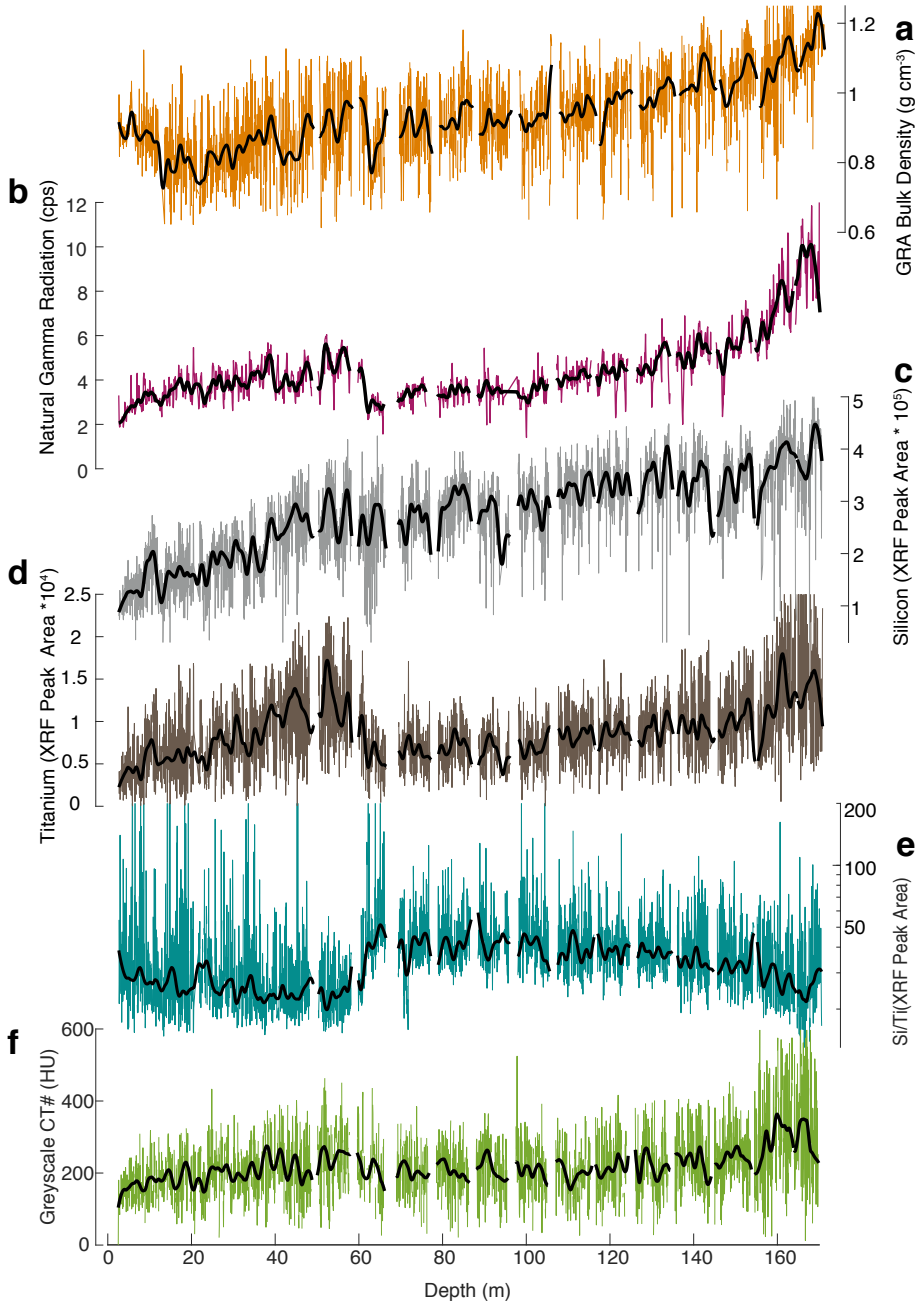

Figure 4.2: **Greyscale data in relation sedimentological changes at the site.** Greyscale data compared to various sedimentology proxies of the core. (a) GRA Bulk Density (b) Natural Gamma Radiation (NGR) (c) XRF peak area of Silicon (d) XRF peak area of Titanium (e) XRF peak area of Silicon/Titanium ratio used to indicate long-term changes in biological productivity (log scale) (f) CT-scan greyscale curve from the CT images.

The differences in resolution and signal-to-noise ratios of the various measurements above could be expected to compromise regression analysis, but despite this the correlation coefficients all display statistical significance between the greyscale data and the XRF data, NGR measurements, and GRA bulk density measurements (Table 4.1).

Greyscale Versus	**XRF Silica**	**XRF Titanium**	**NGR**	**GRA Bulk Density**
Correlation Coefficient (r)	0.43	0.59	0.58	0.33

Table 4.1: Comparison of greyscale data to XRF, NGR, and bulk density measurements

Given the strong similarity in trends and patterns seen in the titanium XRF and CT-scan greyscale record (Figure 4.1, 4.2), it was anticipated that these these records would have even higher correlation coefficient values than 0.59. Visual examination of the core images with XRF scan and the greyscale demonstrate these values are regularly offset by a few mm to cm in places, but a clear relationship between all three datasets can still be identified (Figure 4.2). This offset has occurred due to subtle mm- to cm-scale movements of the cores in the archive core half between physical property measurements, XRF scanning, and CT-scanning, which all occurred several years apart. This minor offset may have occurred as they were U-channelled and re-archived between measurements. While most of these offsets are mm- to cm-scale it would be enough to impact these statistical analyses.

4.2.2 Laminae frequency in the Holocene

Light laminae counts, which identify biogenic bloom events, are binned into 10-year and 100-year intervals and show centennial to millennial scale variations throughout the Holocene (Figure 4.3). Both curves show similar trends, but the 10-year binned record captures higher frequency variations, while the 100 year binned record emphasizes the multi-centennial scale variations more clearly. The laminae number per 100 years also correlates well with the linear sedimentation rate (Figure 4.4) as determined solely using the ^{14}C age model. To verify that these trends in number of laminae per 100 years are not an artefact of the age model, the laminae frequency per meter of core depth was also compared to the LSR curve (Figure 4.4).

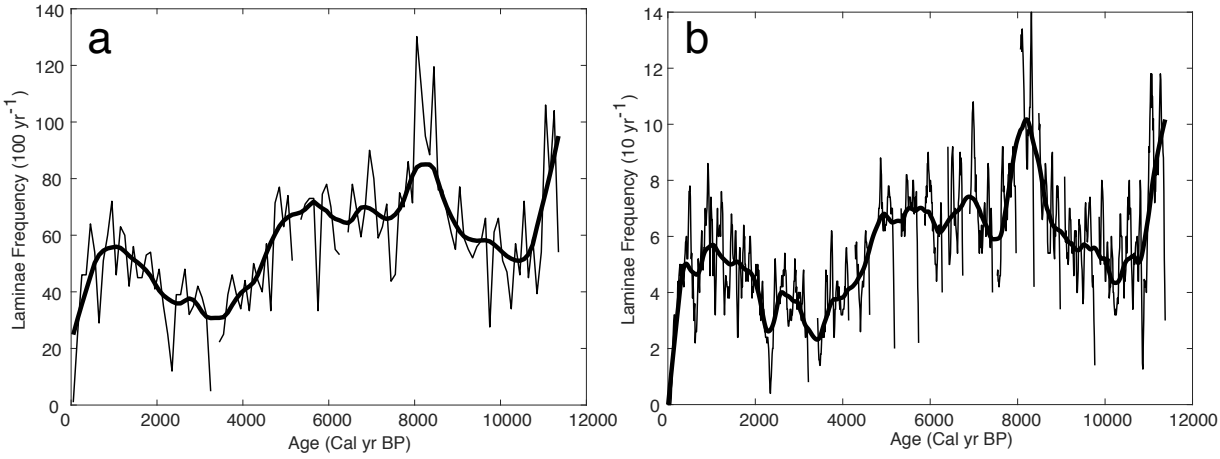

Figure 4.3: **Binned laminae frequency plots** (a) Light laminae counts binned into 100-year intervals, unsmoothed (b) Light laminae counts binned into 10-year intervals, smoothed with a 5-year moving mean. Bold line on both plots is a Robust Locally Weighted Scatter plot Smooth (rlowess) of the raw data (10% for 100-year, 5% for 10-year).

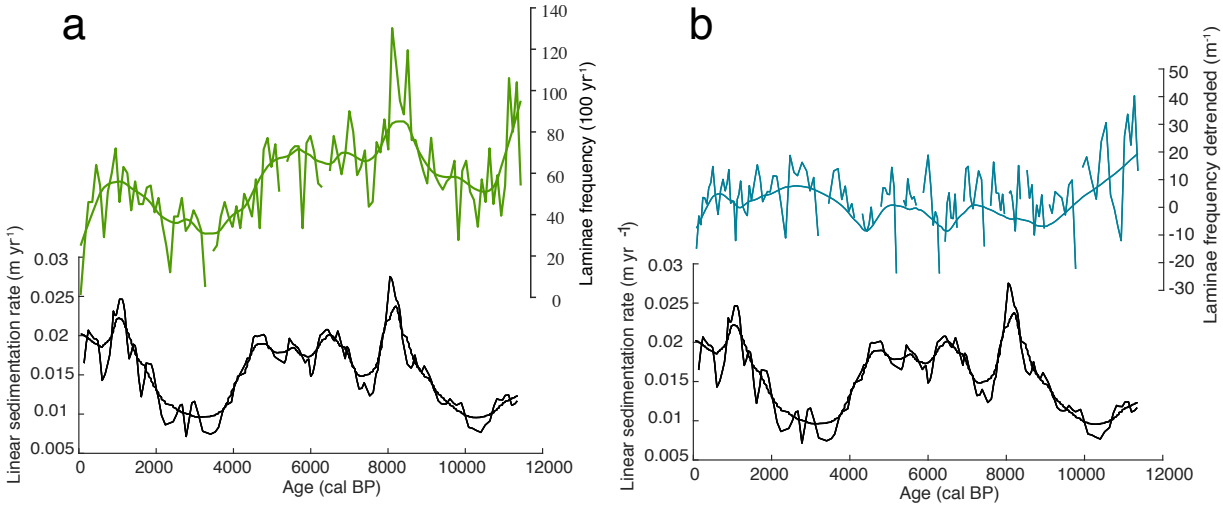

Figure 4.4: **Laminae frequency compared to the linear sedimentation rate (LSR).**(a) LSR versus number of laminae per 100 years (b) LSR versus number of laminae per meter (detrended).

To assess for potential biases introduced by the ^{14}C radiocarbon-based age model, laminae counts are binned into 1-meter intervals. Lower sedimentation rates determined by ^{14}C age model are associated with increased number of laminae per meter of core, as a shorter interval of core represents a longer period of deposition. This provides an independent validation of the age model and sedimentation rates, as it indicates an increase in depositional rate (i.e.

less time per meter) corresponds with a decrease in the frequency of laminae deposition in the depth domain (i.e. fewer laminae per meter). Theoretically, changes in the temporal frequency of bloom events relating to light laminae deposition could potentially offset this relationship, but this is unlikely to occur in a purely linear manner. If there was no periodic component to the laminae deposition, the frequency of their occurrence against the depth scale (laminae per meter) should bear no relationship to the linear sedimentation rate determined. Sedimentation rates vary at the millennial scale between 0.01 and 0.025 m yr^{-1}. After accounting for the overall downhole trend of increasing number of laminae per meter, that is attributed to downhole compaction due to sediment loading, the detrended laminae per meter demonstrate a strong anti-phasing with the linear sedimentation rate (Figure 4.4b). Thus, comparison of laminae frequency per meter (which varies between 20 and 80 laminae per meter, - 20 to 40 laminae per meter detrended) with the linear sedimentation rate curve provides an independent assessment that the laminae counts have a periodic component to their origin, and conversely that subtle changes in sedimentation rate determined by the radiocarbon chronology are real.

4.2.3 Laminae thickness

If the CT-scan greyscale and laminae data reflect changes in sedimentation and biological productivity, changes in light laminae thickness could potentially be indicative of more productive blooms or changes in sediment delivery rates.

A binned scatter plot which quantifies the frequencies of dark and light laminae thicknesses through time is shown in Figure 4.5. Laminae thicknesses are binned into 10 intervals (∼0.012 m wide, from 0 to 0.12 m thick) and 113 time intervals (∼100 years wide).

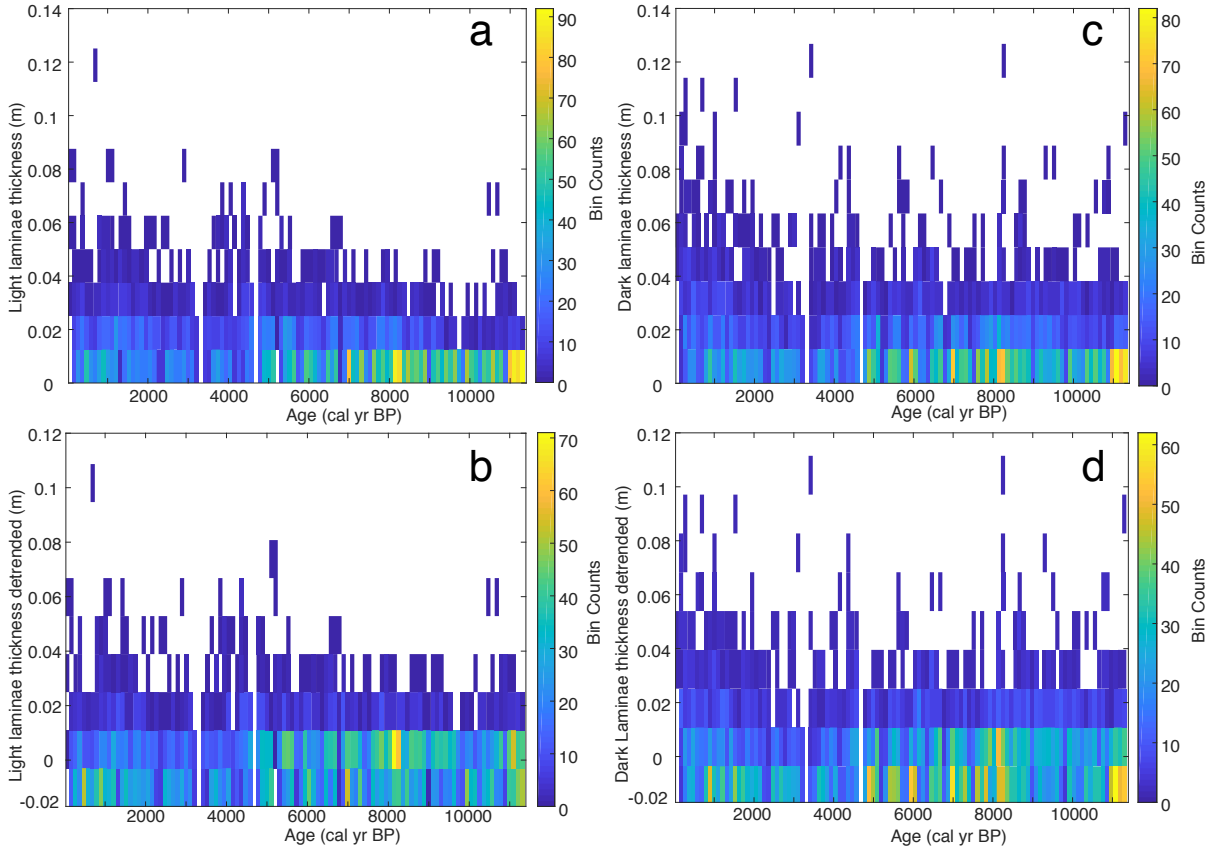

Figure 4.5: **Binned scatterplot of laminae thickness through time**. Laminae thickness are binned into ∼0.02 m intervals, and ∼100 year intervals. Counts of laminae in a particular thickness bin and time bin are indicated by color, with scale shown to the right of the plot. (a) Light laminae thickness (b) Light laminae linearly detrended (c) Dark laminae thickness (d) Dark laminae thickness linearly detrended.

Increased frequency of thin laminae (both dark and light) occurs towards the base of the core, regardless if the data is detrended. Laminae thickness increases towards the top of the core (∼4.5 ka BP to present day), yet this is more noticeable in the light laminae, as there are periods of thicker dark laminae in parts of the core older than ∼4.5 ka BP.

4.2.4 Mass accumulation rates

The pattern of biogenic and terrigenous MARs derived from light and dark laminae couplets (section 3.2.8) appear to track each other throughout the record, with relatively equal input until around ∼8 ka BP (Figure 4.6). After this, biogenic MAR is elevated over terrigenous MAR between ∼8-4.5 ka BP, but after ∼4.5 ka BP, terrigenous MAR is more elevated than biogenic

MAR.

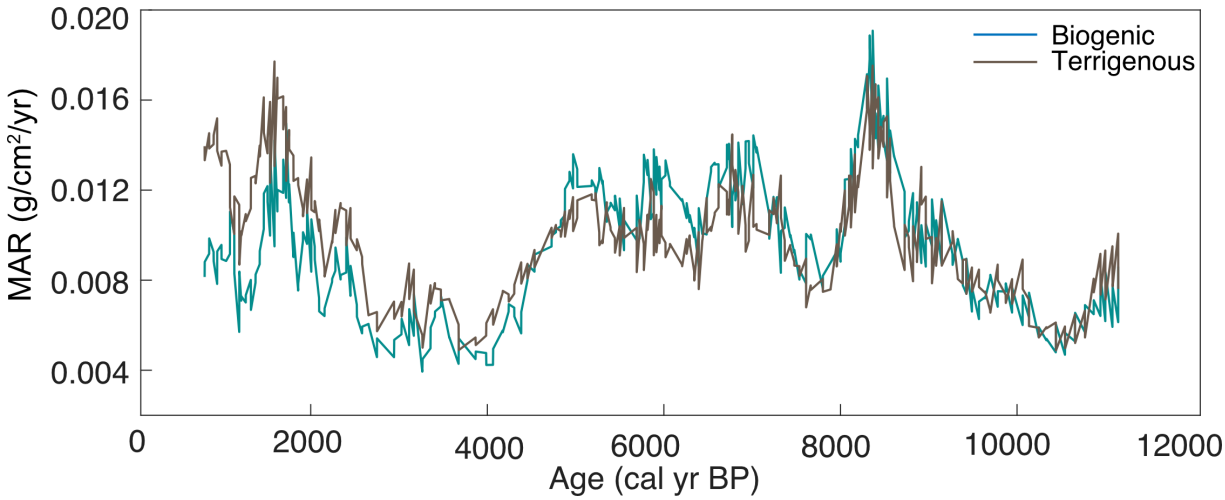

Figure 4.6: Biogenic (teal) and terrigenous (brown) mass accumulation rates

4.2.5 Grain size analysis

The grain size frequency distributions from Albot (2017) are shown in Figure 4.7. Grain size distributions were divided into three intervals which roughly correspond to the intervals discussed in section 4.3. Interval 1 corresponds to the Neoglacial (∼4.5 ka BP to present), Interval 2 corresponds to the Hypsithermal (∼8.2-4.5 ka BP), and Interval 3 corresponds to the Early Holocene (∼11.4-8.2 ka BP).

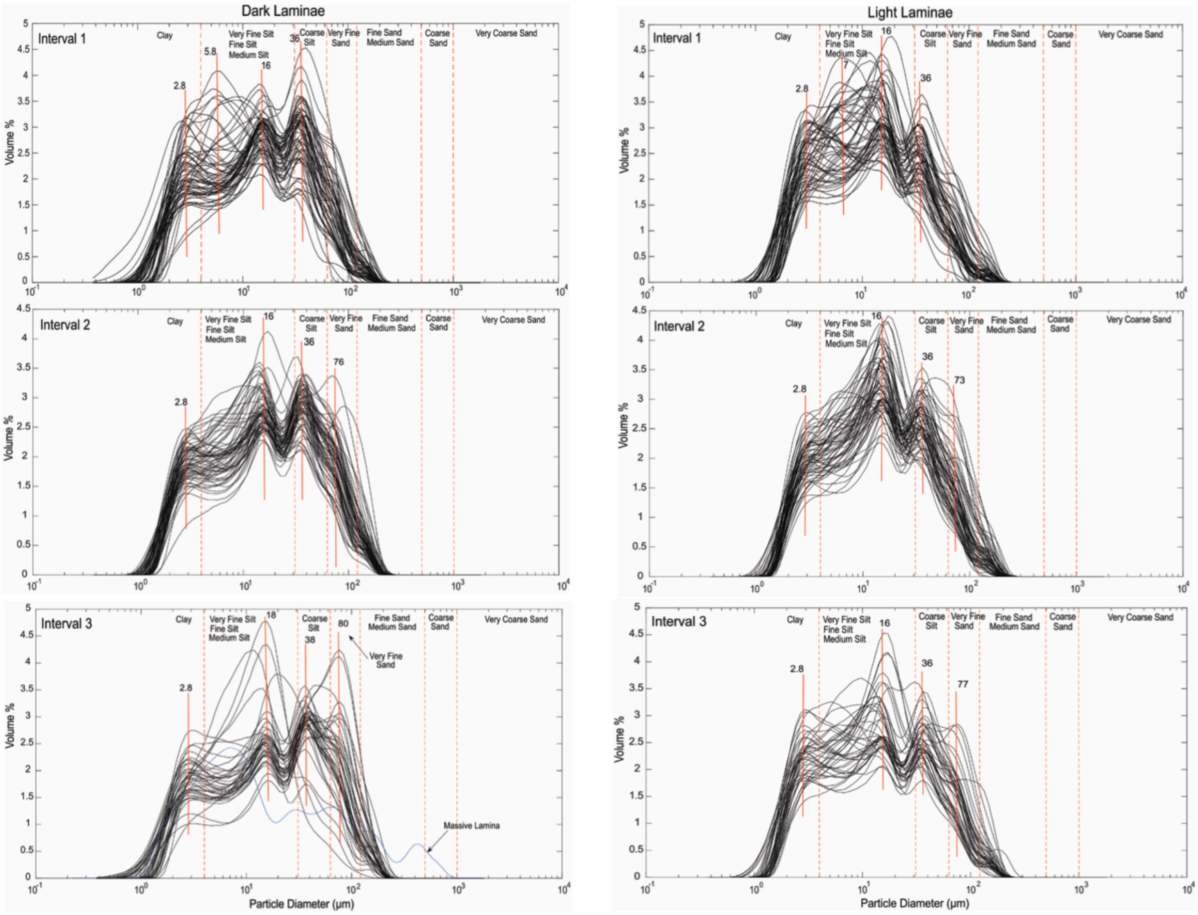

Figure 4.7: Grain size distributions of dark (left) and light (right) laminae for three time intervals. Interval 1 corresponds to ∼4.5 ka BP to present, Interval 2 corresponds to ∼8.2-4.5 ka BP, Interval 3 corresponds to ∼11.4-8.2 ka BP. From Albot (2017).

Intervals 1 and 2 show similar frequency distributions and do not contain grains with diameters greater than 250 μm. Some samples in interval 3 contain samples of fine sands (125-250 μm) to medium sands (250-500 μm), with one sample containing grains larger than 500 μm.

A multimodal distribution exists in the Early Holocene (Interval 3), which is characterised as a muddy diatom ooze. Dominant modes for dark laminae are 18 μm (medium silt) and 80 μm (very fine sand). Light laminae have a dominant mode in medium silt range (16 μm), with another mode at 36 μm (coarse silt) and some grains in the very fine-medium sand range. A massive laminae located at 170 m(csf-d) is indicated in blue (dark laminae, interval 3) and shows grains up to the coarse sand range. This laminae is located at the very bottom of the core and its distribution is abnormal compared to the remaining ∼5,750 laminae. Therefore,

it is disregarded in further analysis.

The grain size distribution in the Hypsithermal (Interval 2) shows a slight decrease in mean grain size relative to the Early Holocene. Similar modes are seen in both laminae as in Interval 1, with distinct modes at 16 μm and 36 μm for both laminae. However, the 16 μm is more dominant in the light laminae, while the 16 μm and 36 μm modes are equally weighted for the dark laminae. On the shoulder of the 36 μm, is an additional mode in the very fine sand fraction for light laminae (73 μm) and dark laminae (76 μm), but this is a minor feature in only a few samples. Sample to sample variability in either laminae type is reduced compared to other time intervals.

The Neoglacial (Interval 1) is described as a muddy diatom ooze, and clay to coarse silt comprising most of the distribution. Both types of laminae show a polymodal distribution encompassing clay (2.8 μm), very fine silt (5.8 μm (dark), 7 μm (light)), medium silt (16 μm), and coarse silt (36 μm). The dominant mode seen in the dark laminae is 36 μm, while the light laminae peaks at 16 μm.

4.2.6 Assessing suitability of grain size metrics in U1357B as a paleocurrent proxy

To assess how well sorted a sediment is and whether it can be used for flow history, McCave and Andrews (2019) suggest using the correlation between sortable silt mean size ($\overline{SS}$) and percentage sortable silt (SS%) in the fine fraction. High degrees of correlation (>0.5) suggest the sediment can be used for flow speed history (McCave and Andrews, 2019). However, grain size analysis from Albot (2017) indicates a bimodal distribution in the sortable silt (10-63 μm) range (Figure 4.7) indicating multiple influences on grain size distributions in this size range. Therefore, application of a standard sortable silt measure may not be applicable in this setting.

To investigate whether changes in maximum current speed are affecting sediment advection and nutrient delivery to stimulate biological productivity in the highly seasonal record of U1357B, several approaches are tested in this chapter. First the traditional $\overline{SS}$ and SS% in the fine fraction is compared to see how the bimodal distribution affects this proxy. Then, to isolate the two populations in the bimodal distribution, the larger mode (36-63 μm) in the sortable silt range (10-63 μm) is examined. Lastly, the the grain size range is extended to 125 μm, and the mean size of 36-125 μm versus the percent of 36-125 μm is analyzed in order to investigate the nature of the distribution around the largest mode (36 μm). Values lower than 36 μm were excluded, as the smaller mode at 16 μm affects the shape of the distribution of the lower 50th percentile of grains associated with the deposition of the larger mode. While

these ranges differ from the traditional sortable silt proxies for reasons discussed in section 4.3.3, many of the guiding principles for using this method in glacial settings are still applied (McCave and Andrews, 2019).

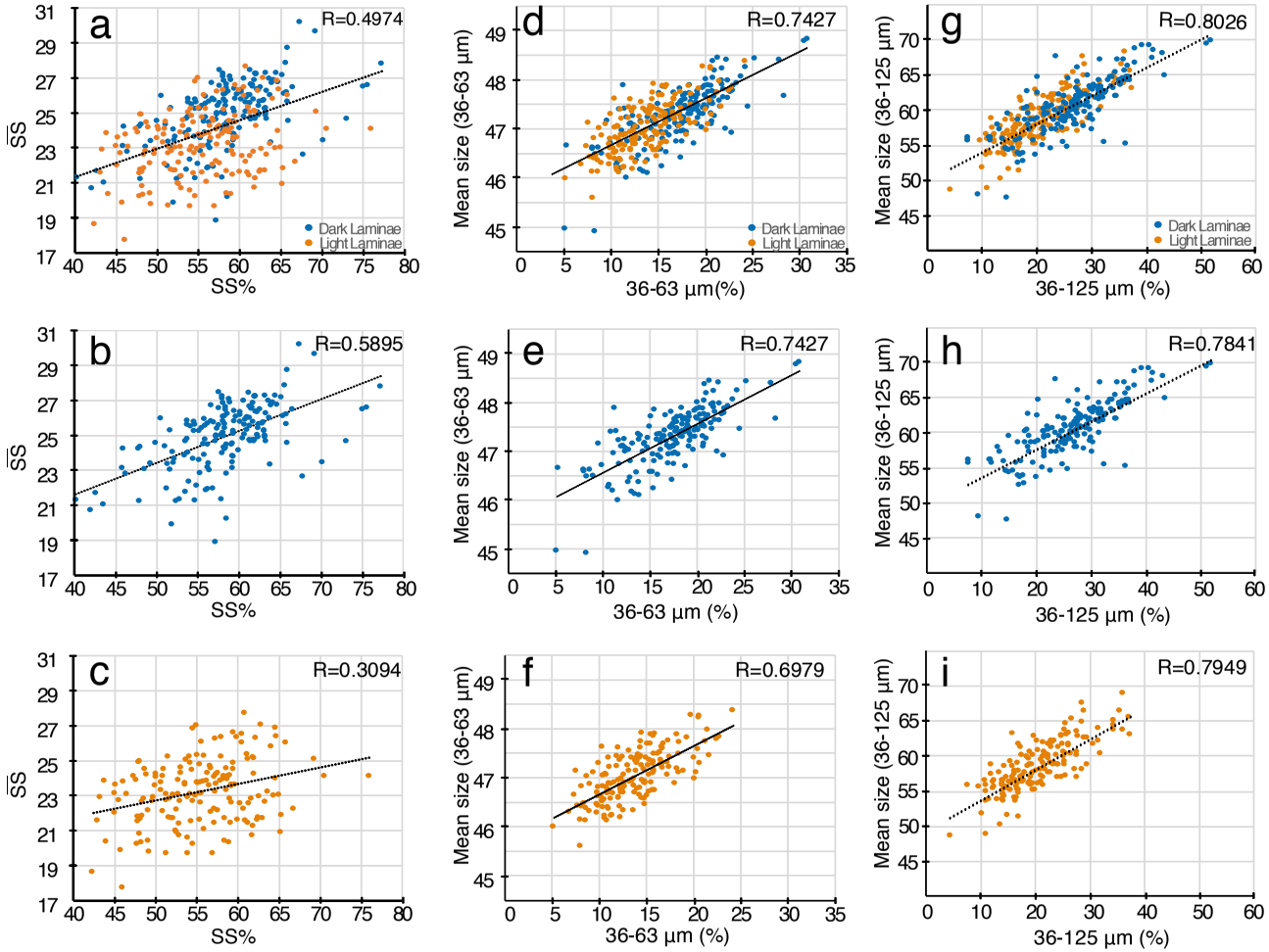

Figure 4.8: Mean grain size versus percentage comparisons. (a-c) is standard $\overline{SS}$ versus SS% (10-63 μm). (d-f) mean size versus percentage (36-63 μm). (g-i) mean size versus percentage (36-125 μm). a,d,g is all laminae, with blue dots indicating dark laminae, and orange indicating light laminae. b,e,h is dark laminae. c,f,i is light laminae. Black dotted line indicates line of best fit. Corresponding R values listed in upper right hand corner of each graph.

A linear relationship (R > 0.5) between the mean sortable silt size and percentage sortable silt are indicative of a well-sorted sediment sample (McCave and Hall, 2006; McCave and Andrews, 2019).

In U1357B, the $\overline{SS}$ - SS% relationship appears to be affected by the bimodal distribution in the sortable silt range, creating a larger spread in the data, with populations existing above and below the line of best fit. This is most apparent in the light laminae plot (Figure 4.8c). While the dark laminae do show a linear relationship (R = 0.59), this plot also appears to be affected by two populations, with the smaller mode (16 μm) creating a larger spread below the line of best fit. As these well-defined modes may indicate separate depositional processes within the sortable silt range, it warrants investigation of whether the larger mode (36 μm) is deposited within a consistent sedimentary process, similar to that of the traditional sortable silt proxy in the deep sea. The new range (36-63 μm) is then used for the same comparisons (Figure 4.8 d-f).

The comparison in the 36 to 63 μm range (Figure 4.8 d-f) shows that all laminae have an R value of 0.74. The light laminae and dark laminae appear in two clusters. When separated, the dark laminae have an R value of 0.74, whereas the light laminae have an R value of 0.69.

When the range is extended up to 125 μm (Figure 4.8 g-i), to account for the full distribution in the upper 50th percentile of this well-sorted mode, the R values increase in all samples. For all laminae, the R value reaches 0.80 (Figure 4.8g). For dark laminae, it is 0.78 (Figure 4.8h). The greatest increase is seen in light laminae, with an R of 0.79 (Figure 4.8i).

The well-sorted sediment in the coarse silt to fine sand fraction indicates a current influence even in areas of ice influence, as larger grain sizes are unlikely to be transported from the area where they are released, and the fine fraction will not be sorted in a sluggish current (McCave and Andrews, 2019). The increase in R when the mode is extend up to 125 μm indicates that fine sand is transported and selectively deposited along with the 36-63 μm fraction (McCave and Andrews, 2019; Mao et al., 2018). The $\overline{SS}$ in a well-sorted sediment can reliably infer the current speed at a location (McCave et al., 2017). However, in this case the mean size of 36-125 μm in all laminae, dark laminae and light laminae is used to determine the paleocurrent at U1357 (Figure 4.9 b,d,f).

For downcore studies, McCave and Andrews (2019) recommended performing a running correlation of the mean grain size and percentage grain size (in this case 36-125 μm), as the correlation can change and invalidate the paleocurrent proxy in certain periods (McCave and Andrews, 2019). A 9-point running correlation between the mean grain size and percentage grain size using all laminae, dark laminae, and light laminae reveals high correlations (R>0.5)

for most of the Holocene (McCave and Andrews, 2019) (Figure 4.9 a, c, f). The current proxy is considered suspect where the correlation falls below 0.5 (McCave and Andrews, 2019) (Figure 4.9, turquoise bars).

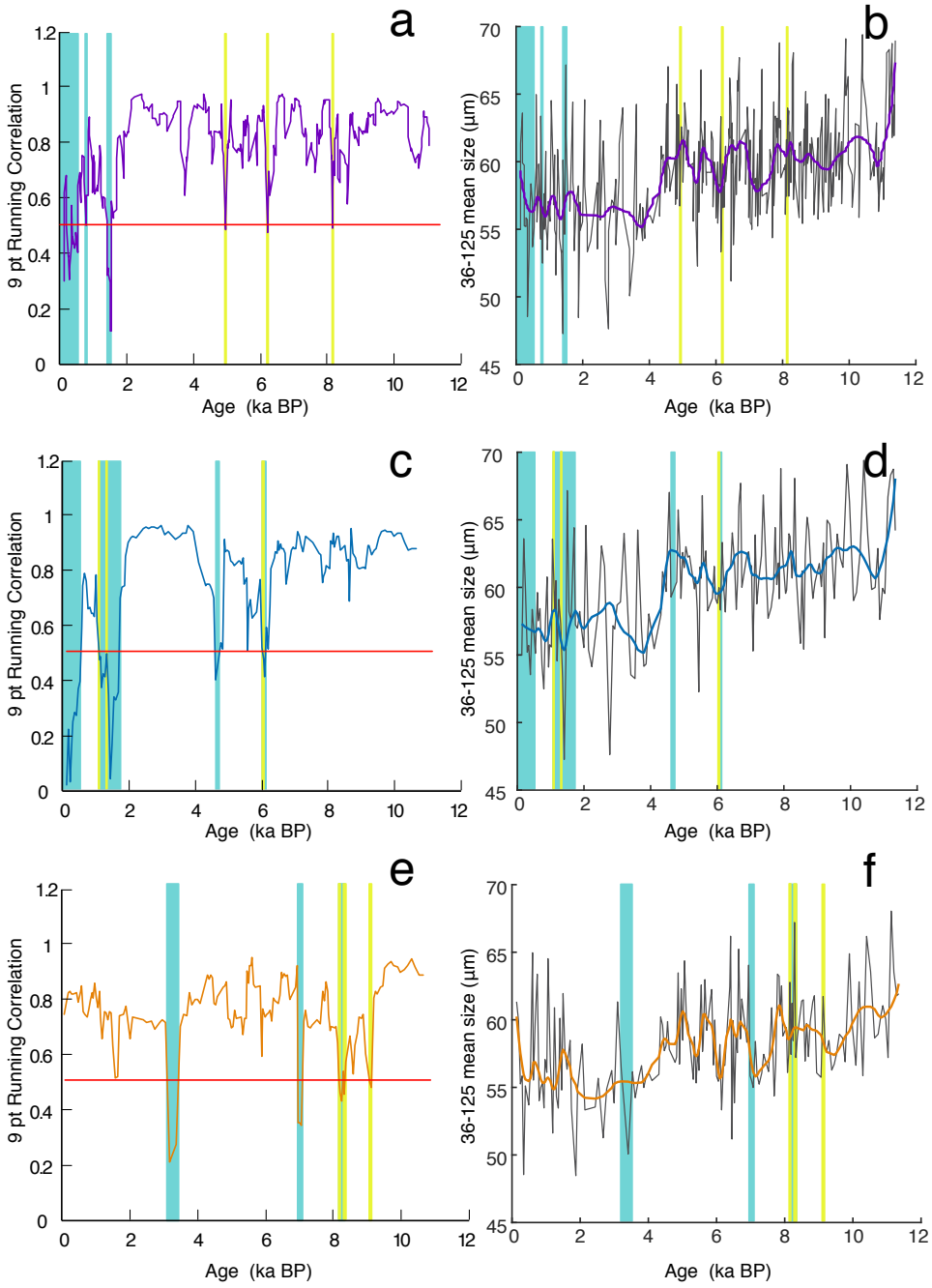

Figure 4.9: **Reliability of the paleocurrent proxy**. (a,c,e) 9-point running correlation of 36-125 μm mean size versus percentage of 36-125 μm (Mean grain size versus percentage comparisons). (b,d,f) is the mean grain size of 36-125 μm which is used as a paleocurrent proxy. (a,b) All Laminae, purple. (c,d) Dark laminae, blue. (e,f) Light Laminae, orange. The red line (a,c,e) indicates the 0.5 threshold for a well-sorted sample. Turquoise bars indicate when the running correlation does not meet the 0.5 correlation threshold, where the usage as a current proxy is not considered valid (McCave and Andrews, 2019). Chartreuse bars indicate where the running correlation is greater than 0.45.

The downcore correlations reveal intermittent periods when the paleocurrent proxy is considered unreliable. If the laminae types are not separated, the paleocurrent proxy is less certain between ~0.245 - 0.340 ka BP, ~0.390-0.543 ka BP, and ~1.407-1.549 ka BP. The remaining suspect periods are single points at 0.133, 4.963, 6.2, and 8.151 ka BP. The paleocurrent proxy using 'all laminae' appears to be reliable for all but a few disruptions in the last ~1.5 ka BP.

Assessing the paleocurrent proxy by laminae type may reveal seasonal current variations. For dark laminae, suspect periods occur between ~0.133-0.543 ka BP, ~1.124-1.703 ka BP, ~6.053-6.097 ka BP, and a single point at ~4.612 ka BP. For light laminae, the current flow proxy is considered suspect from ~3.408-3.534 ka BP, ~7.030-7.141 ka BP, ~8.213-8.288 ka BP, ~9.128-9.187 ka BP, and a single point at ~8.373 ka BP.

Many of the single point suspect periods have correlations greater than 0.45. While less than the 0.5 threshold, these periods are not outrightly dismissed, as they are only one data point amongst other higher correlations, and are quite close to meeting the 'reliable' threshold. Instead these sections are approached with slightly reduced confidence and interpreted alongside other paleoenvironmental indicators.

4.3 Discussion

4.3.1 Linking the CT-scan greyscale profile and laminae counts to changes in sedimentary environment through the Holocene

The similarity between the CT-scan greyscale data and XRF titanium data show that changes in the CT-scan greyscale data, and therefore light laminae counts, reflect changes in sedimentation at the site (Figure 4.1). Additionally, distinct co-varying trends are evident (Figure 4.2) and three baseline shifts in sedimentary depositional environment are recorded and outlined below.

The lowermost ~0.7 m of this core is characterised as poorly sorted mud-rich diatom ooze, as indicated by high NGR and grain size data (Section 4.2.5), with high concentrations of IRD observed in CT-scan images (Figure 4.10). This core interval is interpreted as representing an environment strongly influenced by local outlet glaciers during the deglaciation, which were grounded over the U1357 site at the Last Glacial Maximum (Mackintosh et al., 2014). Ice retreat in this region is interpreted as first occurring in the deep bathymetric trough, with residual ice caps persisting on the bathymetric highs, resulting in an ice-walled fjord – termed

a calving bay (Leventer et al., 2006; Escutia et al., 2011). This is consistent with patterns of post-LGM deglaciation elsewhere along the East Antarctic margin (Mackintosh et al., 2014). The ^{14}C dates in this core interval are assumed to be affected by reworked carbon of pre-Last Glacial Maximum age as they produce anomalously older ages. Consequently, this interval of core is not considered in the analysis presented in this thesis and only sections dated younger than 11.4 ka BP are investigated (Figure 3.5).

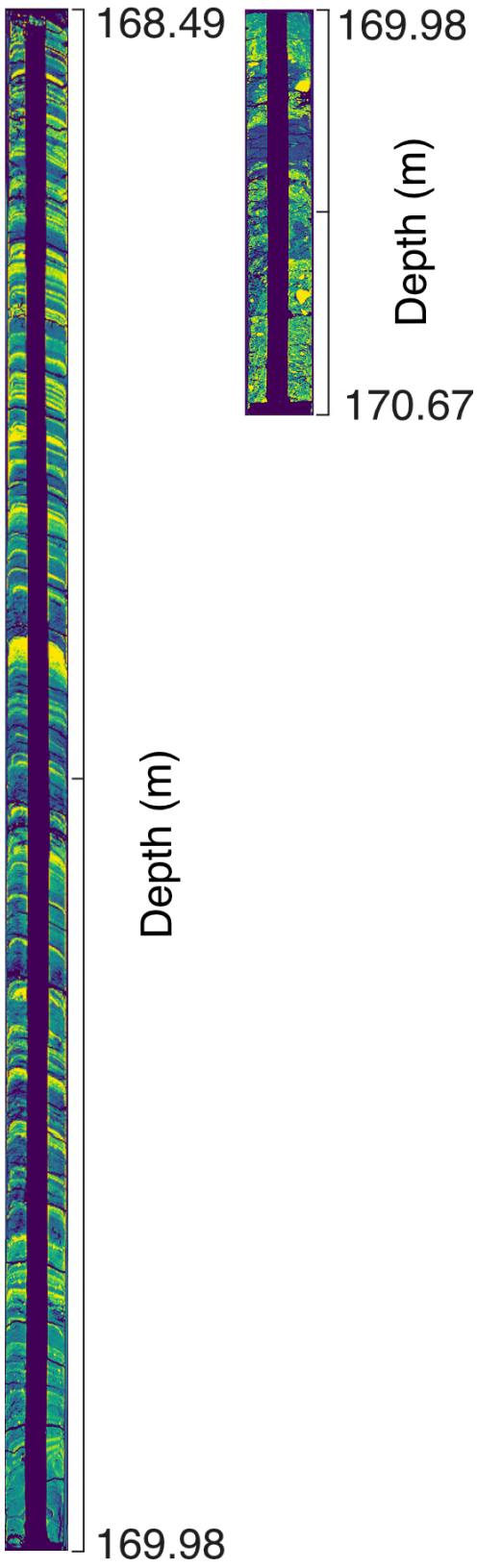

Figure 4.10: **Iceberg rafted debris in U1357B** Section 19H5 (right) is the only section with notable IRD. Section 19H4 (left) shows the sharp transition to mud-rich diatom ooze. Depths are in csf-a. The top of section 19H5 is dated to ~11.37 ka BP.

The lowermost ∼25m (∼11.4-9 ka BP) of U1357B core is described as mud-bearing to mud-rich diatom oozes with common clasts, which grades up into diatom ooze by 145 m (Escutia et al., 2011). The section reflects the glaciomarine sediment supply following deglaciation superimposed on the dominant pelagic sediment source of the diatom ooze (Escutia et al., 2011).

From 145 meters below sea floor (mbsf) to the top (∼9 ka BP to ∼100 years BP), the core is a diatom ooze with a visual decrease in terrigenous sediment content. The second shift occurs from 145-60 mbsf (∼9–4.5 ka BP) and is characterized by low NGR, lower XRF titanium, and fairly stable, to slightly decreasing GRA bulk density, XRF silica, and greyscale density values (Figure 4.2). XRF Si/Ti ratios, a proxy for biological productivity, gradually increase, but then remain steady (Figure 4.2e). This indicates the onset of a relatively stable depositional environment in the core with a decrease in glaciomarine sedimentation and an elevated, but steady supply in biogenic material relative to the lowest most ∼25 m.

At around 60 meters (∼4.5 ka BP), an abrupt increase in all five logs indicate another baseline shift in deposition, with an increase in the NGR values and density values from the CT-scan and GRA datasets (figure 4.2). This suggests a relative increase in terrigenous sediment over biogenic supply as supported by decreasing Si/Ti values. A concomitant increase in relative abundances of the sea-ice related diatom *Fragilariopsis curta* from nearby core MD03-2601 (Denis et al., 2010) and in the fast sea-ice Highly Branched Isoprenoid (HBI) biomarkers (Chapter 5) indicates this shift is directly associated with an increase in sea-ice duration off Adélie Land.

The concomitant changes in all of the proxies indicate that changes in the CT-scan greyscale data are highly coupled to the sedimentary environment and reflect changes in sediment supply, productivity, and sea ice cover. As high frequency variability of the CT-scan greyscale data are indicative of laminae events (Figure 4.1), it reasons that laminae frequency is also driven by these changes.

4.3.2 Quantifying bloom events through frequency analysis

To quantify how well the laminae counts, and subsequent binning of the laminae reflected actual frequency variations in the sedimentology and CT-scan greyscale profile, the manually picked laminae frequency curves (Figure 4.3) are compared to the evolutionary spectra of the CT-scan greyscale curve, Ba/Ti and Si/Ti values from XRF linescan data (Figure 4.11). All four records show covarying shifts in frequencies and further ground the greyscale and laminae data sets as proxies for biological productivity throughout the Holocene.

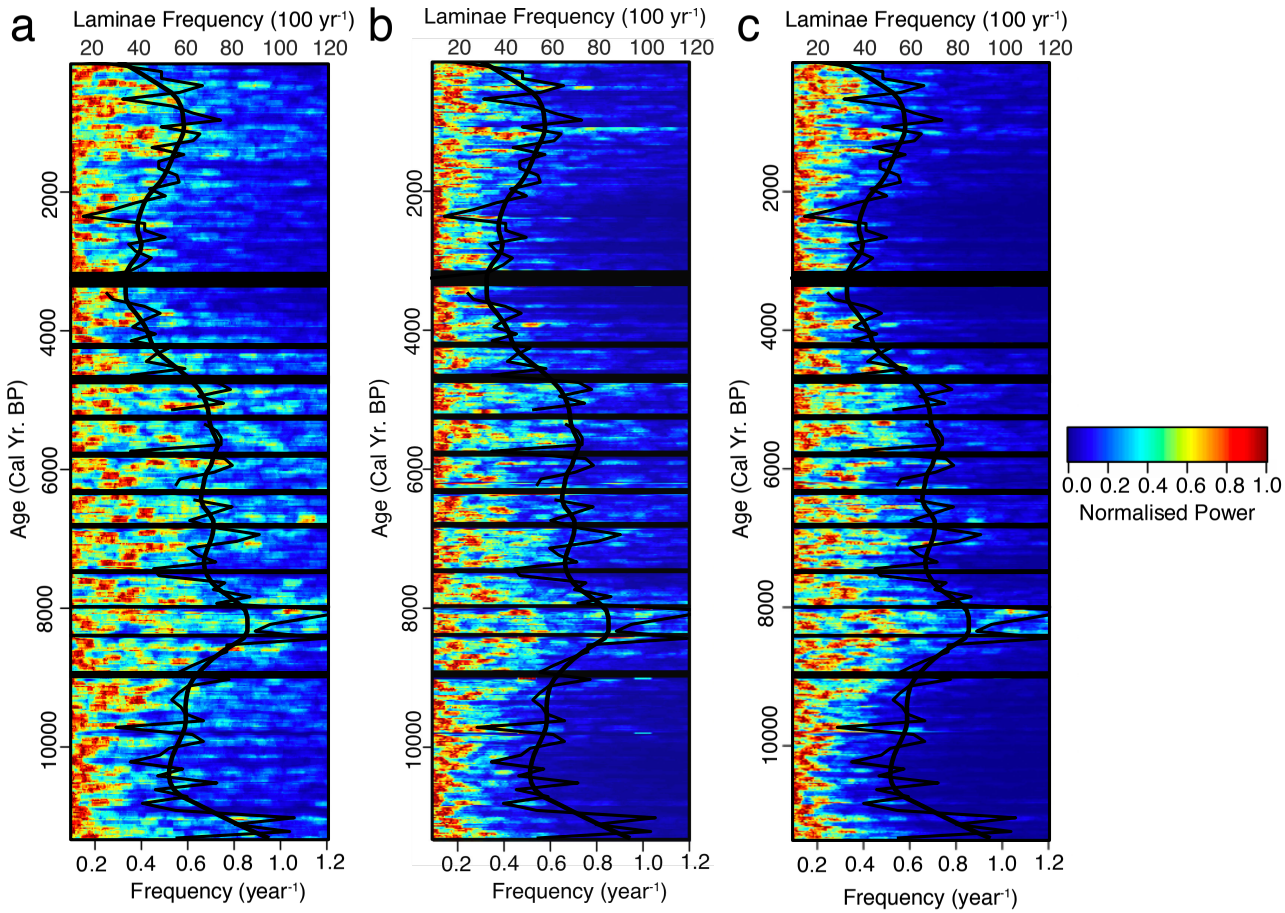

Figure 4.11: **Evolutive Harmonic Analysis (EHA) of the (a) greyscale data, (b) XRF Ba/Ti, and (c) XRF Si/Ti productivity proxies**. Both plot are overlain with laminae frequency per 100 years(black) curves. Normalized power is similar across both proxies, showing a distinct shifts at 8.2 and 4.5 ka. Manual laminae counts binned at 100-year intervals are consistent with the EHA. The black smoothed curve is robust lowess smoothing of the 100-year binned curve using 10% of the data. The black boxes indicate core gaps.

The manual laminae counts binned into 100-year intervals and evolutive harmonic analysis results show consistent centennial-scale shifts in the power of the 2-7 year frequency bands. The 2-7 year frequency band is suggestive of an El Niño-Southern Oscillation influence, which is discussed thoroughly in Chapter 5.

There is a potentially subjective element to the manual picking of laminae counts, but this can be independently assessed by comparison of the evolutive harmonic analysis from the raw CT-scan greyscale curve and the laminae counts. The EHA results show the same sub-decadal frequency shifts throughout the Holocene as the manual laminae counts, and provides a clear independent verification of the frequencies determined by the manual counting (Figure 4.11a).

4.3.3 Sediment delivery to U1357B

To interpret changes in laminae frequency or thickness, sediment delivery to U1357B must be qualitatively and quantitatively assessed. Regional studies on the Adélie Land continental shelf indicate that winnowing by bottom currents of the sediments <125 μm is occurring on the bathymetric high due to bottom current speeds in the range of 20 cm/s (Dunbar et al., 1985). This winnowed sediment is subsequently being focused and deposited into sediment drifts forming in adjacent bathymetric basins, including the Adélie Basin. Consequently, despite the presence of strong currents, the deep bathymetric depression of the Adélie Basin acts as a sediment trap for this winnowed sediment. As a result, selective deposition (as opposed to winnowing) is assumed to be the primary control of deposition of the drift. This assumption of selective deposition is supported by:

1. The observation that surface glaciomarine sediments on bathymetric highs have grain size distributions that indicate some winnowing of particles <125 μm (Dunbar et al., 1985), while the terrigenous particles in the Adélie Basin (Site U1357B) are predominately <125 μm (Figure 4.7).

2. The morphology of the drift which is elongated and aligned with the flow direction of the Antarctic Coastal Current, and is located on the lee side of the Adélie Basin.

3. Biogenic and terrigenous sediment MARs covary (Figure 4.6) indicating these pelagic and winnowed seafloor sediments are being advected, focused, and deposited by the same current.

Selective deposition regulates transport and settling of the sortable silt range (10-63 μm) at current speeds of 10-15 cm/s (McCave and Hall, 2006). In many deep sea settings, these

grain sizes are winnowed at higher speeds (McCave and Hall, 2006). This is consistent with grain size observations on the Mertz and Adélie Banks, where current speeds are inferred to be 20 cm/s and thus, actively winnowing sediments from the adjacent bathymetric highs (Dunbar et al., 1985). However, in the Adélie Basin itself, a large sediment drift has formed where the along slope current speed decreases as the bathymetry rapidly deepens, leading to selective deposition of these winnowed sediments and other sediment suspended in the water column (Figure 4.12). As these westward currents are mainly wind driven (Whitworth et al., 1998; Snow et al., 2016), the strength of this transport will vary with wind strength and sea ice concentration, which reduces the impact of winds on the sea surface (Figure 4.12).

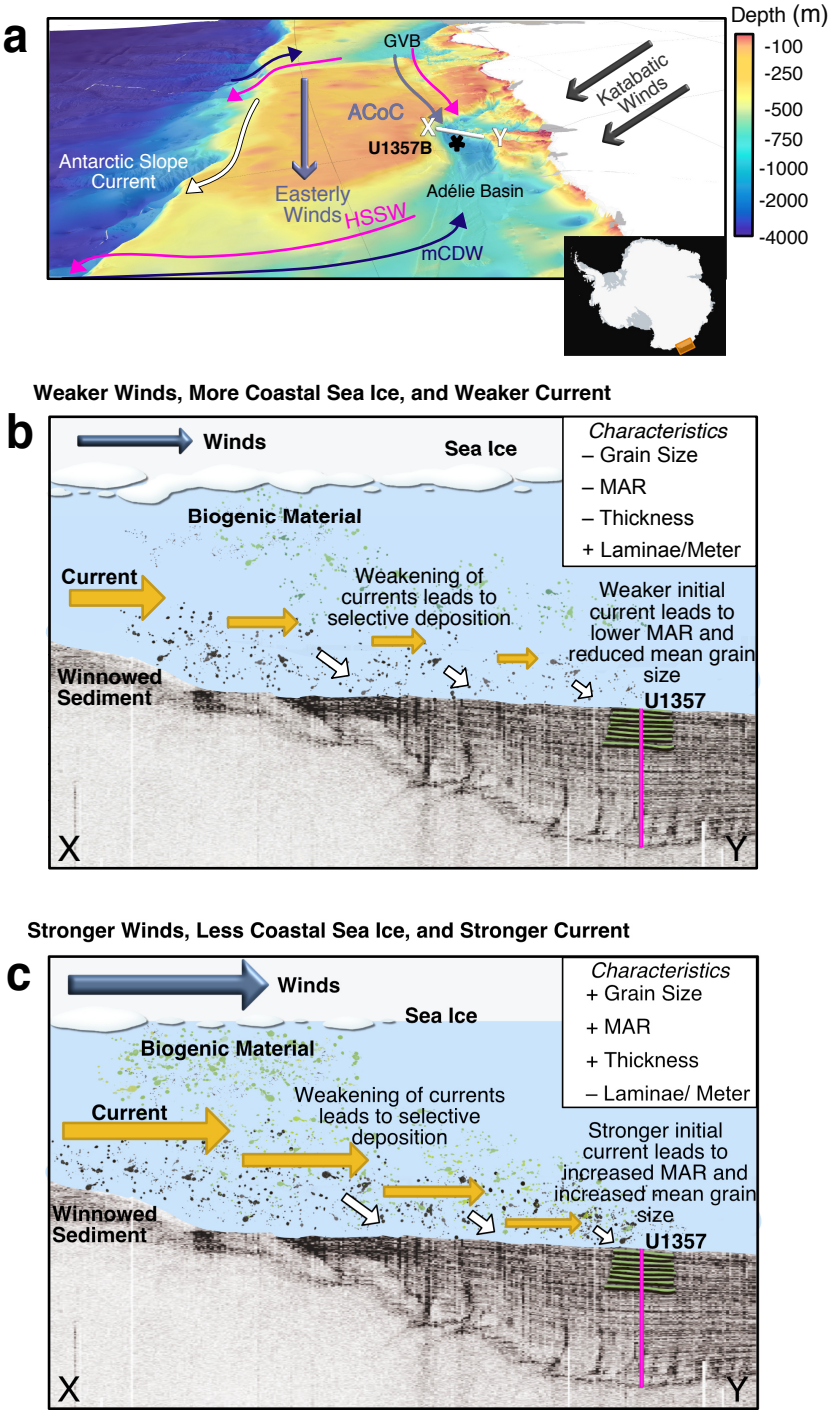

Figure 4.12: **Simplified Adélie Drift Sediment Deposition Model for both dark and light laminae.** (a) Same as Figure 2.10. X-Y (white) marks approximate location and direction of seismic profile shown in (b,c). Bathymetry data from Beaman et al. (2011). (b) Deposition model of Adélie Drift during weaker winds(katabatic/zonal), more sea ice, and subsequent weaker current. Biogenic and winnowed terrigenous material are selectively deposited into drift as water slows over basin. Light and dark laminae indicated by brown and green line. Pink line indicates approximate location of U1357. Blue arrow indicative of winds, yellow arrows indicative of coastal current, and white arrows indicative of selective deposition. Relative strength of winds and currents indicated by size of arrows. Characteristics of this mode are seen as decreased grain size, decreased MAR, decreased laminae thickness, and increased laminae per meter. X,Y marks seismic profile direction as seen in (a). (c) same as (b), but for stronger winds (katabatic/zonal), less sea ice, and stronger current. Seismic profile seen in both (b,c) is ODEC 2000 single-channel seismic line from Escutia et al. (2011).

McCave and Andrews (2019) argued that the transport of the fine fraction ($< 63\ \mu m$) in glacially influenced settings can still be used as a paleocurrent indicator regardless if it was released from ice rafting or sea ice, or sourced from melt-water plumes, as long as it is well sorted. This lies in the idea that slow currents rarely sort both fine and coarse fractions, while higher currents never reach speeds where the coarse fraction can be moved and deposited simultaneously with the fine fraction (McCave and Andrews, 2019). Therefore, a well-sorted fine fraction is only deposited downstream from a region of higher flow and can be used to assess paleocurrent, as long as the IRD content is less than ∼50% (McCave and Andrews, 2019). The CT images (see figure 4.10) and lack of grain sizes greater than 250 μm in nearly all samples suggest that IRD (500 μm) input to the record is minimal. The few dropstones in the core that are present are clearly out sized compared to other grain sizes and are striated suggesting they are of IRD origin (Escutia et al., 2011). The visual core descriptions, CT images, and seismic profiles do not suggest the existence of turbidites or the influence of other gravity flows affecting this location.

While McCave and Andrews (2019) recommend using the $\overline{SS}$ - SS% correlation and down-core moving correlation of these parameters to determine how well-sorted a sediment is, they also note that the sortable silt (10-63 μm) fraction is a somewhat arbitrary classification and not suitable in all depositional settings. As discussed above, the highly variably bathymetry of the Adélie Land continental shelf is likely to result in winnowing on topographic banks of sediment $< 125\ \mu$m, and the majority of this material is likely trapped in sediment drifts in deep bathymetric troughs.

The $\overline{SS}$ - SS% correlation in the Adélie Basin deposit are relatively low ($R = 0.49$, all laminae; R=0.59, dark laminae; R=0.31, light laminae) and grain size distributions in the sortable silt range suggest two modes (Figures 4.8, 4.7). The modes within this 10—63 μm size range form distinct, well-sorted peaks that are indicative of selective deposition by currents (McCave and Hall, 2006). A working hypothesis in this chapter is that these modes represent highly seasonal variations in current strength, and the typical sortable-silt proxy may not be valid in this location. Compared to deep deposits, such seasonality could be preserved in this deposit due to:

1. The laminated nature of the deposit.
2. The ultra-high sedimentation rates (∼1.5-2 cm/yr).
3. The extreme seasonality present in this current-influenced continental shelf setting due to changing seasonal sea ice cover and wind stress on the ocean surface.

This is an important difference from many deep sea settings where the sortable silt proxy is usually applied. In those settings, sedimentation rates are usually several orders of magnitude lower, and are often highly mixed by bioturbation or sediment overturning, and have much lower seasonal variations in current speed (McCave and Hall, 2006). Therefore, sortable silt in those deep sea sediments are measuring a smoothed, integrated measure of current speed over hundreds or thousands of years, and are primarily measuring change in maximum current speeds over those time periods.

Consequently, rather than directly applying the sortable silt to these data, examination of the large dominant silt to fine sand mode is proposed to provide more insights into maximum current speed variation at this site. Previous work on the sortable silt proxy do note that under strong current regimes, sorting can continue into the fine sand range (up to 125 μm) (Lamy et al., 2015; Mao et al., 2018; McCave and Andrews, 2019). Indeed, a visual examination of the frequency distribution curves indicate that a normal distribution approximates the selective deposition of the 36 μm mode and this can most efficiently be characterised by the 36-125 μm size (Figure 4.7). Furthermore, while the laminae types are well sorted when simply excluding the 16 μm mode (36-63 μm, Figure 4.8 d-f), the correlation coefficients of mean versus percent values continue to increase when the range is extended up to 125 μm (Figure 4.8 g-i). This suggests the sorting effect in this core extends up into larger grain sizes, but the strong bi-modal peaks in the silt size range indicate multiple current regimes may be influencing the site. The increasing correlation as larger grain sizes are included imply that very fine sand is moved with sortable silt in bottom currents along Adélie Land (Mao et al., 2018). The strong, positive correlations and downcore correlations between mean 36-125 μm grain size and 36-125 μm percentage show that the laminae contain well-sorted sediment and the mean grain size of the 36-125 μm range can be used to infer paleocurrent speed (Figure 4.9b,d,f).

4.3.4 Deposition of dark and light laminae

The smaller mean size of the 36-125 μm range for light laminae suggest maximum current speeds for light laminae deposition are smaller than the maximum current speed for dark laminae deposition (Figure 4.9 d, f).

Dark laminae are interpreted to be deposited during open ocean conditions when mass biogenic bloom events are not occurring, as is observed in nearby core MD03-2601 (Denis et al., 2006)(Figure 5.1). The increased mean size of the 36-125 μm range of dark laminae implies stronger currents, which is in agreement with the interpretation of deposition during sea-ice free conditions, as wind stress on the ocean surface would be uninhibited by sea ice and able

to influence current strength. However, regrowth of sea ice in late summer and early autumn could also contribute to increased current strength as brine rejection, HSSW production and subsequent export lead to enhanced bottom current strength (Williams et al., 2008, 2010).

The smaller mean size of the 36-125 μm range for light laminae may suggest a shorter deposition time or weaker currents in general, relative to the larger mean size for dark laminae. Light laminae are interpreted to reflect relatively short-lived biogenic bloom events that are rapidly deposited (relative to the dark laminae) and occur after the break-up of sea ice (see 4.3.2) (Denis et al., 2006). Particle flux data suggests a short two month lag between bloom events at the surface and export of that material to the sea floor (Rigual-Hernández et al., 2015). The short time frame for particles to sink and be sorted through the water column could explain why light laminae grain size distributions appear to have lower maximum current speeds than dark laminae. This is because the darker laminae are deposited more slowly, over a longer time period and are therefore likely to capture more storm events and higher maximum current speeds. However, current strength is also an integral component to laminae bloom events, as relatively weaker currents, and therefore relatively weaker winds could support stratification of the water column initiating bloom events (Vaillancourt et al., 2003).

Increased productivity within the Mertz polynya has been linked to sea ice meltwater and inflow of mCDW that brings iron to the surface (Moreau et al., 2019). Snow et al. (2016) suggested onshelf flow of mCDW was strongest in the winter in part due to sea ice formation and subsequent buoyancy fluxes. While Snow et al. (2016) found reduced influence of wind-driven transport of mCDW onto the Adélie Land continental shelf, numerical modelling suggests the nearshore easterly winds exert control on this cross-shelf exchange (Stewart and Thompson, 2012; Spence et al., 2014; Stewart and Thompson, 2015). Regardless of the seasonal timing, increased mCDW appears to seed the water column for bloom events. Increased productivity has been observed in areas around Antarctica where wind-driven upwelling of CDW occurs (Prezelin et al., 2000). Strong katabatic and synoptic winds are essential for the breakup of coastal sea ice and the opening of polynyas along the Adélie Coast(Adolphs and Wendler, 1995; Massom et al., 2001). It follows that in years with stronger winds, increased sea-ice break up and seeding of the water column with nutrients may occur. If stronger winds lead to increased productivity, times of stronger current should reflect this increased productivity as well. This is in agreement with this study, as an increase in laminae frequency (Figure 4.3) occurs during periods of overall increased current speed for both laminae types (Figure 4.9 d,f). Higher wind speeds during dark laminae deposition are inferred to mix the water column and upwell nutrients, thereby seeding the water column for phytoplankton blooms. An overall strengthening of winds would lead to increased mixing of the water column and upwelling of nutrients relative

to a more quiescent wind regime. Blooms events during these periods of higher winds would be more frequent and more productive due to the increase in nutrients in the water column.

4.3.5 Climate modulation of sediment transport and laminae thickness

Since current strength modulates sediment transport and may influence productivity, laminae thickness is likely also controlled by current strength. Increased current strength could lead to thicker laminae as more material is winnowed from the banks, and more pelagic material is advected to the site and deposited. Therefore, variations in current strength during laminae deposition in the Holocene may account for the variation seen in laminae thickness in the Holocene.

There is a higher frequency of thin laminae towards the bottom of the core. While some of this may be partially due to compaction, a similar pattern exists even if the data is linearly detrended (Figure 4.5 b and d). The trend is particularly noticeable around ∼8.2 ka and 11.4 ka BP which correspond to large frequency peaks also seen in laminae counts (Figure 4.3) and EHA (Figure 4.11). From ∼4.5 ka BP towards the present day, there appears to be a slight increase in thicker light and dark laminae (Figure 4.5), particularly in the last ∼1000 years, suggesting that while there is an overall decrease in bloom events, events that do occur may be more productive. However, this could be a compaction effect not accounted for in the linear detrending process.

Thickness variations of light (Figure 4.13a) and dark laminae (Figure 4.14a) do covary with their respective current strength proxies, suggesting laminae thickness changes are not a function of compaction. Mass accumulation rates infer sediment advection to the site, with high MARs indicating increased advection of both terrigenous and pelagic sediment (Figure 4.12). Strong covariance of the 36-125 μm mean grain size between laminae types and the MAR curves, suggest MAR is predominately affected by current strength, with stronger currents leading to increased sediment advection and laminae thickness. Alignment between these various proxies appears strongest after ∼8.2 ka BP. The slight disconnect between laminae thickness, MARs, and current speeds in the records prior to ∼8.2 ka BP, may be due to local deglacial influences affecting the local productivity cycle and the restriction of sediment transport from the east due to grounded ice cover on the bathymetric highs. After ∼8.2 ka BP, increased laminae thickness covaries directly with increased MAR and increased current speed in both laminae types, suggesting that current speed affects laminae thickness.

Evolutive harmonic analysis of laminae thicknesses suggests multi-decadal to sub-decadal climate variability may influence laminae thickness, which may be due to variability in current

strength (Figures 4.14, 4.13). Areas with higher frequency of thickness changes are associated with increased and more variable laminae mean grain size (and therefore stronger, more variable currents), as well as increased MARs. This further indicates that sediment transport plays a key role in laminae thickness variations, and it is not solely a function of productivity.

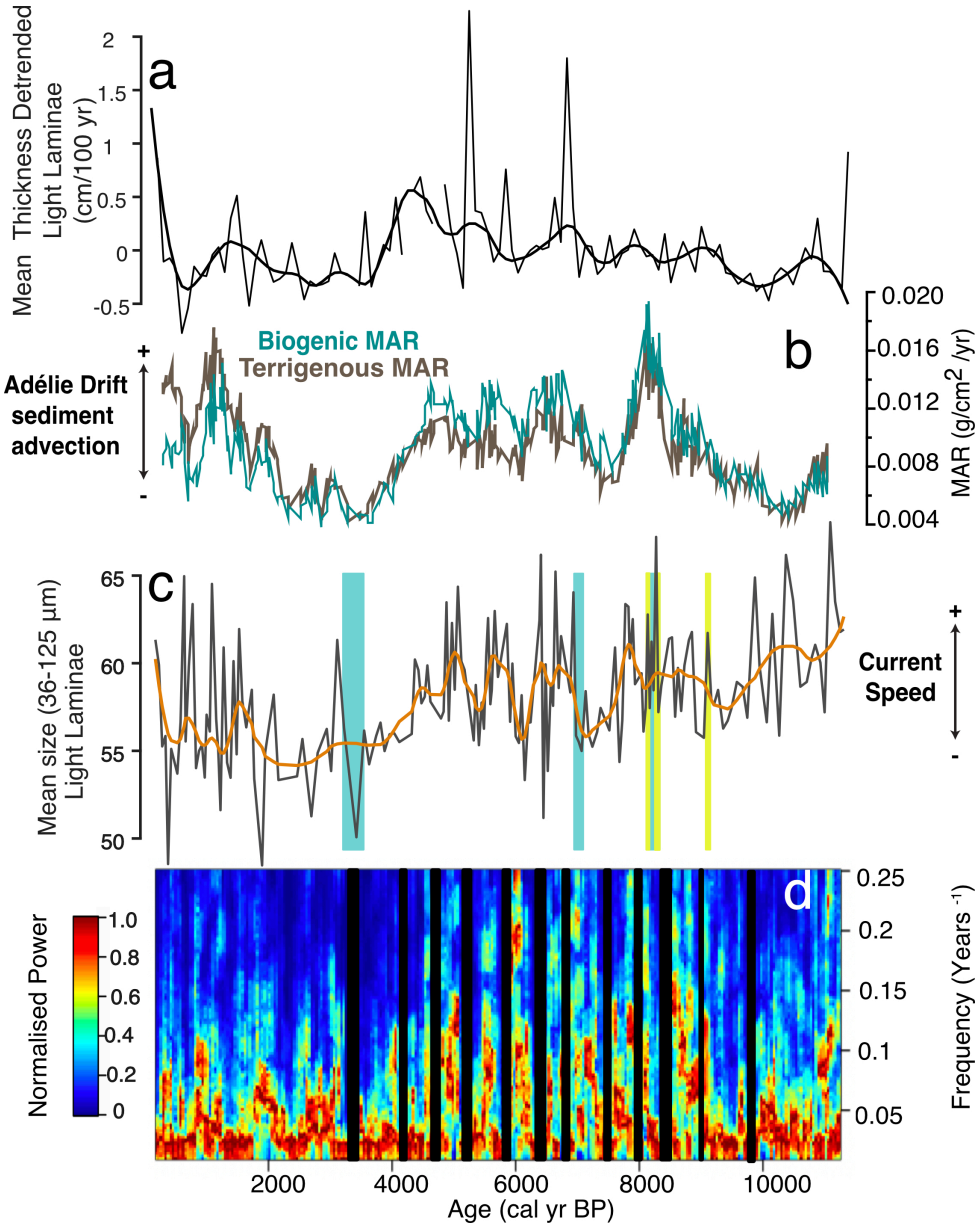

Figure 4.13: (a) Binned 100-year mean of light laminae thickness detrended. (b) Mass Accumulation Rates (Terrigenous, brown; Biogenic, green). (c) Light laminae mean size (36-125 μm) paleocurrent speed proxy. Turquoise bars indicate where paleocurrent proxy is suspect. Chartreuse bars should be interpreted with caution.(d) EHA of light laminae thickness. Power is normalized in (d) so that each window is in unity. The black bars indicate core gaps and areas around core gaps where EHA analysis cannot be performed.

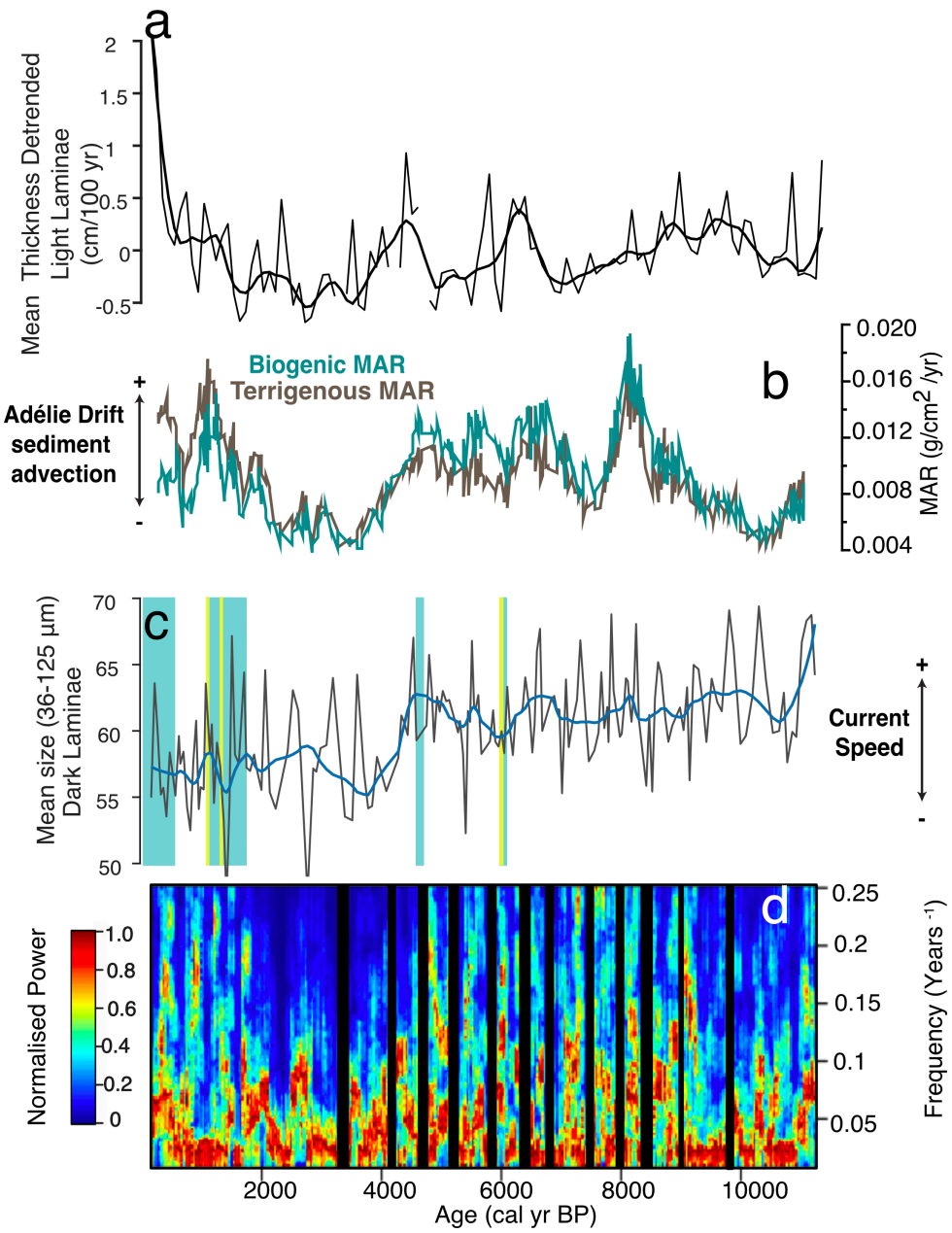

Figure 4.14: (a) Binned 100-year mean of dark laminae thickness detrended. (b) Mass Accumulation Rates (Terrigenous, brown; Biogenic, green). (c) Dark laminae mean size (36-125 μm) paleocurrent speed proxy. Turquoise bars indicate where paleocurrent speed proxy is suspect. Chartreuse bars should be interpreted with caution.(d) EHA of dark laminae thickness. Power is normalized in (d) so that each window is in unity. The black bars indicate core gaps and areas around core gaps where EHA analysis cannot be performed.

Variations in light and dark laminae thickness have a strong 4-7 year frequency from around 9-4.5 ka. While there are likely deglacial influences from 9-8 ka, the variations from 8-4.5 ka could be related to ENSO. However, this is difficult to determine as the lower resolution (2 years) of the laminae thickness data precludes the measurement of frequencies less than 4 years (0.25 yr^{-1}) and strong ENSO bands typically occur in the 2-7 year range. As mentioned previously, the ENSO-Adélie relationship is explored in great detail in Chapter 5, and therefore is not discussed here further.

A second area of strong frequencies in light and dark laminae occur in the decadal to multi-decadal band. This could be related to IPO, which has ∼15-35 year frequency and affects ENSO teleconnections in the Southern Hemisphere (Power et al., 1999; Henley et al., 2015; Magee et al., 2017). It is also suggested to affect sea ice extent and cause surface wind anomalies around Antarctica (Meehl et al., 2016). Indeed, sea salt and sea ice proxies from nearby Law Dome (66.769 °S, 128.807 °E, elevation 1370 m) show decadal to multi-decadal frequencies which are attributed to the IPO affecting surface transport (Vance et al., 2013; Vallelonga et al., 2017).

As the IPO affects wind strength, and is also shown to affect sea ice extent in the modern record, it is likely that the variations in laminae thickness are related to these changes through wind-moderated shifts in sediment advection, as well as affecting the frequency of bloom events. However, the sub-decadal to multidecadal band remains even when sea ice increases massively from ∼4.5 ka onwards (Figure 5.2f). This suggests that wind variations could be the primary driver of changes in current speed and sediment advection that cause these frequency variations in laminae thickness.

Unfortunately, only one IPO reconstruction exists at this time, and only goes back a millennia (Vance et al., 2015). Additionally, other tropical influences in the Adélie Land region (ENSO, IOD, SAM), which are also known to affect wind strength around Antarctica are poorly understood. Future studies are needed to better understand tropical teleconnections and the affect on wind and current strength in the region.

4.4 Conclusion

IODP U1357B is a high-resolution continuously laminated sediment core from offshore Adélie Land, East Antarctica. The CT-scan greyscale profile and manual laminae counts extracted from CT images of sediment core U1357B covary with physical core properties and XRF productivity data showing that changes in the CT-scan greyscale profile and laminations reflect changes in

biological sedimentation. Binned laminae frequencies match up with frequencies derived from XRF productivity ratios, indicating that the interpretation of light laminae as a record of high productivity bloom events is robust. The binned laminae frequencies per meter independently verify that the ^{14}C age model is robust, due to the distinct antiphasing of the binned record with the ^{14}C derived linear sedimentation rates. This comparison also upholds the manual approach to laminae picking in this record. The accuracy of laminae counts are further supported by the independent evolutive harmonic analysis of the greyscale and XRF data.

Clear millennial scale shifts in sedimentary patterns are noted throughout the Holocene, and the physical drivers for these local depositional shifts are investigated by reassessing previously measured grain size distributions, but with a new assessment of paleocurrent proxy application. Grain size distributions of light and dark laminae in U1357B are not influenced by IRD and contain well sorted modes in the silt and fine sand fractions, making them useful for paleocurrent reconstructions.

Light and dark laminae are deposited under different regimes, therefore, assessing paleocurrent from both light and dark laminae may highlight seasonal differences throughout the Holocene. MARs and grain size covary with laminae thickness indicating sediment advection is primarily a depositional process driven by current strength. However, an overall increase in current strength, and therefore inferred wind strength, is associated with increased laminae thicknesses and shifts in laminae frequency. This suggests that productivity may be modulated by wind driven upwelling of nutrients, which precondition the water column for large bloom events. Both light and dark laminae records indicate that laminae thickness varies on decadal to multi-decadal timescales, which is provisionally attributed to surface wind anomalies caused by IPO affecting current strength and therefore sediment transport to the site. A significant implication of this work is that bloom events are not an annual occurrence and appear to be regulated by these decadal to sub-decadal climate modes which affect the zonal winds.

Chapter 5

El Niño-Southern Oscillation influences on East Antarctic biological productivity

This chapter is constructed as a standalone short format manuscript and is currently in review. Components of chapters 3 and 4 were combined and submitted with this manuscript as supplementary material.

Authors: **Katelyn M. Johnson** [1,2], Robert M. McKay[1], Nancy A.N. Bertler[1,2], Johan Etourneau[3,4,5], Francisco J. Jiménez-Espejo[3], Anya Albot[1], Christina R. Riesselman[6], Huw J. Horgan[1], Xavier Crosta[5], James Bendle[7], Carlota Escutia[3], Robert B. Dunbar[8]

Abstract

Antarctic sea-ice extent, primary productivity, ocean circulation, and bottom water formation are important components of the global carbon cycle and climate system. Evaluating sub-decadal to centennial scale variability of these systems in Antarctica's coastal oceans is challenging as observational data are too limited to resolve the timescales of interest and future projections remain ambiguous due to existing model uncertainties. Integrated Ocean Drilling Program (IODP) sediment core U1357B, collected offshore of Adélie Land in East Antarctica, is a unique archive of near annually-resolved biologi-

[1] Antarctic Research Centre, Victoria University of Wellington, New Zealand, [2] GNS Science, National Ice Core Research Laboratory, Lower Hutt, New Zealand, [3] Andaluz Institute of Earth Sciences, CSIC-University of Granada, Granada, Spain [4]EPHE, PSL University, Paris, France [5] UMR 5805 EPOC CNRS, University of Bordeaux, Bordeaux, France [6] Department of Marine Science and Geology, University of Otago, Dunedin, New Zealand [7] School of Geography, Earth, and Environmental Sciences, University of Birmingham, UK [8] School of Earth, Energy, and Environmental Sciences, Stanford University, California, USA

cally influenced sedimentation in a key Antarctic Bottom Water (AABW) formation site. Centimetre-scale laminations exist throughout the entire record, resulting from deposition of mass phytoplankton bloom events. Here, we use X-ray Computed Tomography, $IPSO_{25}$, diatom analysis, and physical/geochemical core properties to identify large productivity shifts associated with changing climatic conditions over the past 11,400 years. The ultra-high resolution of this record identifies that bloom events occur at 2-7-year intervals throughout the Holocene, suggesting a strong coupling to the El Niño-Southern Oscillation (ENSO), and other sub-decadal climate modes. However, rapid baseline shifts in climate and sea-ice state appear to control bloom frequency, indicating the existence of sea ice tipping points that act to modulate low- to high-latitude teleconnections. These results suggest projected intensification of tropical climate modes of variability will have a significant impact on primary productivity in Antarctica, altering food webs and carbon-cycling processes. However, the magnitude of this response will be primarily modulated by changes in sea-ice state.

5.1 Introduction

Antarctica's marine margin is a complex biological and oceanographic system in which sea-ice growth, Antarctic Bottom Water (AABW) formation, and high primary productivity act as a global CO_2 sink and ventilate the Southern Ocean (Arrigo et al., 2008a; Rintoul, 1998). Areas of high productivity occur where nutrients are brought to the surface, including oceanographic fronts (Moore and Abbott, 2000), polynyas (Arrigo and van Dijken, 2003), upwelling near the continental shelf break (Smith and Gordon, 1997), and the marginal ice zone (MIZ) (Smith and Nelson, 1986), all of which are influenced by Antarctic wind fields. However, high productivity and export events around Antarctica are also associated with changing insolation and stratification associated with sea-ice break up (Rigual-Hernández et al., 2015). Large-scale climate oscillations, including ENSO and the Southern Annular Mode (SAM), are known to affect both sea ice (Yuan, 2004; Nuncio and Yuan, 2015) and zonal circulation (L'Heureux and Thompson, 2006) around Antarctica and thus influence primary productivity (Arrigo and Van Dijken, 2004). In the austral summer of 2016, a strong El Niño resulted in a melt event across the Ross Ice Shelf and into the interior of the West Antarctic Ice Sheet (Nicolas et al., 2017), and was preceded by an anomalous springtime breakup of sea ice around Antarctica during a very negative SAM index (Turner et al., 2017a). Extreme ENSO events are expected to occur more frequently in coming decades (Cai et al., 2015), and clarifying how these climate oscillations have affected Antarctic coastal systems in the past is required if we are to determine how these

sub-decadal oscillations will affect the Antarctic marine margin in the future (Mayewski et al., 2004).

Here, we investigate a 180 m (IODP Site U1357B) thick sediment core recovered from the Wilkes Land Margin continental shelf in the Adélie Basin (Escutia et al., 2011) (Figure 5.1).

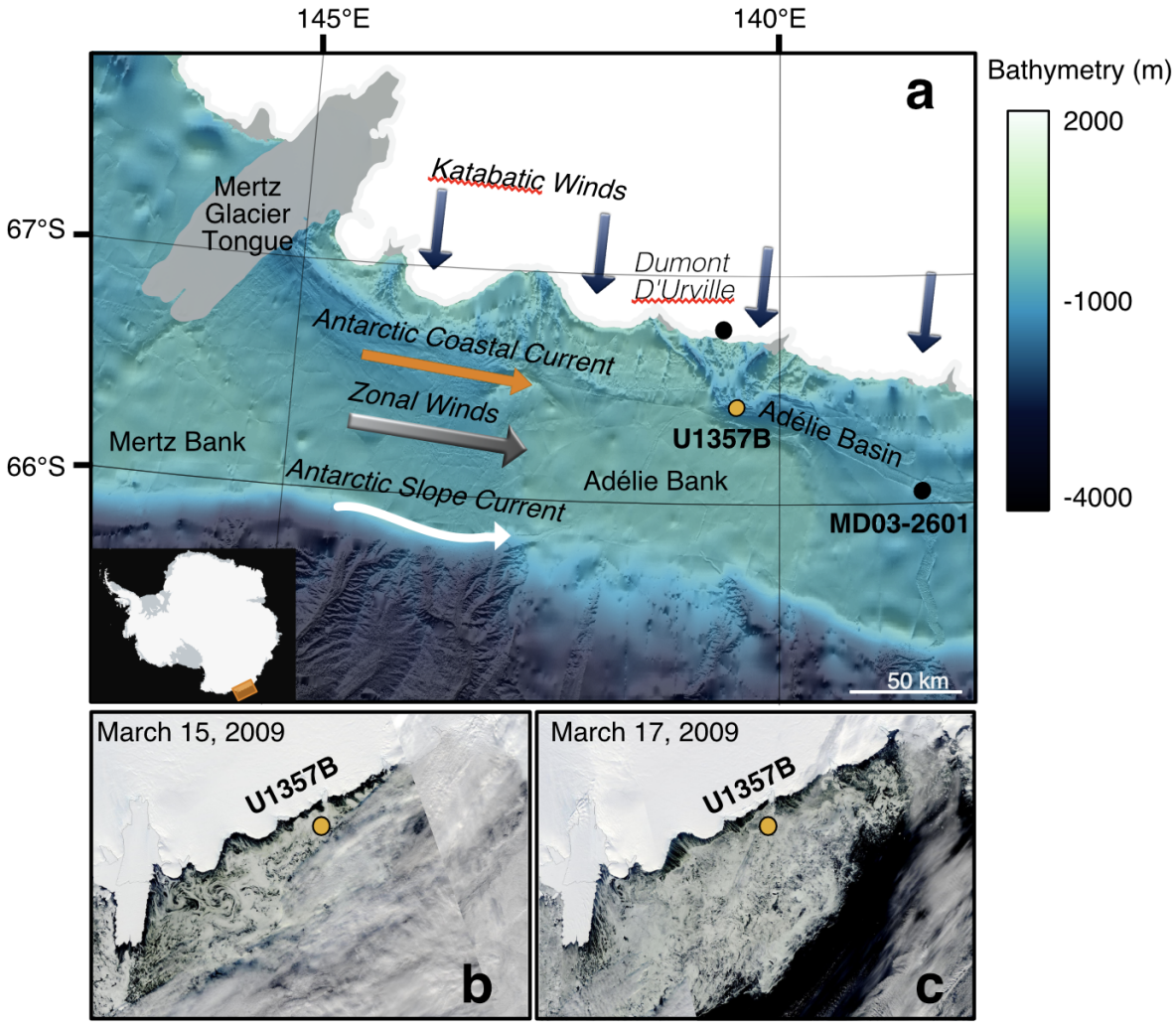

Figure 5.1: **Study area**. (A) Map of the Adélie Land and site locations of U1357B, MD03-2601, and Dumont d'Urville (DDU) station. Primary bathymetric features (Beaman et al., 2011), wind directions, and current locations indicated.(B,C) Satellite images capture the green tinge of a large phytoplankton bloom event occurring for several days over the site location (NASA Worldview).

The Adélie Basin is a region of intense biological productivity as it is positioned near the

MIZ, but also lies beneath a large polynya system, and the westward-flowing Antarctic Coastal Current. This core targeted an expanded sediment drift (Adélie Drift) and provides an ultra-high resolution Holocene record of climate and oceanographic variability adjacent to the Mertz Polynya system, one of the largest exporters of sea ice and AABW along the East Antarctic margin (Rintoul, 1998). Sedimentation is dominated by pelagic (biogenic) sedimentation with accumulation rates averaging ∼1.5-2 cm/year, and it is the most expanded marine Holocene archive collected globally. Previous Antarctic cores have orders of magnitude lower sedimentation rates, and commonly alternate between massive (bioturbated) and laminated diatom ooze (Pike et al., 2013), which obscures the ability to resolve high-frequency change at sub-decadal scales. However, U1357B is continuously laminated, and combined with high sedimentation rates, affords an unprecedented opportunity to assess sub-decadal climate and biological responses at the Antarctic oceanic margin.

5.2 An ultra-high-resolution record of marine biogenic blooms

The elongated east-west orientation of the Adélie Drift lies parallel to the wind-driven Antarctic Coastal Current. Consequently, the Mass Accumulation Rate (MAR)(Section 4.2.4) in this drift may be a function of the current strength, and only partially reflects changes in biological productivity. Nearby core MD03-2601 shows covariance of the sedimentation rates with U1357B throughout the Holocene, indicating the sediment advection process is a regional signal (Figure 3.5). Comparison of the co-varying siliciclastic (detrital) and biogenic MAR (Figure 5.2c), suggests detrital and biogenic sediments are advected to the site together under the influence of wind-driven currents and focussed into the Adélie Basin.

Iceberg rafted debris (IRD) are negligible (Figure 4.10), aside from the very bottom of the core (>168 mbsf) suggesting direct glacial sediment supply is limited. Bathymetric highs in this region are characterised by poorly sorted diamicts and muddy sands, and grain size frequency distributions in those settings indicate the partial winnowing of the <125 μm component by bottom currents (Dunbar et al., 1985). However, detrital siliciclastic material in the bathymetric troughs, including the Adélie Drift deposit, are consistently <125 μm with a well-defined silt-fine sand mode (Figures 4.10 and 4.7). This is interpreted to represent the suspension settling of winnowed muds derived from diamicts on the adjacent highs, suggesting the primary control on sedimentation is current strength and sediment advection. Hence, we infer sand percentage in U1357B is related to the suspension settling velocity and can be used as a proxy for variation in Antarctic Coastal Current strength (Dunbar et al., 1985). This is supported by the covariance of sand percent with the MAR curves calculated by the radiocarbon age model

(Figure5.2 c,e).

The site traps biogenic material produced in the Dumont d'Urville polynya above the site (Arrigo and van Dijken, 2003), as well as biogenic material advected to the site from the Mertz Polynya to the east. While we do not have measurements to determine the biogenic contribution from each source, it is assumed local biogenic material dominates (Escutia et al., 2011). Large phytoplankton bloom events along Antarctica's coastal margins are suggested to be induced by a fresh meltwater layer originating from seasonal sea-ice melt, typically from December-March (Arrigo and van Dijken, 2003; Smith and Nelson, 1986). Diatom analysis of laminae from nearby cores interprets light laminae as biogenic bloom events, occurring during spring sea-ice retreat, which are rapidly exported to the seafloor (Denis et al., 2006; Maddison et al., 2012). Seasonal sea-ice break up in the region is strongly affected by changes in katabatic and zonal wind intensity (Massom et al., 2013).

The top and bottom of each light laminae bloom event were manually determined using X-ray Computed Tomography (CT) images and compared to statistical analysis on a greyscale curve extracted from the raw CT data (Figure 4.1). Comparisons to GRA bulk density, Natural Gamma Ray (NGR), XRF silica, XRF titanium, and the greyscale curve (Figure 4.2) show changes in the CT profile are primarily associated with changes in the composition of the laminae. This is further tested by independent time series analysis conducted on the greyscale and productivity indicators in the XRF data (Figure 5.3). To assess for potential biases introduced by the ^{14}C radiocarbon-based age model, laminae counts are binned into 1-meter intervals, as well as into 100-year intervals using the age model (Figure 4.4). $IPSO_{25}$ (Belt et al., 2016) data from U1357B, as well as diatom analysis from nearby core MD03-2601 are used to assess the influence of sea-ice conditions on sedimentology and bloom frequency. $IPSO_{25}$ is a proxy for fast ice (Belt et al., 2016), whereas increases in *Fragilariopsis curta* indicate cooler temperatures and later spring sea-ice melting (Crosta et al., 2007).

5.3 ENSO teleconnections with East Antarctic margin biological bloom events

The manual laminae counts do not indicate the presence of a persistent annual signal, but instead occur at 2-7-year intervals throughout the record, with distinct baseline shifts at the centennial- to millennial-scale (Figure 5.2 d). These subdecadal frequencies, as well as the baseline shifts, are independently upheld by evolutionary spectral analysis of the both the CT-scan greyscale data and the XRF productivity ratio Si/Ti (Figure 5.3). Comparison of these

data with the MAR curve, $IPSO_{25}$, and diatom assemblage data indicate three distinct climate states in the Holocene which are also noted in other Antarctic records (Figure 5.2, 5.3, Figure 4.2) (Crosta et al., 2007; Verleyen et al., 2011).

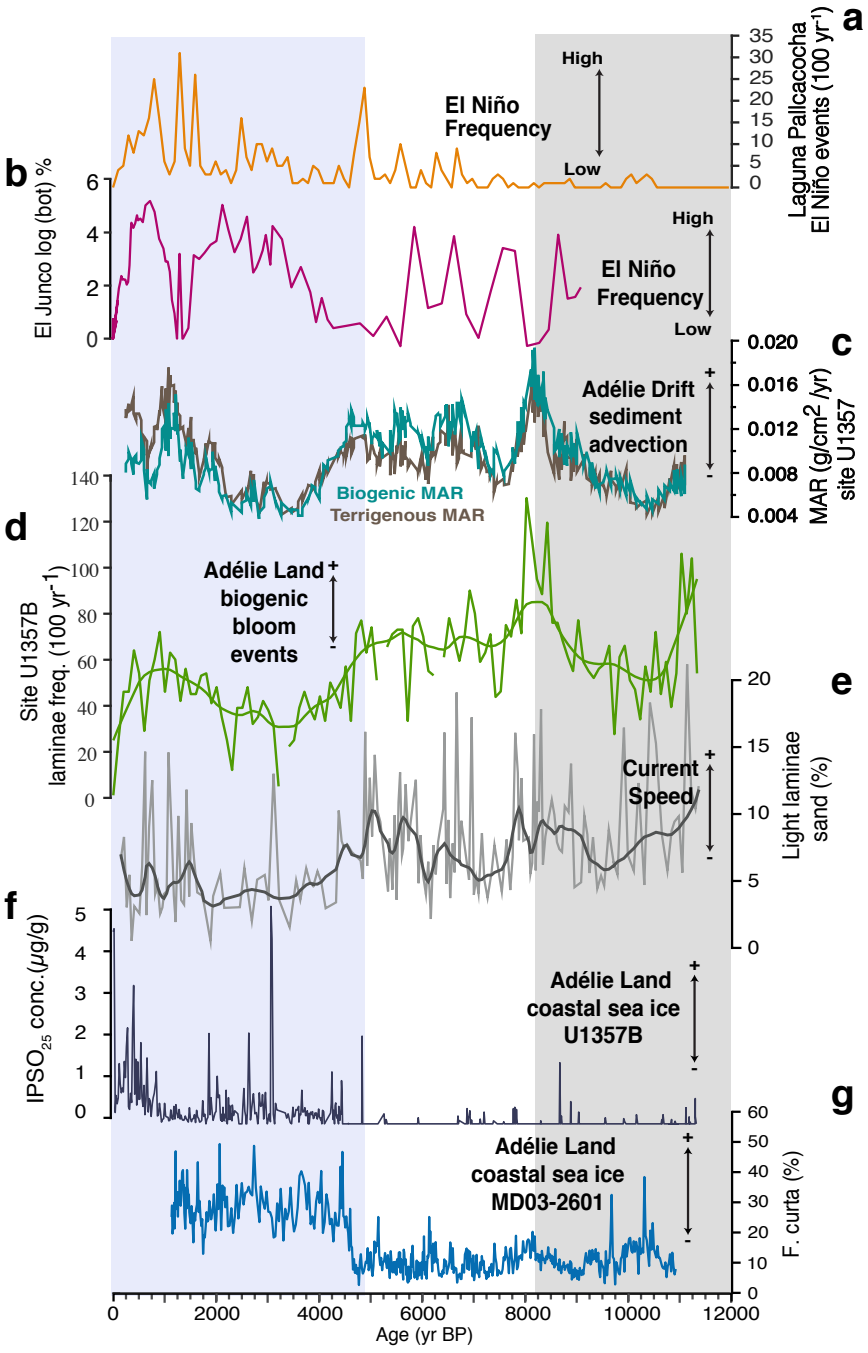

Figure 5.2: **Holocene proxy records illustrating potential climate forcing mechanisms in Adélie Land**. (a) Laguna Pallcacocha laminae record of El Niño frequency (b) El Junco lake *Botryococcus braunii* record of El Niño frequency (c) Mass Accumulation Rates from U1357B. Green is biogenic MAR, brown is terrigenous (d) Laminae frequency per 100 years at U1357B with an rlowess smoothing using 10% span of the data points (e) Sand percentage of the light laminae, which is representative of current speed (f) $IPSO_{25}$ concentration from U1357B, a proxy for fast-ice conditions (g) Percentage of *Fragilariopsis Curta* from MD03-2601, a diatom species indicative of coastal sea ice. Grey shaded band indicates the Early Holocene, while the blue band indicates the Neoglacial.

From 4.5 ka onwards, a baseline shift occurs making blooms less frequent relative to the overall record, but still occur at intervals consistent with modern day ENSO frequencies (Figure 5.2, 5.3). As ENSO impacts the physical drivers of bloom events (e.g. sea ice (Yuan, 2004) and zonal winds (L'Heureux and Thompson, 2006)), it is likely ENSO also impacts bloom frequency.

To assess how bloom events in the Adélie Land region are influenced by ENSO processes in the Holocene, we compared our results to the El Junco lake *Botryococcus braunii* record from the Galapagos Islands (Zhang et al., 2014) and the laminated sediment record from Laguna Pallcacocha in Ecuador (Moy et al., 2002) (Figure 5.2 a,b). *Botryococcus braunii* bloom after extreme rain events typical during an El Niño event and thus provide a proxy for El Niño frequency (Zhang et al., 2014), while Laguna Pallcacocha identifies El Niño events as anomalously high rainfall events that increase sediment load into the basin, creating light laminae (Moy et al., 2002). To compare these records, the datasets are binned into 100-year intervals (Figure 5.2 a,d), although we note higher resolution signals can be identified at site U1357B (Figure 5.3). Although these are El Niño proxies, due to uncertainties in how El Niño teleconnections manifest themselves in Adélie Land, we use them to broadly infer increases in ENSO frequency through the Holocene.

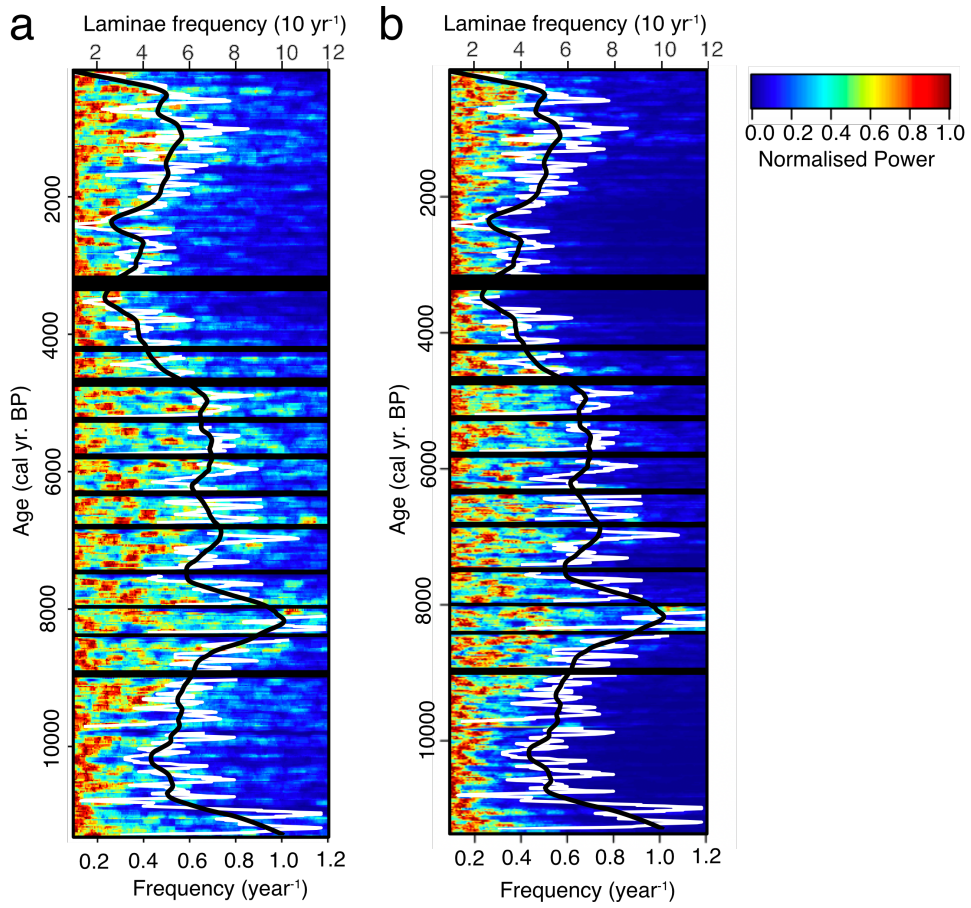

Figure 5.3: Evolutive harmonic analysis (EHA) of the (a)greyscale data and (b) XRF Si/Ti productivity proxies. Both plot are overlain with laminae frequency per 10 years (white and black) curves. Normalized power is similar across both proxies, showing a distinct shift to fewer bloom events and reduced productivity at 4.5 ka. Manual laminae counts binned at 10-year intervals are consistent with the EHA and display higher frequency shifts in bloom events than shown in the 100-year binned record. The white curve is the 10-year binned record smoothed in a 5 point moving mean, while the black curve is an robust lowess smoothing, using a 5% span of the unsmoothed 10-year binned record. The black boxes indicate core gaps.

5.3.1 Early Holocene (11.4 ka - 8 ka) – local deglaciation influences on bloom events

Bloom events reach a near annual frequency at 11.4 ka before passing into an interval of biennial bloom events (∼50 laminae per 100 years) between 10.8-9 ka. Bloom event frequency was highest at ∼8.2 ka, with one or more events occurring every year. The base of this sec-

tion is poorly sorted with IRD visible in the CT images (Figure 4.10), but IRD is largely absent in the CT images and grainsize frequency distributions after ∼11.3 ka (Figure 4.7). We attribute the high-frequency occurrences of the laminae peaks in this interval to freshwater pulses from the final phases of local EAIS retreat, with deglacial reconstructions indicating a calving bay re-entrant pattern, whereby ice retreats first in the bathymetric troughs, and later from the adjacent bathymetric highs (Mackintosh et al., 2014; Leventer et al., 2006). This is supported by the gradual declines in NGR and mean grain size, and gradual increased sorting of the detrital fraction upcore inferred to represent a declining glaciomarine sediment influence (Figure 4.2b, 4.10). The low MAR during this period may indicate less lateral advection of sediments as bathymetric highs were still ice-covered, restricting sediment advection from the east. However, the MAR reaches a peak at 8.2 ka indicating an increase of advected material as the local bathymetric highs fully deglaciated (Figure 5.2c). The high proportion of *Chaetoceros Hyalochaete* resting spores in diatom assemblages from nearby MD03-2601 indicate a more stratified and stabilized water column than in later parts of the Holocene, supporting the interpretation of enhanced glacial meltwater at this time (Crosta et al., 2008; Denis et al., 2009a). Highly stratified and nutrient-rich glacial meltwater (Gerringa et al., 2012) likely created favourable conditions for bloom events. Due to the dominance of a local, deglacial signal on sedimentation, we suggest that the relationship between ENSO and Adélie Land bloom events were overprinted by regional processes during this period.

5.3.2 Hypsithermal (8 – 4.5 ka) – increased coupling to far-field ENSO records

By ∼8 ka, U1357B sedimentation rates, grain size values and physical properties (e.g. NGR and CT density values) stabilise (Figure 5.2, Figure 4.2), consistent with regional interpretations that glacial retreat is largely complete in the region (Mackintosh et al., 2014). As proximal glaciomarine influences diminish, the potential for remote influences to modulate seasonal sea-ice melt processes and trigger short-duration periods of stratification is greater. During the Hypsithermal, bloom events occur every ∼1-2 years. Sea-ice reconstruction from *F. curta* in nearby MD03-2601 along with $IPSO_{25}$ data from U1357B indicate low sea-ice duration and reduced fast ice cover during this period. A reduction in coastal sea ice reduces stratification, altering the nutrient delivery processes currently observed to trigger modern diatom blooms in the Mertz polynya (Shadwick et al., 2013). If the primary control on bloom events was the breakup and melting of fast ice, conditions were favourable for nearly biennial blooms. This is feasible in the relatively warmer climate state of the Hypsithermal (Crosta et al., 2008), as

coastal fast ice is reduced, and seasonal melt events are likely to be more frequent. Additionally, strong currents and high terrigenous sediment advection (Figure 5.2 c,e) occurred during this reduced sea-ice state, suggesting stronger wind speeds, which could further enhance nutrient delivery via wind-driven upwelling (Prezelin et al., 2000). Increased laminae frequency (Figure 5.2d) also corresponds to relatively low frequency and/or shifts in location of El Niño events (Zhang et al., 2014; Moy et al., 2002; Carré et al., 2014) (Figure 5.2a). Changes in mid-Holocene ENSO variance are difficult to reconcile amongst paleoclimate records, and may reflect spatial variations of ENSO (e.g. Central Pacific (CP) ENSO versus Eastern Pacific (EP) ENSO) whereby eastern Pacific records fail to capture CP ENSO events (Carré et al., 2014; Karamperidou et al., 2017). If ENSO affected bloom events during this period, these records suggest it potentially did so from the central Pacific, and on the background of a lower sea-ice state, whereby the threshold for breaking up sea ice and inducing a bloom event was lower.

5.3.3 Neoglacial (∼4.5 ka to present) – sea ice intensification and onset of modern ENSO variability

Around 4.5 ka a sharp shift occurs in all records, where the monsoon starts weakening, ENSO intensity and frequency increase, and bloom events occur at modern day ENSO frequencies of 2-7 years (Figure 5.2, Figure 5.3). The shift in MAR and laminae frequency coincides with a widespread shift in global climate at ∼5 ka (Marcott et al., 2013). It has previously been suggested that the onset of the modern ENSO system occurred close to or shortly after 4.5 ka (Carré et al., 2014). Laminae frequency tracks closely with the Laguna Pallcacocha record (Figure 2a) and the El Junco *Botryococcus braunii* record (Figure 5.2b). This relationship, as well as the 2-7-year frequency of biogenic bloom events during this period indicates ENSO became a strong control of coastal bloom events.

In Adélie Land, this shift is immediately preceded by an increase in sea-ice diatom occurrence and in $IPSO_{25}$ content (Belt et al., 2016; Crosta et al., 2008; Denis et al., 2010) (Figure 5.2f, g). An associated drop in biological productivity is expected with increased sea-ice cover, due to reduced light availability and shorter growing season (Denis et al., 2009b). Increased duration of sea ice and greater fast ice extent would also reduce the occurrence of bloom events, as sea ice breakup would occur less frequently, thereby reducing water stratification and nutrient delivery. Reduced MAR (Figure 5.2c) and sand percent (Figure 5.2e) suggest the influence of along slope currents on sediment advection are reduced as well. This is a presumed consequence of enhanced sea-ice coverage reducing the wind stress on the ocean surface and the vigour of the coastal current. A slowdown in sedimentation rate is also observed at nearby

core MD03-2601 (Figure 3.5).

5.4 Modern teleconnections and implications for future Antarctic coastal productivity under shifting sea ice state and subdecadal scale climate variability.

Studies on observational timescales have identified a link between ENSO and Antarctic sea-ice variability (Yuan, 2004). Regional sea-ice changes during ENSO events are largely driven by wind changes resulting from pressure anomalies, but these pressure anomalies also occur during changes in the SAM (Stammerjohn et al., 2008). Furthermore, ENSO impacts in East Antarctica are observed to be modulated by the phase of SAM, and when these modes are in phase with one another (negative SAM, El Niño), the greatest impact is in the austral summer (L'Heureux and Thompson, 2006; Fogt et al., 2011; Schneider et al., 2012). Impacts on the Adélie land region are less clear as ENSO studies focusing on this specific region (136 -142°E) are rare. Positive surface air temperature anomalies along coastal East Antarctic weather stations during the austral summer have a strong positive correlation with positive temperature and rainfall anomalies in the eastern Pacific, and negative SST and rainfall anomalies in the western Pacific (Schneider et al., 2012). Moreover, Rossby wave trains (Mo and Paegle, 2001) associated with CP El Niño events (Rodrigues et al., 2015), induce anomalously high poleward heat fluxes and onshore winds (Marshall and Thompson, 2016) near Adélie Land. Consequently, during an El Niño year, temperatures appear to be warmer in Adélie Land (DDU station in Figure 5.1) in the austral summer. Additionally, autumnal coastal sea-ice concentrations appear to be influenced by the phase of SAM, with warmer temperatures and negative sea-ice anomalies occurring during negative SAM (Clem et al., 2018). In a year with a negative SAM and an El Niño event amplifying one another, it is probable that less sea ice and warmer conditions prevail, creating favourable conditions to allow seasonal sea-ice melt and mass bloom events. However, when El Niño events are coupled with the Indian Ocean Dipole (IOD), a Rossby wave train directed at Adélie Land leads to increased sea-ice and colder meridional flows (Nuncio and Yuan, 2015). To unravel the ENSO mechanism and phasing affecting bloom events, focused studies on this region are needed.

Regardless of the uncertainties associated with teleconnection mechanisms discussed above, our record shows mass biogenic bloom events in the coastal polynyas of Adélie Land, East Antarctica are strongly modulated by ENSO throughout the Holocene. Importantly, shifting

biological responses to large background shifts in climate and sea-ice state indicate tipping points exist in the system that influence the magnitude of these teleconnections. Changing seasonality of coastal sea ice and shifts in zonal winds are observed to be modulated by ENSO under modern conditions, and it is likely a combination of these interlinked factors causing ENSO-induced biogenic blooms. However, with uncertainties in future trends of sea-ice concentrations (Parkinson, 2019) and SAM phasing (Thompson et al., 2011) over coming decades, alongside projections of increasing ENSO frequencies (Cai et al., 2014a) and enhanced IOD activity (Cai et al., 2014b) we are entering a non-analogue state compared to other climate shifts noted in the Holocene. Adélie Land climate anomalies associated with tropical climate modes differ among reanalysis studies (Nuncio and Yuan, 2015; Schneider et al., 2012; Marshall and Thompson, 2016; Ciasto et al., 2015) while climate models also struggle to capture recent sea ice trends, due to the complexities of ocean and atmospheric feedbacks in the Antarctic (IPCC, 2019). Consequently, critical processes appear to be underrepresented in models used to project the future response of Antarctic coastal systems to increased tropical variability. Our data highlights the importance of sea ice tipping points in regulating ENSO's impact on biological productivity along Adélie Land's coastal marine margin. If sea ice continues to decline (Parkinson, 2019), our results suggest a greatly enhanced response to ENSO forcing and more frequent bloom events. This may have profound implications for foodwebs in the Antarctic, as well as carbon cycling process in the Southern Ocean.

Chapter 6

Abrupt change in the Ross Sea and Adélie Land regions

6.1 Introduction

Exported bottom water from the Ross Sea and Adélie Land Region is estimated to contribute up to 25% of all AABW (Rintoul, 1998), in part due the Ross Sea and Mertz Polynyas acting as sea ice factories and altering surface water masses to form precursor water masses for AABW formation (Chapter 2). In recent decades, freshening of shelf waters due to ice sheet and seasonal sea ice melt, and changing precipitation patterns, are linked to freshening of Ross Sea Bottom Water (Jacobs et al., 2002), which may have important implications on density driven global thermohaline circulation (Chapter 2). Ice shelf retreat is primarily driven by ocean warming, through the wind driven upwelling of mCDW and production of HSSW during sea ice formation (Section 2.3.2). Upwelling of mCDW is also thought to be an important source of nutrients that drive phytoplankton activity in the Ross Sea and Adélie Land regions (Sedwick et al., 2011; Moreau et al., 2019). The interconnectedness and feedbacks associated with these systems affect the global carbon cycle and ocean circulation, and potentially have tipping points that disrupt these systems (Chapters 1,5). However, modern day observations of these systems are sparse, and short-lived measurement campaigns (seasonal to yearly) are too limited in resolution to provide insight into long term responses of abrupt climate change.

A tipping point for rapid deglaciation of the West Antarctic Ice Sheet (WAIS) (IPCC, 2019), may be the loss of the Ross Ice Shelf, which models show is a percursory event to the collapse of the WAIS (Mercer, 1978; Pollard and DeConto, 2009). The deglacial history of the Ross Ice Shelf (RIS) is subject to debate given conflicting hypotheses on the pattern and timing of

retreat, as well as the lack of reliable age constraints on existing paleoclimate records (Conway et al., 1999; McKay et al., 2016; Lee et al., 2017; Golledge et al., 2014; Lowry et al., 2019). However, there is support from onshore records and modelling studies to suggest the RIS retreat happened in stages, with quiescent periods followed by pulses of rapid retreat over millennial timescales (Halberstadt et al., 2016; Spector et al., 2017). While the timing and pattern of the RIS is unclear, the release of freshwater from breakup and retreat of the RIS would not only impact sea ice conditions and productivity changes in the Ross Sea, it could also have downstream affects in the Adélie Land region due to surface water transport (Ashley et al.,*in review*).

Integrated paleoclimate reconstructions of the Ross Sea and Adélie Land regions during the Holocene provide a unique opportunity to assess the long-term response and regional variations in climate during times of ice sheet retreat. In particular, integration of the RICE ice core and U1357B sediment core provides a unique opportunity in that U1357B is the first sediment core that has a resolution equivalent to that of an ice core. However, integrating paleoclimate records are difficult due to differences in age model construction, and the uncertainties associated with each age model. There is the potential for volcanic ash layers or meteorite impacts to provide well-dated contemporaneous 'tie points', to circumvent these age uncertainties, but these have not yet been identified in the RICE and U1357B records. Furthermore, while these ice and sediment records are both able to provide information about sea ice extent or primary productivity, the underlying proxies are different. This is particularly relevant for sea ice reconstructions. While sediment core records can provide a site specific measure of these proxies, ice cores are reliant on transport processes and provide a regional view (Abram et al., 2013). This makes interpretations of core-to-core correlations difficult and is identified within the wider palecolimate community as a limitation for paleo-sea ice reconstructions (Thomas et al., 2019).

Despite these limitations, integrated reconstructions improve spatial coverage and provide a more robust measure of changing primary productivity, sea ice extent, and wind strength by incorporating multiple measures of change. Here, a first order attempt at integrating these marine and ice core records is made by looking at abrupt change on the millennial to centennial timescales. I investigate the timing of phasing of abrupt change in the Holocene histories of U1357B, RICE, Talos Dome (TALDICE), and Taylor Dome (Figure 6.1) and place them in the context of the Ross Ice Shelf retreat history. This provides records from the eastern Ross Sea, western Ross Embayment, and Wilkes Land Margin to capture the downstream effects of ice sheet retreat. The ice core records provide a measure of sea salt aerosols which have been used to infer sea ice extent (Abram et al., 2013; Severi et al., 2017; Schüpbach et al., 2013), and

non-sea-salt aerosols are used to quantify the strength of atmospheric circulation (Dixon et al., 2012; Röthlisberger et al., 2002; Schüpbach et al., 2013). MSA^- is an indicator of biological productivity, though its relationship to sea ice varies by location (Abram et al., 2013). Isotopic deuterium (δD) data are primarily indicative of temperature changes, but can be influenced by changes in sea ice extent, elevation, and transport pathways or source regions. Lastly, the laminae record and sand percentage record provide downstream current and polynya activity information, which are inferred to be influenced by the breakup and retreat of the RIS. These proxies provide a regional context of changing environmental Holocene conditions, and in turn are used to discuss the timing and pattern RIS grounding line retreat.

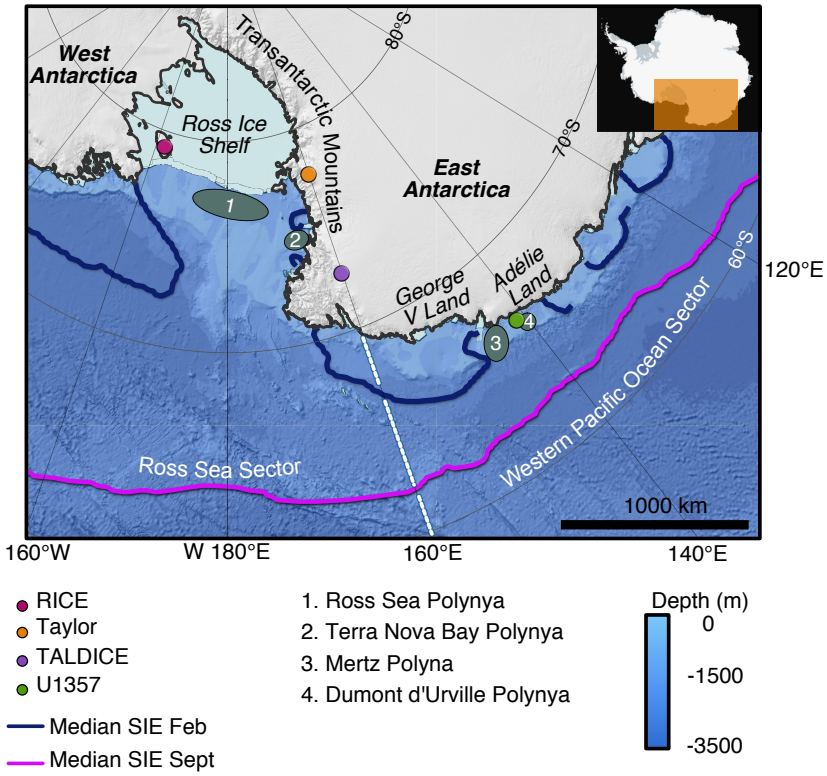

Figure 6.1: **Study location and setting** RICE ice core (pink), Taylor Dome ice core (orange), TALDICE (purple) ice core, U1357B sediment core (green). Approximate location of relevant polynyas indicated by green ellipses and numbered (Arrigo and van Dijken, 2003). Median sea ice extent (1981-2010) for February (navy blue) and September (pink) from (Fetterer et al., 2017). White dotted line indicates separation between Ross Sea and Western Pacific Ocean sectors.

6.2 Data

To compare the RICE and Adélie sediment core, these records are placed in the broader context of the Ross Sea Region and include two additional Holocene records from the Taylor Dome ice core and TALDICE. I restrict the analysis to include δD, ssNa^{+}, nssCa^{2+}, and MSA^{-} data for Taylor Dome and TALDICE (Table 6.1). Most of these records presented in this compilation have been previously published, with the exception of new data presented in this thesis, the complete Holocene RICE CFA Ca^{2+} record provided by Paul Vallelonga (University of Copenhagen, Denmark), and the TALDICE MSA^{-} record which was provided by Rita Traversi (University of Florence, Italy).

		RICE	Taylor Dome	TALDICE	U1357B
Site Information	Coordinates	161.71°W, 79.36°S	158.72°E, 77.8°S	159.18°E, 72.82°S	140.43°E, 66.41°S
	Elevation/Depth	550 (masl)	2365 (masl)	2315 (masl)	1017 (mbsl)
	Dist. from Coast (km)$^{+}$	90	125	260	35
	Dist. from Winter Sea Ice Limit (km)$^{+}$	1800	1700	1250	425
Age Model	Max and *Mean* Uncertainty	185, *85*	*250 (0-6 ka BP BP), 500 (>6 ka BP BP)*	315	268, *160*
	Reference	Lee et al. (2018)	Baggenstos et al. (2018)*	Severi et al. (2012) Bazin et al. (2013)	Dunbar et al. (in prep)
δD	Mean Holocene Resolution (yrs)	1	34	18	
	Reference	Bertler et al., *in prep.*	Steig et al. (1998)	Mezgec et al. (2017)	
Major Ion	Type	Ca^{2+}	$ssNa^{+}$, *MSA^{-}*	$ssNa^{+}$, $nssCa^{2+}$, *MSA^{-}*
	Mean Holocene Resolution (yrs)	0.4	5.7, *26*	17.4, *19*
	Reference	Kjær et al. (2016)	Stager and Mayewski (1997) Mayewski et al. (1996) Steig et al. (2000)	Mezgec et al. (2017) *Provided by Rita Traversi*

*Age error estimation based off delta age uncertainty used to calculate the ice age in Holocene (Monnin et al., 2004)
$^{+}$ Distances are approximate. Winter sea ice extent refers to median September sea ice extent (1981-2010)(Fetterer et al., 2017)

Table 6.1: Holocene data sets

To eliminate the influence of age model uncertainties when comparing the records, the δD and major ion data for each ice core record were binned into 100-year intervals and the mean value of each bin was used for analysis. The 100-year intervals also enable easy comparison to the 100-year binned laminae data from U1357. Moreover, sea ice proxies from ice cores may be more reliable on the centennial scale, when short term circulation changes are less likely to bias the interpretation (Abram et al., 2013).

While the Adélie and RICE records (laminae counts, light laminae sand percent, $IPSO_{25}$, and δD and Ca^{2+}, respectively) used in this chapter have been discussed in detail in Chapters 3, 4, and 5, the Taylor Dome and TALDICE records and site specific proxy interpretations are briefly described.

6.2.1 Taylor Dome

Taylor Dome is located approximately 125 km from the coast in the western Ross Sea, interior to the Transantarctic Mountains at the margin of the East Antarctic Ice Sheet (Steig et al., 1998). The 554 m ice core was drilled in 1994 and contains ice from marine isotope stages 6 and 7 (Steig et al., 2000).

The Taylor Dome age model was recently updated based on new data from Taylor Glacier which shifted the age of the Holocene record by up to 1,500 years (Baggenstos et al., 2018). The previously published MSA^- and $ssNa^+$ data (Stager and Mayewski, 1997; Mayewski et al., 1996; Steig et al., 2000, 1998; Mezgec et al., 2017) were updated to the new age model in this thesis by linearly interpolating the depth of these samples to the new model.

6.2.2 Talos Dome

Talos Dome is located in East Antarctica, around 260 km northwest of the Ross Sea and 300 km from the George V Land coast. Most of the 1620 m core was drilled during the 2006-2007 season. Talos Dome is unique in that it is influenced by air masses from both the Western Pacific/Eastern Indian ocean and Ross Sea sector (Mezgec et al., 2017; Scarchilli et al., 2011; Stenni et al., 2011). While these different sources sometimes make it difficult to discern contributions from either location, this core provides an atmospheric tie point between the Adélie sediment record and Ross Sea region.

The δD, $ssNa^+$, and $nssCa^{2+}$ data have been published and interpreted previously (e.g. Stenni et al., 2011; Severi et al., 2017; Mezgec et al., 2017). The Holocene MSA^- data have been partially published in Poluianov et al. (2014), and MSA^- data from the past 140 years has

been published and interpreted by Becagli et al. (2009).

6.2.3 Site specific MSA^- interpretations

Methylsulfonic acid (MSA^-) is an indicator of biological activity, and therefore an indicator of polynya activity, sea ice extent, and open ocean conditions. The Ross Sea region is one of the largest sources of MSA^- in Antarctica due to the dominant species of phytoplankton emitting high concentrations of dimethysulfide, a precursor to MSA^-, in the Ross Sea Polynya (DiTullio and Smith, 1995; Abram et al., 2013). MSA^- is volatile and several studies have used it to reconstruct sea ice, but its relationship to sea ice extent varies with the location of the core site (Abram et al., 2013; De Vernal et al., 2013).

While MSA^- at Taylor Dome has been suggested to be related to winter sea ice cover as decreasing δD corresponds to an increasing MSA^- (Steig et al., 1998), another satellite-based study showed no relationship between sea ice extent and MSA^- (Welch et al., 1993). Even though the latter study was based on a limited data set (<20 years), more recent studies from cores and snow pit samples taken near the Ross Sea, show MSA^- correlates significantly with biological activity, meaning that higher concentrations of MSA^- are indicative of a larger polynya, and thus more open water and less sea ice (Kreutz et al., 2000; Rhodes et al., 2009, 2012; Abram et al., 2013). Here, MSA^- at Taylor Dome is interpreted to primarily reflect productivity in open water conditions.

As RICE is located near areas of extensive summer sea ice and polynya activity, MSA^- at RICE is interpreted to reflect primary productivity due to open water in the summer.

MSA^- at Talos Dome has been correlated to positive sea ice anomalies in the Ross Sea (Becagli et al., 2009), due to enhanced productivity after years with increased winter sea ice extent (Abram et al., 2013). However, increases in MSA^- are also related to the strength of atmospheric transport, which must be considered when interpreting the record (Becagli et al., 2009).

6.3 A multiproxy reconstruction

6.3.1 The Holocene

Temperature, sea ice extent, atmospheric transport/wind strength, and productivity proxies are compared at the four locations, where available (Figure 6.2). Temperature and/or elevation changes are identified through δD records at RICE, Taylor Dome, and TALDICE. Sea

ice extent is measured through $ssNa^{+}$ aerosols at Taylor Dome and TALDICE, whereas fast ice presence is measured using the $IPSO_{25}$ concentrations at U1357. Wind strength is inferred from Ca^{2+} concentrations at RICE (Chapter 3), $nssCa^{2+}$ concentrations at TALDICE, and inferred from the current strength proxy at U1357B (light laminae 36-125 μm mean grain size) which is influenced by wind (Chapter 4). Productivity is measured using MSA^{-} concentrations at TALDICE, Taylor Dome, RICE, and laminae frequency at U1357B. While the full Holocene RICE MSA^{-} record has not yet been measured, the portion measured in this thesis (Chapter 3) helps interpret Ross Sea productivity in the Early Holocene.

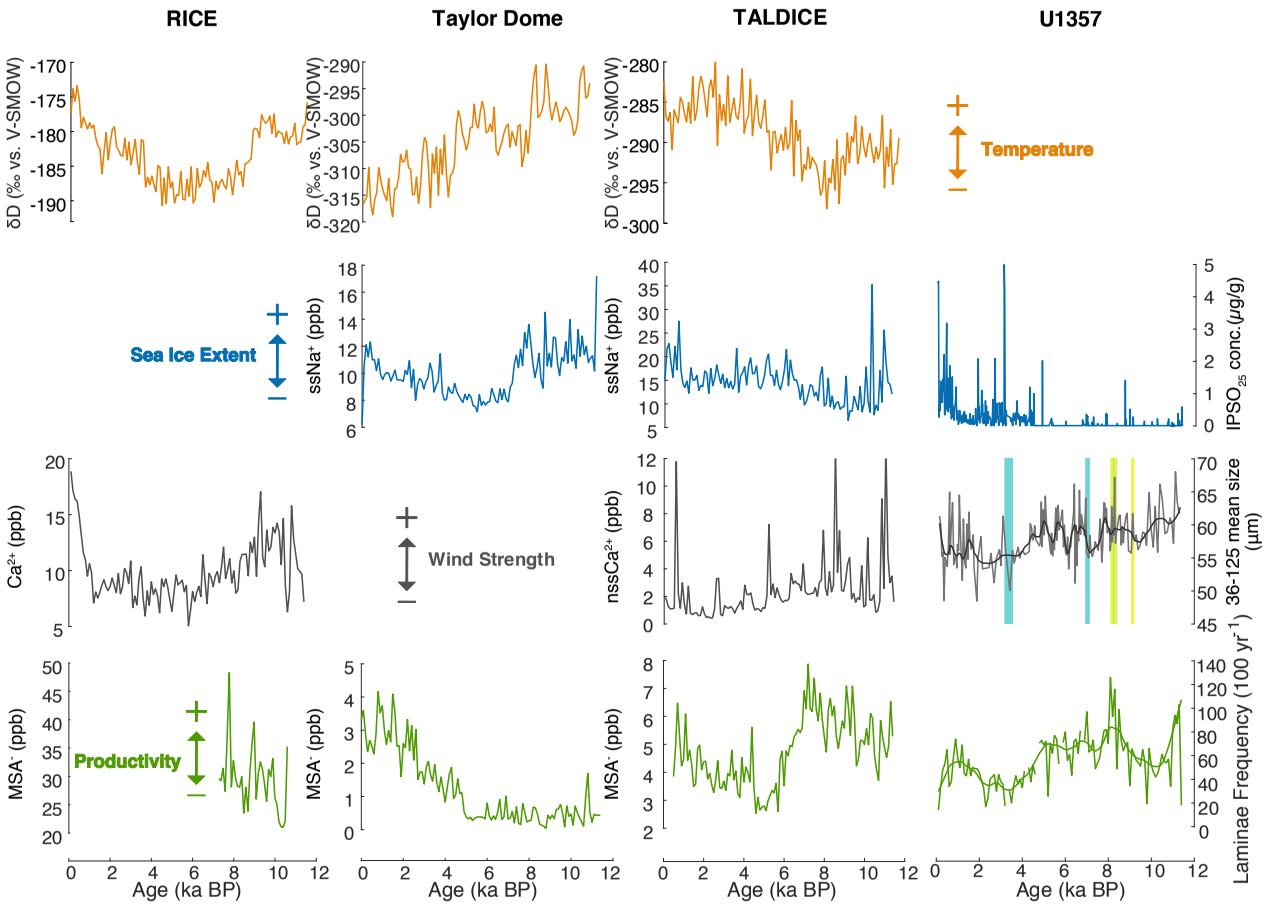

Figure 6.2: **Holocene Proxy Compilation** Left to Right: RICE, Taylor Dome, TALDICE, and U1357. Top row (orange) are temperature proxies including δD records from RICE, Taylor Dome, and TALDICE. Second row (blue) are sea ice proxies including $ssNa^{+}$ records from Taylor Dome and TALDICE, with the $IPSO_{25}$ record from U1357B. Third row (grey) are wind strength proxies, including Ca^{2+} from RICE, $nssCa^{2+}$ from TALDICE, and light laminae 36-125 μm mean grain size from U1357B. Last row (green) are productivity proxies, including MSA^{-} from RICE, Taylor Dome, and TALDICE, and laminae counts from U1357B. All ice core records and the laminae record are binned into 100 year intervals. Bold lines on laminae counts and light laminae 36-125 μm mean grain size are an robust LOESS smoothing using a 10% span of the data.

At RICE, Ca^{2+} follows a similar trend to that of the δD. Concentrations are slightly elevated in the Early Holocene, depressed during the Hypsithermal, and then rise in the Neoglacial. Both the δD and Ca^{2+} show a rapid increase ∼1 ka BP. The RICE MSA^{-} record shows a lull in productivity around 10 ka BP, followed by peaks at ∼8.9 ka BP and 7.8 ka BP.

At Taylor Dome, the Early Holocene is marked by increased sea ice extent and reduced productivity. Sea ice extent remains elevated during the transition to the Hypsithermal, but sharply decreases between 8 and 6 ka BP offshore. Productivity remains low during the Hypsithermal, but gradually begins to increase at ∼5ka BP. During the Neoglacial, sea ice extent increases gradually, while productivity continues to ramp up with another large increase at ∼2 ka BP.

At TALDICE, sea ice extent is briefly elevated in the Early Holocene before decreasing to its lowest value. $nssCa^{2+}$ values are elevated, and productivity is high. During the Hypsithermal, sea ice extent gradually increases with a concomitant decrease in $nssCa^{2+}$ and a sharp decrease in productivity at ∼7ka BP. The Neoglacial is marked by a fairly steady concentration of $ssNa^{+}$, with a large increase at ∼1 ka BP. Productivity sharply increases during the Neoglacial, whereas wind strength remains low, but like $ssNa^{+}$, both records show a sharp increase at ∼1 ka BP.

6.3.2 Holocene changepoints

There are marked shifts in the ice core isotopes and ion records, as well as the Adélie sediment core record. These shifts appear to occur at similar times in the records (within <500 years) and may be indicative of regional climate change or global Holocene climate transitions (Chapter 2). Thus, mean and slope changepoints in the various records are identified (see section 3.4) to help narrow down the timing of large shifts and gradual transitions in the records. The δD is chosen for the ice cores as this typically has the most straight forward climate interpretation. To compare the Adélie laminae frequency record with the ice core data, the productivity records (MSA^{-}) are used.

The δD and productivity (laminae frequency and MSA^{-}) data are assessed using 100-year data bins and simple resampling at finer time scales depending on timeseries resolution (1-year, 10-year, 20-year, 30-year, for RICE, U1357, TALDICE, and Taylor, respectively). The resolutions were varied to determine the most representative changepoint and to asses any bias introduced through smoothing. Due to the incomplete Holocene record, the RICE MSA^{-} record is not included.

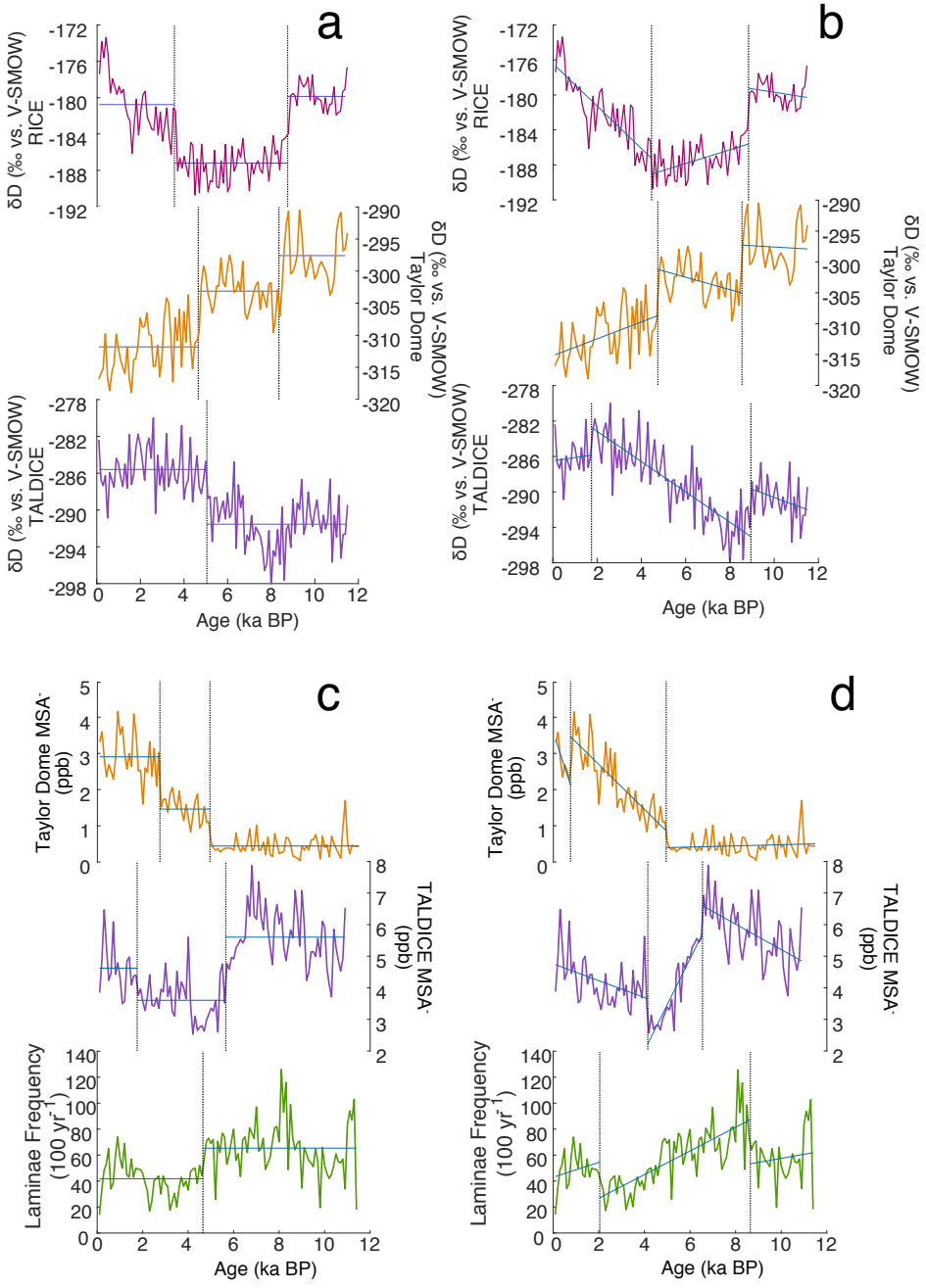

Figure 6.3: **Changepoints in Holocene δD and productivity records.** RICE (pink), Taylor Dome (orange), TALDICE (purple), U1357 (green). (a) δD mean changepoints, (b) δD slope changepoints, (c) Productivity mean changepoints, (d) Productivity slope changepoints. Data have been binned into 100-year intervals. Dotted lines indicate change points in each record, with solid blue horizontal lines showing the mean or line of best fit for that section.

For the mean changepoints in δD, both Taylor Dome and RICE have two distinct change points, while TALDICE only has one. For RICE, changepoints occur at ~8.8 and 3.6 ka BP, for Taylor Dome at ~8.5 and 4.7 ka BP, and at ~5.0 ka BP at TALDICE (Figure 6.3). The RICE δD record has elevated values prior to ~8.8 ka BP, which then decrease through to ~3.6ka BP, and increase afterwards. Taylor Dome shows a consistent, but stepped decrease in value over the Holocene. TALDICE has relatively low δD values with a marked change at 5.0 ka BP.

Changepoints in the slope of the δD records provide insight into the phasing of Holocene changes at each site. Taylor Dome slope changepoints occur at roughly the same time as the mean change, only leading the mean changepoints by ~100 years. Perhaps more interesting is the slightly increasing slope during from ~8.5 to 4.7 ka BP. The timing of the first slope changepoint at RICE is also quite similar to the first mean changepoint at RICE. However, the second slope changepoint begins at 4.4 ka BP, indicating the gradual warming in the Early Holocene started nearly 1,000 years before the mean δD changes. The slope changepoints at TALDICE are interesting in that there are two slope changepoints (8.9 and 1.7 ka BP), while there is only one mean changepoint (5.0 ka BP). Prior to 8.9 ka BP there is a gradual increasing trend, with a very large increasing trend between 8.9 to 1.7 ka BP before decreasing slightly at 1.7 ka BP.

Changepoints in the productivity proxies are also determined. For the mean changepoints, Taylor Dome shows a step-wise increase at 4.9 and 2.7 ka BP. TALIDCE indicates higher values prior to 6.1 ka BP, at which point the mean MSA^- value decreases substantially. At 2.2 ka BP, the mean value increases again. At Adélie, there is only one mean changepoint at 4.8 ka BP, with the mean value of laminae frequency lower from 4.8 ka BP onward.

The first slope changepoint for Taylor Dome productivity is at 4.9 ka BP, which coincides with the first mean changepoint at Taylor Dome. A second occurs at 0.7 ka BP coinciding with a sharp decline in MSA^-, but afterwards it slowly recovers. The changepoint at 0.7 ka BP does not exist in the more highly resolved record, therefore I do not consider it further. TALDICE indicates gradually increasing MSA^- values until 7.0 ka BP, followed by a large decline until 4.6 ka BP, at which point MSA^- values start increasing again. Slope changepoints of laminae frequency at U1357 are also quite different from the mean value changepoints in that there are two at 8.7 and 2.1 ka BP. From 8.7 ka BP, there is an overall decline in laminae frequency, until 2.1 ka BP, when laminae frequency starts slowly increasing.

Interestingly, both the mean and slope changepoints of TALDICE and laminae frequency at U1357 are closely aligned. This suggests these records are closely related, even though the TALDICE δD record reflects temperature, and laminae frequency reflects productivity.

A summary of the changepoints is presented in Table 6.2 for clarity.

	RICE	Taylor Dome	TALDICE	U1357
δD Mean	8.8, 3.6	8.5, 4.7	5.0	
δD Slope	*8.8, 4.4*	*8.5, 4.7*	*8.9, 1.7*	
MSA$^-$ or Laminae Freq. Mean		4.9, 2.7	6.1, 2.2	4.8
MSA$^-$ or Laminae Freq. Slope		*4.9, 0.7**	*7.0 , 4.6*	*8.7, 2.1*

*Only exists in the binned record

Table 6.2: Timing of changepoints at RICE, TALDICE, Taylor Dome, and U1357. All changepoints in years in ka BP

6.4 Abrupt shifts and multi-millennial variability in the Ross Sea and Adélie Land regions

All of the Holocene proxies show well defined, multi-millennial shifts in temperature, sea ice extent, wind strength and productivity at various phases throughout the Holocene, although there are several hundred year differences between sites. While age uncertainties associated with the various age models (Table 6.1) may contribute to these differences, it is also recognised that local environmental conditions can respond at different times.

Two distinct events are evident in all records. The first is between ∼8.9 and 8.5 ka BP, and is characterised by a step-wise change in the Ross Sea region, but a more gradual shift near TALDICE and Adélie Land region. The second shift happens between ∼5 and 4.5 ka BP. Within the age uncertainty of the records, these transitions are nearly synchronous (max. ±500, Table 6.1) to the global Early Holocene-Hypsithermal and Hypsithermal-Neoglacial transitions and highlight Antarctica's connectivity to the global climate system. While drivers of these climate periods (Early Holocene, Hypsithermal, and Neoglacial) have been identified globally (Chapter 2), this discussion focuses on the regional change, in response to these global drivers.

6.4.1 The Holocene environment prior to 9 ka BP

Radiocarbon dated foramanifera indicate the RIS grounding line was still located at outer continental shelf at the start of the Holocene in the easternmost Ross Sea (11.5 ± 0.3 ka BP) (Bart et al., 2018), but in the Western Ross Sea both the grounding and calving lines of the Ross Ice Shelf had retreated to near Ross Island by 8.6 ka BP (McKay et al., 2016). Model experiments that fit well with these data constraints, indicate grounding line retreat in the central Ross Sea could have initiated as early as 15 ka (McKay et al., 2016; Lowry et al., 2019). In Adélie Land,

the chronology of retreat is poorly constrained, but IODP Site U1537B indicates EAIS outlet glaciers had largely retreated by 11.4 ka, but local ice domes may persisted on the bathymetric highs to form a calving bay environment as late as 8 ka BP (Chapter 4, 5). Consequently, although exact timing of retreat is difficult to constrain, it is clear that this was period of residual ice dome retreat in Adélie Land, but a period of major grounding line retreat and opening up of oceanic waters with seasonal sea ice in the Ross Sea.

Elevated RICE and Taylor Dome δD measurements are characteristic of the Antarctic Early Holocene climate optimum seen in many ice and sediment cores (11.5-9 ka BP) (Masson et al., 2000; Steig et al., 2000; Verleyen et al., 2011). Increased concentrations of Ca^{2+} at RICE, suggest increased atmospheric transport (Chapter 3). The Taylor Dome record also shows elevated $ssNa^{+}$ concentrations during this period, suggesting an increase in sea ice. This seems counter-intuitive to the increased δD, as increased sea ice extent should lengthen the distance to the moisture source and deplete δD at Taylor Dome (Steig et al., 1998). The increase in $ssNa^{+}$ near Taylor Dome could reflect two different mechanisms. First, if increased atmospheric transport extended into the western Ross Sea, as is evident in the RICE record, this increase may partially reflect increased transport strength of $ssNa^{+}$ to Taylor Dome. Alternatively, the record could indeed reflect increased sea ice extent in direct response to the retreat of the grounded ice sheet in the Central to Western Ross Sea, resulting in closer proximity of seasonally open oceanic waters. An associated increase in meltwater produced during this period of grounding line retreat between 11.5 and 9 ka BP could also enhance stratification and potentially lead to increases in sea ice (Spector et al., 2017; McKay et al., 2016; Lee et al., 2017; Lowry et al., 2019; Bart et al., 2018).

Relatively low levels of MSA^{-} suggest relatively limited productivity at Taylor Dome compared to later intervals. This is consistent with the interpretation of widespread sea ice cover, and less open water areas during the summer, but geological data also indicates residual ice masses persisted until 7.6 ka in the Western Ross Sea, and were sourced from Transantarctic Mountains (Hall et al., 2013; Jones et al., 2015; McKay et al., 2016; Lee et al., 2017; Greenwood et al., 2018). At Taylor Dome, this would have resulted in a more distal source region of open ocean with seasonal sea ice, compared to later periods when these ice masses retreated. However, elevated MSA^{-} levels at RICE indicate productivity was occurring near that location. While the magnitude of productivity at RICE during this period relative to the entire Holocene is impossible to quantify relative to longer term trends, these values are similar to average values of the last 2,000 years (Brightley, 2017), and suggest open water existed in the Ross Embayment in the summer during this period. Productivity differences between the Eastern and Western Ross Sea could be associated with the presence of residual ice masses in the West-

ern Ross Sea, although icebergs associated with the breakup and retreat of the RIS could have also affected primary productivity and sea ice coverage in the Ross Sea, as has been observed in modern times (Robinson and Williams, 2012).

Although temperatures appear elevated at RICE and Taylor Dome, the δD at TALDICE is lower than at any other point in its record, but there is a slight warming trend up until ∼8.9 ka BP. While the TALDICE record suggests a small increase in sea ice extent at this time, the $IPSO_{25}$ does not reflect an increase in fast ice. TALDICE is influenced by air masses from the southwest Pacific/east Indian Ocean sector, as well as the Pacific/Ross Sea sector (Stenni et al., 2011; Albani et al., 2012; Scarchilli et al., 2011). The increased in $ssNa^+$ could reflect a contribution from the northwestern Ross Sea, in agreement with the Taylor Dome core which suggests elevated sea ice extent relative to Adélie Land in the western Ross Sea. However, transport from the Pacific Ross Sea sector is thought to have been reduced prior to the retreat of the RIS, with reorganization of transport pathways not occurring until after ∼8.2 ka BP (Albani et al., 2012; Stenni et al., 2011). Hence, changing atmospheric transport pathways does not fully explain the TALDICE record. Additionally, the TALDICE record shows an increase in productivity, which is not reflected in the western Ross Sea, but is observed in the Adélie record, suggesting transport from the southwest Pacific/East Indian sector is dominant. Elevated $nssCa^{2+}$ suggests increased transport strength, which aligns with the stronger currents along the Adélie Land coast. This indicates that the increase in $ssNa^+$ may better reflect the increase in transport strength at this time.

6.4.2 Early Holocene-Hypsithermal transition: Rapid change in the Ross Sea region between 9 and 8 ka BP

The end of the Early Holocene and transition into the Hypsithermal is marked by the first changepoint in the ice core δD records and correspond to reduced δD values at both Taylor Dome and RICE. The near synchronous change in both slope and mean of the δD values support the suggestion of an abrupt shift in the environmental conditions in the Ross Sea region. Starting at 8.8 ka BP, δD values rapidly decrease at RICE. While this could be related to a rapid cooling, comparison of the isotopic profile to various modelled elevation changes (Lowry et al., 2019; Golledge et al., 2014) during this period of the Holocene suggest only a modest decrease in temperature (Eling, 2019). At Taylor Dome, the step-wise reduction in δD is unlikely to be the result of elevation changes, and thus represents cooling entering the Hypsithermal (Steig et al., 1998). Sea ice appears to also decline during this period, as does wind strength at RICE. The apparent reduction in sea ice extent near Taylor Dome could be due in part to reduced

atmospheric transport, but diatom records in the western Ross Sea suggest this area remained ice free longer on a yearly basis (Mezgec et al., 2017). This is difficult to reconcile, as a longer ice free season would generally suggest warmer, and not cooler conditions.

The concurrent timing of change at Taylor Dome and RICE suggests a common or related mechanism. The elevation change at RICE coincides to a period of rapid thinning among coastal glaciers between 9-7.6 ka BP in the western and southwestern Ross Sea related to grounding line retreat (Jones et al., 2015; Spector et al., 2017). Foramanifera based radiocarbon ages also indicate open water conditions near Ross Island at 8.6 ± 0.25 ka BP (McKay et al., 2016). While Taylor Dome is not suggested to have been affected by elevation changes directly (Steig et al., 1998), regional circulation changes due to surrounding elevation changes, the RIS grounding line retreat, and the opening of the western and central Ross Sea could reconcile this difference. Trajectory models show that air masses reaching Taylor Dome are often displaced eastward by local circulation features in the Ross Sea and thus, cross over the Ross Ice Shelf before reaching Taylor Dome (Scarchilli et al., 2011). Therefore, any shift in the geometry of the RIS that leads to open water, or changing elevations around the Ross Sea likely affected circulation pathways towards Taylor Dome.

TALDICE responds differently at the Early Holocene-Hypsithermal transition with only a slight warming signature beginning at ∼8.9 ka BP and no discernible step-wise change. There is also a slight increase in $ssNa^+$ during this time, suggesting an increase in sea ice extent. This is not reflected in the U1357 $IPSO_{25}$ record. The apparent increase in sea ice extent is curious as this is not reflected at Taylor Dome either. Mezgec et al. (2017) argued that the $ssNa^+$ record was reflective of seasonal pack ice formed in deeper water, whereas the Taylor Dome $ssNa^+$ record is more representative of fast ice based on principal component analysis (PCA) with Ross Sea diatom records. However, care must be taken when using this interpretation, as not all of these diatom records resolve the entire Holocene and the sediment age models are far coarser with few dates (4) of acid-insoluble organic matter. These are also from very short cores with high potential for reworking of old carbon, as evidenced by core top ages of 3.8 ka, and these correlations were done using the old Taylor Dome age model. However, the Mezgec et al. (2017) interpretation is consistent with the discrepancy in sea ice records, with reduced fast ice conditions leading to low $ssNa^+$ and $IPSO_{25}$ concentrations at Taylor Dome and U1357, respectively, and increased seasonal pack ice conditions leading to elevated $ssNa^+$ at TALDICE. Winds at TALDICE also appear to decrease during the Hyspithermal. However, the suggested reorganization of atmospheric circulation due to the retreat of the RIS may have reduced transport over dust sources (Albani et al., 2012). Therefore, the reduction in wind strength may only be minor. This is in agreement with the Adélie Land record, where only a

minor reduction in current strength is noted.

Interestingly, MSA^- concentrations at TALDICE, peak at ∼7.2 ka BP which is almost 1000 years later than the laminae frequency peak at U1357, and is also reflected in the slope change-points of these proxies. However, the decrease in productivity at U1357 is much more gradual than that at TALDICE. The sharp drop at TALDICE could also be related to reorganization of atmospheric circulation, with TALDICE being more sensitive to air masses in the Ross Sea region as the ice sheet in the Ross Sea retreated. Given the relatively low productivity in the western Ross Sea, as indicated by the Taylor Dome MSA^- record, more air masses from the Ross Sea region could dilute the productivity signal from the western Pacific/Indian ocean sector, leading to an overall reduction in MSA^- concentration at TALDICE (Figure 6.4).

During the Hypsithermal, there appears to be two distinct environmental responses between the Ross Sea region and Wilkes Land margin. While there is a general cooling in the Ross Sea region, there is an apparent warming trend at TALDICE and near U1357 as well (Crosta et al., 2008). However, the cooling trend in the Ross Sea appears to be an artefact of continuing deglaciation, whereby elevation lowering and retreat of the RIS allowed air masses to intrude further south into the Ross Embayment. In addition, circulation features such as the Amundsen Sea Low (ASL) increasingly affect these inland sites, as the ice shelf and ice sheet progressively approached its modern configuration (Mayewski et al., 2013; Lachlan-cope et al., 2001). This reorganization affected both Taylor Dome and TALDICE (Figure 6.4). Indeed, the productivity records may indicate an increased coupling of TALDICE to the Ross Sea region, as the atmospheric transport from the Ross Sea region towards TALDICE increased (Stenni et al., 2011; Albani et al., 2012).

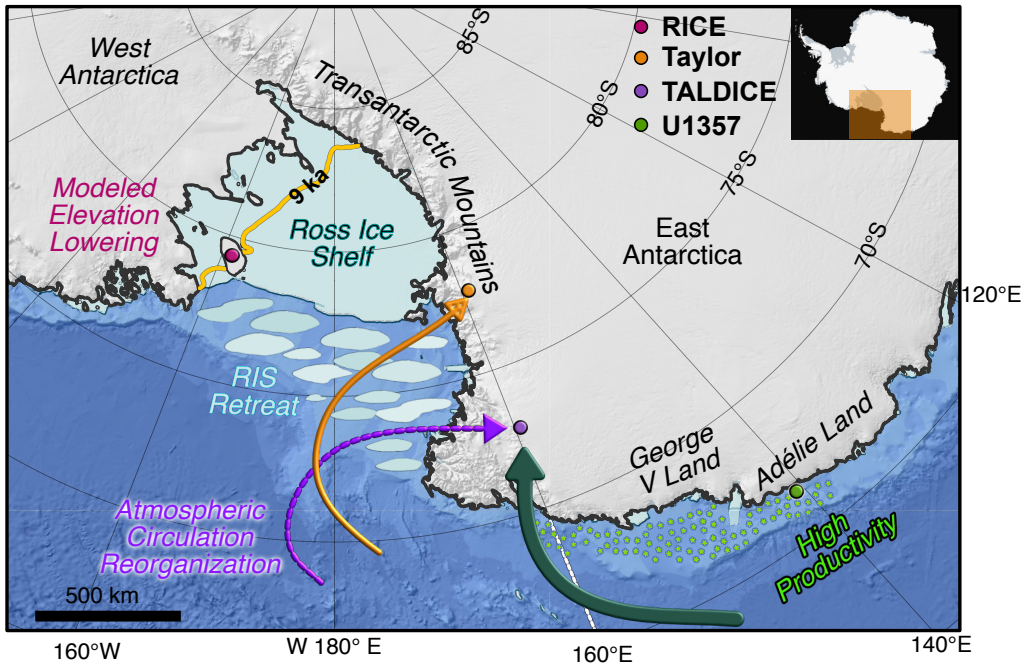

Figure 6.4: **Schematic of environmental change at 8.2 ka BP** RICE (pink circle), Taylor Dome (orange circle), TALDICE (purple circle), U1357 (green circle). Dominant atmospheric transport pathways shown in green, purple, and orange arrows, adapted from Scarchilli et al. (2011). Green arrow is predominant pathway for TALDICE, but purple becomes more common as RIS retreats, as does orange for Taylor Dome. Yellow line indicates modelled RIS grounding line from Lowry et al. (2019).

6.4.3 Hypsithermal to Neoglacial transition: A regional event

The Hypsithermal to Neoglacial transition marks another abrupt change in Ross Sea and Adélie Land Regions, with changes occurring in both the δD and/or productivity records at all locations. At 4.4 ka BP, temperatures begin to increase at RICE, with two sharp jumps at 1.5 and 0.5 ka BP. While wind strength appears to increase from around 4.4 ka BP onward as well, sharp shifts occur at 1.2 and 0.9 ka BP. The concomitant increase in temperature and wind strength suggest increased transport of warmer air masses from lower latitudes and reduced distance to open water.

At Taylor Dome, another step-wise cooling event occurs at 4.7 ka BP, which coincides with

a slight increase in sea ice extent. There is also sharp increase in productivity at 4.9 ka BP. Concomitant increases in sea ice extent and productivity could indicate stronger polynya activity (Mezgec et al., 2017). In the modern day, increased biological productivity is observed in the spring after winters with increased sea ice extent, and these records may also reflect this process (Venables et al., 2013; Saba et al., 2014). However, the increase in sea ice extent may have been limited to the coastal areas (Steig et al., 1998; Mezgec et al., 2017), and may not be reflective of sea ice conditions closer to the central Ross Sea Polynya. This could suggest these processes are decoupled. Regardless, increased biological productivity in the Ross Sea is evident at this time.

At TALDICE, temperature continues to increase up until around 1.7 ka BP. Sea ice extent gradually increases through the Neoglacial with a sea ice expansion in the last 1 ka BP. Wind strength declines slightly relative to the Hypsithermal, but increases sharply in the last 1 ka BP. Despite these environmental changes, MSA^- gradually increases throughout the neoglacial from 4.6 ka BP.

At U1357, a sharp increase in fast ice occurs from 4.5 ka BP onward, suggesting an overall deterioration in climate. As discussed in Chapter 5, this increase in sea ice extent is associated with a reduction in current strength due to reduced wind stress on the ocean surface and an overall decrease in productivity.

The relatively simultaneous change in δD at RICE and Taylor Dome, increasing MSA^- values at Taylor Dome and TALDICE, and rapid increase in fast ice extent, and subsequent decline in laminae frequency suggests an abrupt change affecting atmospheric, oceanic, and biologic systems. The increase in sea ice extent at U1357, TALDICE, and Taylor Dome post 4.5 ka BP is contrary to the mid-late Holocene climate optimum in other East Antarctic and Peninsular records which saw reduced sea ice in these regions (Verleyen et al., 2011; Bentley et al., 2009). This suggests a more regional change in the Ross Sea and Adélie Land regions and that U1357 is highly sensitive to conditions in the Ross Sea, rather than areas further west.

Data and model simulations suggest grounding line retreat to the South of Ross Island was ongoing between 8.6 and 0 ka BP in the Ross Sea (Spector et al., 2017; Lowry et al., 2019). While open marine foraminifera were deposited in sediments at the modern day calving line of the Ross Ice Shelf at 8.6 ka, onshore cosmogenic records indicate the grounding line continued retreating into the Late Holocene. These cosmogenic data indicate outlet glaciers feeding into the Ross Ice Shelf were still thinning up to ∼3.4 ka BP, and infer it was at this time that the RIS grounding line reached its modern day position (Spector et al., 2017). In contrast, Yokoyama et al. (2016) suggested widespread collapse of the RIS through 1.5 ka BP primarily along the western edge of the Ross Sea. However, this study used ^{10}Be concentrations to distinguish

between open water and sub-ice shelf environments, and others have suggested that more work is needed to confidently interpret ^{10}Be concentrations in sub ice-shelf environments (White et al., 2019).

The increase in sea ice extent during this period could be in direct response to freshening of surface waters due the final stages of the RIS grounding line retreat. Surface waters from the Ross sea take less than a year to reach the Adélie Land region due to fast coastal currents, suggesting changes in surface water properties between the site would be near immediate in the context of the paleoclimate record. However, the suggestion that glacial meltwater is responsible for the shift in sea ice state conflicts with the paleoclimate records which consistently show a sustained shift in sea ice state and no substantial reduction post 3.4 ka BP, when the grounding line is thought to have reached its current location. Decreasing meltwater contributions at Adélie Land around 4.5 ka BP, believed to be sourced from the Ross Sea as local sources are unlikely to exist (see Chapter 3), do not support the theory of continued deglaciation and ice shelf collapse through 1.5 ka BP either (Ashley et al., *in review*). In order for sea ice extent to remain elevated well after meltwater contributions taper off, a sustained forcing must exist.

The northward position of the modern calving line relative to the grounding line infers the formation of the modern ice shelf cavity occurred sometime between 8.6 ka BP and 3.4 ka BP. Modelling studies suggest that formation of large 'cold' sub ice-shelf cavities lead to cooling and freshening of Antarctic surface water, driving sea ice production in the immediate vicinity and along downstream pathways (Hellmer, 2004). Using compound specific isotope on fatty acids derived from marine algae, combined with modelling experiments, (Ashley et al., *in review*) propose that the Ross Ice Shelf reached a critical threshold size whereby waters began to circulate beneath it for long enough forming extremely fresh ice shelf water and once these waters reemerged from the cavity they triggered enhanced sea ice in the Ross Sea and Adélie Land regions. Site specific simulations of the freshening of Antarctic surface water in response to the formation of the sub-ice shelf cavity are able to explain the increase seen in sea ice extent near Taylor Dome, TALDICE, and downstream from the Ross Sea in the Adélie Land region (Ashley et al., *in review*).

While the Early Holocene-Hypsithermal transition marked increased sensitivity of TALDICE to the Ross Sea region, the transition at 4.5 ka BP is supportive of the increased sensitivity of U1357 to Ross Sea change and ice shelf cavity expansion at this time, and is consistent with the establishment of the modern relationship between these two locations (Figure 6.5). Additionally, the increased influence of the ASL (Mayewski et al., 2013) would be ongoing during this period as the RIS approached its modern configuration, and air masses intruding further west into the Ross Sea would be able to reach Taylor Dome.

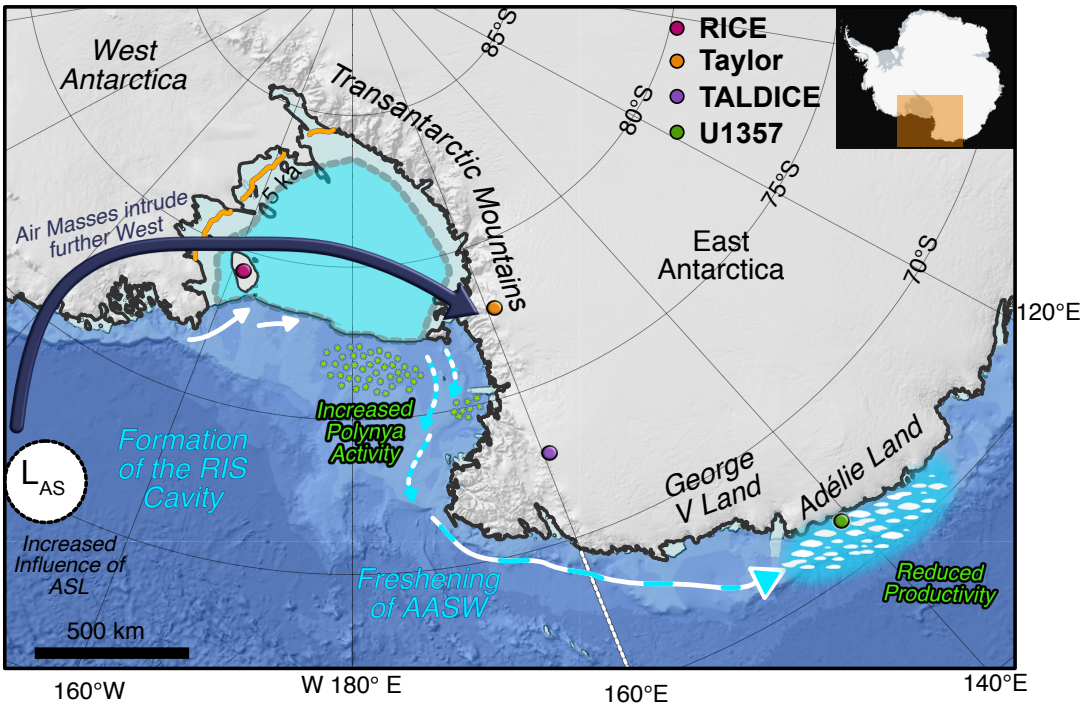

Figure 6.5: **Schematic of environmental change at 4.5 ka BP** RICE (pink circle), Taylor Dome (orange circle), TALDICE (purple circle), U1357 (green circle). Atmospheric transport pathways (orange, purple, and green arrows not shown) same as Figure 6.4, however, additional navy arrow indicates increased transport to Taylor Dome from areas further east, adapted from Scarchilli et al. (2011). Consistent Amundsen Sea Low influence as ice sheet reaches modern configuration (Mayewski et al., 2013). Simplified transport of Antarctic surface waters (white). Formation of RIS cavity (cyan) and modified Antarctic surface waters (striped) arrows, lead to increased sea ice extent in Adélie Land. Orange line indicates modelled RIS grounding line from Lowry et al. (2019).

6.4.4 A unique link between TALDICE and Adélie Land

A unique relationship appears to exist between the δD at TALDICE and laminae frequency at U1357. The mean and slope changepoints are near simultaneous, but in opposite directions. Generally, as TALDICE warms, bloom events become less frequent along the Adélie Land coast. The lack of coherency between sea ice records at TALDICE and Adélie Land, suggest that this relationship is not driven by sea ice conditions. Instead, this relationship appears to be related to atmospheric transport and the opening of the Ross Sea Embayment. Wind proxy records from both TALDICE and U1357 follow similar trends throughout the Holocene. However, increased

windiness at TALDICE (higher nssCa^{2+}) is associated with cooler temperatures, whereas increased windiness (higher 36-125μm mean grain size) at U1357 is linked to more frequent blooms. Whether this relationship is solely due to changes in westerly or katabatic winds is difficult to deconvolve. The increasing trend of δD has been suggested to occur due to the ongoing retreat of the RIS, and increased contributions of Ross Sea air masses (Albani et al., 2012). It is possible that as the Ross Sea Embayment opened up, the reorganization of atmospheric circulation enabled a gradual warming along the eastern portion of east Antarctica. This gradual warming would reduce the temperature and density gradient that drives katabatic winds, weakening a key driver of phytoplankton blooms (see Chapter 5). While U1357 is nearly 1,000 km northwest of TALDICE, persistent katabatics flow from this area down towards the Mertz glacier (Parish and Bromwich, 1987). Alternatively, if weakening of the westerly winds solely affects the air mass source at TALDICE and has no effect on katabatics at Adélie Land, weakening of westerly winds throughout the region would still result in fewer blooms.

6.5 Conclusion

Ross Sea and Adélie Land paleoclimate records are used to assess the sensitivity of the region to RIS retreat through the Holocene. The RICE, Taylor Dome, TALDICE, and U1357 record all show distinct, large-scale shifts between ∼8.9-8.5 ka BP and ∼5-4.5 ka BP. These large-scale shifts are attributed to the retreat of the Ross Ice Shelf and the opening up of the Ross Sea Embayment, and reflect the reorganization of atmospheric and oceanography systems during the Holocene.

The first step-wise transition at ∼8.9-8.5 reflects the regional reorganization of atmospheric circulation as ice sheets deflated and the Ross Embayment opened up. This altered transport pathways at both Taylor Dome and TALDICE. While the change at RICE and Taylor Dome may support the theory of rapid removal of ice from the Ross Sea (Anderson et al., 2014; McKay et al., 2016; Spector et al., 2017; Lowry et al., 2019), at this stage, the other ice core records cannot fully reconcile this. The reorganization may simply reflect a tipping point in the system, whereby ice had retreated enough to allow new circulation patterns. The second abrupt transition occurred at 4.5 ka BP and is attributed to ocean forcing due to the formation of the Ross Ice Shelf cavity. The formation of the cavity led to the perpetual creation of freshened surface waters which lead to an increase in coastal sea ice in Adélie Land since 4.5 ka BP. Interestingly, temperatures at the TALDICE record and laminae frequency in U1357 appear to be coupled throughout the Holocene. This is attributed to sensitivity of these proxies to changes in atmospheric transport strength.

These results indicate a strong connectivity between the Ross Sea and Adélie Land that increased as the RIS retreated. This happened first through changing atmospheric circulation pathways bringing Ross sea air masses over to the Eastern Plateau. The second occurred through the modification of water masses by ice shelf cavities developing in the Ross Sea that directly influence Adélie Land. These proxies suggest that neither of these processes were present in the Early to Mid Holocene when the Ross Ice Shelf extended to the continental shelf edge and during its initial retreat phase.

The relationship between the Ross Sea and Adélie Land heightens the importance of understanding the ocean-ice sheet interactions and the stability of the RIS under future climate change. Surface waters in the Ross Sea are freshening in part due to meltwater contributions from the Amundsen Sea (Jacobs et al., 2002; Hillenbrand et al., 2017), but the magnitude of this contribution is unknown, and likely impacts Adélie Land due to its connectivity with the Ross Sea. As the Ross Sea and Adélie Land regions are an important source of AABW formation and home to the largest Antarctic polynyas, circulation changes around and beneath the RIS, and surface water changes upstream from the Ross Sea, will directly affect coastal regions in East Antarctica, including Adélie Land. This will likely have widespread impacts on Antarctica's coastal biological and oceanographic systems, as well as downstream impacts on global heat transport and the carbon cycle.

Chapter 7

Conclusion and Future Work

7.1 Conclusion

The primary aim of this thesis is to develop a reconstruction of Antarctic environmental conditions and identify key drivers and feedbacks during the Holocene period to improve our ability to predict response of Antarctic coastal oceanographic settings to future change. To achieve this, the study takes advantage of two new, highly-resolved climate archives - the IODP U1357B Adélie Basin sediment and RICE ice core records. These near annually-resolved records from the Adélie Land and Ross Sea regions, respectively, capture change along Antarctica's highly dynamic coastal margins. To contribute to the development and interpretation of the IODP U1357B record, I analysed X-ray Computed Tomography images and created a CT-scan greyscale line profile of sedimentary changes in the core, as well as manually identifying light laminations to identify changes in biological sedimentation. Comparison of these datasets to existing datasets are used to develop a comprehensive sedimentation model for this site that allows for reconstructions of environmental change through the Holocene. A key additional contribution in this work is that the laminae count provides an independent verification of the accuracy of the ^{14}C age model. For the RICE ice core record, I jointly measured a total of 3,160 Ion Chromatography samples from ~7,285 to 10,625 cal yr BP with fellow PhD student Lukas Eling. I used these data to provide insights into the atmospheric conditions in the Holocene and investigated the influence of atmospheric circulation on sea ice and marine primary productivity.

The thesis identified several objectives. Here, the main findings are summarized and future priorities for Antarctic paleoclimate reconstructions are suggested based on these results.

Objective 1: *What are the environmental controls on the depositional processes in Adélie Land?*

Comparison of the greyscale profile and light laminae counts to XRF and physical core property data indicate that light laminations represent biologically influenced sedimentation, whereas dark laminations correspond to increased terrigenous input during open water conditions. Building on the arguments of McCave and Andrews (2019), and grain size results from U1357B conducted by Albot (2017), distinct modes within the grain size distributions of light and dark laminae are shown to be well sorted, and comparisons with sediment advection rates indicate this provides an effective measure of current speed throughout the Holocene. Light and dark laminae are deposited under different environmental conditions and highlight seasonal differences. Deposition of both light and dark laminae appear to be highly sensitive to the vigour of wind-driven currents. Dark laminae are deposited under higher maximum current speeds, as dark laminae deposition occurs during ice free conditions, when wind stress can more effectively drive Ekman pumping and the subsequent geostrophic current, increasing current speeds. They are also inferred to be deposited over a longer time, and thus more likely to capture more storm events. Light laminae are highly dependent on biological processes, which have numerous influences such as sea ice extent, wind stress on the ocean surface, and availability of nutrients. While high winds during dark laminae deposition can invigorate upwelling of mCDW and bring nutrients into the water column, wind stress needs to relax for stratification to occur, and thus lower current speeds, to enable the bloom events represented by the light laminae. Decadal to multi-decadal variations in laminae thickness are attributed to the Inter-Decadal Pacific Oscillation, which can alter surface wind strength, thereby altering current strength and sediment transport to U1357B. A major outcome of this work is that it is demonstrated that these bloom events are not an annual occurrence and appear to be partially modulated by sub-decadal to multi-decadal climate variations. Overall, when current strength is elevated during light and dark laminae deposition, laminae thickness also increases as a consequence of enhanced sediment advection, and suggests increased productivity during stronger currents is related to elevated nutrients levels from wind driven mixing.

Objective 2: *What are the drivers of biological productivity in Adélie Land and how has this changed through the Holocene?*

Primary productivity variations indicate three distinct climate states. The Early Holocene (∼11.4-8.2 ka BP) has more frequent bloom events relative to the entire record which are attributed to enhanced stratification and nutrient availability due to the final pulses of EAIS deglaciation. The Hypsithermal (∼8.2-4.5 ka BP) represents a more stable period,

where bloom events occur roughly ∼2 years, and this frequency remains relatively steady compared to the Early Holocene. Deglaciation is assumed to be complete in the Adélie Land region at this time, and a reduced sea ice state enables more frequent blooms by reducing the energy needed to break up sea ice and induce bloom events. The Neoglacial (∼4.5 to present) has a sharp reduction in productivity which occurs simultaneously with a rapid increase in fast ice extent.

Bloom events during the Neoglacial occur at a 2-7 year intervals, suggesting an ENSO influence. However, the ENSO teleconnection at this location is highly dependent on SAM phasing, and can also be affected by IOD activity. Furthermore, there is poor agreement from reanalysis studies on the resultant climate impacts from ENSO at Site U1357, suggesting that the relationship is more complex than currently understood.

Despite these uncertainties regarding ENSO, SAM, and IOD interactions through the Holocene, these results indicate sea ice state strongly modulates bloom frequency at U1357, and it is suggested that the rapid change at ∼4.5 ka BP is a tipping point in the system, making Site U1357 less sensitive to sub-decadal climate modes. The increase in sea ice extent acts as a barrier to bloom events. During times when sea ice extent is reduced, the forcing needed to initiate a bloom event is reduced as well.

The uncertainty in sea ice predictions and frequency/intensity of sub-decadal climate modes has important implications for the Southern Ocean carbon cycle. Reduced sea ice state and increased frequency of sub-decadal climate modes could mean increased frequency of bloom events and increased carbon uptake along the Adélie Land margin. Conversely, increased outgassing of CO_2 from reduced sea ice extent may counteract the uptake.

Objective 3: *How does the observed environmental change at Roosevelt Island and Adélie Land correspond to known Ross Ice Shelf grounding line dynamics?*

Productivity, sea ice extent, temperature, and atmospheric transport proxies for RICE, Taylor Dome, TALDICE, and the U1357B record are binned into 100-year intervals to correlate the ice and marine records and assess abrupt climate shifts at each location throughout the Holocene and compared with regional modelling experiments. Distinct events occur between ∼8.9-8.5 ka BP and ∼5-4.5 ka BP in all records.

The first transition at ∼8.9-8.5 ka BP is marked by a stepwise reduction in temperature at Taylor Dome and a modelled lowering of elevation at RICE, and a gradual increase in temperature at TALDICE, and gradual reduction in productivity at U1357B. This change

reflects the alteration of atmospheric circulation as the RIS retreated, leading to increased marine air incursions along the western Ross Sea towards TALDICE and increased influence of the ASL in the Ross Sea Region. The gradual warming at TALDICE and reduction at productivity at U1357B may be related to the sensitivity of these proxies to atmospheric transport strength.

Between ~5.0-4.5 ka BP, a second reduction in temperature at Taylor Dome occurs, followed by an increase in temperature at RICE. Increases in productivity at Taylor Dome and TALDICE are noted, while productivity decreases at U1357B. The alteration in both temperature and productivity at all locations suggests a regional change and is potentially attributed to the formation of the Ross Ice Shelf cavity, which led to freshening of surface waters in the Ross Sea, that are subsequently transported towards Adélie Land by the Antarctic Coastal Current. This enhanced interaction between oceanic water and the ice shelf cavity is proposed to have led to a sustained increase in sea ice extent at U1357B, which in turn reduced productivity.

The oceanic and atmospheric connection between the Ross Sea and Adélie Land appears to significantly strengthen as the RIS retreats. First, changes in atmospheric circulation allow Ross Sea air masses to affect the East Antarctic Plateau. Second, the formation of the Ross Ice Shelf cavity and subsequently, the grounding line retreating to its modern day position at ~4.5 ka BP modified surface water masses that directly impact sea ice concentrations at Site U1357. These proxies indicate that the influence of the Ross Sea on Adélie Land was less pronounced when the RIS extended to the continental shelf. Furthermore, the influence of ice cover on the Ross Sea continental margin has a large influence on surface water conditions in Adélie Land.

This connection raises the importance of understanding the stability of the Ross Ice Shelf. Future changes in the Ross Sea due to the retreat of the RIS in a warming climate has the potential to directly impact Adélie Land margin of East Antarctica, significantly altering primary productivity and AABW formation in two of Antarctica's largest polynyas and AABW formation sites.

7.2 Enduring questions and future research

The U1357B record is the first continuously laminated marine sediment record with annual resolution up to ~11.4 ka BP. As such, it provides a first-ever opportunity to directly compare with ice core records of equal resolution, and allows assessment of ice-ocean-atmosphere in-

teractions at sub-decadal resolution for the entire Holocene. It is important to note that while this is a first order attempt at integrating these records, early results are promising. Several lines of future work are suggested to build on these exciting findings and further development of proxy records from the U1357B and RICE records will allow testing of hypotheses presented in this thesis, and potentially enable integration at a higher resolution scale.

The current age model for U1357B remains unpublished. While 87 ^{14}C bulk organic carbon dates show a consistent stratigraphic order, ^{14}C dates can be problematic due to reworking of older carbon into the sample (Rosenheim et al., 2013). Typically, a core top correction age is applied to account for this reworked carbon (e.g. Leventer et al., 1993; Andrews et al., 1999; Domack et al., 2001), but this correction may not be consistent down core (Shevenell et al., 1996; Rosenheim et al., 2008). While this age model is consistent with that of nearby MD03-2601, anomalous compound specific ages in U1357A exist. Therefore, additional dating of U1357B may help resolve these discrepancies. Ramped Pyrolysis radiocarbon dating isolates the autochthonous organic carbon (Rosenheim et al., 2008), but sites with high in-situ productivity are likely to be similar to bulk organic carbon dates (Rosenheim et al., 2013). A preferred alternative is to radiocarbon date foraminifera (Gordon and Harkness, 1992; Bart and Cone, 2012), which offer more reliable ages than bulk organic carbon (Andrews et al., 1999). Foraminifera are present in the U1357 cores, and efforts are ongoing to isolate enough specimens for radiocarbon dating.

In Chapter 4, grain size data were used to create a paleocurrent proxy. Provided adequate samples are still available, increased sampling of light and dark laminae couplets, and subsequent grain size analysis on these couplets could increase the resolution of this proxy. The current resolution varies between ∼50-200 years, so finer sampling could infer current speed changes due to sub-decadal oscillations.

In Chapter 5, sub-decadal oscillations were identified in laminae frequency. These were attributed to ENSO, however, Adélie Land is also influenced by the SAM and the IOD. Therefore, a direct mechanism for the subdecadal driver was not identified as climate anomalies associated with these climate modes differ among reanalysis studies (Schneider et al., 2012; Nuncio and Yuan, 2015; Ciasto et al., 2015; Marshall and Thompson, 2016). To understand sub-decadal climate oscillations at Site U1357, a site specific modelling/reanalysis study should be completed. This should incorporate data from the Dumont d'Urville weather station, which has consistent records since 1957 (Turner et al., 2004). While the Ross Sea and Antarctic Peninsula region have a plethora of ENSO-related studies, increased focus on the Adélie Land region would allow for assessment of how these sub-decadal modes affect productivity in the Mertz Polynya, which has global implications for AABW formation and the carbon cycle. Finally,

detailed analysis of the diatoms from U1357B should be undertaken to better elucidate the seasonality and oceanographic drivers for the deposition of the light and dark laminae.

Chapter 6 was the first attempt at integrating the RICE ice core and U1357B records by smoothing the age models in order to reduce age uncertainty. To integrate these records at higher resolution, additional work is required.

The first priority is to identify well-dated contemporaneous tie points in each record. The RICE ice core record has several volcanic ash layers. Recent work has highlighted the usefulness of cryptotephras (Davies, 2015), and this methodology has been applied in Antarctic marine sediments (Di Roberto et al., 2019). If cryptotephras are identified in U1357B, these may provide a direct tie point to RICE. Another alternative would be to use meteorite impacts. Nearby MD03-2601 is proposed to contain a meteorite impact layer (Crosta et al., 2007), so it is likely that U1357B is also affected. Nanodiamonds and elements such as platinum and iridium in ice have been attributed to meteorite impacts (Kurbatov et al., 2010; Petaev et al., 2013), but measurements of these elements has yet to be completed on RICE. Measurement of these elements should continue to ∼4-5 ka BP, when this impact is suspected to have occurred.

The second priority is to extend the RICE ice core ion chromatography record through the Holocene which requires the analysis of ∼40,000 samples. Complete records of all of ions will help with the integration of the RICE ice core record to the U1357B core/site. Additionally, this will provide a more detailed Holocene record of the Eastern Ross Sea. This will be particularly useful to understand how the reorganization of atmospheric circulation affected RICE from ∼8.5 ka BP onward. In addition, any impacts to the ion record at ∼4.5 ka BP may provide further insight into the oceanic changes at this time.

Completion of the Holocene record will enable separation of sea-salt and non-sea salt components and to identify the drivers of calcium and magnesium variations. However, identifying the drivers of ion variability (e.g. sea ice versus open ocean for Na^+ or MSA^-) is difficult. Therefore, comparison of ionic concentrations from snow samples and firn layers, to reanalysis data may help characterise these sources. Furthermore, air sampling at the RICE drill site should be undertaken to further characterise the seasonality of ion variability. This may also help identify if the magnesium depletion in the RICE Early Holocene record is a real signal, and if so, could provide valuable insights into the extent of the RIS during the Holocene.

On a broader scale, meltwater contributions from the Amundsen Sea may have impacted Ross Sea waters during the Holocene (Hillenbrand et al., 2017), but the magnitude of this contribution is unknown. Additional cores from the eastern Ross Sea have the potential to address this impact, and provide greater understanding of changes in the Ross Sea during the Holocene. Isotope enabled climate modelling for all ice core records would also be very useful

to help distinguish the influence of elevation changes, atmospheric circulation changes, and temperature changes, and could explain some of the differences in the timing of abrupt change in the Holocene.

7.3 Concluding statement

The development of the U1357B sediment core record and RICE ice core record in this thesis is a significant contribution to the current understanding of Holocene change in the Ross Sea and Adélie Land regions. This record is the first to provide a proxy for Holocene current strength along the Adélie Land Margin. This is also the first record to identify Antarctic polynya primary productivity cycles at a near annual resolution in the Holocene. Most primary productivity studies are observational and/or satellite based and are limited in time and resolution. Coastal polynyas are an important CO_2 sink (Arrigo et al., 2008a) and globally, phytoplankton are on the decline in warming waters (Boyce et al., 2010). This record also highlights the role tipping points in sea ice conditions have played in modulating the response of the Antarctic oceanic margin to the ENSO influence. This is important as climate models struggle to capture modern Antarctic sea ice trends, with the recent IPCC Special Report on Ocean and Cryosphere (2019) citing a *low confidence* in these predictive Antarctic Sea Ice models. These data indicate past tipping points in sea ice conditions do exist and this significantly affects high- to low-latitude climatic teleconnections. Consequently, models projecting future response of the high latitudes to increasing ENSO forcing over coming decades may be performing poorly and misrepresenting these teleconnections. Finally, these records highlight the downstream impact of the development of the Ross Ice Shelf cavity. It is through this development that conditions in the Ross Sea directly impact conditions along Adélie Land, and any future changes in surface water processes in the Ross Sea, or upstream from the Ross Sea, will have downstream affects along the Adélie Land Margin.

Appendices

Appendix A: IODP U1357B CT-scan greyscale data

Appendix B: IODP U1357B manual laminae counts

Appendix C: RICE Early Holocene ICS data

References

Abram, N. J., Wolff, E. W., and Curran, M. A. J. 2013. A review of sea ice proxy information from polar ice cores. *Quaternary Science Reviews*, 79:168–183. ISSN 02773791. doi: 10.1016/j.quascirev.2013.01.011.

Adolphs, U. and Wendler, G. 1995. A pilot study on the interactions between katabatic winds and polynyas at the Adblie Coast , eastern Antarctica. *Antarctic Science*, 7(3):307–314. ISSN 13652079. doi: 10.1017/S0954102095000423.

Agnihotri, R., Altabet, M. A., Herbert, T. D., and Tierney, J. E. 2008. Subdecadally resolved paleoceanography of the Peru margin during the last two millennia. *Geochemistry, Geophysics, Geosystems*, 9(5). ISSN 15252027. doi: 10.1029/2007GC001744.

Ainley, D. G. and Jacobs, S. S. 1981. Sea-bird affinities for ocean and ice boundaries in the Antarctic. *Deep Sea Research Part A, Oceanographic Research Papers*, 28(10):1173–1185. ISSN 01980149. doi: 10.1016/0198-0149(81)90054-6.

Albani, S., Delmonte, B., Maggi, V., Baroni, C., Petit, J.-r., Stenni, B., Mazzola, C., and Frezzotti, M. 2012. Interpreting last glacial to Holocene dust changes at Talos Dome (East Antarctica): implications for atmospheric variations from regional to hemispheric scales. 8:741–750. doi: 10.5194/cp-8-741-2012.

Albot, A. B. 2017. *Holocene sediment transport and climate variability of offshore Adélie Land, East Antarctica*. PhD thesis, Victoria University of Wellington.

Alley, K., Patacca, K., Pike, J., Dunbar, R. B., and Leventer, A. 2018. Iceberg Alley, East Antarctic Margin: Continuously laminated diatomaceous sediments from the late Holocene. *Marine Micropaleontology*, 140(November 2017):56–68. ISSN 03778398. doi: 10.1016/j.marmicro.2017.12.002.

Anderson, J. The Antarctic continental shelf: results from marine geological and geophysical investigations. In Tingey, R. J., editor, *The Geology of Antarctica*, page 680. Oxford: Clarendon Press, 1991. ISBN 0198544677.

Anderson, J. B., Shipp, S. S., Lowe, A. L., Wellner, J. S., and Mosola, A. B. 2002. The Antarctic Ice Sheet during the Last Glacial Maximum and its subsequent retreat history: A review. *Quaternary Science Reviews*. ISSN 02773791. doi: 10.1016/S0277-3791(01)00083-X.

Anderson, J. B., Conway, H., Bart, P. J., Witus, A. E., Greenwood, S. L., McKay, R. M., Hall, B. L., Ackert, R. P., Licht, K., Jakobsson, M., and Stone, J. O. 2014. Ross Sea paleo-ice sheet drainage and deglacial history during and since the LGM. *Quaternary Science Reviews*, 100: 31–54. ISSN 02773791. doi: 10.1016/j.quascirev.2013.08.020.

Andrews, J. T., Domack, E. W., Cunningham, W. L., Leventer, A., Licht, K. J., Jull, A. J., DeMaster, D. J., and Jennings, A. E. 1999. Problems and possible solutions concerning radiocarbon dating of surface marine sediments, Ross Sea, Antarctica. *Quaternary Research*. ISSN 00335894. doi: 10.1006/qres.1999.2047.

Aoki, S., Rintoul, S. R., Ushio, S., Watanabe, S., and Bindoff, N. L. 2005. Freshening of the Adélie Land Bottom Water near 140°E. *Geophysical Research Letters*, 32(L23601). ISSN 0094-8276. doi: 10.1029/2005GL024246.

Arrigo, K. R. and van Dijken, G. L. 2003. Phytoplankton dynamics within 37 Antarctic coastal polynya systems. *Journal of Geophysical Research C: Oceans*, 108(C8):1–18. ISSN 01480227. doi: 10.1029/2002jc001739.

Arrigo, K. R. and Van Dijken, G. L. 2004. Annual changes in sea-ice, chlorophyll a, and primary production in the Ross Sea, Antarctica. *Deep-Sea Research Part II: Topical Studies in Oceanography*. ISSN 09670645. doi: 10.1016/j.dsr2.2003.04.003.

Arrigo, K. R., Worthen, D. L., Lizotte, M. P., Dixon, P., and Dieckmann, G. 1997. Primary production in Antarctic sea ice. volume 276. ISBN 00368075\r10959203. doi: 10.1126/science.276.5311.394.

Arrigo, K. R., Weiss, A. M., and Smith, W. O. 1998. Physical forcing of phytoplankton dynamics in the southwestern Ross Sea. *Journal of Geophysical Research: Oceans*, 103(C1):1007–1021. ISSN 01480227. doi: 10.1029/97JC02326.

Arrigo, K. R., van Dijken, G., and Long, M. 2008a. Coastal Southern Ocean: A strong anthropogenic CO2 sink. *Geophysical Research Letters*, 35(21). ISSN 00948276. doi: 10.1029/2008GL035624.

Arrigo, K. R., van Dijken, G. L., and Bushinsky, S. 2008b. Primary production in the Southern Ocean, 1997–2006. *Journal of Geophysical Research*, 113(C8):C08004. ISSN 0148-0227. doi: 10.1029/2007JC004551.

Arrigo, K. R., van Dijken, G. L., and Strong, A. L. 2015. Environmental controls of marine productivity hot spots around Antarctica. *Journal of Geophysical Research: Oceans*, 120: 5545–5565. ISSN 21699275. doi: 10.1002/jgrc.20224.

Ashley, K., Bendle, J., McKay, R. M., Etourneau, J., Jimenez-Espejo, F. J., Condron, A., Albot, A. B., Crosta, X., Riesselman, C. R., Seki, O., Masse, G., Golledge, N. R., Gasson, E. G. W., Lowry, D. P., Barrand, N. E., Johnson, K. M., Bertler, N. A., Escutia, C., and Dunbar, R. B. Mid-Holocene Antarctic sea-ice increase driven by marine ice sheet retreat.

Ashok, K. and Yamagata, T. 2009. Climate change: The El Niño with a difference. *Nature*, 461 (7263):481–484. ISSN 00280836. doi: 10.1038/461481a.

Ashok, K., Guan, Z., and Yamagata, T. 2003. A look at the relationship between the ENSO and the Indian Ocean Dipole. *Journal of the Meteorological Society of Japan*, 81(1):41–56. ISSN 00261165. doi: 10.2151/jmsj.81.41.

Ashok, K., Behera, S. K., Rao, S. A., Weng, H., and Yamagata, T. 2007. El Niño Modoki and its possible teleconnection. *Journal of Geophysical Research*, 112(C11):C11007. ISSN 0148-0227. doi: 10.1029/2006JC003798.

Baggenstos, D., Severinghaus, J. P., Mulvaney, R., McConnell, J. R., Sigl, M., Maselli, O., Petit, J. R., Grente, B., and Steig, E. J. 2018. A Horizontal Ice Core From Taylor Glacier, Its Implications for Antarctic Climate History, and an Improved Taylor Dome Ice Core Time Scale. *Paleoceanography and Paleoclimatology*, 33(7):778–794. doi: 10.1029/2017PA003297.

Baines, P. G. and Fraedrich, K. 1989. Topographic effects on the mean tropospheric flow patterns around Antarctica. *Journal of the Atmospheric Sciences*, 46(22):3401–3415. ISSN 00224928. doi: 10.1175/1520-0469(1989)046<3401:TEOTMT>2.0.CO;2.

Baldwin, M. P. 2001. Annular modes in global daily surface pressure. *Geophysical Research Letters*, 28(21):4115–4118. ISSN 00948276. doi: 10.1029/2001GL013564.

Ball, F. 1957. The Katabatic Winds of Adélie Land and King George V Land. *Tellus*, IX(2): 201–208.

Barber, D. G. and Massom, R. A. The Role of Sea Ice in Arctic and Antarctic Polynyas. In Smith Jr., W. O. and Barber, D., editors, *Polynyas: Windows to the World*, volume 74, chapter 1, pages 1–54. Elsevier Oceanography Series, 2007. ISBN 9780444529527. doi: 10.1016/S0422-9894(06)74001-6.

Bart, P. J. and Cone, A. N. 2012. Early stall of West Antarctic Ice Sheet advance on the eastern Ross Sea middle shelf followed by retreat at 27,500 14CyrBP. *Palaeogeography, Palaeoclimatology, Palaeoecology*. ISSN 00310182. doi: 10.1016/j.palaeo.2011.08.007.

Bart, P. J., DeCesare, M., Rosenheim, B. E., Majewski, W., and McGlannan, A. 2018. A centuries-long delay between a paleo-ice-shelf collapse and grounding-line retreat in the Whales Deep Basin, eastern Ross Sea, Antarctica. *Scientific Reports*, 8(1):1–9. ISSN 20452322. doi: 10.1038/s41598-018-29911-8.

Bassis, J. N., Petersen, S. V., and Mac Cathles, L. 2017. Heinrich events triggered by ocean forcing and modulated by isostatic adjustment. *Nature*, 542(7641):332–334. ISSN 0028-0836. doi: 10.1038/nature21069.

Baumgartner, M., Kindler, P., Eicher, O., Floch, G., Schilt, A., Schwander, J., Spahni, R., Capron, E., Chappellaz, J., Leuenberger, M., Fischer, H., and Stocker, T. F. 2014. NGRIP CH4 concentration from 120 to 10 kyr before present and its relation to a δ15N temperature reconstruction from the same ice core. *Climate of the Past*, 10(2):903–920. ISSN 18149332. doi: 10.5194/cp-10-903-2014.

Bazin, L., Landais, A., Lemieux-Dudon, B., Toyé Mahamadou Kele, H., Veres, D., Parrenin, F., Martinerie, P., Ritz, C., Capron, E., Lipenkov, V., Loutre, M. F., Raynaud, D., Vinther, B., Svensson, A., Rasmussen, S. O., Severi, M., Blunier, T., Leuenberger, M., Fischer, H., Masson-Delmotte, V., Chappellaz, J., and Wolff, E. 2013. An optimized multi-proxy, multi-site Antarctic ice and gas orbital chronology (AICC2012): 120-800 ka. *Climate of the Past*, 9 (4):1715–1731. ISSN 18149324. doi: 10.5194/cp-9-1715-2013.

Beaman, R. J. and Harris, P. T. 2003. Seafloor morphology and acoustic facies of the George V Land shelf. *Deep-Sea Research Part II: Topical Studies in Oceanography*, 50(8-9):1343–1355. ISSN 09670645. doi: 10.1016/S0967-0645(03)00071-7.

Beaman, R. J., O 'Brien, P. E., Post, A. L., and De Santis, L. 2011. A new high-resolution bathymetry model for the Terre Adélie and George V continental margin, East Antarctica. *Antarctic Science*, 23(1):95–103. ISSN 09541020. doi: 10.1017/S095410201000074X.

Becagli, S., Castellano, E., Cerri, O., Curran, M., Frezzotti, M., Marino, F., Morganti, A., Proposito, M., Severi, M., Traversi, R., and Udisti, R. 2009. Methanesulphonic acid (MSA) stratigraphy from a Talos Dome ice core as a tool in depicting sea ice changes and southern atmospheric circulation over the previous 140 years. *Atmospheric Environment*, 43(5):1051–1058. ISSN 13522310. doi: 10.1016/j.atmosenv.2008.11.015.

Belt, S. T., Smik, L., Brown, T. A., Kim, J.-H., Rowland, S. J., Allen, C. S., Gal, J.-K., Shin, K.-H., Lee, J. I., and Taylor, K. W. R. 2016. Source identification and distribution reveals the potential of the geochemical Antarctic sea ice proxy IPSO25. *Nature Communications*, 7(1): 12655. ISSN 2041-1723. doi: 10.1038/ncomms12655.

Belt, S. T., Massé, G., Rowland, S. J., Poulin, M., Michel, C., and LeBlanc, B. 2007. A novel chemical fossil of palaeo sea ice: IP25. *Organic Geochemistry*, 38(1):16–27. ISSN 01466380. doi: 10.1016/j.orggeochem.2006.09.013.

Bentley, M. J., Hodgson, D. A., Smith, J. A., Cofaigh, C. [U+FFFD], Domack, E. W., Larter, R. D., Roberts, S. J., Brachfeld, S., Leventer, A., Hjort, C., Hillenbrand, C. D., and Evans, J. 2009. Mechanisms of Holocene palaeoenvironmental change in the Antarctic Peninsula region. *Holocene*, 19(1):51–69. ISSN 09596836. doi: 10.1177/0959683608096603.

Berkman, P. A. and Forman, S. L. 1996. Pre-bomb radiocarbon and the reservoir correction for calcareous marine species in the Southern Ocean. *Geophysical Research Letters*, 23(4): 363–366. ISSN 00948276. doi: 10.1029/96GL00151.

Bertler, N. A., Conway, H., Dahl-Jensen, D., Emanuelsson, D. B., Winstrup, M., Vallelonga, P. T., Lee, J. E., Brook, E. J., Severinghaus, J. P., Fudge, T. J., Keller, E. D., Troy Baisden, W., Hindmarsh, R. C. A., Neff, P. D., Blunier, T., Edwards, R., Mayewski, P. A., Kipfstuhl, S., Buizert, C., Canessa, S., Dadic, R., Kjaer, H. A., Kurbatov, A., Zhang, D., Waddington, E. D., Baccolo, G., Beers, T., Brightley, H. J., Carter, L., Clemens-Sewall, D., Ciobanu, V. G., Delmonte, B., Eling, L., Ellis, A., Ganesh, S., Golledge, N. R., Haines, S., Handley, M., Hawley, R. L., Hogan, C. M., Johnson, K. M., Korotkikh, E., Lowry, D. P., Mandeno, D., McKay, R. M., Menking, J. A., Naish, T. R., Noerling, C., Ollive, A., Orsi, A., Proemse, B. C., Pyne, A. R., Pyne, R. L., Renwick, J., Scherer, R. P., Semper, S., Simonsen, M., Sneed, S. B., Steig, E. J., Tuohy, A., Ulayottil Venugopal, A., Valero-Delgado, F., Venkatesh, J., Wang, F., Wang, S.,

Winski, D. A., Holly, V., Winton, L., Whiteford, A., Xiao, C., Yang, J., and Zhang, X. Ross Sea Deglaciation History.

Bertler, N. A., Barrett, P. J., Mayewski, P. A., Fogt, R. L., Kreutz, K. J., and Shulmeister, J. 2004. El Niño suppresses Antarctic warming. *Geophysical Research Letters*, 31(15):2–5. ISSN 00948276. doi: 10.1029/2004GL020749.

Bertler, N. A., Naish, T. R., Mayewski, P. A., Barrett, P. J., and Ni, E. 2006. Opposing oceanic and atmospheric ENSO influences on the Ross Sea Region , Antarctica. *Advances In Geosciences*, 6:83–86.

Bertler, N. A., Conway, H., Dahl-Jensen, D., Emanuelsson, D. B., Winstrup, M., Vallelonga, P. T., Lee, J. E., Brook, E. J., Severinghaus, J. P., Fudge, T. J., Keller, E. D., Troy Baisden, W., Hindmarsh, R. C. A., Neff, P. D., Blunier, T., Edwards, R., Mayewski, P. A., Kipfstuhl, S., Buizert, C., Canessa, S., Dadic, R., Kjaer, H. A., Kurbatov, A., Zhang, D., Waddington, E. D., Baccolo, G., Beers, T., Brightley, H. J., Carter, L., Clemens-Sewall, D., Ciobanu, V. G., Delmonte, B., Eling, L., Ellis, A., Ganesh, S., Golledge, N. R., Haines, S., Handley, M., Hawley, R. L., Hogan, C. M., Johnson, K. M., Korotkikh, E., Lowry, D. P., Mandeno, D., McKay, R. M., Menking, J. A., Naish, T. R., Noerling, C., Ollive, A., Orsi, A., Proemse, B. C., Pyne, A. R., Pyne, R. L., Renwick, J., Scherer, R. P., Semper, S., Simonsen, M., Sneed, S. B., Steig, E. J., Tuohy, A., Ulayottil Venugopal, A., Valero-Delgado, F., Venkatesh, J., Wang, F., Wang, S., Winski, D. A., Holly, V., Winton, L., Whiteford, A., Xiao, C., Yang, J., and Zhang, X. 2018. The Ross Sea Dipole-temperature, snow accumulation and sea ice variability in the Ross Sea region, Antarctica, over the past 2700 years. *Clim. Past*, 14:193–214. doi: 10.5194/cp-14-193-2018.

Bindoff, N. L., Williams, G. D., and Allison, I. 2001. Sea-ice growth and water-mass modification in the Mertz Glacier polynya, East Antarctica, during winter. *Annals of Glaciology*, 33: 399–406. ISSN 0260-3055. doi: 10.3189/172756401781818185.

Bindoff, N. L., Rintoul, S. R., and Massom, R. A. 2000. BOTTOM WATER FORMATION AND POLYNYAS IN ADELIE LAND, ANTARCTICA. *Papers and Proceedings of the Royal Society of Tasmnia*, 133(3):51–56.

Bjerknes, J. 1969. ATMOSPHERIC TELECONNECTIONS FROM THE EQUATORIAL PACIFIC. *Monthly Weather Review*, 97(3):163–172. ISSN 0027-0644. doi: 10.1175/1520-0493(1969)097<0163:ATFTEP>2.3.CO;2.

Blaauw, M. and Christen, J. A. 2011. Flexible paleoclimate age-depth models using an autoregressive gamma process. *Bayesian Analysis*, 6(3):457–474. ISSN 19360975. doi: 10.1214/11-BA618.

Boespflug, X., Long, B. F., and Occhietti, S. 1995. CAT-scan in marine stratigraphy: a quantitative approach. *Marine Geology*. ISSN 00253227. doi: 10.1016/0025-3227(94)00129-9.

Bowen, H. 1979. Environmental Chemistry of the Elements. Academic Press, London.

Boyce, D. G., Lewis, M. R., and Worm, B. 2010. Global phytoplankton decline over the past century. *Nature*, 466(7306):591–596. ISSN 0028-0836. doi: 10.1038/nature09268.

Boyd, P. W. 2002. Environmental factors controlling phytoplankton processes in the Southern Ocean. *Journal of Phycology*, 38(5):844–861. ISSN 00223646. doi: 10.1046/j.1529-8817.2002.t01-1-01203.x.

Brightley, H. J. 2017. *A Paleoclimate Reconstruction of the Little Ice Age to Modern Era Climate Conditions in the Eastern Ross Sea, Antarctica as captured in the RICE Ice Core*. PhD thesis, Victoria University of Wellington.

Brinkmann, T., Specht, C. H., and Frimmel, F. H. 2002. Non-linear calibration functions in ion chromatography with suppressed conductivity detection using hydroxide eluents. *Journal of Chromatography A*, 957:99–109. ISSN 00219673. doi: 10.1016/S0021-9673(02)00308-4.

Bromwich, D. H. and Wang, S. H. 2008. A review of the temporal and spatial variability of Arctic and Antarctic atmospheric circulation based upon ERA-40. *Dynamics of Atmospheres and Oceans*, 44(3-4):213–243. ISSN 03770265. doi: 10.1016/j.dynatmoce.2007.09.001.

Bromwich, D. H., Carrasco, J. F., Liu, Z., and Tzeng, R.-Y. 1993. Hemispheric atmospheric variations and oceanographic impacts associated with katabatic surges across the Ross ice shelf, Antarctica. *Journal of Geophysical Research*, 98:13045. ISSN 0148-0227. doi: 10.1029/93JD00562.

Brown, E. T. Estimation of Biogenic Silica Concentrations Using Scanning XRF: Insights from Studies of Lake Malawi Sediments. In Croudace, I. w. and Rothwell, R. G., editors, *Micro-XRF Studies of Sediment Cores. Developments in Paleoenvironmental Research*, chapter 9, pages 267–277. Springer, 2015. doi: 10.1007/978-94-017-9849-5{_}9.

Brown, M. S., Munro, D. R., Feehan, C. J., Sweeney, C., Ducklow, H. W., and Schofield, O. M. 2019. Enhanced oceanic CO2 uptake along the rapidly changing West Antarctic Peninsula. *Nature Climate Change*, 9(9):678–683. ISSN 1758-678X. doi: 10.1038/s41558-019-0552-3.

Buckley, M. W. and Marshall, J. 2015. Observations, inferences, and mechanisms of the Atlantic Meriodional Overturning Circulation: A Review. *Reviews of Geophysics*, 54:5–63. doi: 10.1002/2015RG000493.Received.

Budillon, G., Castagno, P., Aliani, S., Spezie, G., and Padman, L. 2011. Thermohaline variability and Antarctic bottom water formation at the Ross Sea shelf break. *Deep-Sea Research Part I: Oceanographic Research Papers*. ISSN 09670637. doi: 10.1016/j.dsr.2011.07.002.

Buizert, C., Cuffey, K. M., Severinghaus, J. P., Baggenstos, D., Fudge, T. J., Steig, E. J., Markle, B. R., Winstrup, M., Rhodes, R. H., Brook, E. J., Sowers, T. A., Clow, G. D., Cheng, H., Edwards, R. L., Sigl, M., McConnell, J. R., and Taylor, K. C. 2015. The WAIS Divide deep ice core WD2014 chronology – Part 1: Methane synchronization (68-31 ka BP) and the gas age-ice age difference. *Climate of the Past*, 11(2):153–173. ISSN 18149332. doi: 10.5194/cp-11-153-2015.

Bull, D. and Kemp, A. E. 1996. Composition and origins of laminae in late Quaternary and Holocene sediments from the Santa Barbara Basin. *Geological Society Special Publication*, 116:143–156. ISSN 03058719. doi: 10.1144/GSL.SP.1996.116.01.13.

Cai, W., van Rensch, P., Cowan, T., and Hendon, H. H. 2011. Teleconnection pathways of ENSO and the IOD and the mechanisms for impacts on Australian rainfall. *Journal of Climate*, 24 (15):3910–3923. ISSN 08948755. doi: 10.1175/2011JCLI4129.1.

Cai, W., Borlace, S., Lengaigne, M., van Rensch, P., Collins, M., Vecchi, G., Timmermann, A., Santoso, A., McPhaden, M. J., Wu, L., England, M. H., Wang, G., Guilyardi, E., and Jin, F.-F. 2014a. Increasing frequency of extreme El Niño events due to greenhouse warming. *Nature Climate Change*, 4(2):111–116. ISSN 1758-678X. doi: 10.1038/nclimate2100.

Cai, W., Santoso, A., Wang, G., Weller, E., Wu, L., Ashok, K., Masumoto, Y., and Yamagata, T. 2014b. Increased frequency of extreme Indian ocean dipole events due to greenhouse warming. *Nature*, 510(7504):254–258. ISSN 14764687. doi: 10.1038/nature13327.

Cai, W., Santoso, A., Wang, G., Yeh, S. W., An, S. I., Cobb, K. M., Collins, M., Guilyardi, E., Jin, F. F., Kug, J. S., Lengaigne, M., Mcphaden, M. J., Takahashi, K., Timmermann, A., Vecchi, G.,

Watanabe, M., and Wu, L. 2015. ENSO and greenhouse warming. *Nature Climate Change*, 5(9):849–859. ISSN 17586798. doi: 10.1038/nclimate2743.

Campagne, P., Crosta, X., Houssais, M., Swingedouw, D., Schmidt, S., Martin, A., Devred, E., Capo, S., Marieu, V., Closset, I., and Massé, G. 2015. Glacial ice and atmospheric forcing on the Mertz Glacier Polynya over the past 250 years. *Nature Communications*, 6(6642). ISSN 2041-1723. doi: 10.1038/ncomms7642.

Capotondi, A., Wittenberg, A. T., Newman, M., Di Lorenzo, E., Yu, J. Y., Braconnot, P., Cole, J., Dewitte, B., Giese, B., Guilyardi, E., Jin, F. F., Karnauskas, K., Kirtman, B., Lee, T., Schneider, N., Xue, Y., and Yeh, S. W. 2015. Understanding enso diversity. *Bulletin of the American Meteorological Society*, 96(6):921–938. ISSN 00030007. doi: 10.1175/BAMS-D-13-00117.1.

Carré, M., Sachs, J. P., Purca, S., Schauer, A. J., Braconnot, P., Falcón, R. A., Julien, M., and Lavallée, D. 2014. Holocene history of ENSO variance and asymmetry in the eastern tropical Pacific. *Science*, 345(6200):1045–1047. ISSN 10959203. doi: 10.1126/science.1252220.

Carter, L., McCave, I. N., and Williams, M. J. 2008. Chapter 4 Circulation and Water Masses of the Southern Ocean: A Review. *Developments in Earth and Environmental Sciences*, 8(08): 85–114. ISSN 15719197. doi: 10.1016/S1571-9197(08)00004-9.

Cavalieri, D. J. and Martin, S. A passive microwave study of polynyas along the Antarctic Wilkes Land coast. pages 227–252. American Geophysical Union (AGU), 1985. doi: 10.1029/AR043p0227.

Chiu, L. S. Antarctic Sea Ice Variations 1973–1980. In *Variations in the Global Water Budget*, pages 301–311. Springer Netherlands, Dordrecht, 1983. doi: 10.1007/978-94-009-6954-4{_}23.

Ciasto, L. M., Simpkins, G. R., England, M. H., Ciasto, L. M., Simpkins, G. R., and England, M. H. 2015. Teleconnections between Tropical Pacific SST Anomalies and Extratropical Southern Hemisphere Climate. *Journal of Climate*, 28(1):56–65. ISSN 0894-8755. doi: 10.1175/JCLI-D-14-00438.1.

Clark, P. U., Dyke, A. S., Shakun, J. D., Carlson, A. E., Clark, J., Wohlfarth, B., Mitrovica, J. X., Hostetler, S. W., and Mccabe, A. M. The Last Glacial Maximum. Technical report.

Clem, K. R., Renwick, J. A., and McGregor, J. 2018. Autumn Cooling of Western East Antarctica Linked to the Tropical Pacific. *Journal of Geophysical Research: Atmospheres*, 123(1):89–107. ISSN 2169897X. doi: 10.1002/2017JD027435.

Comiso, J. C., McClain, C. R., Sullivan, C. W., Ryan, J. P., and Leonard, C. L. 1993. Coastal Zone Color Scanner pigment concentrations in the Southern Ocean and relationships to geophysical surface features. *Journal of Geophysical Research*, 98(C2):2419–2451. ISSN 01480227. doi: 10.1029/92JC02505.

Conway, H., Hall, B., Denton, G., Gades, A., and Waddington, E. 1999. Past and Future Grounding-Line Retreat of the West Antarctic Ice Sheet. *Science*, 286(5438):280–283. ISSN 00368075. doi: 10.1126/science.286.5438.280.

Cook, C. P., Hill, D. J., Van De Flierdt, T., Williams, T., Hemming, S. R., Dolan, A. M., Pierce, E. L., Escutia, C., Harwood, D., Cortese, G., and Gonzales, J. J. 2014. Sea surface temperature control on the distribution of far-traveled Southern Ocean ice-rafted detritus during the Pliocene. *Paleoceanography*, 29(6):533–548. ISSN 19449186. doi: 10.1002/2014PA002625.

Cooper, L. W., Grebmeier, J. M., Larsen, I. L., Egorov, V. G., Theodorakis, C., Kelly, H. P., and Lovvorn, J. R. 2002. Seasonal variation in sedimentation of organic materials in the St. Lawrence Island polynya region, Bering Sea. *Marine Ecology Progress Series*, 226(March 2014):13–26. ISSN 01718630. doi: 10.3354/meps226013.

Costa, E., Dunbar, R. B., Kryc, K. A., Mucciarone, D. A., Brachfeld, S., Roark, E. B., Manley, P. L., Murray, R. W., and Leventer, A. 10th Internacional Symposium on Antarctic Earth Sciences. In *Online Proceedings of the 10th ISAES X, edited by A. K. Cooper and C. R. Raymond et al., USGS Open-File Report 2007-1047, Short Research Paper 036*, page 6, 2007. doi: 10.3133/of2007-1047.srp036.

Costanza, C. A., Lazzara, M. A., Keller, L. M., and Cassano, J. J. 2016. The surface climatology of the Ross Ice Shelf Antarctica. *International Journal of Climatology*, 36(15):4929–4941. ISSN 10970088. doi: 10.1002/joc.4681.

Cougnon, E. A., Galton-Fenzi, B. K., Rintoul, S. R., Legrésy, B., Williams, G. D., Fraser, A. D., and Hunter, J. R. 2017. Regional Changes in Icescape Impact Shelf Circulation and Basal Melting. *Geophysical Research Letters*, 44(22):519–11. ISSN 19448007. doi: 10.1002/2017GL074943.

Crosta, X., Denis, D., and Ther, O. 2008. Sea ice seasonality during the Holocene, Adélie Land, East Antarctica. *Marine Micropaleontology*. ISSN 03778398. doi: 10.1016/j.marmicro.2007.10.001.

Crosta, X., Debret, M., Denis, D., Courty, M. A., and Ther, O. 2007. Holocene long-and short-term climate changes off Adélie Land, East Antarctica. *Geochemistry Geophysics Geosystems*, 8(11):1–15. ISSN 1525-2027. doi: 10.1029/2007GC001718.

Davies, S. M. 2015. Cryptotephras: The revolution in correlation and precision dating. *Journal of Quaternary Science*, 30(2):114–130. ISSN 10991417. doi: 10.1002/jqs.2766.

de Leeuw, G., Andreas, E. L., Anguelova, M. D., Fairall, C. W., Lewis, E. R., Dowd, C. O., Schulz, M., and Schwartz, S. E. 2011. Production Flux of Sea Spray Aerosol. *Reviews of Geophysics*, 49(2010):1–39. ISSN 8755-1209. doi: 10.1029/2010RG000349.1.INTRODUCTION.

De Vernal, A., Gersonde, R., Goosse, H., Seidenkrantz, M. S., and Wolff, E. W. 2013. Sea ice in the paleoclimate system: The challenge of reconstructing sea ice from proxies - an introduction. *Quaternary Science Reviews*, 79:1–8. ISSN 02773791. doi: 10.1016/j.quascirev.2013.08.009.

Deacon, G. E. R. 1937. The Hydrology of the Southern Ocean. *Discovery Reports*, 15:3–122.

Death, R., Wadham, J. L., Monteiro, F., Le Brocq, A. M., Tranter, M., Ridgwell, A., Dutkiewicz, S., and Raiswell, R. 2014. Antarctic ice sheet fertilises the Southern Ocean. *Biogeosciences*, 11:2635–2644. doi: 10.5194/bg-11-2635-2014.

Deb, P., Dash, M. K., and Pandey, P. C. 2014. Effect of Pacific warm and cold events on the sea ice behavior in the Indian sector of the Southern Ocean. *Deep Sea Research Part I: Oceanographic Research Papers*, 84:59–72. ISSN 0967-0637. doi: 10.1016/J.DSR.2013.10.002.

DeConto, R. M. and Pollard, D. 2016. Contribution of Antarctica to past and future sea-level rise. *Nature*, 531(7596):591–597. ISSN 0028-0836. doi: 10.1038/nature17145.

DeJong, H. B., Dunbar, R. B., and Lyons, E. A. 2018. Late Summer Frazil Ice-Associated Algal Blooms around Antarctica. *Geophysical Research Letters*, 45(2):826–833. ISSN 19448007. doi: 10.1002/2017GL075472.

Denis, D., Crosta, X., Zaragosi, S., Romero, O., Martin, B., and Mas, V. 2006. Seasonal and subseasonal climate changes recorded in laminated diatom ooze sediments,

Adélie Land, East Antarctica. *The Holocene*, 16(8):1137–1147. ISSN 0959-6836. doi: 10.1177/0959683606069414.

Denis, D., Crosta, X., Schmidt, S., Carson, D. S., Ganeshram, R. S., Renssen, H., Bout-Roumazeilles, V., Zaragosi, S., Martin, B., Cremer, M., and Giraudeau, J. 2009a. Holocene glacier and deep water dynamics, Adélie Land region, East Antarctica. *Quaternary Science Reviews*, 28(13-14):1291–1303. ISSN 02773791. doi: 10.1016/j.quascirev.2008.12.024.

Denis, D., Crosta, X., Schmidt, S., Carson, D. S., Ganeshram, R. S., Renssen, H., Crespin, J., Ther, O., Billy, I., and Giraudeau, J. 2009b. Holocene productivity changes off Adélie Land (East Antarctica). *Paleoceanography*, 24(3).

Denis, D., Crosta, X., Barbara, L., Massé, G., Renssen, H., Ther, O., and Giraudeau, J. 2010. Sea ice and wind variability during the Holocene in East Antarctica: insight on middle–high latitude coupling. *Quaternary Science Reviews*, 29(27-28):3709–3719. ISSN 0277-3791. doi: 10.1016/J.QUASCIREV.2010.08.007.

Depoorter, M. A., Bamber, J. L., Griggs, J. A., Lenaerts, J. T. M., Ligtenberg, S. R. M., Van Den Broeke, M. R., and Moholdt, G. 2013. Calving fluxes and basal melt rates of Antarctic ice shelves. *Nature*, 502:89–93. doi: 10.1038/nature12567.

Devries, T. 2014. The oceanic anthropogenic CO 2 sink: Storage, air-sea fluxes, and transports over the industrial era. *Global Biogeochemical Cycles*, 28(7):631–647. ISSN 19449224. doi: 10.1002/2013GB004739.

Di Roberto, A., Colizza, E., Del Carlo, P., Petrelli, M., Finocchiaro, F., and Kuhn, G. 2019. First marine cryptotephra in Antarctica found in sediments of the western Ross Sea correlates with englacial tephras and climate records. *Scientific Reports*, 9(1). ISSN 2045-2322. doi: 10.1038/s41598-019-47188-3.

Dickson, A. J., Leng, M. J., Maslin, M. A., and Röhl, U. 2010. Oceanic, atmospheric and ice-sheet forcing of South East Atlantic Ocean productivity and South African monsoon intensity during MIS-12 to 10. *Quaternary Science Reviews*. ISSN 02773791. doi: 10.1016/j.quascirev.2010.09.014.

Ding, Q., Steig, E. J., Battisti, D. S., and Küttel, M. 2011. Winter warming in West Antarctica caused by central tropical Pacific warming. *Nature Geoscience*, 4(6):398–403. ISSN 17520894. doi: 10.1038/ngeo1129.

Dinniman, M. S., Klinck, J. M., and Smith, W. O. 2011. A model study of Circumpolar Deep Water on the West Antarctic Peninsula and Ross Sea continental shelves. *Deep-Sea Research II*, 58:1508–1523.

Dinniman, M. S., Klinck, J. M., and Hofmann, E. E. 2012. Sensitivity of circumpolar deep water transport and ice shelf basal melt along the west antarctic peninsula to changes in the winds. *Journal of Climate*, 25(14):4799–4816. ISSN 08948755. doi: 10.1175/JCLI-D-11-00307.1.

DiTullio, G. R. and Smith, W. O. 1995. Relationship between dimethylsulfide and phytoplankton pigment concentrations in the Ross Sea, Antarctica. *Deep-Sea Research Part I*, 42(6):873–892. ISSN 09670637. doi: 10.1016/0967-0637(95)00051-7.

Dixon, D. A., Mayewski, P. A., Goodwin, I. D., Marshall, G. J., Freeman, R., Maasch, K. A., and Sneed, S. B. 2012. An ice-core proxy for northerly air mass incursions into West Antarctica. *International Journal of Climatology*, 32(10):1455–1465. ISSN 08998418. doi: 10.1002/joc.2371.

Domack, E. W., Leventer, A., Dunbar, R. B., Taylor, F., Brachfeld, S., and Sjunneskog, C. 2001. Chronology of the Palmer Deep site, Antarctic Peninsula: A Holocene palaeoenvironmental reference for the circum-Antarctic. *Holocene*, 11(1):1–9. ISSN 09596836. doi: 10.1191/095968301673881493.

Donders, T. H., Wagner, F., Dilcher, D. L., and Visscher, H. 2005. Mid- to late-Holocene El Nino-Southern Oscillation dynamics reflected in the subtropical terrestrial realm. *Proceedings of the National Academy of Sciences of the United States of America*, 102(31):10904–8. ISSN 0027-8424. doi: 10.1073/pnas.0505015102.

Donders, T. H., Wagner-Cremer, F., and Visscher, H. 2008. Integration of proxy data and model scenarios for the mid-Holocene onset of modern ENSO variability. *Quaternary Science Reviews*, 27(5-6):571–579. ISSN 0277-3791. doi: 10.1016/J.QUASCIREV.2007.11.010.

Dragon, A.-C., Houssais, M.-N., Herbaut, C., and Charrassin, J.-B. 2014. A note on the intraseasonal variability in an Antarctic polynia: Prior to and after the Mertz Glacier calving. *Journal of Marine Systems*, 130:46–55. ISSN 0924-7963. doi: https://doi.org/10.1016/j.jmarsys.2013.06.006.

Dunbar, R. B., Anderson, J. B., Domack, E. W., and Jacobs, S. S. Oceanographic influences on sedimentation along the Antarctic continental shelf. In Jacobs, S. S., editor, *Oceanology*

of the Antarctic continental shelf, pages 309–312. American Geophysical Union, 43 edition, 1985. doi: 10.1029/AR043p0291.

Dunbar, R. B., Leventer, A. R., and Mucciarone, D. A. 1998. Water column sediment fluxes in the Ross Sea, Antarctica: Atmospheric and sea ice forcing. *Journal of Geophysical Research: Oceans*, 103(C13):30741–30759. ISSN 2169-9291. doi: 10.1029/1998jc900001.

Eayrs, C., Holland, D., Francis, D., Wagner, T., Kumar, R., and Li, X. 2019. Understanding the Seasonal Cycle of Antarctic Sea Ice Extent in the Context of Longer [U+2010] Term Variability. *Reviews of Geophysics*, 2018:1–28. ISSN 8755-1209. doi: 10.1029/2018rg000631.

Eittreim, S. L., Cooper, A. K., and Wannesson, J. 1995. Seismic stratigraphic evidence of ice-sheet advances on the Wilkes Land margin of Antarctica. *Sedimentary Geology*, 96(1-2): 131–156. ISSN 0037-0738. doi: 10.1016/0037-0738(94)00130-M.

Ekman, V. W. 1905. On the influence of the Earth's Rotation on Ocean-Currents. *Arkiv For Matematik, Astronomi Och Fysik.*, 2:1–52. ISSN 10960783. doi: 10.1016/0022-1236(71)90006-1.

Eling, L. 2019. *Early Holocene Antarctic climate variability- drivers and consequences by major ions in the Roosevelt Island Climate Evolution (RICE) ice core*. PhD thesis, Victoria University of Wellington.

Emanuelsson, B. D., Baisden, W. T., Bertler, N. A., Keller, E. D., Gkinis, V., and to, C. 2015. High-resolution continuous-flow analysis setup for water isotopic measurement from ice cores using laser spectroscopy. *Atmos. Meas. Tech*, 8:2869–2883. doi: 10.5194/amt-8-2869-2015.

Emanuelsson, B. D. 2016. High-Resolution Water Stable Isotope Ice-Core Record : Roosevelt Island , Antarctica Victoria University of Wellington , 2016.

Emanuelsson, B. D., Bertler, N. A., Neff, P. D., Renwick, J. A., Markle, B. R., Baisden, W. T., and Keller, E. D. 2018. The role of Amundsen–Bellingshausen Sea anticyclonic circulation in forcing marine air intrusions into West Antarctica. *Climate Dynamics*, 51(9-10):3579–3596. ISSN 14320894. doi: 10.1007/s00382-018-4097-3.

Endo, S. and Tozuka, T. 2016. Two flavors of the Indian Ocean Dipole. *Climate Dynamics*, 46 (11-12):3371–3385. ISSN 14320894. doi: 10.1007/s00382-015-2773-0.

Escutia, C., Brinkhuis, H., Klaus, A., and Scientists, E. . Site U1357. Technical report, 2011.

Favier, L., Durand, G., Cornford, S. L., Gudmundsson, G. H., Gagliardini, O., Gillet-Chaulet, F., Zwinger, T., Payne, A. J., and Le Brocq, A. M. 2014. Retreat of Pine Island Glacier controlled by marine ice-sheet instability. *Nature Climate Change*, 5. doi: 10.1038/NCLIMATE2094.

Fetterer, F., Knowles, K., Meier, W., and Savoie, M., 2017. Sea Ice Index, Version 3 (updated daily).

Fogt, R. L., Bromwich, D. H., and Hines, K. M. 2011. Understanding the SAM influence on the South Pacific ENSO teleconnection. *Climate Dynamics*, 36(7-8):1555–1576. ISSN 0930-7575. doi: 10.1007/s00382-010-0905-0.

Foster, T. D. and Carmack, E. C. 1976. Frontal zone mixing and Antarctic Bottom water formation in the southern Weddell Sea. *Deep-Sea Research and Oceanographic Abstracts*. ISSN 00117471. doi: 10.1016/0011-7471(76)90872-X.

Fretwell, P., Pritchard, H. D., Vaughan, D. G., Bamber, J. L., Barrand, N. E., Bell, R., Bianchi, C., Bingham, R. G., Blankenship, D. D., Casassa, G., Catania, G., Callens, D., Conway, H., Cook, A. J., Corr, H. F., Damaske, D., Damm, V., Ferraccioli, F., Forsberg, R., Fujita, S., Gim, Y., Gogineni, P., Griggs, J. A., Hindmarsh, R. C., Holmlund, P., Holt, J. W., Jacobel, R. W., Jenkins, A., Jokat, W., Jordan, T., King, E. C., Kohler, J., Krabill, W., Riger-Kusk, M., Langley, K. A., Leitchenkov, G., Leuschen, C., Luyendyk, B. P., Matsuoka, K., Mouginot, J., Nitsche, F. O., Nogi, Y., Nost, O. A., Popov, S. V., Rignot, E., Rippin, D. M., Rivera, A., Roberts, J., Ross, N., Siegert, M. J., Smith, A. M., Steinhage, D., Studinger, M., Sun, B., Tinto, B. K., Welch, B. C., Wilson, D., Young, D. A., Xiangbin, C., and Zirizzotti, A. 2013. Bedmap2: Improved ice bed, surface and thickness datasets for Antarctica. *Cryosphere*, 7(1):375–393. ISSN 19940416. doi: 10.5194/tc-7-375-2013.

Fujino, K., Lewis, E. L., and Perkin, R. G. 1974. FREEZING POINT OF SEAWATER AT PRESSURES UP TO 100 BARS. *J Geophys Res*, 79(12):1792–1797. doi: 10.1029/JC079i012p01792.

Fukamachi, Y., Wakatsuchi, M., Taira, K., Kitagawa, S., Furukawa, T., and Fukuchi, M. 2000. Seasonal variability of bottom water properties off Adlie Land , Antarctica. *Journal of Climate*, 105(C3):6531–6540.

Gallagher, C., Lund, R., and Robbins, M. 2013. Changepoint Detection in Climate Time Series with Long-Term Trends. *Journal of Climate*, 26(14):4994–5006. ISSN 0894-8755. doi: 10.1175/JCLI-D-12-00704.1.

Gergis, J., Braganza, K., Fowler, A., Mooney, S., and Risbey, J. S. 2006. Reconstructing El Niño–Southern Oscillation (ENSO) from high-resolution palaeoarchives. *Journal of Quaternary Science*, 21(7):707–722. ISSN 0267-8179. doi: 10.1002/jqs.1070.

Gerringa, L. J., Alderkamp, A.-C., Laan, P., Thuróczy, C.-E., De Baar, H. J., Mills, M. M., van Dijken, G. L., and Haren, H. v. 2012. Iron from melting glaciers fuels the phytoplankton blooms in Amundsen Sea (Southern Ocean): Iron biogeochemistry. *Deep Sea Research Part II: Topical Studies in Oceanography*, 71-76:16–31. ISSN 0967-0645. doi: 10.1016/J.DSR2.2012.03.007.

Gill, A. E. 1973. Circulation and bottom water production in the Weddell Sea. *Deep-Sea Research and Oceanographic Abstracts*. ISSN 00117471. doi: 10.1016/0011-7471(73)90048-X.

Goldberg, E. D. and G.O.S., A. 1958. Chemistry of Pacific pelagic sediments. *Geochimica et Cosmochimica Acta*. ISSN 00167037. doi: 10.1016/0016-7037(58)90046-2.

Golledge, N. R., Menviel, L., Carter, L., Fogwill, C. J., England, M. H., Cortese, G., and Levy, R. H. 2014. Antarctic contribution to meltwater pulse 1A from reduced Southern Ocean overturning. *Nature Communications*, 5:1–10. ISSN 2041-1723. doi: 10.1038/ncomms6107.

Golledge, N. R., Kowalewski, D. E., Naish, T. R., Levy, R. H., Fogwill, C. J., and Gasson, E. G. W. 2015. The multi-millennial Antarctic commitment to future sea-level rise. *Nature*, 526 (7573):421–425. ISSN 0028-0836. doi: 10.1038/nature15706.

Gong, D. and Wang, S. 1999. Definition of Antarctic oscillation index. *Geophysical Research Letters*, 26(4):459–462. ISSN 00948276. doi: 10.1029/1999GL900003.

Goodwin, I. D. 1993. Holocene deglaciation, sea-level change, and the emergence of the Windmill Islands, Budd Coast, Antarctica. *Quaternary Research*. ISSN 00335894. doi: 10.1006/qres.1993.1057.

Gordon, A. L., Huber, B. A., Hellmer, H. H., and Ffield, A. 1993. Deep and Bottom Water of the Weddell Sea's Western Rim. *Science*, 262(5130):95–97. ISSN 0036-8075. doi: 10.1126/science.262.5130.95.

Gordon, A. L. 1975. An Antarctic oceanographic section along 170°E. *Deep-Sea Research and Oceanographic Abstracts*, 22(6). ISSN 00117471. doi: 10.1016/0011-7471(75)90060-1.

Gordon, A. L. and Tchernia, P. 1972. Waters of the Continental Margin off Adelie Coast, Antarctica. *Antarctic Oceanology II: The Australian-New Zealand Sector, Antarctic Research Series*, 19:59–69.

Gordon, J. E. and Harkness, D. D. 1992. Magnitude and geographic variation of the radiocarbon content in Antarctic marine life: Implications for reservoir corrections in radiocarbon dating. *Quaternary Science Reviews*. ISSN 02773791. doi: 10.1016/0277-3791(92)90078-M.

Gordon, L. I., Codispoti, L. A., Jennings, J., Millero, F. J., Morrison, J. M., and Sweeney, C. 2000. Seasonal evolution of hydrographic properties in the Ross Sea, Antarctica, 1996-1997. *Deep-Sea Research Part II: Topical Studies in Oceanography*. ISSN 09670645. doi: 10.1016/S0967-0645(00)00060-6.

Grazioli, J., Genthon, C., Boudevillain, B., Duran-alarcon, C., Guasta, M. D., Madeleine, J.-b., and Berne, A. 2017. Measurements of precipitation in Dumont d 'Urville, Adélie Land, East Antarctica. *The Cryosphere*, 11:1797–1811.

Greenwood, S. L., Simkins, L. M., Halberstadt, A. R. W., Prothro, L. O., and Anderson, J. B. 2018. Holocene reconfiguration and readvance of the East Antarctic Ice Sheet. *Nature Communications*, 9(1):1–12. ISSN 20411723. doi: 10.1038/s41467-018-05625-3.

Gruber, N., Landschützer, P., and Lovenduski, N. S. 2019. The Variable Southern Ocean Carbon Sink. *Annual Review of Marine Science*, 11:159–186. ISSN 23752548. doi: https://doi.org/10.1146/annurev-marine-121916-063407.

Guelle, W., Schulz, M., Balkanski, Y., and Dentener, F. 2001. Influence of the source formulation on modeling the atmospheric global distribution of sea salt aerosol. *Journal of Geophysical Research Atmospheres*, 106(D21):27509–27524. ISSN 01480227. doi: 10.1029/2001JD900249.

Hagadorn, J. W. 1996. Laminated sediments of Santa Monica Basin, California continental borderland. *Geological Society Special Publication*, 116:111–120. ISSN 03058719. doi: 10.1144/GSL.SP.1996.116.01.11.

Halberstadt, A. R. W., Simkins, L. M., Greenwood, S. L., and Anderson, J. B. 2016. Past ice-sheet behaviour: retreat scenarios and changing controls in the Ross Sea, Antarctica. *The Cryosphere*, 10(3):1003–1020. ISSN 1994-0424. doi: 10.5194/tc-10-1003-2016.

Hall, A. and Visbeck, M. 2002. Synchronous variability in the Southern Hemisphere atmosphere, sea ice, and ocean resulting from the annular mode. *Journal of Climate*, 15(21): 3043–3057. ISSN 08948755. doi: 10.1175/1520-0442(2002)015<3043:SVITSH>2.0.CO;2.

Hall, B. L., Denton, G. H., Stone, J. O., and Conway, H. 2013. History of the grounded ice sheet in the Ross Sea sector of Antarctica during the last glacial maximum and the last termination. *Geological Society Special Publication*, 381(1):167–181. ISSN 03058719. doi: 10.1144/SP381.5.

Hara, K., Osada, K., Yabuki, M., and Yamanouchi, T. 2012. Seasonal variation of fractionated sea-salt particles on the Antarctic coast. *Geophysical Research Letters*, 39(17):1–5. ISSN 00948276. doi: 10.1029/2012GL052761.

Hara, K., Matoba, S., Hirabayashi, M., and Yamasaki, T. 2017. Frost flowers and sea-salt aerosols over seasonal sea-ice areas in northwestern Greenland during winter-spring. *Atmospheric Chemistry and Physics*, 17(13):8577–8598. ISSN 16807324. doi: 10.5194/acp-17-8577-2017.

Harris, P. T. and Beaman, R. J. 2003. Processes controlling the formation of the Mertz Drift, George Vth continental shelf, East Antarctica: Evidence from 3.5 kHz sub-bottom profiling and sediment cores. *Deep-Sea Research Part II: Topical Studies in Oceanography*. ISSN 09670645. doi: 10.1016/S0967-0645(03)00070-5.

Haumann, F. A., Notz, D., and Schmidt, H. 2014. Anthropogenic influence on recent circulation-driven Antarctic sea ice changes. *Geophysical Research Letters*, 41(23):8429–8437. ISSN 00948276. doi: 10.1002/2014GL061659.

Hellmer, H. H. 2004. Impact of Antarctic ice shelf basal melting on sea ice and deep ocean properties. *Geophysical Research Letters*, 31(L10307):1–4. ISSN 00948276. doi: 10.1029/2004GL019506.

Henley, B. J., Gergis, J., Karoly, D. J., Power, S., Kennedy, J., and Folland, C. K. 2015. A Tripole Index for the Interdecadal Pacific Oscillation. *Climate Dynamics*, 45(11-12):3077–3090. ISSN 14320894. doi: 10.1007/s00382-015-2525-1.

Heywood, K. J., Locarnini, R. A., Frew, R. D., Dennis, P. F., and King, B. A. 1998. Transport and Water Masses of the Antarctic Slope Front System in The Eastern Weddell Sea. Number 75. AGU, Washington, D.C. doi: 10.1029/ar075p0203.

Heywood, K. J., Naveira Garabato, A. C., Stevens, D. P., and Muench, R. D. 2004. On the fate of the Antarctic Slope Front and the origin of the Weddell Front. *Journal of Geophysical Research C: Oceans*, 109(6):1–13. ISSN 01480227. doi: 10.1029/2003JC002053.

Hillenbrand, C.-D., Smith, J. A., Hodell, D. A., Greaves, M., Poole, C. R., Kender, S., Williams, M., Andersen, T. J., Jernas, P. E., Elderfield, H., Klages, J. P., Roberts, S. J., Gohl, K., Larter, R. D., and Kuhn, G. 2017. West Antarctic Ice Sheet retreat driven by Holocene warm water incursions. *Nature*, 547(7661):43–48. ISSN 0028-0836. doi: 10.1038/nature22995.

Ho, M., Kiem, A. S., and Verdon-Kidd, D. C. 2012. The Southern Annular Mode: A comparison of indices. *Hydrology and Earth System Sciences*, 16(3):967–982. ISSN 10275606. doi: 10.5194/hess-16-967-2012.

Hoegh-Guldberg, O., Jacob, D., Taylor, M., Bindi, M., Brown, S., Camilloni, I., Diedhiou, A., Djalante, R., Ebi, K., Engelbrecht, F., J. Guiot, Hijioka, Y., Mehrotra, S., Payne, A., Seneviratne, S., Thomas, A., Warren, R., and Zhou, G. 2018. Impacts of 1.5°C of Global Warming on Natural and Human Systems. *Global Warming of 1.5°C. An IPCC SPECIAL REPORT Global Warming of 1.5°C above pre-industrial levels and related global greenhouse gas emission pathways, in the context of strengthening the global response to the threat of climate change.*, 177: 175–311.

Holland, M. M., Landrum, L., Kostov, Y., and Marshall, J. 2017. Sensitivity of Antarctic sea ice to the Southern Annular Mode in coupled climate models. *Climate Dynamics*, 49(5-6): 1813–1831. ISSN 14320894. doi: 10.1007/s00382-016-3424-9.

Holland, P. R. and Kwok, R. 2012. Wind-driven trends in Antarctic sea-ice drift. *Nature Geoscience*, 5(12):872–875. ISSN 1752-0894. doi: 10.1038/ngeo1627.

HorosProject.org, 2017. Horos Project.

Hosking, J. S., Orr, A., Marshall, G. J., Turner, J., and Phillips, T. 2013. The influence of the amundsen-bellingshausen seas low on the climate of West Antarctica and its representation in coupled climate model simulations. *Journal of Climate*, 26(17):6633–6648. ISSN 08948755. doi: 10.1175/JCLI-D-12-00813.1.

Hosking, S. and National Center for Atmospheric Research Staff, 2019. The Climate Data Guide: Amundsen Sea Low Indices.

Hounsfield, G. N. 1973. Computerized transverse axial scanning (tomography): Part I. Description of system. *British Journal of Radiology*, 46:1016–1022.

Hurwitz, M. M., Newman, P. A., Oman, L. D., and Molod, A. M. 2011. Response of the antarctic stratosphere to two types of el niño events. *Journal of the Atmospheric Sciences*, 68(4):812–822. ISSN 00224928. doi: 10.1175/2011JAS3606.1.

IPCC. 2019. Special Report: The Ocean and Cryosphere in a Changing Climate. (September): in preparation. doi: https://www.ipcc.ch/report/srocc/.

Iwasaki, S., Takahashi, K., Ogawa, Y., Uehara, S., and Vogt, C. 2014. Alkaline leaching characteristics of biogenic opal in Eocene sediments from the central Arctic Ocean: A case study in the ACEX cores. *Journal of Oceanography*, 70(3):241–249. ISSN 09168370. doi: 10.1007/s10872-014-0227-7.

Izumo, T., Vialard, J., Lengaigne, M., De Boyer Montegut, C., Behera, S. K., Luo, J. J., Cravatte, S., Masson, S., and Yamagata, T. 2010. Influence of the state of the Indian Ocean Dipole on the following years El Nĩo. *Nature Geoscience*, 3(3):168–172. ISSN 17520894. doi: 10.1038/ngeo760.

Jacobs, S., Giulivi, C., Dutrieux, P., Rignot, E., Nitsche, F., and Mouginot, J. 2013. Getz Ice Shelf melting response to changes in ocean forcing. *Journal of Geophysical Research: Oceans*, 118(9):4152–4168. ISSN 21699291. doi: 10.1002/jgrc.20298.

Jacobs, S. S. and Giulivi, C. F. Thermohaline Data and Ocean Circulation on the Ross Sea Continental Shelf. In *Oceanography of the Ross Sea Antarctica*, pages 3–16. Springer Milan, Milano, 1999. doi: 10.1007/978-88-470-2250-8{_}1.

Jacobs, S. S. 1991. On the nature and significance of the Antarctic Slope Front. *Marine Chemistry*, 35(1-4):9–24. ISSN 03044203. doi: 10.1016/S0304-4203(09)90005-6.

Jacobs, S. S. 2004. Bottom water production and its links with the thermohaline circulation. *Antarctic Science*, 16(4):427–437. ISSN 0954-1020. doi: 10.1017/S095410200400224X.

Jacobs, S. S. and Comiso, J. C. 1989. Sea ice and oceanic processes on the Ross Sea continental shelf. *Journal of Geophysical Research*, 94(C12):18195. ISSN 0148-0227. doi: 10.1029/JC094iC12p18195.

Jacobs, S. S. and Giulivi, C. F. Interannual ocean and sea ice variability in the Ross Sea. In *Ocean, Ice, and Atmosphere: Interactions at the Antarctic Continental Margin*, volume 75, pages 135–150. 1998. ISBN 9781118668238. doi: 10.1029/AR075p0135.

Jacobs, S. S. and Giulivi, C. F. 2010. Large multidecadal salinity trends near the Pacific-Antarctic continental margin. *Journal of Climate*, 23(17):4508–4524. ISSN 08948755. doi: 10.1175/2010JCLI3284.1.

Jacobs, S. S., Amos, A. F., and Bruchhausen, P. M. 1970. Ross sea oceanography and antarctic bottom water formation. *Deep-Sea Research and Oceanographic Abstracts*, 17(6):935–962. ISSN 00117471. doi: 10.1016/0011-7471(70)90046-X.

Jacobs, S. S., Helmer, H., Doake, C., Jenkins, A., and Frolich, R. 1992. Melting of ice shelves and the mass balance of Antarctica. *Journal of Glaciology*, 38(130):375–387.

Jacobs, S. S., Hellmer, H. H., and Jenkins, A. 1996. Antarctic ice sheet melting in the Southeast Pacific. *Geophysical Research Letters*, 23(9):957–960.

Jacobs, S. S., Giulivi, C. F., and Mele, P. A. 2002. Freshening of the Ross Sea during the Late 20th Century. *Source: Science, New Series J. Clim. Northwest Sci. J. Clim. Northwest Sci*, 297 (64):386–389.

Jacobs, S. S., Jenkins, A., Giulivi, C. F., and Dutrieux, P. 2011. Stronger ocean circulation and increased melting under Pine Island Glacier ice shelf. *Nature Geoscience*, 4(8):519–523. ISSN 17520894. doi: 10.1038/ngeo1188.

Jenkins, A. Gravity currents beneath ice shelves. In *Glaciers-Ocean-Atmosphere Interactions*, volume 208, pages 177–182. IAHS Publ, 1991.

Jin, D. and Kirtman, B. P. 2009. Why the Southern Hemisphere ENSO responses lead ENSO. *J. Geophys. Res*, 114:23101. doi: 10.1029/2009JD012657.

Jones, R. S., Mackintosh, A. N., Norton, K. P., Golledge, N. R., Fogwill, C. J., Kubik, P. W., Christl, M., and Greenwood, S. L. 2015. Rapid Holocene thinning of an East Antarctic outlet glacier driven by marine ice sheet instability. *Nature Communications*, 6(1):1–9. ISSN 20411723. doi: 10.1038/ncomms9910.

Jonkers, L., Barker, S., Hall, I. R., and Prins, M. A. 2015. Correcting for the influence of ice-rafted detritus on grain size-based paleocurrent speed estimates. *Paleoceanography*, 30(10): 1347–1357. ISSN 19449186. doi: 10.1002/2015PA002830.

Joughin, I. and Alley, R. B. 2011. Stability of the West Antarctic ice sheet in a warming world. *Nature Geoscience*, 4(8):506–513. ISSN 1752-0894. doi: 10.1038/ngeo1194.

Jourdain, N. C., Mathiot, P., Merino, N., Durand, G., Le Sommer, J., Spence, P., Dutrieux, P., and Madec, G. 2017. Ocean circulation and sea-ice thinning induced by melting ice shelves in the Amundsen Sea. *Journal of Geophysical Research: Oceans*, 122(3):2550–2573. ISSN 21699291. doi: 10.1002/2016JC012509.

Kao, H. Y. and Yu, J. Y. 2009. Contrasting Eastern-Pacific and Central-Pacific types of ENSO. *Journal of Climate*, 22(3):615–632. ISSN 08948755. doi: 10.1175/2008JCLI2309.1.

Karamperidou, C., Di Nezio, P. N., Timmermann, A., Jin, F.-F., and Cobb, K. M. 2017. The response of ENSO flavors to mid-Holocene climate: Implications for proxy interpretation. *Paleoceanography*, 30:527–547. ISSN 09729038. doi: 10.1002/2014PA002742.

Karoly, D. J. 1989. Southern Hemisphere Circulation Features Associated with El Niño-Southern Oscillation Events. *Journal of Climate*, 2:1239–1252.

Keene, W. C., Pszenny, A. A. P., Galloway, J. N., and Hawley, M. E. 1986. Sea-salt corrections and interpretation of constituent ratios in marine precipitation. *Journal of Geophysical Research*, 91(D6):6647. ISSN 0148-0227. doi: 10.1029/jd091id06p06647.

Keller, E. D., Troy Baisden, W., Bertler, N. A., Daniel Emanuelsson, B., Canessa, S., and Phillips, A. 2018. Calculating uncertainty for the RICE ice core continuous flow analysis water isotope record. *Atmos. Meas. Tech*, 11:4725–4736. doi: 10.5194/amt-11-4725-2018.

Kemp, A. E. Laminated sediments as palaeo-indicators. Technical report, 1996.

Kidson, J. W. 1999. Principal modes of Southern Hemisphere low-frequency variability obtained from NCEP-NCAR reanalyses. *Journal of Climate*, 12(9):2808–2830. ISSN 08948755. doi: 10.1175/1520-0442(1999)012<2808:PMOSHL>2.0.CO;2.

Killick, R., Fearnhead, P., and Eckley, I. A. 2012. Optimal Detection of Changepoints With a Linear Computational Cost. *Journal of the American Statistical Association*, 107(500):1590–1598. ISSN 0162-1459. doi: 10.1080/01621459.2012.737745.

Killworth, P. D. 1983. Deep convection in the World Ocean. *Reviews of Geophysics*, 21(1):1–26. ISSN 19449208. doi: 10.1029/RG021i001p00001.

King, J. and Turner, J. 1997. Antarctic Meteorology and Climatology. Cambridge University Press, New York. ISBN 0521465605.

Kjær, H. A., Vallelonga, P., Svensson, A., Elleskov Kristensen, M. L., Tibuleac, C., Winstrup, M., and Kipfstuhl, S. 2016. An Optical Dye Method for Continuous Determination of Acidity in Ice Cores. *Environmental Science and Technology*, 50(19):10485–10493. ISSN 15205851. doi: 10.1021/acs.est.6b00026.

König-Langlo, G., King, J. C., and Pettré, P. 1998. Climatology of the three coastal Antarctic stations Dumont d'Urville, Neumayer, and Halley. *Journal of Geophysical Research D: Atmospheres*, 103(3339):10935–10946. ISSN 01480227.

Koutavas, A., Lynch-Stieglitz, J., Marchitto, T. M., and Sachs, J. P. 2002. El Niño-like pattern in ice age tropical Pacific sea surface temperature. *Science*, 297(5579):226–230. ISSN 00368075. doi: 10.1126/science.1072376.

Kreutz, K. J., Mayewski, P. A., Pittalwala, I. I., Meeker, L. D., Twickler, M. S., and Whitlow, S. I. 2000. Sea level pressure variability in the Amundsen Sea region inferred from a West Antarctic glaciochemical record. *Journal of Geophysical Research Atmospheres*, 105(D3):4047–4059. ISSN 01480227. doi: 10.1029/1999JD901069.

Kug, J.-S., Jin, F.-F., An, S.-I., Kug, J.-S., Jin, F.-F., and An, S.-I. 2009. Two Types of El Niño Events: Cold Tongue El Niño and Warm Pool El Niño. *Journal of Climate*, 22(6):1499–1515. ISSN 0894-8755. doi: 10.1175/2008JCLI2624.1.

Kurbatov, A. V., Mayewski, P. A., Steffensen, J. P., West, A., Kennett, D. J., Kennett, J. P., Bunch, T. E., Handley, M., Introne, D. S., Hee, S. S., Mercer, C., Sellers, M., Shen, F., Sneed, S. B., Weaver, J. C., Wittke, J. H., Stafford, T. W., Donovan, J. J., Xie, S., Razink, J. J., Stich, A., Kinzie, C. R., and Wolbach, W. S. 2010. Discovery of a nanodiamond-rich layer in the Greenland ice sheet. *Journal of Glaciology*, 56(199):747–757. ISSN 00221430. doi: 10.3189/002214310794457191.

Kusahara, K., Hasumi, H., and Williams, G. D. 2011. Dense shelf water formation and brine-driven circulation in the Adélie and George V Land region. *Ocean Modelling*, 37(3-4):122–138. ISSN 14635003. doi: 10.1016/j.ocemod.2011.01.008.

Kwok, R. and Comiso, J. C. 2002a. Southern Ocean climate and sea ice anomalies associated with the Southern Oscillation. *Journal of Climate*, 15(5):487–501. ISSN 08948755. doi: 10.1175/1520-0442(2002)015<0487:SOCASI>2.0.CO;2.

Kwok, R. and Comiso, J. C. 2002b. Spatial patterns of variability in Antarctic surface temperature: Connections to the Southern Hemisphere Annular Mode and the Southern Oscillation. *Geophysical Research Letters*, 29(14):50–1. ISSN 00948276. doi: 10.1029/2002GL015415.

Kwok, R., Comiso, J. C., Lee, T., and Holland, P. R. 2016. Linked trends in the South Pacific sea ice edge and Southern Oscillation Index. *Geophysical Research Letters*, 43(19):295–10. ISSN 00948276. doi: 10.1002/2016GL070655.

Lacarra, M., Houssais, M.-N., Herbaut, C., Sultan, E., and Beauverger, M. 2014. Dense shelf water production in Adélie Depression, East Antarctica, 2004-2012: Impact of the Mertz Glacier calving. *Journal of Geophysical Research : Oceans*, 119:5203–5220. doi: 10.1002/2013JC009124.

Lachlan-cope, T. A., Connolley, W. M., and Turner, J. 2001. The Role of the Non-Axisymmetric Antarctic Orography in forcing the Obersved Pattern of Variability of the Antarctic Climate. *Geophysical Research Letters*, 28(21):4111–4114.

Lamy, F., Arz, H. W., Kilian, R., Lange, C. B., Lembke-Jene, L., Wengler, M., Kaiser, J., Baeza-Urrea, O., Hall, I. R., Harada, N., and Tiedemann, R. 2015. Glacial reduction and millennial-scale variations in Drake Passage throughflow. *Proceedings of the National Academy of Sciences of the United States of America*, 112(44):13496–13501. ISSN 10916490. doi: 10.1073/pnas.1509203112.

Lavielle, M. 2005. Using penalized contrasts for the change-point problem. *Signal Processing*, 85:1501–1510. doi: 10.1016/j.sigpro.2005.01.012.

Ledbetter, M. T. 1986a. A Late Pleistocene time-series of bottom-current speed in the Vema Channel. *Palaeogeography, Palaeoclimatology, Palaeoecology*. ISSN 00310182. doi: 10.1016/0031-0182(86)90040-4.

Ledbetter, M. T. 1986b. Bottom-current pathways in the Argentine Basin revealed by mean silt particle size. pages 423–425.

Lee, J. I., McKay, R. M., Golledge, N. R., Yoon, H. I., Yoo, K. C., Kim, H. J., and Hong, J. K. 2017. Widespread persistence of expanded East Antarctic glaciers in the southwest Ross Sea during the last deglaciation. *Geology*, 45(5):403–406. ISSN 19432682. doi: 10.1130/G38715.1.

Lee, J. E., Brook, E. J., Bertler, N. A. N., Buizert, C., Baisden, T., Blunier, T., Ciobanu, V. G., Conway, H., Dahl-Jensen, D., Fudge, T. J., Hindmarsh, R., Keller, E. D., Parrenin, F., Severinghaus, J. P., Vallelonga, P., Waddington, E. D., and Winstrup, M. 2018. An 83,000 year old

ice core from Roosevelt Island, Ross Sea, Antarctica. *Climate of the Past Discussions*, pages 1–44. ISSN 1814-9359. doi: 10.5194/cp-2018-68.

Lee Drbohlav, H. K., Gualdi, S., and Navarra, A. A diagnostic study of the Indian Ocean dipole mode in El Niño and non-El Niño years. In *Journal of Climate*, volume 20, pages 2961–2977, 2007. doi: 10.1175/JCLI4153.1.

Legrand, M. and Mayewski, P. A. 1997. Glaciochemistry of polar ice cores: A review. *Reviews of Geophysics*, 35(3):219–243. ISSN 8755-1209. doi: 10.1029/96RG03527.

Lenton, A. and Matear, R. J. 2007. Role of the Southern Annular Mode (SAM) in Southern Ocean CO2 uptake. *Global Biogeochemical Cycles*, 21(2). ISSN 08866236. doi: 10.1029/2006GB002714.

Lenton, T. M., Held, H., Kriegler, E., Hall, J. W., Lucht, W., Rahmstorf, S., and Schellnhuber, H. J., 2008. Tipping elements in the Earth's climate system. ISSN 00278424.

Leventer, A., Dunbar, R. B., and DeMaster, D. J. 1993. Diatom Evidence for Late Holocene Climatic Events in Granit Harbor, Antarctica. *Paloceanography*, 8(3):373–386.

Leventer, A., Domack, E., Barkoukis, A., McAndrews, B., and Murray, J. 2002. Laminations from the Palmer Deep: A diatom-based interpretation. *Paleoceanography*, 17(3):3–1. ISSN 0883-8305. doi: 10.1029/2001pa000624.

Leventer, A., Domack, E. W., Dunbar, R. B., Pike, J., Stickley, C., Maddison, E. J., Brachfeld, S., Manley, P., and McClennen, C. E. 2006. Marine sediment record from the East Antarctic margin reveals dynamics of ice sheet recession. *GSA TODAY*, 16(12). doi: 10.1130/GSAT01612A.1.

Levine, J. G., Yang, X., Jones, A. E., and Wolff, E. W. 2014. Sea salt as an ice core proxy for past sea ice extent: A process-based model study. *Journal of Geophysical Research: Atmospheres*, 119(9):5737–5756. ISSN 2169897X. doi: 10.1002/2013JD020925.

L'Heureux, M. L. and Thompson, D. W. J. 2006. Observed relationships between the El-Niño-Southern oscillation and the extratropical zonal-mean circulation. *Journal of Climate*, 19(1): 276–287. ISSN 08948755. doi: 10.1175/JCLI3617.1.

Limpasuvan, V. and Hartmann, D. L. 1999. Eddies and the annular modes of climate variability 1. *Geophysical Research Letters*, 26(20):3133–3136. ISSN 00948276. doi: 10.1029/1999gl010478.

Livingstone, S. J., Ó Cofaigh, C., Stokes, C. R., Hillenbrand, C. D., Vieli, A., and Jamieson, S. S. 2012. Antarctic palaeo-ice streams. *Earth-Science Reviews*. ISSN 00128252. doi: 10.1016/j.earscirev.2011.10.003.

Ljungqvist, F. C. 2010. A new reconstruction of temperature variability in the extra-tropical northern hemisphere during the last two millennia. *Geografiska Annaler, Series A: Physical Geography*, 92(3):339–351. ISSN 04353676. doi: 10.1111/j.1468-0459.2010.00399.x.

Lowry, D. P., Golledge, N. R., Bertler, N. A., Selwyn Jones, R., and McKay, R. M. 2019. Deglacial grounding-line retreat in the Ross Embayment, Antarctica, controlled by ocean and atmosphere forcing. *Science Advances*, 5(8). ISSN 23752548. doi: 10.1126/sciadv.aav8754.

Lythe, M. B. and Vaughan, D. G. 2001. BEDMAP: A new ice thickness and subglacial topographic model of Antarctica. *Journal of Geophysical Research: Solid Earth*, 106(B6):11335–11351. doi: 10.1029/2000jb900449.

Mackintosh, A., White, D., Fink, D., Gore, D. B., Pickard, J., and Fanning, P. C. 2007. Exposure ages from mountain dipsticsk in Mac. Robertson Land, East Antarctica, indicate little change in ice-sheet thickness since the Last Glacial Maximum. *Geology*, 35(6):551–554. ISSN 00917613. doi: 10.1130/G23503A.1.

Mackintosh, A., Golledge, N., Domack, E. W., Dunbar, R. B., Leventer, A., White, D., Pollard, D., DeConto, R., Fink, D., Zwartz, D., Gore, D., and Lavoie, C. 2011. Retreat of the East Antarctic ice sheet during the last glacial termination. *Nature Geoscience*, 4(3):195–202. doi: 10.1038/ngeo1061.

Mackintosh, A. N., Verleyen, E., O'Brien, P. E., White, D. A., Jones, R. S., McKay, R. M., Dunbar, R. B., Gore, D. B., Fink, D., Post, A. L., Miura, H., Leventer, A., Goodwin, I., Hodgson, D. A., Lilly, K., Crosta, X., Golledge, N. R., Wagner, B., Berg, S., Van Ommen, T. D., Zwartz, D., Roberts, S. J., Vyverman, W., and Masse, G. 2014. Retreat history of the East Antarctic Ice Sheet since the Last Glacial Maximum. *Quaternary Science Reviews*, 100:10–30. ISSN 0277-3791. doi: 10.1016/J.QUASCIREV.2013.07.024.

Maddison, E. J., Pike, J., and Dunbar, R. B. 2012. Seasonally Laminated diatom-rich sediments from Dumont d'Urville Trough, East Antarctic Margin: Late-Holocene Neoglacial sea-ice conditions. *The Holocene*, 22(8):857–875. doi: 10.1177/0959683611434223.

Magee, A. D., Verdon-Kidd, D. C., Diamond, H. J., and Kiem, A. S. 2017. Influence of ENSO, ENSO Modoki, and the IPO on tropical cyclogenesis: a spatial analysis of the southwest

Pacific region. *International Journal of Climatology*, 37:1118–1137. ISSN 10970088. doi: 10.1002/joc.5070.

Maksym, T. 2019. Arctic and Antarctic Sea Ice Change: Contrasts, Commonalities, and Causes. *Annual Review of Marine Science*, 11(1):187–213. ISSN 1941-1405. doi: 10.1146/annurev-marine-010816-060610.

Mantua, N. J., Hare, S. R., Zhang, Y., Wallace, J. M., and Francis, R. C. 1997. A Pacific Interdecadal Climate Oscillation with Impacts on Salmon Production. *Bulletin of the American Meteorological Society*, 78(6):1069–1079. ISSN 00030007. doi: 10.1175/1520-0477(1997)078<1069:APICOW>2.0.CO;2.

Mao, L., Piper, D. J., Saint-Ange, F., and Andrews, J. T. 2018. Labrador Current fluctuation during the last glacial cycle. *Marine Geology*. ISSN 00253227. doi: 10.1016/j.margeo.2017.10.012.

Marcott, S. A., Shakun, J. D., Clark, P. U., and Mix, A. C. 2013. A reconstruction of regional and global temperature for the past 11,300 years. *Science (New York, N.Y.)*, 339(6124):1198–201. ISSN 1095-9203. doi: 10.1126/science.1228026.

Marsh, R., Mills, R. A., Green, D. R., Salter, I., and Taylor, S. 2007. Controls on sediment geochemistry in the Crozet region. *Deep-Sea Research Part II: Topical Studies in Oceanography*. ISSN 09670645. doi: 10.1016/j.dsr2.2007.06.004.

Marshall, G. J. 2003. Trends in the Southern Annular Mode from observations and reanalyses. *Journal of Climate*, 16(24):4134–4143. ISSN 08948755. doi: 10.1175/1520-0442(2003)016<4134:TITSAM>2.0.CO;2.

Marshall, G. J. and Thompson, D. W. J. 2016. The signatures of large-scale patterns of atmospheric variability in Antarctic surface temperatures. *Journal of Geophysical Research: Atmospheres*, 121(7):3276–3289. ISSN 2169897X. doi: 10.1002/2015JD024665.

Marsland, S. J., Bindoff, N. L., Williams, G. D., and Budd, W. F. 2004. Modeling water mass formation in the Mertz Glacier Polynya and Adélie Depression, East Antarctica. *Journal of Geophysical Research*, 109(C11):C11003. ISSN 0148-0227. doi: 10.1029/2004JC002441.

Martinson, D. G. 2012. Antarctic circumpolar current's role in the Antarctic ice system: An overview. *Palaeogeography, Palaeoclimatology, Palaeoecology*, 335-336:71–74. ISSN 00310182. doi: 10.1016/j.palaeo.2011.04.007.

Massom, R. A., Harris, P. T., Michael, K. J., and Potter, M. J. 1998. The distribution and formative processes of latent-heat polynyas in East Antarctica. *Annals of Glaciology*, 27: 420–426. ISSN 02603055.

Massom, R. A., Hill, K. L., Lytle, V. I., Worby, A. P., Paget, M., and Allison, I. 2001. Effects of regional fast-ice and iceberg distributions on the behaviour of the Mertz Glacier polynya, East Antarctica. *Annals of Glaciology*, 33:391–398. ISSN 0260-3055. doi: 10.3189/172756401781818518.

Massom, R. A., Stammerjohn, S. E., Lefebvre, W., Harangozo, S. A., Adams, N., Scambos, T. A., Pook, M. J., and Fowler, C. 2008. West Antarctic Peninsula sea ice in 2005: Extreme ice compaction and ice edge retreat due to strong anomaly with respect to climate. *Journal of Geophysical Research: Oceans*, 113(2):1–23. ISSN 21699291. doi: 10.1029/2007JC004239.

Massom, R. A., Giles, A. B., Fricker, H. A., Warner, R. C., Legrésy, B., Hyland, G., Young, N., and Fraser, A. D. 2010. Examining the interaction between multi-year landfast sea ice and the Mertz Glacier Tongue, East Antarctica: Another factor in ice sheet stability? *Journal of Geophysical Research: Oceans*, 115(12):1–15. ISSN 21699291. doi: 10.1029/2009JC006083.

Massom, R. A., Reid, P., Stammerjohn, S. E., Raymond, B., Fraser, A., and Ushio, S. 2013. Change and variability in East antarctic sea ice seasonality, 1979/80-2009/10. *PloS one*, 8 (5):e64756. ISSN 1932-6203. doi: 10.1371/journal.pone.0064756.

Massom, R. A., Giles, A. B., Warner, R. C., Fricker, H. A., Legresy, B., Hyland, G., Lescarmontier, L., and Young, N. 2015. External influences on the Mertz Glacier Tongue (East Antarctica) in the decade leading up to its calving in 2010. *Journal of Geophysical Research: Earth Surface*, (120):490–506. doi: 10.1002/2014JF003223.

Masson, V., Vimeux, F., Jouzel, J., Morgan, V., Delmotte, M., Ciais, P., Hammer, C., Johnsen, S., Lipenkov, V. Y., Mosley-Thompson, E., Petit, J. R., Steig, E. J., Stievenard, M., and Vaikmae, R. 2000. Holocene climate variability in Antartica based on 11 ice-core isotopic records. *Quaternary Research*, 54:348–358. ISSN 00335894. doi: 10.1006/qres.2000.2172.

Masson-Delmotte, V., Schulz, M., Abe-Ouchi, A., Beer, J., Ganopolski, A., González-Rouco, J. F., Jansen, E., Lambeck, K., Luterbacher, J., Naish, T. R., Osborn, T., Otto-Bliesner, B., Quinn, T. M., Ramesh, R., Rojas, M., Shao, X., and Timmermann, A. 2013: Information from Paleoclimate Archives. In Stocker, T. F., Qin, D., Plattner, G.-K., Tignor, M., Allen, S., Boschung, J., Nauels, A., Xia, Y., Bex, V., and Midgley, P., editors, *Climate Change 2013: The*

Physical Science Basis. Contribution of Working Group I to the Fifth Assessment Report of the Intergovernmental Panel On Climate Change. Cambridge University Press, Cambridge, United Kingdom and New York, NY, USA, 2013.

Mayet, C., Testut, L., Legresy, B., Lescarmontier, L., and Lyard, F. 2013. High-resolution barotropic modeling and the calving of the Mertz Glacier, East Antarctica. *Journal of Geophysical Research: Oceans*, 118(10):5267–5279. ISSN 21699291. doi: 10.1002/jgrc.20339.

Mayewski, P. A., Twickler, M. S., Whitlow, S. I., Meeker, L. D., Yang, Q., Thomas, J., Kreutz, K., Grootes, P. M., Morse, D. L., Steig, E. J., Waddington, E. D., Saltzman, E. S., Whung, P. Y., and Taylor, K. C. 1996. Climate change during the last deglaciation in Antarctica. *Science*, 272(5268):1636–1638. ISSN 00368075. doi: 10.1126/science.272.5268.1636.

Mayewski, P. A., Maasch, K. A., Dixon, D., Sneed, S. B., Oglesby, R., Korotkikh, E., Potocki, M., Grigholm, B., Kreutz, K., Kurbatov, A. V., Spaulding, N., Stager, J. C., Taylor, K. C., Steig, E. J., White, J., Bertler, N. A., Goodwin, I., Simões, J. C., Jaña, R., Kraus, S., and Fastook, J. 2013. West Antarctica's sensitivity to natural and human-forced climate change over the Holocene. *Journal of Quaternary Science*, 28(1):40–48. ISSN 02678179. doi: 10.1002/jqs.2593.

Mayewski, P. A., Rohling, E. E., Stager, J. C., Karlén, W., Maasch, K. A., Meeker, L. D., Meyerson, E. A., Gasse, F., van Kreveld, S., Holmgren, K., Lee-Thorp, J., Rosqvist, G., Rack, F., Staubwasser, M., Schneider, R. R., and Steig, E. J. 2004. Holocene climate variability. *Quaternary Research*, 62(3):243–255. ISSN 00335894. doi: 10.1016/j.yqres.2004.07.001.

Mayewski, P. A., Carleton, A., Birkel, S., Dixon, D., Kurbatov, A., Korotkikh, E., McConnell, J., Curran, M., Cole-Dai, J., Jiang, S., Plummer, C., Vance, T., Maasch, K., Sneed, S., and Handley, M. 2017. Ice core and climate reanalysis analogs to predict Antarctic and Southern Hemisphere climate changes. *Quaternary Science Reviews*, 155:50–66. ISSN 0277-3791. doi: 10.1016/J.QUASCIREV.2016.11.017.

McCave, I. N. and Andrews, J. T. 2019. Distinguishing current effects in sediments delivered to the ocean by ice. I. Principles, methods and examples. *Quaternary Science Reviews*, 212: 92–107. ISSN 02773791. doi: 10.1016/j.quascirev.2019.03.031.

McCave, I. N. and Hall, I. R. 2006. Size sorting in marine muds: Processes, pitfalls, and prospects for paleoflow-speed proxies. *Geochemistry, Geophysics, Geosystems*, 7(10). ISSN 15252027. doi: 10.1029/2006GC001284.

McCave, I. N., Manighetti, B., and Robinson, S. G. 1995. Sortable silt and fine sediment size/composition slicing: Parameters for palaeocurrent speed and palaeoceanography. *Paleoceanography*, 10(3):593–610. ISSN 08838305. doi: 10.1029/94PA03039.

McCave, I. N., Thornalley, D. J., and Hall, I. R. 2017. Relation of sortable silt grain-size to deep-sea current speeds: Calibration of the 'Mud Current Meter'. *Deep-Sea Research Part I*, 127:1–12. ISSN 09670637. doi: 10.1016/j.dsr.2017.07.003.

McGlone, M. S., Kershaw, A. P., and Markgraf, V. 1993. El Nino/Southern Oscillation climatic variability in Australasian and South American paleoenvironmental records. *El Nino: historical and paleoclimatic aspects of the Southern Oscillation*, pages 435–462.

McKay, R. M., Browne, G., Carter, L., Cowan, E., Dunbar, G., Krissek, L., Naish, T., Powell, R., Reed, J., Talarico, F., and Wilch, T. 2009. The stratigraphic signature of the late Cenozoic Antarctic Ice Sheets in the Ross Embayment. *Bulletin of the Geological Society of America*, 121(11-12):1537–1561. ISSN 00167606. doi: 10.1130/B26540.1.

McKay, R. M., Golledge, N. R., Maas, S., Naish, T. R., Levy, R., Dunbar, G., and Kuhn, G. 2016. Antarctic marine ice-sheet retreat in the Ross Sea during the early Holocene. *Geology*, 44 (1):7–10. ISSN 19432682. doi: 10.1130/G37315.1.

McMullen, K., Domack, E., Leventer, A., Olson, C., Dunbar, R. B., and Brachfeld, S. 2006. Glacial morphology and sediment formation in the Mertz Trough, East Antarctica. *Palaeogeography, Palaeoclimatology, Palaeoecology*, 231(1-2):169–180. ISSN 0031-0182. doi: 10.1016/J.PALAEO.2005.08.004.

Meehl, G. A., Arblaster, J. M., Bitz, C. M., Chung, C. T. Y., and Teng, H. 2016. Antarctic sea-ice expansion between 2000 and 2014 driven by tropical Pacific decadal climate variability. *Nature Geoscience*, 9(8):590–595. ISSN 1752-0894. doi: 10.1038/ngeo2751.

Mengel, M. and Levermann, A. 2014. Ice plug prevents irreversible discharge from east Antarctica. *Nature Climate Change*, 4(6):451–455. ISSN 17586798. doi: 10.1038/nclimate2226.

Mercer, J. 1978. West Antarctic ice sheet and CO2 greenhouse effect: a threat of disaster. *Nature*, 271:321–325.

Meyers, S. 2014. Astrochron: An R package for astrochronology.

Mezgec, K., Stenni, B., Crosta, X., Masson-Delmotte, V., Baroni, C., Braida, M., Ciardini, V., Colizza, E., Melis, R., Salvatore, M. C., Severi, M., Scarchilli, C., Traversi, R., Udisti, R., and Frezzotti, M. 2017. Holocene sea ice variability driven by wind and polynya efficiency in the Ross Sea. *Nature Communications*, 8(1). ISSN 2041-1723. doi: 10.1038/s41467-017-01455-x.

Miles, B. W. J., Stokes, C. R., and Jamieson, S. S. R. 2016. Pan-ice-sheet glacier terminus change in East Antarctica reveals sensitivity of Wilkes Land to sea-ice changes. *Science Advances*, 2 (5).

Mix, A. C., Bard, E., and Schneider, R. 2001. Environmental processes of the ice age: Land, oceans, glaciers (EPILOG). *Quaternary Science Reviews*, 20(4):627–657. ISSN 02773791. doi: 10.1016/S0277-3791(00)00145-1.

Mo, K. C. and Paegle, J. N. 2001. The Pacific-South American Modes and Their Downstream Effects. *Int. J. Climatol*, 21:1211–1229. doi: 10.1002/joc.685.

Mo, K. C., Pfaendtner, J., Kalnay, E., Mo, K. C., Pfaendtner, J., and Kalnay, E. 1987. A GCM Study on the Maintenance of the June 1982 Blocking in the Southern Hemisphere. *Journal of the Atmospheric Sciences*, 44(8):1123–1142. ISSN 0022-4928. doi: 10.1175/1520-0469(1987)044<1123:AGSOTM>2.0.CO;2.

Monnin, E., Steig, E. J., Siegenthaler, U., Kawamura, K., Schwander, J., Stauffer, B., Stocker, T. F., Morse, D. L., Barnola, J. M., Bellier, B., Raynaud, D., and Fischer, H. 2004. Evidence for substantial accumulation rate variability in Antarctica during the Holocene, through synchronization of CO2 in the Taylor Dome, Dome C and DML ice cores. *Earth and Planetary Science Letters*. ISSN 0012821X. doi: 10.1016/j.epsl.2004.05.007.

Moore, J. K. and Abbott, M. R. 2000. Phytoplankton chlorophyll distributions and primary production in the Southern Ocean. *Journal of Geophysical Research: Oceans*, 105(C12): 28709–28722. ISSN 01480227. doi: 10.1029/1999jc000043.

Moore, J. K., Fu, W., Primeau, F., Britten, G. L., Lindsay, K., Long, M., Doney, S. C., Mahowald, N., Hoffman, F., and Randerson, J. T. 2018. Sustained climate warming drives declining marine biological productivity. *Science*, 359(6380):113–1143. ISSN 10959203. doi: 10.1126/science.aao6379.

Morales Maqueda, M. A., Willmott, A. J., and Biggs, N. R. T. 2004. Polynya Dynamics: a Review of Observations and Modeling. *Reviews of Geophysics*, 42(1):RG1004. ISSN 8755-1209. doi: 10.1029/2002RG000116.

Moreau, S., Lannuzel, D., Janssens, J., Arroyo, M. C., Corkill, M., Cougnon, E., Genovese, C., Legresy, B., Lenton, A., Puigcorbé, V., Ratnarajah, L., Rintoul, S., Roca-Martí, M., Rosenberg, M., Shadwick, E. H., Silvano, A., Strutton, P. G., and Tilbrook, B. 2019. Sea Ice Meltwater and Circumpolar Deep Water Drive Contrasting Productivity in Three Antarctic Polynyas. *Journal of Geophysical Research: Oceans*, 124(5):2943–2968. ISSN 21699291. doi: 10.1029/2019JC015071.

Mortlock, R. A. and Froelich, P. N. 1989. A simple method for the rapid determination of biogenic opal in pelagic marine sediments. *Deep Sea Research Part A, Oceanographic Research Papers*. ISSN 01980149. doi: 10.1016/0198-0149(89)90092-7.

Moy, C. M., Seltzer, G. O., Rodbell, D. T., and Anderson, D. M. 2002. Variability of El Niño/Southern Oscillation activity at millennial timescales during the Holocene epoch. *Nature*, 420(6912):162–165. ISSN 0028-0836. doi: 10.1038/nature01194.

NASA Worldview. NASA Worldview.

Neff, P. D. 2014. A review of the brittle ice zone in polar ice cores. *Annals of Glaciology*, 55 (68):72–82. ISSN 02603055. doi: 10.3189/2014AoG68A023.

NGRIP Community Members, Andersen, K. K., Azuma, N., Barnola, J. M., Bigler, M., Biscaye, P., Caillon, N., Chappellaz, J., Clausen, H. B., Dahl-Jensen, D., Fischer, H., Flückiger, J., Fritzsche, D., Fujii, Y., Goto-Azuma, K., Grønvold, K., Gundestrup, N. S., Hansson, M., Huber, C., Hvidberg, C. S., Johnsen, S. J., Jonsell, U., Jouzel, J., Kipfstuhl, S., Landais, A., Leuenberger, M., Lorrain, R., Masson-Delmotte, V., Miller, H., Motoyama, H., Narita, H., Popp, T., Rasmussen, S. O., Raynaud, D., Rothlisberger, R., Ruth, U., Samyn, D., Schwander, J., Shoji, H., Siggard-Andersen, M. L., Steffensen, J. P., Stocker, T., Sveinbjörnsdóttir, A. E., Svensson, A., Takata, M., Tison, J. L., Thorsteinsson, T., Watanabe, O., Wilhelms, F., and White, J. W. 2004. High-resolution record of Northern Hemisphere climate extending into the last interglacial period. *Nature*, 431(7005):147–151. ISSN 00280836. doi: 10.1038/nature02805.

Nicolas, J. P., Vogelmann, A. M., Scott, R. C., Wilson, A. B., Cadeddu, M. P., Bromwich, D. H., Verlinde, J., Lubin, D., Russell, L. M., Jenkinson, C., Powers, H. H., Ryczek, M., Stone, G., and Wille, J. D. 2017. January 2016 extensive summer melt in West Antarctica favoured by strong El Niño. *Nature Communications*, 8(15799):1–10. ISSN 20411723. doi: 10.1038/ncomms15799.

Nigro, M. A. and Cassano, J. J. 2014. Identification of surface wind patterns over the Ross Ice Shelf, Antarctica, using self-organizing maps. *Monthly Weather Review*, 142(7):2361–2378. ISSN 15200493. doi: 10.1175/MWR-D-13-00382.1.

Nuncio, M. and Yuan, X. 2015. The influence of the Indian Ocean dipole on Antarctic sea ice. *Journal of Climate*, 28(7):2682–2690. ISSN 08948755. doi: 10.1175/JCLI-D-14-00390.1.

Olbers, D. and Visbeck, M. 2005. A model of the zonally averaged stratification and overturning in the Southern Ocean. *Journal of Physical Oceanography*, 35(7):1190–1205. ISSN 00223670. doi: 10.1175/JPO2750.1.

Orsi, A. H. and Whitworth, T. Hydrographic Atlas of the World Ocean Circulation Experiment (WOCE). In Sparrow, M., Chapman, P., and Gould, J., editors, *Southern Ocean*. International WOCE Project Office, Southhamptom, UK, 2005. ISBN 0-904175-49-9.

Orsi, A. H. and Wiederwohl, C. L. 2009. A recount of Ross Sea waters. *Deep-Sea Research Part II: Topical Studies in Oceanography*, 56(13-14):778–795. ISSN 09670645. doi: 10.1016/j.dsr2.2008.10.033.

Orsi, A. H., Whitworth, T., and Nowlin, W. D. 1995. On the meridional extent and fronts of the Antarctic Circumpolar Current. *Deep-Sea Research Part I*, 42(5):641–673. ISSN 09670637. doi: 10.1016/0967-0637(95)00021-W.

Orsi, A. H., Johnson, G. C., and Bullister, J. L. 1999. Circulation, mixing, and production of Antarctic Bottom Water. *Progress in Oceanography*, 43(1):55–109. ISSN 00796611. doi: 10.1016/S0079-6611(99)00004-X.

Orsi, A. H., Jacobs, S. S., Gordon, A. L., and Visbeck, M. 2001. Cooling and ventilating the abyssal ocean. *Geophysical Research Letters*, 28(15):2923–2926. ISSN 00948276. doi: 10.1029/2001GL012830.

Orsi, A. H., Smethie, W. M., and Bullister, J. L. 2002. On the total input of Antarctic waters to the deep ocean: A preliminary estimate from chlorofluorocarbon measurements. *Journal of Geophysical Research C: Oceans*, 107(8):31–1. ISSN 01480227.

Orsi, T. H., Edwards, C. M., and Anderson, A. L. 1994. X-ray computed tomography: a non-destructive method for quantitative analysis of sediment cores. *Journal of Sedimentary Research*, A64:690–693.

Parish, T. R. and Bromwich, D. H. 1987. The surface windfield over the Antarctic ice sheets. *Nature*, 328:51–54. ISSN 0028-0836. doi: 10.1038/328051a0.

Parish, T. R. and Bromwich, D. H. 1997. On the forcing of seasonal changes in surface pressure over Antarctica. *Journal of Geophysical Research*, 102(D12):13785–13792. ISSN 01480227. doi: 10.1029/96JD02959.

Parish, T. R. and Walker, R. 2006. A re-examination of the winds of Adélie Land , Antarctica. 55:105–117. ISSN 00049743.

Parish, T. R. and Wendler, G. 1991. The katabatic wind regime at Adelie Land, Antarctica. *International Journal of Climatology*, 11(1):97–107. ISSN 10970088. doi: 10.1002/joc.3370110108.

Parish, T. R., Cassano, J. J., and Seefeldt, M. W. 2006. Characteristics of the Ross Ice Shelf air stream as depicted Antarctic Mesoscale Prediction System simulations. *Journal of Geophysical Research Atmospheres*, 111(12):1–12. ISSN 01480227. doi: 10.1029/2005JD006185.

Parkinson, C. L. 2014. Global sea ice coverage from satellite data: Annual cycle and 35-yr trends. *Journal of Climate*, 27(24):9377–9382. ISSN 08948755. doi: 10.1175/JCLI-D-14-00605.1.

Parkinson, C. L. 2019. A 40-y record reveals gradual Antarctic sea ice increases followed by decreases at rates far exceeding the rates seen in the Arctic. *Proceedings of the National Academy of Sciences*, 116(29):14414–14423. ISSN 0027-8424. doi: 10.1073/pnas.1906556116.

Pasteris, D. R., McConnell, J. R., Das, S. B., Criscitiello, A. S., Evans, M. J., Maselli, O. J., Sigl, M., and Layman, L. 2014. Seasonally resolved ice core records from West Antarctica indicate a sea ice source of sea-salt aerosol and a biomass burning source of ammonium. *Journal of Geophysical Research*, 119:9168–9182. ISSN 21562202. doi: 10.1002/2013JD020720.

Pausata, F. S. R., Zhang, Q., Muschitiello, F., Lu, Z., Chafik, L., Niedermeyer, E. M., Stager, J. C., Cobb, K. M., and Liu, Z. 2017. Greening of the Sahara suppressed ENSO activity during the mid-Holocene. *Nature Communications*, 8:1–12. ISSN 2041-1723. doi: 10.1038/ncomms16020.

Petaev, M. I., Huang, S., Jacobsen, S. B., and Zindler, A. 2013. Large Pt anomaly in the Greenland ice core points to a cataclysm at the onset of Younger Dryas. *Proceedings of the National Academy of Sciences*, 110(32):12917–12920. ISSN 00278424. doi: 10.1073/pnas.1303924110.

Pike, J., Swann, G. E. A., Leng, M. J., and Snelling, A. M. 2013. Glacial discharge along the west Antarctic Peninsula during the Holocene. *Nature Geoscience*, 6(3):199–202. ISSN 1752-0894. doi: 10.1038/ngeo1703.

Pollard, D. and DeConto, R. M. 2009. Modelling West Antarctic ice sheet growth and collapse through the past five million years. *Nature*, 458(7236):329–332. ISSN 0028-0836. doi: 10.1038/nature07809.

Poluianov, S., Traversi, R., and Usoskin, I. 2014. Cosmogenic production and climate contributions to nitrate record in the TALDICE Antarctic ice core. *Journal of Atmospheric and Solar-Terrestrial Physics*, 121(PA):50–58. ISSN 13646826. doi: 10.1016/j.jastp.2014.09.011.

Powell, R. and Domack, G. W. Modern glaciomarine environments. In *Modern and Past Glacial Environments*, pages 361–389. Elsevier, 2002. doi: 10.1016/b978-075064226-2/50015-5.

Power, S., Casey, T., Folland, C., Colman, A., and Mehta, V. 1999. Inter-decadal modulation of the impact of ENSO on Australia. *Climate Dynamics*, 15(5):319–324. ISSN 0930-7575. doi: 10.1007/s003820050284.

Presti, M., Barbara, L., Denis, D., Schmidt, S., De Santis, L., and Crosta, X. 2011. Sediment delivery and depositional patterns off Adélie Land (East Antarctica) in relation to late Quaternary climatic cycles. *Marine Geology*. ISSN 00253227. doi: 10.1016/j.margeo.2011.03.012.

Prezelin, B. B., Hofmann, E. E., Mengelt, C., and Klinck, J. M. 2000. The linkage between Upper Circumpolar Deep Water (UCDW) and phytoplankton assemblages on the west Antarctic Peninsula continental shelf. *Journal of Marine Research*, 58(2):165–202. ISSN 00222402. doi: 10.1357/002224000321511133.

Prins, M. A., Bouwer, L. M., Beets, C. J., Troelstra, S. R., Weltje, G. J., Kruk, R. W., Kuijpers, A., and Vroon, P. Z. 2002. Ocean circulation and iceberg discharge in the glacial North Atlantic: Inferences from unmixing of sediment size distributions. *Geology*, 30(6):555–558. ISSN 00917613. doi: 10.1130/0091-7613(2002)030<0555:OCAIDI>2.0.CO;2.

Pritchard, H. D., Ligtenberg, S. R. M., Fricker, H. A., Vaughan, D. G., van den Broeke, M. R., and Padman, L. 2012. Antarctic ice-sheet loss driven by basal melting of ice shelves. *Nature*, 484(7395):502–505. ISSN 0028-0836. doi: 10.1038/nature10968.

Pyne, R. L., Keller, E. D., Canessa, S., Bertler, N. A. N., Pyne, A. R., Mandeno, D., Vallelonga, P., Semper, S., Kjaer, H. A., Hutchinson, E. D., and Troy Baisden, W. 2018. A novel approach to

process brittle ice for continuous flow analysis of stable water isotopes. *Journal of Glaciology*, 64(244):289–299. doi: 10.1017/jog.2018.19.

Ragueneau, O., Tréguer, P., Leynaert, A., Anderson, R. F., Brzezinski, M. A., DeMaster, D. J., Dugdale, R. C., Dymond, J., Fischer, G., François, R., Heinze, C., Maier-Reimer, E., Martin-Jézéquel, V., Nelson, D. M., and Quéguiner, B. 2000. A review of the Si cycle in the modern ocean: Recent progress and missing gaps in the application of biogenic opal as a paleoproductivity proxy. *Global and Planetary Change*. ISSN 09218181. doi: 10.1016/S0921-8181(00)00052-7.

Rankin, A. M., Auld, V., and Wolff, E. W. 2000. Frost flowers as a source of fractionated sea salt aerosol in the polar regions. *Geophysical Research Letters*, 27(21):3469–3472. ISSN 00948276. doi: 10.1029/2000GL011771.

Raphael, M. N., Marshall, G. J., Turner, J., Fogt, R. L., Schneider, D., Dixon, D. A., Hosking, J. S., Jones, J. M., and Hobbs, W. R. 2016. The Amundsen sea low: Variability, change, and impact on Antarctic climate. *Bulletin of the American Meteorological Society*, 97(1):111–121. ISSN 00030007. doi: 10.1175/BAMS-D-14-00018.1.

Raphael, M. N. and Hobbs, W. 2014. The influence of the large-scale atmospheric circulation on Antarctic sea ice during ice advance and retreat seasons. *Geophysical Research Letters*, 41: 5037–5045. doi: 10.1002/2014GL060365.Received.

Raphael, M. N., Holland, M. M., Landrum, L., and Hobbs, W. R. 2019. Links between the Amundsen Sea Low and sea ice in the Ross Sea: seasonal and interannual relationships. *Climate Dynamics*, 52(3-4):2333–2349. ISSN 0930-7575. doi: 10.1007/s00382-018-4258-4.

Rasmussen, S. O., Andersen, K. K., Svensson, A. M., Steffensen, J. P., Vinther, B. M., Clausen, H. B., Siggaard-Andersen, M. L., Johnsen, S. J., Larsen, L. B., Dahl-Jensen, D., Bigler, M., Röthlisberger, R., Fischer, H., Goto-Azuma, K., Hansson, M. E., and Ruth, U. 2006. A new Greenland ice core chronology for the last glacial termination. *Journal of Geophysical Research Atmospheres*, 111(6):1–16. ISSN 01480227. doi: 10.1029/2005JD006079.

Rasmusson, E. M. and Carpenter, T. H. 1982. Variations in Tropical Sea Surface Temperature and Surface Wind Fields Associated with the Southern Oscillation/El Niño. *Monthly Weather Review*, 110(5):354–384. ISSN 0027-0644. doi: 10.1175/1520-0493(1982)110<0354:VITSST>2.0.CO;2.

Raymond, C. F. 1983. Deformation in the vicinity of ice divides. *Journal of Glaciology*, 29(103): 357–373. ISSN 00221430. doi: 10.1017/S0022143000030288.

Reilly, B. T., Stoner, J. S., and Wiest, J. 2017. SedCT: MATLAB^{TM} tools for standardized and quantitative processing of sediment core computed tomography (CT) data collected using a medical CT scanner. *Geochemistry, Geophysics, Geosystems*, 18(8):3231–3240. ISSN 15252027. doi: 10.1002/2017GC006884.

Renwick, J. A. 2005. Persistent positive anomalies in the Southern Hemisphere circulation. *Monthly Weather Review*, 133(4):977–988. ISSN 00270644. doi: 10.1175/MWR2900.1.

Rhodes, R. H., Bertler, N. A., Baker, J. A., Steen-Larsen, H. C., Sneed, S. B., Morgenstern, U., and Johnsen, S. J. 2012. Little Ice Age climate and oceanic conditions of the Ross Sea, Antarctica from a coastal ice core record. *Climate of the Past*, 8(4):1223–1238. ISSN 18149324. doi: 10.5194/cp-8-1223-2012.

Rhodes, R. H., Bertler, N. A., Baker, J. A., Sneed, S. B., Oerter, H., and Arrigo, K. R. 2009. Sea ice variability and primary productivity in the Ross Sea, Antarctica, from methylsulphonate snow record. *Geophysical Research Letters*, 36(10):1–5. ISSN 00948276. doi: 10.1029/2009GL037311.

Rignot, E., Jacobs, S., Mouginot, J., and Scheuchl, B. 2013. Ice-shelf melting around antarctica. *Science*, 341(6143):266–270. ISSN 10959203. doi: 10.1126/science.1235798.

Rignot, E., Mouginot, J., Morlighem, M., Seroussi, H., and Scheuchl, B. 2014. Widespread, rapid grounding line retreat of Pine Island, Thwaites, Smith, and Kohler glaciers, West Antarctica, from 1992 to 2011. *Geophysical Research Letters*, 41(10):3502–3509. ISSN 00948276. doi: 10.1002/2014GL060140.

Rignot, E., Mouginot, J., Scheuchl, B., Van Den Broeke, M., Van Wessem, M. J., and Morlighem, M., 2019. Four decades of Antarctic ice sheet mass balance from 1979–2017. ISSN 10916490.

Rigual-Hernández, A. S., Trull, T. W., Bray, S. G., Closset, I., and Armand, L. K. 2015. Seasonal dynamics in diatom and particulate export fluxes to the deep sea in the Australian sector of the southern Antarctic Zone. *Journal of Marine Systems*, 142:62–74. ISSN 09247963. doi: 10.1016/j.jmarsys.2014.10.002.

Rintoul, S., Hughes, C., and Olbers, D. 2001. The Antarctic Circumpolar Current System. ISBN 0126413517. doi: 10.1002/ajp.20122.

Rintoul, S. R. 1998. On the Origin and Influence of Adélie Land Bottom Water. *Antarctic Research Series*, 75:151–171. doi: 10.1029/ar075p0151.

Rintoul, S. R. 2007. Rapid freshening of Antarctic Bottom Water formed in the Indian and Pacific oceans. *Geophysical Research Letters*, 34(6):1–5. ISSN 00948276. doi: 10.1029/2006GL028550.

Rintoul, S. R. 2018. The global influence of localized dynamics in the Southern Ocean. *Nature*, 558(7709):209–218. ISSN 0028-0836. doi: 10.1038/s41586-018-0182-3.

Robinson, N. J. and Williams, M. J. M. 2012. Iceberg-induced changes to polynya operation and regional oceanography in the southern Ross Sea, Antarctica, from in situ observations. *Antarctic Science*, 24(5):514–526. doi: 10.1017/S0954102012000296.

Rodbell, D. T., Seltzer, G. O., Anderson, D. M., Abbott, M. B., Enfield, D. B., and Newman, J. H. 1999. An ˜15,000-year record of El Nino-driven alluviation in Southwestern Ecuador. *Science*, 283(5401):516–520. ISSN 00368075. doi: 10.1126/science.283.5401.516.

Rodrigues, R. R., Campos, E. J. D., and Haarsma, R. 2015. The impact of ENSO on the south Atlantic subtropical dipole mode. *Journal of Climate*, 28(7):2691–2705. ISSN 08948755. doi: 10.1175/JCLI-D-14-00483.1.

Rogers, J. C., van Loon, H., Rogers, J. C., and Loon, H. v. 1982. Spatial Variability of Sea Level Pressure and 500 mb Height Anomalies over the Southern Hemisphere. *Monthly Weather Review*, 110(10):1375–1392. ISSN 0027-0644. doi: 10.1175/1520-0493(1982)110<1375:SVOSLP>2.0.CO;2.

Rosenheim, B. E., Day, M. B., Domack, E., Schrum, H., Benthien, A., and Hayes, J. M. 2008. Antarctic sediment chronology by programmed-temperature pyrolysis: Methodology and data treatment. *Geochemistry, Geophysics, Geosystems*, 9(4):1–16. ISSN 15252027. doi: 10.1029/2007GC001816.

Rosenheim, B. E., Santoro, J. A., Gunter, M., and Domack, E. W. 2013. Improving Antarctic Sediment 14 C Dating Using Ramped Pyrolysis: An Example from the Hugo Island Trough . *Radiocarbon*, 55(1):115–126. ISSN 0033-8222. doi: 10.2458/azu{_}js{_}rc.v55i1.16234.

Röthlisberger, R., Mulvaney, R., Wolff, E. W., Hutterli, M. A., Bigler, M., Sommer, S., and Jouzel, J. 2002. Dust and sea salt variability in central East Antarctica (Dome C) over the last 45 kyrs and its implications for southern high-latitude climate. *Geophysical Research Letters*, 29(20):24–1. ISSN 0094-8276. doi: 10.1029/2002gl015186.

Rothwell, R. G. and Croudace, I. W. Twenty Years of XRF Core Scanning Marine Sediments: What Do Geochemical Proxies Tell Us? In Croudace, I. W. and Rothwell, R. G., editors, *Micro-XRF Studies of Sediment Cores. Developments in Paleoenvironmental Research*, pages 25–102. Springer, 2015. doi: 10.1007/978-94-017-9849-5{_}2.

Ruggieri, E., Herbert, T., Lawrence, K. T., and Lawrence, C. E. 2009. Change point method for detecting regime shifts in paleoclimatic time series: Application to δ18O time series of the Plio-Pleistocene. *Paleoceanography*, 24(1):1–15. ISSN 08838305. doi: 10.1029/2007PA001568.

Saba, G. K., Fraser, W. R., Saba, V. S., Iannuzzi, R. A., Coleman, K. E., Doney, S. C., Ducklow, H. W., Martinson, D. G., Miles, T. N., Patterson-Fraser, D. L., Stammerjohn, S. E., Steinberg, D. K., and Schofield, O. M. 2014. Winter and spring controls on the summer food web of the coastal West Antarctic Peninsula. *Nature Communications*, 5:1–8. ISSN 20411723. doi: 10.1038/ncomms5318.

Saji, N. H. and Yamagata, T. 2003. Possible impacts of Indian Ocean Dipole mode events on global climate. *Climate Research*, 25(2):151–169. ISSN 0936577X. doi: 10.3354/cr025151.

Saji, N. H., Goswami, B. N., Vinayachandran, P. N., and Yamagata, T. 1999. A dipole mode in the tropical Indian ocean. *Nature*, 401(6751):360–363. ISSN 00280836. doi: 10.1038/43854.

Saji, N. H., Ambrizzi, T., and Ferraz, S. E. 2005. Indian Ocean Dipole mode events and austral surface air temperature anomalies. *Dynamics of Atmospheres and Oceans*, 39(1-2 SPEC. ISS.): 87–101. ISSN 03770265. doi: 10.1016/j.dynatmoce.2004.10.015.

Salinger, M. J., Renwick, J. A., and Mullan, A. B. 2001. Interdecadal Pacific Oscillation and South Pacific climate. *International Journal of Climatology*, 21(14):1705–1721. ISSN 08998418. doi: 10.1002/joc.691.

Sancetta, C. Laminated diatomaceous sediments: Controls on formation and strategies for analysis. Technical report, 1996.

Sandweiss, D. H., III, J. B. R., Reitz, E. J., Rollins, H. B., and Maasch, K. A. 1996. Geoarchaeological Evidence from Peru for a 5000 Years B.P. Onset of El Niño. *Science*, 273(5281): 1531–1533.

Saunders, K. M., Roberts, S. J., Perren, B., Butz, C., Sime, L., Davies, S., Van Nieuwenhuyze, W., Grosjean, M., and Hodgson, D. A. 2018. Holocene dynamics of the Southern Hemisphere

westerly winds and possible links to CO2 outgassing. *Nature Geoscience*, 11(9):650–655. ISSN 17520908. doi: 10.1038/s41561-018-0186-5.

Scarchilli, C., Frezzotti, M., and Ruti, P. M. 2011. Snow precipitation at four ice core sites in East Antarctica: Provenance, seasonality and blocking factors. *Climate Dynamics*, 37(9-10): 2107–2125. ISSN 09307575. doi: 10.1007/s00382-010-0946-4.

Schindelin, J., Arganda-Carreras, I., Frise, E., Kaynig, V., Longair, M., Pietzsch, T., Preibisch, S., Rueden, C., Saalfeld, S., Schmid, B., Tinevez, J.-Y., White, D. J., Hartenstein, V., Eliceiri, K., Tomancak, P., and Cardona, A. 2012. Fiji: an open-source platform for biological-image analysis. *Nature Methods*, 9(7):676–682. ISSN 1548-7091. doi: 10.1038/nmeth.2019.

Schneider, D. P., Okumura, Y., Deser, C., Schneider, D. P., Okumura, Y., and Deser, C. 2012. Observed Antarctic Interannual Climate Variability and Tropical Linkages. *Journal of Climate*, 25(12):4048–4066. ISSN 0894-8755. doi: 10.1175/JCLI-D-11-00273.1.

Schoof, C. 2007. Ice sheet grounding line dynamics: Steady states, stability, and hysteresis. *Journal of Geophysical Research*, 112(F3):F03S28. ISSN 0148-0227. doi: 10.1029/2006JF000664.

Schüpbach, S., Federer, U., Kaufmann, P. R., Albani, S., Barbante, C., Stocker, T. F., and Fischer, H. 2013. High-resolution mineral dust and sea ice proxy records from the Talos Dome ice core. *Clim. Past*, 9:2789–2807. doi: 10.5194/cp-9-2789-2013.

Sedwick, P. N., Marsay, C. M., Sohst, B. M., Aguilar-Islas, A. M., Lohan, M. C., Long, M. C., Arrigo, K. R., Dunbar, R. B., Saito, M. A., Smith, W. O., and Ditullio, G. R. 2011. Early season depletion of dissolved iron in the Ross Sea polynya: Implications for iron dynamics on the Antarctic continental shelf. *Journal of Geophysical Research: Oceans*, 116(12):1–19. ISSN 21699291. doi: 10.1029/2010JC006553.

Severi, M., Udisti, R., Becagli, S., Stenni, B., and Traversi, R. 2012. Volcanic synchronisation of the EPICA-DC and TALDICE ice cores for the last 42 kyr BP. 8:509–517. doi: 10.5194/cp-8-509-2012.

Severi, M., Becagli, S., Caiazzo, L., Ciardini, V., Colizza, E., Giardi, F., Mezgec, K., Scarchilli, C., Stenni, B., Thomas, E. R., Traversi, R., and Udisti, R. 2017. Sea salt sodium record from Talos Dome (East Antarctica) as a potential proxy of the Antarctic past sea ice extent. *Chemosphere*, 177:266–274. ISSN 18791298. doi: 10.1016/j.chemosphere.2017.03.025.

Shadwick, E. H., Rintoul, S. R., Tilbrook, B., Williams, G. D., Young, N., Fraser, A. D., Marchant, H., Smith, J., and Tamura, T. 2013. Glacier tongue calving reduced dense water formation and enhanced carbon uptake. *Geophysical Research Letters*, 40:904–909. ISSN 00948276. doi: 10.1002/grl.50178.

Shakun, J. D. and Carlson, A. E. 2010. A global perspective on Last Glacial Maximum to Holocene climate change. *Quaternary Science Reviews*. ISSN 02773791. doi: 10.1016/j.quascirev.2010.03.016.

Shen, Q., Wang, H., Shum, C. K., Jiang, L., Hsu, H. T., and Dong, J. 2018. Recent high-resolution Antarctic ice velocity maps reveal increased mass loss in Wilkes Land, East Antarctica. *Scientific Reports*, 8(1):1–8. ISSN 20452322. doi: 10.1038/s41598-018-22765-0.

Shevenell, A. E., Domack, E. W., and Kernan, G. M. 1996. Record of Holocene palaeoclimate change along the Antarctic Peninsula: evidence from glacial marine sediments, Lallemand Fjord. *Papers and Proceedings - Royal Society of Tasmania*, 130(2):55–64. ISSN 00804703. doi: 10.26749/rstpp.130.2.55.

Sigl, M., Fudge, T. J., Winstrup, M., Cole-Dai, J., Ferris, D., McConnell, J. R., Taylor, K. C., Welten, K. C., Woodruff, T. E., Adolphi, F., Bisiaux, M., Brook, E. J., Buizert, C., Caffee, M. W., Dunbar, N. W., Edwards, R., Geng, L., Iverson, N., Koffman, B., Layman, L., Maselli, O. J., McGwire, K., Muscheler, R., Nishiizumi, K., Pasteris, D. R., Rhodes, R. H., and Sowers, T. A. 2016. The WAIS Divide deep ice core WD2014 chronology - Part 2: Annual-layer counting (0-31 ka BP). *Climate of the Past*, 12(3):769–786. ISSN 18149332. doi: 10.5194/cp-12-769-2016.

Sloyan, B. M. and Rintoul, S. R. 2001. The Southern Ocean limb of the global deep overtuning circulation. *Journal of Physical Oceanography*, 31(1):143–173. ISSN 00223670. doi: 10.1175/1520-0485(2001)031<0143:TSOLOT>2.0.CO;2.

Smith, S. R. and Stearns, C. R. 1993. Antarctic Pressure and Temperature Anomalies Surrounding the Minimum in the Southern Oscillation Index. *Journal of Geophysical Research*, 98(D7):13071–13083.

Smith, S. D., Muench, R. D., and Pease, C. H. 1990. Polynyas and leads: An overview of physical processes and environment. *Journal of Geophysical Research*, 95(C6):9461. ISSN 0148-0227. doi: 10.1029/jc095ic06p09461.

Smith, W. O. and Comiso, J. C. 2008. Influence of sea ice on primary production in the Southern Ocean: A satellite perspective. *Journal of Geophysical Research: Oceans*, 113(5):1–19. ISSN 21699291. doi: 10.1029/2007JC004251.

Smith, W. O. and Gordon, L. I. 1997. Hyperproductivity of the Ross Sea (Antarctica) polynya during austral spring. *Geophysical Research Letters*, 24(3):233–236. ISSN 00948276. doi: 10.1029/96GL03926.

Smith, W. O. and Nelson, D. M. 1986. Importance of Ice Edge Phytoplankton Production in the Southern Ocean. *BioScience*, 36(4):251–257. ISSN 00063568. doi: 10.2307/1310215.

Smith, W. O., Marra, J., Hiscock, M. R., and Barber, R. T. 2000. The seasonal cycle of phytoplankton biomass and primary productivity in the Ross Sea, Antarctica. *Deep-Sea Research Part II: Topical Studies in Oceanography*. ISSN 09670645. doi: 10.1016/S0967-0645(00)00061-8.

Smith Jr., W. O., Sedwick, P. N., Arrigo, K. R., Ainley, D. G., and Orsi, A. H. 2012. The Ross Sea: In a Sea of Change. *Oceanography*, 25(3, SI):90–103. ISSN 1042-8275.

Snow, K., Sloyan, B. M., Rintoul, S. R., Hogg, A. M. C., and Downes, S. M. 2016. Controls on circulation, cross-shelf exchange, and dense water formation in an Antarctic polynya. *Geophysical Research Letters*, 43(13):7089–7096. ISSN 19448007. doi: 10.1002/2016GL069479.

Sokolov, S. and Rintoul, S. R. 2007. On the relationship between fronts of the Antarctic Circumpolar Current and surface chlorophyll concentrations in the Southern Ocean. *Journal of Geophysical Research*, 112(C7):C07030. ISSN 0148-0227. doi: 10.1029/2006JC004072.

Spector, P., Stone, J., Cowdery, S. G., Hall, B., Conway, H., and Bromley, G. 2017. Rapid early-Holocene deglaciation in the Ross Sea, Antarctica. *Geophysical Research Letters*, 44(15):7817–7825. ISSN 19448007. doi: 10.1002/2017GL074216.

Speer, K., Rintoul, S. R., and Sloyan, B. 2000. The diabatic Deacon cell. *Journal of Physical Oceanography*, 30(12):3212–3222. ISSN 00223670. doi: 10.1175/1520-0485(2000)030<3212:TDDC>2.0.CO;2.

Spence, P., Griffies, S. M., England, M. H., Hogg, A. M., Saenko, O. A., and Jourdain, N. C. 2014. Rapid subsurface warming and circulation changes of Antarctic coastal waters by poleward shifting winds. *Geophysical Research Letters*, 41(1):4601–4610. ISSN 00948276. doi: 10.1002/2014GL060613.Received.

St-Onge, G. and Long, B. F. 2009. CAT-scan analysis of sedimentary sequences: An ultrahigh-resolution paleoclimatic tool. *Engineering Geology*, 103:127–133. doi: 10.1016/j.enggeo.2008.06.016.

Stager, J. C. and Mayewski, P. A. 1997. Abrupt early to mid-holocene climatic transition registered at the equator and the poles. *Science*, 276(5320):1834–1836. ISSN 00368075. doi: 10.1126/science.276.5320.1834.

Stammerjohn, S. E., Martinson, D. G., Smith, R. C., Yuan, X., and Rind, D. 2008. Trends in Antarctic annual sea ice retreat and advance and their relation to El Niño–Southern Oscillation and Southern Annular Mode variability. *Journal of Geophysical Research*, 113(C3): C03S90. ISSN 0148-0227. doi: 10.1029/2007JC004269.

Steig, E. J., Hart, C. P., White, J. W., Cunningham, W. L., Davis, M. D., and Saltzman, E. S. 1998. Changes in climate, ocean and ice-sheet conditions in the Ross embayment, Antarctica, at 6 ka. *Annals of Glaciology*, 27:305–310. ISSN 02603055. doi: 10.3189/1998AoG27-1-305-310.

Steig, E. J., Morse, D. L., Waddington, E. D., Stuiver, M., Grootes, P. M., Mayewski, P. A., Twickler, M. S., and Whitlow, S. I. 2000. Wisconsinan and Holocene Climate History from an Ice Core at Taylor Dome, Western Ross Embayment, Antarctica. *Geografiska Annaler, Series A: Physical Geography*, 82(2-3):213–235. ISSN 0435-3676. doi: 10.1111/j.0435-3676.2000.00122.x.

Stenni, B., Buiron, D., Frezzotti, M., Albani, S., Barbante, C., Bard, E., Barnola, J. M., Baroni, M., Baumgartner, M., Bonazza, M., Capron, E., Castellano, E., Chappellaz, J., Delmonte, B., Falourd, S., Genoni, L., Iacumin, P., Jouzel, J., Kipfstuhl, S., Landais, A., Lemieux-Dudon, B., Maggi, V., Masson-Delmotte, V., Mazzola, C., Minster, B., Montagnat, M., Mulvaney, R., Narcisi, B., Oerter, H., Parrenin, F., Petit, J. R., Ritz, C., Scarchilli, C., Schilt, A., Schüpbach, S., Schwander, J., Selmo, E., Severi, M., Stocker, T. F., and Udisti, R. 2011. Expression of the bipolar see-saw in Antarctic climate records during the last deglaciation. *Nature Geoscience*, 4(1):46–49. ISSN 17520894. doi: 10.1038/ngeo1026.

Stewart, A. L. and Thompson, A. F. 2012. Sensitivity of the ocean's deep overturning circulation to easterly Antarctic winds. *Geophysical Research Letters*, 39(17):1–6. ISSN 00948276. doi: 10.1029/2012GL053099.

Stewart, A. L. and Thompson, A. F. 2015. Eddy-mediated transport of warm Circumpolar Deep Water across the Antarctic Shelf Break. *Geophysical Research Letters*, 42(2):432–440. ISSN 19448007. doi: 10.1002/2014GL062281.

Stuecker, M. F., Timmermann, A., Jin, F. F., Chikamoto, Y., Zhang, W., Wittenberg, A. T., Widiasih, E., and Zhao, S. 2017. Revisiting ENSO/Indian Ocean Dipole phase relationships. *Geophysical Research Letters*, 44(5):2481–2492. ISSN 19448007. doi: 10.1002/2016GL072308.

Takahashi, T., Sutherland, S. C., Sweeney, C., Poisson, A., Metzl, N., Tilbrook, B., Bates, N., Wanninkhof, R., Feely, R. A., Sabine, C., Olafsson, J., and Nojiri, Y. 2002. Global sea-air CO2 flux based on climatological surface ocean pCO2, and seasonal biological and temperature effects. *Deep-Sea Research Part II: Topical Studies in Oceanography*. ISSN 09670645. doi: 10.1016/S0967-0645(02)00003-6.

Takahashi, T., Sutherland, S. C., Wanninkhof, R., Sweeney, C., Feely, R. A., Chipman, D. W., Hales, B., Friederich, G., Chavez, F., Sabine, C., Watson, A., Bakker, D. C., Schuster, U., Metzl, N., Yoshikawa-Inoue, H., Ishii, M., Midorikawa, T., Nojiri, Y., Körtzinger, A., Steinhoff, T., Hoppema, M., Olafsson, J., Arnarson, T. S., Tilbrook, B., Johannessen, T., Olsen, A., Bellerby, R., Wong, C. S., Delille, B., Bates, N. R., and de Baar, H. J. 2009. Climatological mean and decadal change in surface ocean pCO2, and net sea-air CO2 flux over the global oceans. *Deep-Sea Research Part II: Topical Studies in Oceanography*. ISSN 09670645. doi: 10.1016/j.dsr2.2008.12.009.

Takeda, S. 1998. Influence of iron availability on nutrient consumption ratio of diatoms in oceanic waters. *Nature*, 393(6687):774–777. ISSN 00280836. doi: 10.1038/31674.

Tamura, T., Williams, G. D., Fraser, A., and Ohshima, K. 2012. Potential regime shift in decreased sea ice production after the Mertz Glacier calving. *Nature Communications*, 3:826. ISSN 2041-1723. doi: 10.1038/ncomms1820.

Tamura, T., Ohshima, K. I., and Nihashi, S. 2008. Mapping of sea ice production for Antarctic coastal polynyas. *Geophysical Research Letters*, 35(7):1–5. ISSN 00948276. doi: 10.1029/2007GL032903.

Tamura, T., Ohshima, K. I., Fraser, A. D., and Williams, G. D. 2016. Sea ice production variability in Antarctic coastal polynyas. *Journal of Geophysical Research: Oceans*, 121(5):2967–2979. ISSN 21699275. doi: 10.1002/2015JC011537.

The RAISED Consortium, Bentley, M. J., Ocofaigh, C., Anderson, J. B., Conway, H., Davies, B., Graham, A. G., Hillenbrand, C. D., Hodgson, D. A., Jamieson, S. S., Larter, R. D., Mackintosh, A., Smith, J. A., Verleyen, E., Ackert, R. P., Bart, P. J., Berg, S., Brunstein, D., Canals, M., Colhoun, E. A., Crosta, X., Dickens, W. A., Domack, E., Dowdeswell, J. A., Dunbar, R. B., Ehrmann, W., Evans, J., Favier, V., Fink, D., Fogwill, C. J., Glasser, N. F., Gohl, K., Golledge, N. R., Goodwin, I., Gore, D. B., Greenwood, S. L., Hall, B. L., Hall, K., Hedding, D. W., Hein, A. S., Hocking, E. P., Jakobsson, M., Johnson, J. S., Jomelli, V., Jones, R. S., Klages, J. P., Kristoffersen, Y., Kuhn, G., Leventer, A., Licht, K., Lilly, K., Lindow, J., Livingstone, S. J., Massé, G., McGlone, M. S., McKay, R. M., Melles, M., Miura, H., Mulvaney, R., Nel, W., Nitsche, F. O., O'Brien, P. E., Post, A. L., Roberts, S. J., Saunders, K. M., Selkirk, P. M., Simms, A. R., Spiegel, C., Stolldorf, T. D., Sugden, D. E., van der Putten, N., van Ommen, T., Verfaillie, D., Vyverman, W., Wagner, B., White, D. A., Witus, A. E., and Zwartz, D. 2014. A community-based geological reconstruction of Antarctic Ice Sheet deglaciation since the Last Glacial Maximum. *Quaternary Science Reviews*. ISSN 02773791. doi: 10.1016/j.quascirev.2014.06.025.

Thomas, E. R., Allen, C. S., Etourneau, J., King, A. C. F., Severi, M., Winton, V. H. L., Mueller, J., Crosta, X., and Peck, V. L. 2019. Antarctic Sea Ice Proxies from Marine and Ice Core Archives Suitable for Reconstructing Sea Ice over the past 2000 Years. *Geosciences*, 9(506):1–33. doi: 10.3390/geosciences9120506.

Thomas, R. H. and Bentley, C. R. 1978. A model for Holocene retreat of the West Antarctic Ice Sheet. *Quaternary Research*, 10(2):150–170. ISSN 10960287. doi: 10.1016/0033-5894(78)90098-4.

Thompson, A. F., Stewart, A. L., Spence, P., and Heywood, K. J. 2018. The Antarctic Slope Current in a Changing Climate. *Reviews of Geophysics*, 56:741–770.

Thompson, D. W. J. and Wallace, J. M. 2000a. Annular modes in the extratropical circulation. Part II: Trends. *Journal of Climate*, 13(5):1018–1036. ISSN 08948755. doi: 10.1175/1520-0442(2000)013<1018:AMITEC>2.0.CO;2.

Thompson, D. W. and Wallace, J. M. 2000b. Annular modes in the extratropical circulation. Part I: Month-to-month variability. *Journal of Climate*, 13(5):1000–1016. ISSN 08948755. doi: 10.1175/1520-0442(2000)013<1000:AMITEC>2.0.CO;2.

Thompson, D. W., Solomon, S., Kushner, P. J., England, M. H., Grise, K. M., and Karoly,

D. J. 2011. Signatures of the Antarctic ozone hole in Southern Hemisphere surface climate change. *Nature Geoscience*, 4(11):741–749. ISSN 17520894. doi: 10.1038/ngeo1296.

Trauth, M. H., Larrasoaña, J. C., and Mudelsee, M. 2009. Trends, rhythms and events in Plio-Pleistocene African climate. *Quaternary Science Reviews*, 28(5-6):399–411. ISSN 02773791. doi: 10.1016/j.quascirev.2008.11.003.

Tréguer, P. and Pondaven, P. Climatic changes and the carbon cycle in the Southern Ocean: A step forward. In *Deep-Sea Research Part II: Topical Studies in Oceanography*, 2002. doi: 10.1016/S0967-0645(02)00002-4.

Tremblay, J. E. and Smith, W. O. Primary Production and Nutrient Dynamics in Polynyas. In Smith Jr., W. O., editor, *Elsevier Oceanography Series*, volume 74, pages 239–269. Elsevier Oceanography Series, 74 edition, 2007. ISBN 9780444529527. doi: 10.1016/S0422-9894(06)74008-9.

Trenberth, K. E. and Stepaniak, D. P. 2001. Indices of El Niño evolution. *Journal of Climate*, 14(8):1697–1701. ISSN 08948755. doi: 10.1175/1520-0442(2001)014<1697:LIOENO>2.0.CO;2.

Trenberth, K. E. 1980. Planetary Waves at 500 mb in the Southern Hemisphere. *Monthly Weather Review*, pages 1378–1389.

Trenberth, K. E., Branstator, G. W., Karoly, D., Ng Lau, N.-C. [U+FFFD] Ropelewski, C., and Kumar, A. Progress during TOGA in understanding and modeling global teleconnections associated with tropical sea surface temperatures • National Cente• for Atmospheric Researchl Boulder, Col-orado. Technical Report C7, 1998.

Turner, J. ARCTIC AND ANTARCTIC | Antarctic Climate. In North, G. R., Pyle, J., and Zhang, F. B. T. E. o. A. S. S. E., editors, *Encyclopedia of Atmospheric Sciences*, pages 98–106. Academic Press, Oxford, second edition, 2015. ISBN 978-0-12-382225-3. doi: https://doi.org/10.1016/B978-0-12-382225-3.00044-X.

Turner, J. 2004. The El Niño-Southern Oscillation and Antarctica. *International Journal of Climatology*, 24(1):1–31. ISSN 08998418. doi: 10.1002/joc.965.

Turner, J., Colwell, S. R., Marshall, G. J., Lachlan-Cope, T. A., Carleton, A. M., Jones, P. D., Lagun, V., Reid, P. A., and Iagovkina, S. 2004. The SCAR READER project: Toward a high-quality database of mean Antarctic meteorological observations. *Journal of Climate*, 17(14):

2890–2898. ISSN 08948755. doi: 10.1175/1520-0442(2004)017<2890:TSRPTA>2.0.CO;2.

Turner, J., Phillips, T., Hosking, J. S., Marshall, G. J., and Orr, A. 2013. The amundsen sea low. *International Journal of Climatology*, 33(7):1818–1829. ISSN 08998418. doi: 10.1002/joc.3558.

Turner, J., Orr, A., Gudmundsson, G. H., Jenkins, A., Bingham, R. G., Hillenbrand, C. D., and Bracegirdle, T. J. 2017a. Atmosphere-ocean-ice interactions in the Amundsen Sea Embayment, West Antarctica. *Reviews of Geophysics*, 55(1):235–276. ISSN 19449208. doi: 10.1002/2016RG000532.

Turner, J., Phillips, T., Marshall, G. J., Hosking, J. S., Pope, J. O., Bracegirdle, T. J., and Deb, P. 2017b. Unprecedented springtime retreat of Antarctic sea ice in 2016. *Geophysical Research Letters*, 44(13):6868–6875. ISSN 19448007. doi: 10.1002/2017GL073656.

Vaillancourt, R. D., Sambrotto, R. N., Green, S., and Matsuda, A. 2003. Phytoplankton biomass and photosynthetic competency in the summertime Mertz Glacier Region of East Antarctica. *Deep Sea Research Part II: Topical Studies in Oceanography*, 50(8-9):1415–1440. ISSN 0967-0645. doi: 10.1016/S0967-0645(03)00077-8.

Vallelonga, P., Maffezzoli, N., Moy, A. D., Curran, M. A. J., Vance, T. R., Edwards, R., Hughes, G., Barker, E., Spreen, G., Saiz-Lopez, A., Corella, J. P., Cuevas, C. A., and Spolaor, A. 2017. Sea-ice-related halogen enrichment at Law Dome, coastal East Antarctica. *Climate of the Past*, 13(2):171–184. ISSN 1814-9332. doi: 10.5194/cp-13-171-2017.

Vance, T. R., Roberts, J. L., Plummer, C. T., Kiem, A. S., and Van Ommen, T. D. 2015. Interdecadal Pacific variability and eastern Australian megadroughts over the last millennium. *Geophysical Research Letters*, 42(1):129–137. ISSN 19448007. doi: 10.1002/2014GL062447.

Vance, T. R., Van Ommen, T. D., Curran, M. A., Plummer, C. T., and Moy, A. D. 2013. A millennial proxy record of ENSO and eastern Australian rainfall from the law dome ice core, east Antarctica. *Journal of Climate*, 26(3):710–725. ISSN 08948755. doi: 10.1175/JCLI-D-12-00003.1.

Vance, T. R., Roberts, J. L., Moy, A. D., Curran, M. A. J., Tozer, C. R., Gallant, A. J. E., Abram, N. J., Van Ommen, T. D., Young, D. A., Grima, C., Blankenship, D. D., and Siegert, M. J. 2016. Optimal site selection for a high-resolution ice core record in East Antarctica. *Clim. Past*, 12:595–610. doi: 10.5194/cp-12-595-2016.

Vega, C. P., Isaksson, E., Schlosser, E., Divine, D., Martma, T., Mulvaney, R., Eichler, A., and Schwikowski-Gigar, M. 2018. Variability of sea salts in ice and firn cores from Fimbul Ice Shelf, Dronning Maud Land, Antarctica. *The Cryosphere*, 12:1681–1697. doi: 10.5194/tc-12-1681-2018.

Venables, H. J., Clarke, A., and Meredith, M. P. 2013. Wintertime controls on summer stratification and productivity at the western Antarctic Peninsula. *Limnology and Oceanography*, 58(3):1035–1047. ISSN 00243590. doi: 10.4319/lo.2013.58.3.1035.

Verleyen, E., Hodgson, D. A., Sabbe, K., Cremer, H., Emslie, S. D., Gibson, J., Hall, B., Imura, S., Kudoh, S., Marshall, G. J., McMinn, A., Melles, M., Newman, L., Roberts, D., Roberts, S. J., Singh, S. M., Sterken, M., Tavernier, I., Verkulich, S., de Vyver, E. V., Van Nieuwenhuyze, W., Wagner, B., and Vyverman, W. 2011. Post-glacial regional climate variability along the East Antarctic coastal margin—Evidence from shallow marine and coastal terrestrial records. *Earth-Science Reviews*, 104(4):199–212. ISSN 0012-8252. doi: 10.1016/J.EARSCIREV.2010.10.006.

Wagenbach, D., Ducroz, F., Mulvaney, R., Keck, L., Minikin, A., Legrand, M., Hall, J. S., and Wolff, E. W. 1998. Sea-salt aerosol in coastal Antarctic regions. *Journal of Geophysical Research D: Atmospheres*, 103(3339):10961–10974. ISSN 01480227. doi: 10.1029/97jd01804.

Wåhlin, A. K., Yuan, X., Björk, G., and Nohr, C. 2010. Inflow of warm Circumpolar Deep Water in the central Amundsen shelf. *Journal of Physical Oceanography*, 40(6):1427–1434. ISSN 00223670. doi: 10.1175/2010JPO4431.1.

Walker, G. 1923. Correlation in seasonal variation of weather. VIII : A preliminary study of world weatherWALKER, G. T. (1923). Correlation in seasonal variation of weather. VIII : A preliminary study of world weather. Memoirs of India Meteorological Department, 24, 75–13. *Memoirs of India Meteorological Department*, 24:75–131.

Walker, G. 1924. Correlations in seasoWALKER, G. T. (1924). Correlations in seasonal variations of weather. I. A further study of world weather. Mem. Indian Meteorol. Dep., 24, 275–332. Retrieved from https://ci.nii.ac.jp/naid/10030539394/nal variations of weather. I. A f. *Mem. Indian Meteorol. Dep.*, 24:275–332.

Walker, M. J., Berkelhammer, M., Björck, S., Cwynar, L. C., Fisher, D. A., Long, A. J., Lowe, J. J., Newnham, R. M., Rasmussen, S. O., and Weiss, H. 2012. Formal subdivision of the

Holocene Series/Epoch: A Discussion Paper by a Working Group of INTIMATE (Integration of ice-core, marine and terrestrial records) and the Subcommission on Quaternary Stratigraphy (International Commission on Stratigraphy). *Journal of Quaternary Science*, 27(7):649–659. ISSN 02678179. doi: 10.1002/jqs.2565.

Wang, H., Murtugudde, R., and Kumar, A. 2016. Evolution of Indian Ocean dipole and its forcing mechanisms in the absence of ENSO. *Climate Dynamics*, 47(7-8):2481–2500. ISSN 14320894. doi: 10.1007/s00382-016-2977-y.

Wang, H., Kumar, A., Murtugudde, R., Narapusetty, B., and Seip, K. L. 2019. Covariations between the Indian Ocean dipole and ENSO: a modeling study. *Climate Dynamics*. ISSN 0930-7575. doi: 10.1007/s00382-019-04895-x.

Wanner, H., Mercolli, L., Grosjean, M., and Ritz, S. P. 2015. Holocene climate variability and change; a data-based review. *Journal of the Geological Society*, 172(2):254–263. ISSN 00167649. doi: 10.1144/jgs2013-101.

Wanner, H., Solomina, O., Grosjean, M., Ritz, S. P., and Jetel, M. 2011. Structure and origin of Holocene cold events. *Quaternary Science Reviews*, 30(21-22):3109–3123. ISSN 02773791. doi: 10.1016/j.quascirev.2011.07.010.

Webster, P. J., Moore, A. M., Loschnigg, J. P., and Leben, R. R. 1999. Coupled ocean-atmosphere dynamics in the Indian Ocean during 1997-98. *Nature*, 401(6751):356–360. ISSN 00280836. doi: 10.1038/43848.

Weertman, J. 1974. STABILITY OF THE JUNCTION OF AN ICE SHEET AND AN ICE SHELF. *Journal of GlacioJoD*, 13(67).

Welch, K. A., Mayewski, P. A., and Whitlow, S. I. 1993. Methanesulfonic Acid in Coastal Antarctic Snow Related to Sea-Ice Extent. *Geophysical Research Letters*, 20(6):443–446.

Wendler, G., Stearns, C., Weidner, G., Dargaud, G., and Parish, T. 1997. On the extraordinary katabatic winds of Adélie Land. *Journal of Geophysical Research*, 102(D4):4463. ISSN 0148-0227. doi: 10.1029/96JD03438.

White, D. A., Fink, D., Post, A. L., Simon, K., Galton-Fenzi, B., Foster, S., Fujioka, T., Jeromson, M. R., Blaxell, M., and Yokoyama, Y. 2019. Beryllium isotope signatures of ice shelves and sub-ice shelf circulation. *Earth and Planetary Science Letters*. ISSN 0012821X. doi: 10.1016/j.epsl.2018.10.004.

White, W. B. and Peterson, R. G. 1996. An Antarctic Circumpolar Wave in Surface Pressure, Wind, Temperature and Sea-Ice Extent. *Nature*, 380:699–702. doi: https://doi.org/10.1038/380699a0.

Whitworth, T. 1988. The Antarctic Circumpolar Current. *Oceanus*, 32:53–58.

Whitworth, T. 2002. Two modes of bottom water in the Australian-Antarctic Basin. *Geophysical Research Letters*, 29(5):11–17. ISSN 0094-8276. doi: 10.1029/2001GL014282.

Whitworth, T., Orsi, A. H., Kim, S. J., Nowlin Jr., W. D., Locarnini, R. A., and Nowlin Jr., W. Water masses and mixing near the Antarctic Slope Front. In Jacobs, S. S. and Weiss, R. F., editors, *Ocean, Ice, and Atmosphere: Interactions at the Antarctic Continental Margin*, volume 75, pages 1–27. American Geophysical Union, 1998. ISBN 9781118668238. doi: 10.1029/AR075p0001.

Wieners, C. E., Dijkstra, H. A., and de Ruijter, W. P. 2017. The influence of the Indian Ocean on ENSO stability and flavor. *Journal of Climate*, 30(7):2601–2620. ISSN 08948755. doi: 10.1175/JCLI-D-16-0516.1.

Williams, G. D. and Bindoff, N. L. 2003. Wintertime oceanography of the Adélie Depression. *Deep-Sea Research Part II: Topical Studies in Oceanography*, 50(8-9):1373–1392. ISSN 09670645. doi: 10.1016/S0967-0645(03)00074-2.

Williams, G. D., Bindoff, N. L., Marsland, S. J., and Rintoul, S. R. 2008. Formation and export of dense shelf water from the Adélie depression, East Antarctica. *Journal of Geophysical Research: Oceans*, 113(4):1–12. ISSN 21699291. doi: 10.1029/2007JC004346.

Williams, G. D., Aoki, S., Jacobs, S. S., Rintoul, S. R., Tamura, T., and Bindoff, N. L. 2010. Antarctic Bottom Water from the Adélie and George V Land coast, East Antarctica (140–149°E). *Journal of Geophysical Research*, 115(C4):C04027. ISSN 0148-0227. doi: 10.1029/2009JC005812.

Williams, G. D., Herraiz-Borreguero, L., Roquet, F., Tamura, T., Ohshima, K. I., Fukamachi, Y., Fraser, A. D., Gao, L., Chen, H., McMahon, C. R., Harcourt, R., and Hindell, M. 2016. The suppression of Antarctic bottom water formation by melting ice shelves in Prydz Bay. *Nature Communications*, 7(6):12577. ISSN 2041-1723. doi: 10.1038/ncomms12577.

Winstrup, M., Vallelonga, P., Kjær, H. A., Fudge, T. J., Lee, J. E., Riis, M. H., Edwards, R., Bertler, N. A., Blunier, T., Brook, E. J., Buizert, C., Ciobanu, G., Conway, H., Dahl-Jensen, D., Ellis,

A., Emanuelsson, B. D., Hindmarsh, R. C., Keller, E. D., Kurbatov, A. V., Mayewski, P. A., Neff, P. D., Pyne, R. L., Simonsen, M. F., Svensson, A., Tuohy, A., Waddington, E. D., and Wheatley, S. 2019. A 2700-year annual timescale and accumulation history for an ice core from Roosevelt Island, West Antarctica. *Climate of the Past*, 15(2):751–779. ISSN 18149332. doi: 10.5194/cp-15-751-2019.

Wolff, E. W., Fischer, H., Fundel, F., Ruth, U., Twarloh, B., Littot, G. C., Mulvaney, R., Röthlisberger, R., De Angelis, M., Boutron, C. F., Hansson, M., Jonsell, U., Hutterli, M. A., Lambert, F., Kaufmann, P., Stauffer, B., Stocker, T. F., Steffensen, J. P., Bigler, M., Siggaard-Andersen, M. L., Udisti, R., Becagli, S., Castellano, E., Severi, M., Wagenbach, D., Barbante, C., Gabrielli, P., and Gaspari, V. 2006. Southern Ocean sea-ice extent, productivity and iron flux over the past eight glacial cycles. *Nature*, 440(7083):491–496. ISSN 14764687. doi: 10.1038/nature04614.

Wolff, E. W., Rankin, A. M., and Röthlisberger, R. 2003. An ice core indicator of Antarctic sea ice production? *Geophysical Research Letters*, 30(22):2–5. ISSN 00948276. doi: 10.1029/2003GL018454.

Wyrtki, K. 1961. The thermohaline circulation in relation to the general circulation in the oceans. *Deep-Sea Research*, 8:39–64.

Yamane, M., Yokoyama, Y., Miyairi, Y., Suga, H., Matsuzaki, H., Dunbar, R. B., and Ohkouchi, N. 2014. Compound-Specific 14 C Dating of IODP Expedition 318 Core U1357A Obtained Off the Wilkes Land Coast, Antarctica . *Radiocarbon*, 56(3):1009–1017. ISSN 0033-8222. doi: 10.2458/56.17773.

Yang, X., Pyle, J. A., and Cox, R. A. 2008. Sea salt aerosol production and bromine release: Role of snow on sea ice. *Geophysical Research Letters*, 35(16):1–5. ISSN 00948276. doi: 10.1029/2008GL034536.

Yeh, S. W., Kug, J. S., Dewitte, B., Kwon, M. H., Kirtman, B. P., and Jin, F. F. 2009. El Niño in a changing climate. *Nature*, 461(7263):511–514. ISSN 00280836. doi: 10.1038/nature08316.

Yokoyama, Y., Anderson, J. B., Yamane, M., Simkins, L. M., Miyairi, Y., Yamazaki, T., Koizumi, M., Suga, H., Kusahara, K., Prothro, L., Hasumi, H., Southon, J. R., and Ohkouchi, N. 2016. Widespread collapse of the Ross Ice Shelf during the late Holocene. *Proceedings of the National Academy of Sciences*, 113(9):2354–2359. ISSN 0027-8424. doi: 10.1073/pnas.1516908113.

Young, D. A., Wright, A. P., Roberts, J. L., Warner, R. C., Young, N. W., Greenbaum, J. S., Schroeder, D. M., Holt, J. W., Sugden, D. E., Blankenship, D. D., Van Ommen, T. D., and Siegert, M. J. 2011. A dynamic early East Antarctic Ice Sheet suggested by ice-covered fjord landscapes. *Nature*, 474(7349):72–75. ISSN 00280836. doi: 10.1038/nature10114.

Young, N., Legresy, B., Coleman, R., and Massom, R. A. 2010. Mertz Glacier tongue unhinged by giant iceberg — Australian Antarctic Program. *Australian Antarctic Magazine*, (18):19.

Yu, M. and Ruggieri, E. 2019. Change point analysis of global temperature records. *International Journal of Climatology*, 39(8):3679–3688. ISSN 10970088. doi: 10.1002/joc.6042.

Yuan, N., Ding, M., Ludescher, J., and Bunde, A. 2017. Increase of the Antarctic Sea Ice Extent is highly significant only in the Ross Sea. *Scientific Reports*, 7. ISSN 20452322. doi: 10.1038/srep41096.

Yuan, X. 2004. ENSO-related impacts on Antarctic sea ice: A synthesis of phenomenon and mechanisms. *Antarctic Science*, 16(4):415–425. ISSN 09541020. doi: 10.1017/S0954102004002238.

Yuan, X. and Li, C. 2008. Climate modes in southern high latitudes and their impacts on Antarctic sea ice. *Journal of Geophysical Research*, 113(C6):C06S91. ISSN 0148-0227. doi: 10.1029/2006JC004067.

Yuan, X. and Martinson, D. G. Antarctic Sea Ice Extent Variability and Its Global Connectivity*. Technical report, 2000.

Zhang, Z., Leduc, G., and Sachs, J. P. 2014. El Niño evolution during the Holocene revealed by a biomarker rain gauge in the Galápagos Islands. *Earth and Planetary Science Letters*, 404: 420–434. ISSN 0012821X. doi: 10.1016/j.epsl.2014.07.013.

Zwally, H. J., Comiso, J. C., and Gordon, A. L. Antarctic offshore leads and polynyas and oceanographic effects. In Jacobs, S., editor, *Oceanology of the Antarctic Continental Shelf*, pages 203–226. 1985. ISBN 9780875901961. doi: 10.1029/ar043p0203.